Fatigue life prediction of an aluminium alloy automotive component using finite element analysis of surface topography

Sigmund Kyrre Ås

A dissertation submitted in partial fulfillment of the requirements for the degree of Doctor of Philosophy.

NTNU
Norwegian University of Science and Technology
Department of Structural Engineering

Department of Structural Mechanics
Faculty of Engineering Science and Technology
Norwegian University of Science and Technology
7491 Trondheim, Norway
Published 2006

Doctoral thesis 2006:25
ISSN 1503-8181
ISBN 82-471-7791-9 (printed)
ISBN 82-471-7790-0 (pdf)

Contents

List of Figures

List of Tables

Abstract

A 6082 aluminium alloy has been characterized with regard to the influence of surface roughness on fatigue strength. Earlier results from this work have been reported elsewhere[1]. Fatigue life testing of smooth specimens was used to establish reference curves for the material in extruded and forged T6 condition. The extruded material was found to have better fatigue strength than the forged material, although the cyclic stress-strain response was similar for both. The forged material was tested in T5, T6 and T7 tempers, showing no significant difference in fatigue strength.

Surface roughness was created by circumferential grinding of cylindrical test specimens, and the surface topography was measured using a white light interferometry microscope. The measurements proved to be accurate, although errors were observed for certain surface features. Residual stresses were quantified by X-ray diffraction. Compressive residual stresses of around 150 MPa were found in both rough and smooth specimens. Load cycling did not significantly alter the surface residual stresses.

Stress solutions ahead of all major surface grooves were found using a linear elastic material model. Estimates of cyclic stresses and strains were calculated in the notch roots using different Neuber corrections of the linear solution. The results were compared to finite element analysis employing a bilinear kinematic hardening model. A generalized version of the Neuber correction was found to be within 20% of the nonlinear finite element results.

Several empirical models for the notch sensitivity factor were investigated. These were found to be unable to describe the notch influence on fatigue life and initiation life. In order to follow this approach, it was recommended that different test specimens should be used where the short fatigue crack growth could be monitored.

It was shown that microstructural fracture mechanics theories could be used to estimate the fatigue limit of rough surfaces. In some cases, initiation from material defects or weaknesses would override the influence of surface geometry. In one specimen, the initiation appeared to have started as at a de-bonded grain, while in other cases, initiation was thought to have started at larger second phase particles embedded in notch roots. Further work in this area should focus on statistical descriptions of surface roughness, inherent material defects, and their interaction.

[1]S.K. Ås and B. Skallerud. Localised cyclic plasticity and initiation of fatigue cracks in aluminium using measured surface topography, In *Proc LCF5*, Berlin, 2003.

S.K. Ås, B. Skallerud, B.W. Tveiten, and B. Holme. Study of fatigue crack initiation in rough surfaces using the finite element method and measured surface topography, In *Proc ECF15*, Stockholm, 2004

S.K. Ås, B. Skallerud, B.W. Tveiten, and B. Holme. *Fatigue life prediction of machined components using finite element analysis of surface topography*, Int J Fat, 27:1590-1596, 2005.

Preface

This work has been supported by the Research Council of Norway and the Norwegian light metals industry through the NorLight project. I have been part of the Fatigue & Durability project, which is managed by SINTEF. I have also received support in the form of computing time from Notur, the Norwegian center for high performance computing.

I feel fortunate to have been surrounded by inspirational colleagues at both NTNU and SINTEF. I would like to thank my supervisor Prof. Bjørn Skallerud[*] and co-supervisor Bård W. Tveiten[†] for their encouragement, ideas, and valuable comments. Børge Holme[†] is acknowledged for developing WLI measurement procedures, in addition to contributing with ideas in topics outside of his background in physics. Also, thanks to Martin Fleissner[†] who continued Børge's work with WLI measurements, Odd Nerdahl[†] who provided invaluable support in the laboratory, Ragnvald Mathiesen[†] for guidance on interpreting synchrotron X-ray results, Ketill Pedersen[†] for feedback on metallurgical topics, Tone Anzjøn[†] and Birgitte Karlsen[†] who prepared specimens for testing and characterization, Trond Furu[‡] who kindly performed chemical analyses, and John Rasmus Leinum[*] and Prof. Jarle Hjelen[*] for assistance with the SEM. Thanks also to my contacts in the industry; Steinar Sørbø[§], Prof. Ola Jensrud[*§], and Øystein Ruste[¶] for their openness and insightful comments. I would like to thank Prof. Huseyin Sehitoglu for hosting me four months at the University of Illinois at Urbana-Champaign.

[*]NTNU
[†]SINTEF, The Foundation of Scientific and Industrial Research.
[‡]Hydro Aluminium
[§]Raufoss Technology and Industrial Management
[¶]Raufoss Technology

Chapter 1

Introduction

A large part of engineering design involves assessment of strength in structures and components. Depending on the intended application of the product, different failure modes are considered, each with its corresponding theoretical framework. A structure can fail due to buckling where the theory of elasticity is a central element, or due to static overload where plasticity theory is used. Fatigue failure can occur if the structure is subjected to alternating loads below what is required to cause static failure. This can occur after thousands or millions of load cycles, indicating that the material weakens or experiences *fatigue damage* due to the repeated loads.

Whereas the conditions for yielding can be determined quite accurately using a single plasticity analysis, the fatigue process is composed of several stages that require different analysis strategies. In the broadest sense, one of two assumptions about the material is made:

1. The material is homogenous and free of initial defects.
2. The material is homogenous, but contains an initial defect or crack.

If the first assumption is reasonable, the *fatigue initiation life* can be estimated from the cyclic stress state in the surface of a given structure. The stresses are calculated analytically or numerically from an idealized model of the structure, and the fatigue life is found by correlating fatigue lives of small-scale specimens tested under similar stress states. In the second assumption, a mathematical model of an idealized crack is used to predict the *crack propagation life* from an initial defect. An appropriate length and shape of the idealized crack must be assumed, and can for instance be the largest possible crack that may pass quality inspection without being detected.

The two assumptions require different mathematical models and test procedures to establish relevant material properties. Test specimens for initiation and propagation of fatigue cracks are shown in Figure 1.1. A compact-tension specimen is typically used in fracture mechanics testing, and a round bar is used in strain controlled fatigue testing. The round bar specimen represents the material behavior in the notch of a component, and the fatigue life to fatigue

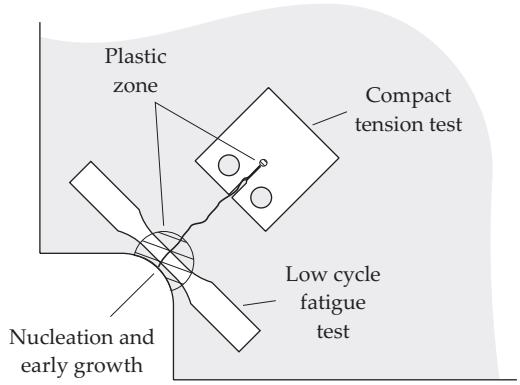

Figure 1.1: Different laboratory test specimens are used to quantify the material's resistance to fatigue failure. The low cycle fatigue specimen is here assumed to represent the material at a geometric stress concentration in a component, while the compact tension test simulates the conditions for a long crack [1].

crack initiation life for this specimen is assumed to coincide with the actual component. When the crack has grown further into the component, a compact tension specimen can be used to estimate the crack growth rate at a given crack length.

Material data in engineering design is typically derived from small scale specimens, since testing on full scale components is expensive or even impossible if very high loads are required. However, using test data obtained from small scale specimens poses a significant challenge. The component geometry is quite different in terms of geometry and surface finish, and will experience environmental attacks as well as different loading conditions than the test specimens. Although it is, to a certain extent, possible to establish empirical relations for such influences separately, it is not feasible to test every combination of influence factors. In order to establish methods with general life prediction abilities, it is of interest to limit the empiricism associated with fatigue strength in favor of physical models with broader applicability.

Quantification of surface roughness with regard to fatigue crack initiation is the topic of this study. Material from a car suspension arm, shown in Figure 1.2, is used for testing and evaluation of fatigue prediction methods. In the following sections, a motivation for this research is given, along with an introduction to engineering methods used in fatigue life prediction.

1.1 Aluminium in automotive design

Using aluminium alloys in passenger cars is not a new idea; the Ford Model-T for instance featured an aluminium body as early as 1922 [2]. Since then, aluminium alloys have been limited in use due to their higher cost and less developed

Figure 1.2: The suspension arm in a Saab 9-3 Convertible.

manufacturing processes compared to steel. Aluminium does, however, offer the advantage of lower weight, and has therefore been used in high performance cars where the higher cost can be justified.

Vehicle weight reduction has become increasingly important in the past decades. The US Government has imposed some of the strictest standards on fuel efficiency and exhaust emissions since the 1970s, in large parts due to the 1973 oil crisis [3]. Also, the mounting problems of air pollution in larger cities during this period promoted emission legislations in both Europe and USA. The immediate response from the car industry was to reduce the size of passenger cars and discontinue the larger engine options [4]. Weight reduction influences fuel economy directly, since less energy is needed for acceleration, and indirectly, since a smaller engine is required in a lighter car.

In order to reduce vehicle weight, the car industry has seen a continuous increase in aluminium usage in the last 30 years, mainly as cast engine blocks, engine parts, and transmissions where significant weight savings can be achieved [5, 6]. In the last decade, aluminium has also found use in structural applications in mass market cars, such as brake components, steering components and suspension control arms – areas where safety is of great concern and traditional steel solutions used to dominate. Vehicles with extensive use of aluminium, such as in body structures and panels, are still mainly found in the high-end market. A notable exception is the compact Audi A2, produced from 1999 to 2005, which used an aluminium space frame concept developed for the

more expensive Audi A8.

It is paradoxical that, despite the increased use of lightweight chassis designs, the average weight of cars has increased steadily since the mid 1980s. This is especially pronounced in the US, where the average weight for all 2006 models was 1878 kg, up from 1406 kg in 1987, and exceeding the 1975 average by 37 kg [7]. One reason for this is the increased market share of vans and SUVs. Along with pickup trucks, these accounted for 50% of the sales in 2005, up from 19% in 1975. Within each vehicle category, from small cars to large trucks, the weight decreased by less than 1% over the same time period [8]. The reason is that the achievements made in lightweight chassis design have been offset by weight gains in the powertrain and the interior.

Suspension components, along with wheel rims and brake components are unsprung masses, which make weight reduction important for ride quality and response as well as for reducing the total vehicle weight. The suspension arm referred to in this report is currently in use in General Motor's "Epsilon" architecture – a common platform for mid-size, front wheel drive cars such as Opel Vectra, Saab 9-3 and Pontiac G6. The material is a 6082 aluminium alloy, which has good formability and corrosion resistance as well as high impact and fatigue strength. Good formability is important for this component since it is produced by forging. Although stronger aluminium alloys exist, these are less suitable for forging operations and may also lack adequate corrosion resistance [9]. In North America, the 6061 alloy has been used for similar applications due to its better formability, albeit lower strength [6]. Advances in manufacturing technologies have in the past decades established less formable, higher strength alloys as viable and light weight alternatives to steel in car bodies and safety critical components [10, 11].

1.1.1 Design criteria

The high-strength alloys in the 2000 (AlCu) and 7000 (AlZn) series have been subject to extensive fatigue research due to their use in aircraft structures [12]. A so-called damage tolerant design is used in fatigue life assessment, where a certain amount of crack growth is allowed before they need to be replaced. The integrity of the structures is guaranteed by regular inspection intervals. As an additional safety measure, some parts are replaced after a predefined number of takeoffs and landings or miles flown. Fracture mechanics is the foundation of the damage tolerant design, and has proven highly successful for this purpose [13–15]. Ground vehicles for public use cannot rely on frequent inspections and replacement of parts. A safe life design is therefore used, where structures are designed to be safe throughout the service life of the vehicle [9, 16]. This entails a very different fatigue life prediction regime than the fracture mechanics approach used in airplanes. Referring again to Figure 1.1, the damage tolerant and safe life design criteria require material parameters derived from compact tension tests and plain specimen fatigue tests respectively. Whereas aircraft alloys are well characterized in terms of fatigue initiation and crack growth in

the open literature, fatigue data for the alloys emerging in car structures are more scarce. These alloys consist for the most part of the 5000 (AlMg) and 6000 (AlMgSi) series, known for their good corrosion resistance and strength, as well as being applicable in cost effective manufacturing processes involving welding and forming operations [5, 17, 18].

For safety critical components, such as a suspension arm, fatigue life is defined as the time to initiate a small crack, although fracture mechanics can be used to assess the component's integrity in case of a special event loading [19]. Compared to airplane structures, there is more uncertainty as to what loads to expect for a given car component due to individual driving styles and varying geographic road conditions. Furthermore, the prediction of fatigue crack initiation is associated with less accuracy than crack growth predictions, leading to a considerable uncertainty with regard to fatigue strength even under controlled laboratory conditions. In order to account for uncertainties, various empirical safety factors are used, in effect increasing the size of the components so that fatigue failure would be highly unlikely from the expected use. Prediction uncertainty is therefore a competing factor in the aforementioned trend towards reducing vehicle weight – improving life prediction accuracy allows lighter designs to be used.

1.1.2 Virtual prototyping

Development cost and time to market are the governing design aspects in the automotive industry. Releasing new and improved designs can give a significant competitive edge and define the success or failure of an entire product line. A study that aimed at shortening a typical 4 year development programme by 20% suggested an estimated £1 billion in increased sales and cost savings of about £90 millions for a given car manufacturer [20]. At the same time, the cost of a recall after the model has been released can be very high, thus the reduction in development time cannot be made at the expense of quality. Extensive testing of prototypes in laboratory and on proving grounds prior to the release of new models is therefore required in order to guarantee the safety and functionality of the design. With the high production volumes found in the car industry, a significant cost of tooling and automated production lines can be defended, but as a consequence, design changes are very expensive once the production line has been laid out. Computer simulations are therefore used extensively at an early stage in design, and the accuracy of these simulations can reduce or eliminate surprises during final testing [21, 22].

Figure 1.3 shows an example of a quarter car finite element model where strains in the lower suspension arm were found by running dynamical simulations of various road conditions and driving styles [23, 24]. The critical location with regard to fatigue life was identified as shown in the inset figure, where the time history of surface strains for the whole component were used with a strain based damage model. The developments in software and computing power in the last decade has established full vehicle simulations as an efficient design tool,

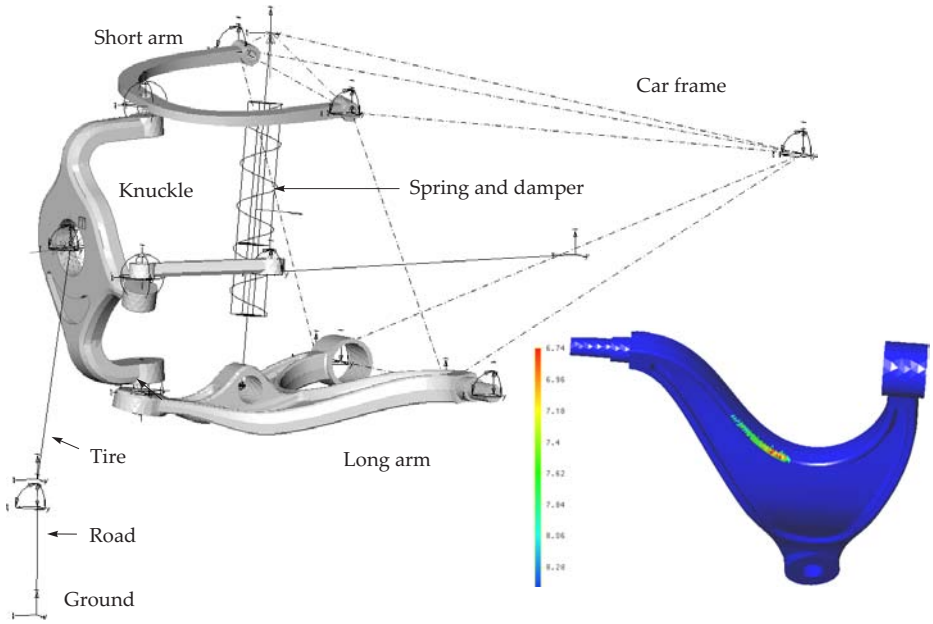

Figure 1.3: A flexible multibody model of a short-long arm (SLA) suspension system. Dynamical simulations of driving yields the estimated fatigue life, shown as log-life color codes to the right [23, 24].

allowing engineers to evaluate road handling, noise, aerodynamics, strength and stiffness [25, 26]. This is commonly referred to as virtual prototyping. One of the goals of the current work is to improve the fatigue life prediction methods used in such simulations[1].

1.1.3 Production monitoring

In-line process inspection is of interest for quality assurance in high volume production. Stopping the production is very expensive, and is not done unless the process clearly operates outside its limits – at the same time, having a faulty process running also leads to lost production time and refinement to scrap down the production line. Visual control is error-prone and ineffective, leading to a strong demand for automatization of product inspection [27]. A white light interferometry (WLI) microscope [28] is used in the current work to measure surface topography. Fast, non-contact measurements can be made using WLI, making the technique attractive as an in-line process inspection tool. By developing a framework for fatigue life prediction based on WLI measurements,

[1] FE-Fatigue from nCode and FEMFAT from Magna are finite element post-processors that support the most common multibody FE codes, such as ABAQUS, ANSYS, FEDEM, ADAMS and HyperMesh.

more accurate criteria can be used for halting and adjusting the production process.

1.2 Fatigue life assessment

A description of the fatigue phenomenon is best illustrated through some of the empirical fatigue life assessment methods developed over the years. Although these methods are quite old, they are still used by engineers in initial design studies or even for final designs where large safety factors are viable.

1.2.1 Fatigue life curves

The beginning of fatigue research, and especially the use of fatigue life curves, is somewhat erroneously credited to Wöhler. He was not the first to study fatigue, nor did he use curves but tables to present fatigue life data [29]. This is not to imply that he does not deserve his current fame; among his most important contributions was the notion of an *endurance limit* and that stress range as opposed to peak stress is a governing parameter. He was also the first to propose an infinite-life concept using safety factors to account for scatter, and he made in-service load measurements on railway axles and built rotating-bending and torsional fatigue test machines to test smooth and notched specimens. The pioneering research he did in the 1860s was unsurpassed in the 19th century. When Basquin, 50 years later, formulated the familiar log-log relation between stress amplitude σ_a and fatigue life N_f as $\sigma_a = A(N_f)^B$, he used Wöhler's fatigue life data [29]. This expression was later reformulated to depend on the number of reversals:

$$\frac{\Delta\sigma}{2} = \sigma_a = \sigma'_f(2N_f)^b, \tag{1.1}$$

where σ'_f is the fatigue strength coefficient and b is the fatigue strength exponent. In this formulation, σ'_f at one half-cycle ($2N_f$=1) is consistent with the definition of monotonic fracture strength σ_f, although their values usually differ [30].

A typical SN curve is shown in Figure 1.4. The stress-life approach is used in the high cycle fatigue region, with N_f typically larger than 10^4 cycles. Above 10^7 cycles, a few materials, most notably low- and medium-strength steels, exhibit a distinct endurance limit σ_0 for constant amplitude loading, while most other materials show a continuously sloping curve [30]. Fatigue testing using ultrasonic frequencies have shown that materials can fail in the 10^8–10^{10} cycle range, with an intermediate plateau around 10^7 [31]. Fatigue crack initiation in this giga-cycle regime occurs inside the material as opposed to on the surface, indicating that an altogether different fatigue mechanism is at work [32, 33].

For shorter lives where the material no longer is elastic, stress is unsuitable to describe the material behavior. In the early 1960s, Coffin and Manson [35] presented a relationship similar to Eq. 1.1 using plastic strain amplitude:

$$\varepsilon_a^p = \varepsilon'_f(2N_f)^c, \tag{1.2}$$

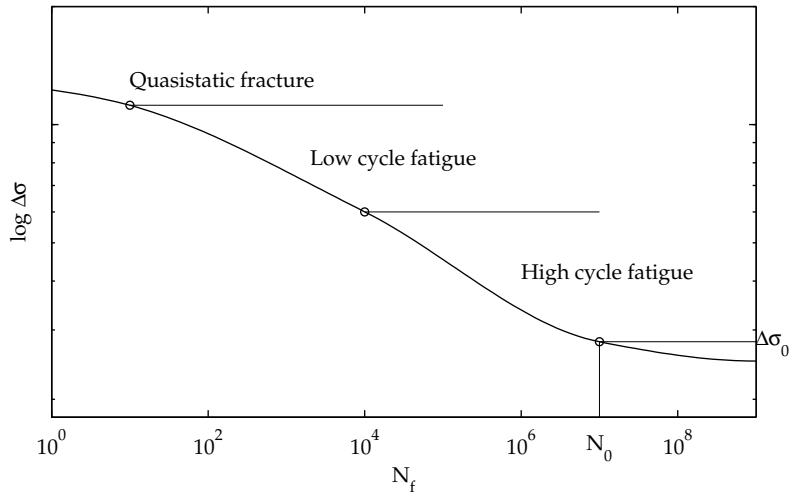

Figure 1.4: A schematic SN curve, showing typical behavior at different load levels [30, 34].

where $\varepsilon'_{\mathrm{f}}$ is the fatigue ductility coefficient and c is the fatigue ductility exponent. This equation can be combined with the stress-life relation to include the high cycle fatigue regime. The stress amplitude in Eq. 1.1 is then expressed by the elastic modulus E and the elastic strain amplitude, which combined with Eq. 1.2 gives the following relation between total strain amplitude and reversals to failure:

$$\varepsilon_{\mathrm{a}} = \varepsilon_{\mathrm{a}}^{\mathrm{e}} + \varepsilon_{\mathrm{a}}^{\mathrm{p}} = \frac{\sigma'_{\mathrm{f}}}{E}(2N_{\mathrm{f}})^{b} + \varepsilon'_{\mathrm{f}}(2N_{\mathrm{f}})^{c}. \tag{1.3}$$

Various attempts have been made to relate the fatigue strength parameters to material properties that are easier to measure, such as monotonic tensile strength, hardness and ductility. Machine design handbooks present methods for estimating σ'_{f} and b this way, and propose different scaling factors for aluminium and steel alloys. When these methods were developed, a limited number of alloys were used by engineers, thus the application of these methods today are highly questionable. A recent statistical treatment of such estimation techniques show a large amount of scatter for various aluminium alloys, and slightly less for steels [36].

1.2.2 Load type effects

The fatigue life curves in the previous section are usually found by fully reversed, uniaxial cycling. This stress state is generally different from load-bearing components, which often have a tensile mean stress as well as torsional loads.

The mean stress is given by

$$\sigma_{\mathrm{m}} = \frac{\sigma_{\max} + \sigma_{\min}}{2}, \tag{1.4}$$

where $\sigma_{\min}$ is the minimum stress for a cycle and $\sigma_{\max}$ is the maximum stress. When running fatigue tests at different stress ranges, the mean stress is commonly expressed by the load ratio

$$R = \frac{\sigma_{\min}}{\sigma_{\max}}, \tag{1.5}$$

so that R=-1 for zero mean stress. The mean stress can be accounted for by replacing the fatigue strength factor σ_{f}' in Eq. 1.1 and Eq. 1.3 by $\sigma_{\mathrm{f}}' - \sigma_{\mathrm{m}}$. In accordance with experimental results, this shifts the SN curve, or the elastic part of the total strain curve, downwards for tensile mean stresses ($\sigma_{\mathrm{m}} > 0$) [37]. Morrow [38] suggested that the stress amplitude in Eq. 1.1 could be replaced by an equivalent stress amplitude

$$\sigma_{\mathrm{am}} = \frac{\sigma_{\mathrm{a}}}{1 - \frac{\sigma_{\mathrm{m}}}{\sigma_{\mathrm{f}}'}}. \tag{1.6}$$

The same correction can be applied to Eq. 1.3:

$$\varepsilon_{\mathrm{a}} = \frac{\sigma_{\mathrm{f}}'}{E}\left(1 - \frac{\sigma_{\mathrm{m}}}{\sigma_{\mathrm{f}}'}\right)(2N_{\mathrm{f}})^{b} + \varepsilon_{\mathrm{f}}'(2N_{\mathrm{f}})^{c}. \tag{1.7}$$

Smith, Watson and Topper [39] proposed a different modification of the total strain life equation:

$$\sigma_{\max}\varepsilon_{\mathrm{a}} = \frac{(\sigma_{\mathrm{f}}')^2}{E}(2N_{\mathrm{f}})^{2b} + \sigma_{\mathrm{f}}'\varepsilon_{\mathrm{f}}'(2N_{\mathrm{f}})^{b+c}, \tag{1.8}$$

which has found widespread use in the local strain approach.

If torsional loads are present, the fatigue life will depend on alternating shear stresses as well as principal stresses. The interaction of shear and normal stresses or strains is complicated and not fully understood, especially in cases where the torsional loads are out of phase with the the tensile load cycles [40]. Findley [41] was among the first to recognize that multiaxial fatigue damage could be related to shear and normal stress components calculated on a *critical plane*. The critical plane was chosen so that the maximum value of the damage parameter

$$\frac{\Delta\tau}{2} + k\sigma_{\perp\max} \tag{1.9}$$

was obtained, where $\Delta\tau$ is the shear stress range in this plane and $\sigma_{\perp\max}$ is the maximum stress normal to the plane during a load cycle. The parameter k was

found by comparing uniaxial and torsional fatigue tests. A similar strain based model was proposed by Brown and Miller [42]:

$$\frac{\Delta\gamma_{\max}}{2} + f(\Delta\varepsilon_{\perp}), \tag{1.10}$$

where $\Delta\gamma_{\max}$ is the maximum shear strain range and $\Delta\varepsilon_{\perp}$ is the strain range normal to the plane of $\Delta\gamma_{\max}$. Kandil et al. [43] later suggested that the simple linear function $f(\Delta\varepsilon_{\perp}) = k\Delta\varepsilon_{\perp}$ could be used in Eq. 1.10 to describe the influence of normal strain. This has showed good correlation between prediction and experiments for in-phase and out of phase loading of a 6061 alloy [44].

1.2.3 Statistical analysis

Fatigue life curves commonly refer to the average fatigue life, i.e. a 50% probability of failure. In engineering design, this is an unacceptably high failure probability, thus a more conservative curve should be used based on the variance of the fatigue data. A high scatter is often observed in fatigue testing, which generally requires a large amount of test specimens to establish fatigue life relations and the associated variance [45]. On the other hand, fatigue testing is expensive and time consuming, thus a limited number of specimens are usually tested [46]. To further decrease costs, tests are often terminated at lives between 2×10^6 and 10^7 cycles, regardless of whether the material is known to exhibit a fatigue limit or not.

A least squares method is commonly used to find the parameters in Eq. 1.1 and 1.3, assuming that the error has a normal distribution. Maximum likelihood methods can alternatively be used, giving more model flexibility. Runouts can be taken into account using censoring and the standard deviation can be defined as a function of applied loading. Various distributions for the estimated parameters can be used as well, although the limited amount of data commonly available in fatigue tests rarely justifies the use of one over the other. The assumptions about spread become important when dealing with the small lower confidence bounds used in engineering design [47].

The standard deviation can be constant or a function of stress level, in order to include the common observation that scatter increases as the stress amplitude approaches the fatigue limit. The standard deviation s for a given fatigue life N_{f} can be modeled as a function of stress level as

$$s(\Delta\sigma) = \sqrt{\mathrm{Var}(\ln(N_{\mathrm{f}}))} = \exp\left(\beta_1 + \beta_2 \ln(\Delta\sigma)\right), \tag{1.11}$$

where $\beta_2 = 0$ results in a constant standard deviation. Different models for the mean fatigue life can be used. As illustrated in Figure 1.4, the stress-life curve is generally not log-linear. A model that can describe the behavior at the fatigue limit has been proposed by Pascual and Meeker [48] as

$$N_{\mathrm{f}}(\Delta\sigma) = \alpha_1 + \alpha_2 \ln(\Delta\sigma - \gamma), \tag{1.12}$$

where the modeled $\Delta\sigma$ approaches the value γ asymptotically with increasing fatigue life. The value of γ is a statistical representation of the fatigue limit for materials that exhibit such behavior, and should not be confused with dedicated fatigue limit testing [49]. Pascual [50] later developed a theoretical framework for planning experiments when using the model in Eq. 1.12.

1.2.4 Surface condition

The surface condition influence the crack initiation stage to a great extent. The significant surface parameters with regard to fatigue life are:

Residual stress: Compressive residual stresses are beneficial while tensile residual stresses are detrimental to fatigue life.

Surface roughness: Rough surfaces introduce stress concentrations which are detrimental to fatigue life.

Surface microstructure: Grain orientation and size as well as precipitates and inclusions affect the initiation and early crack growth.

All of these properties will generally be different in a component compared to the test specimens used to determine the fatigue life curves. In engineering design, these effects are commonly accounted for using reduction factors which modify the endurance limit of the material:

$$\Delta\sigma_{0\,\mathrm{mod}} = k_s \Delta\sigma_0, \tag{1.13}$$

where k_s is the product of individual surface reduction factors for residual stress, surface roughness, and microstructure [37]. Reduction factors may be available in tabular form, usually for specific machining processes, so that the correction factor in reality includes a combination of surface properties.

Residual stress

Machining processes involving material removal can cause the outer material layer to yield in tension, producing compressive residual stresses at the surface due to the constraint of the bulk material. Residual stresses in the surface are also affected by thermal processes such as heat treatment and welding [51]. Residual surface stresses show the same general influence as the mean stress effects from loading described in Section 1.2.2. The same corrections can be applied for fatigue initiation analysis, however, there is some uncertainty with regard to stress relaxation from cyclic loading [52].

Shot peening is a process where compressive stresses are induced in the surface layer to improve fatigue life. Fatigue initiation at locations of peak tensile stresses below the surface have been observed for components treated this way [53], effectively diminishing or overriding the effect of the accompanying surface roughness.

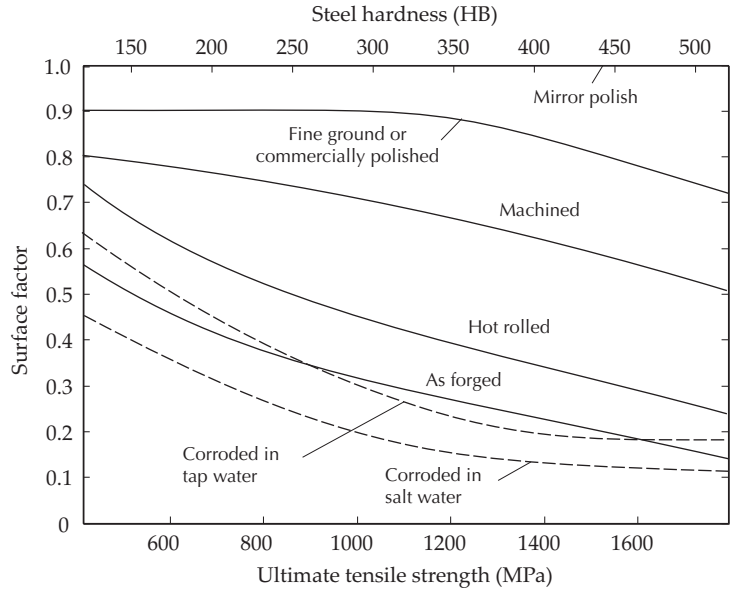

Figure 1.5: Fatigue reduction factors for estimating the effect on surface finish on the fatigue limit of steel structures [54].

Surface roughness

Surface roughness imposes stress concentrations in the surface where fatigue cracks may initiate. Figure 1.5 shows a diagram of reduction factors for steel alloys according to Juvinall [54]. Each curve is based on fatigue limit testing of several steel types, where the observed surface influence stems from a combination of residual stress, roughness, and microstructure.

The most widely used parameters to describe surface roughness in current engineering practice is shown in Table 1.1, where the most commonly used among these are R_a and R_z [55]. Some efforts have been made to quantify surface roughness based on the imposed stress concentration. Neuber [56] proposed an expression for the stress concentration factor as

$$K_t = 1 + 2\sqrt{\lambda R_{10} \rho^{-1}}, \tag{1.14}$$

where ρ is the asperity root radius, λ is the ratio between spacing and depth of the asperities, and R_{10} is the ten-point roughness:

$$R_{10} = \frac{1}{5}\sum_{i=1}^{5}(z_i)_{\max} + \frac{1}{5}\sum_{j=1}^{5}(z_j)_{\min}. \tag{1.15}$$

Eq. 1.14 predicts a smaller K_t for closely spaced asperities as may be expected, but the actual values of λ and ρ are hard to define for generic surface textures. Based

Table 1.1: Surface parameters defined in ISO 4287:1997

Surface height	z	where $\bar{z} = 0$
Maximum peak height	R_p	$z_{\max}$
Maximum valley depth	R_v	$z_{\min}$
Maximum peak to valley height	R_z	$z_{\max} - z_{\min}$
Arithmetical mean over L	R_a	$\frac{1}{L}\int_0^L \lvert z \rvert dx$

on Eq. 1.14, Arola and Williams [57] suggested a different stress concentration factor

$$K_{AR} = 1 + n\frac{R_a R_z}{\bar{\rho} R_{10}}, \tag{1.16}$$

where the dependent parameters are more easily quantifiable. The parameter n take account for load type effects, and the shape of the grooves are taken into account by $\bar{\rho}$, i.e. the average radius of the deepest valleys.

Surface microstructure

Even smooth specimens contain inherent stress concentrations in the form of inclusions and second phase particles with different elastic modulus than the surrounding matrix. Cast alloys usually have voids in the surface, and particles may de-bond to form the equivalent of voids that also act as stress concentrations [58]. Güngör and Edwards [59] found that for a forged 6082 alloy, initiation occurred at coarse particles introduced in the forging process, resulting in a 20% reduction in fatigue life compared to smooth specimen SN data.

A reduction of fatigue life can be observed with the increase in component size. This poses a problem, since fatigue testing is conducted on specimens that are much smaller than the actual components. The difference can be related to the fatigue process; being a weakest-link mechanism, the increase in surface area will lead to a higher probability of encountering microstructural weaknesses. From a production viewpoint, it is also difficult to control the microstructure throughout the volume of larger components, particularly for heat treated alloys [60]. The size effect is most prominent for notched components as will be discussed in the following section, and in more detail in Chapter 2.

1.2.5 Notched components

Since virtually all engineering structures contain notches in one form or another, the treatment of this in fatigue life prediction has received considerable attention over the years. Figure 1.6 shows a finite element analysis of a notched geometry loaded in the axial direction. The stress concentration for this notch can be defined based on either net section stress S_d or the remotely applied stress S_D. In terms of net section stress, the stress concentration reads

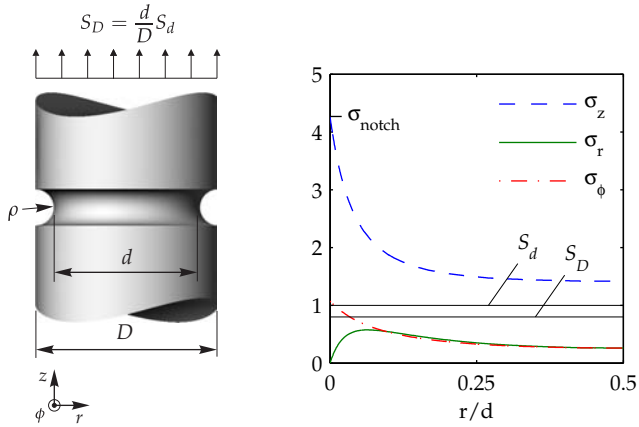

Figure 1.6: Nomenclature for round bar with a circumferential notch. A stress S_D is applied in the axial direction, corresponding to a nominal net section stress of $S_d = 1$. The elastic stress distribution ahead of the notch have been calculated numerically by finite element analysis ($\nu = 0.3$).

$$K_t = \frac{\sigma_{notch}}{S_d}, \tag{1.17}$$

where, σ_{notch} is the axial stress in the notch. Unless otherwise stated, this is the definition of nominal stress used here, where $S = S_d$.

Empirical notch corrections

In fatigue life tests of notched geometries, the effect of K_t appears to have less influence than under static loading, which has led to the definition of a separate fatigue notch factor, K_f. The fatigue notch factor relates the unnotched fatigue strength to the notched, nominal fatigue strength as

$$K_f = \frac{\Delta S_{unnotched}}{\Delta S_{notched}} \tag{1.18}$$

at a given life, usually at 10^7 cycles. The discrepancy between K_t and K_f is expressed by the notch sensitivity factor

$$q = \frac{K_f - 1}{K_t - 1}, \tag{1.19}$$

where the value of q varies from 0 to 1, corresponding to no influence of K_t to full contribution respectively.

The need for a fatigue concentration factor was addressed by Gough in 1924 and later expressed as K_f in Eq. 1.18 (or as β_k in Germany), by Thum and coworkers [29]. The reason for the difference between K_t and K_f is that

surface tensile stresses alone cannot characterize the physical processes of fatigue initiation, which take place in a characteristic volume ahead of the notch. A widely used empirical expression for K_f for different notch geometries was proposed by Neuber [56]. By considering the stress distribution ahead of a notch with a given notch root radius, he arrived at an expression for q based on the average stress up to some distance ahead of the notch:

$$q = \frac{1}{1 + \sqrt{c_N/\rho}}, \tag{1.20}$$

where c_N is a material parameter with a unit of length and ρ is the notch root radius. Neuber assumed that this length was related to a microstructural length over which no stress gradient could exist. Using Eq. 1.19, the notch factor can be written

$$K_f = 1 + \frac{K_t - 1}{1 + \sqrt{c_N/\rho}}. \tag{1.21}$$

For a given K_t, this equation describes a decreasing notch effect with decreasing radius. A sharp notch will have a steep theoretical stress gradient that, according to Neuber, would not affect the material beyond the critical length c_N. A similar theory was proposed by Peterson [61], where instead of averaging the stress ahead of the notch, he used the stress solution at a single location ahead of the notch:

$$K_f = 1 + \frac{K_t - 1}{1 + c_P/\rho}. \tag{1.22}$$

Siebel and Stieler [62] expressed K_f by the relative stress gradient:

$$K_f = \frac{K_t}{1 + \sqrt{c_S \chi}}, \tag{1.23}$$

where, for loading in the z direction using cylindrical coordinates (cf. Figure 1.6), the relative stress gradient is

$$\chi = \frac{1}{\sigma_{\text{notch}}} \left(\frac{\partial \sigma_z}{\partial r} \right)_{\text{notch}}. \tag{1.24}$$

The subscript notch denotes quantities calculated at the notch root.

The fatigue notch factor is typically close to one in the low cycle fatigue region, while approaching the value of K_t for high cycle fatigue. Juvinall [63] and Shigley [64] have suggested using a second fatigue notch factor K_f' at 10^3 cycles, whereby both the slope and the shift of the notched SN curve can be corrected. This is shown schematically in Figure 1.7. A notch sensitivity can be defined at 10^3 cycles, similar to Eq. 1.19:

$$q' = \frac{K_f' - 1}{K_f - 1}. \tag{1.25}$$

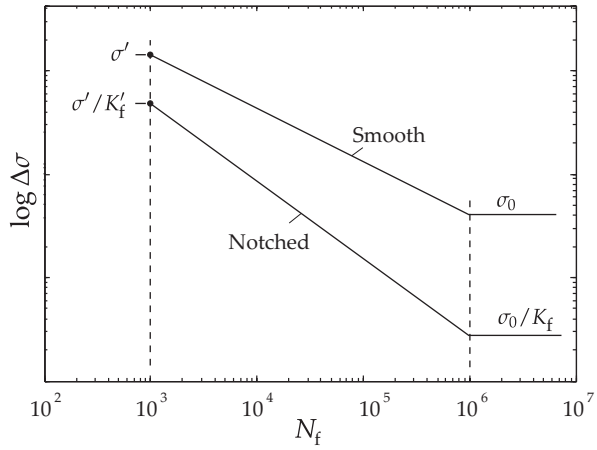

Figure 1.7: Estimate of R=0.1 SN curves for notched components [65]

.

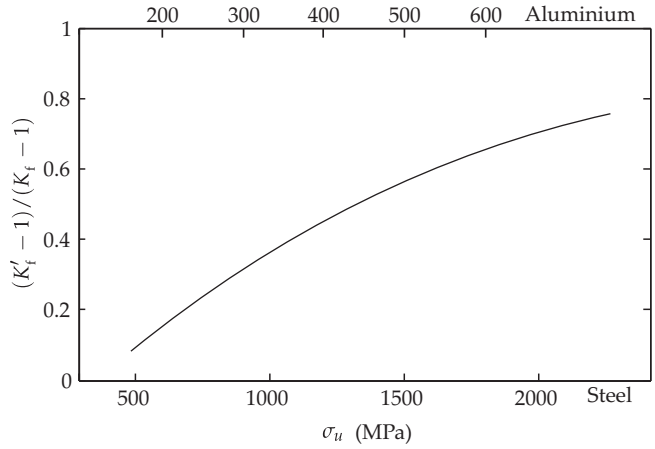

Figure 1.8: Empirical relationship between K'_f and K_f as a function of ultimate strength [54].

Figure 1.8 shows an empirical relation between q' and ultimate tensile strength for aluminium and steel, where it can be seen that the notch effect at short lives diminishes for soft or low strength materials, while stronger materials show an almost constant notch effect at high and low lives.

Plasticity in notches

A plastic zone develops ahead of the notch at higher loads, effectively redistributing stresses and lowering the actual stress concentration factor. Neuber

developed theoretical models for calculating the plastic stress-strain response in shear strained bodies [66]. He found that the theoretical stress concentration factor was related to the actual stress and strain concentration factors as

$$K_t^2 = K_\sigma K_\varepsilon, \tag{1.26}$$

which has become known as Neuber's rule. This was later shown to be applicable to axial loading by Topper, Wetzel and Morrow [67], using

$$K_\varepsilon = \frac{\varepsilon}{e} \quad \text{and} \quad K_\sigma = \frac{\sigma}{S}. \tag{1.27}$$

Nominal strain e is defined similarly to nominal stress (cf. Figure 1.6). While K_t is a constant for the given notch geometry, K_ε increases and K_σ decreases as yielding occurs. Using Eq. 1.22 for K_f, and Eq. 1.26 through 1.27, Topper et. al presented the following form of Neuber's rule, with nominal values of stress and strain on the left hand side and local values on the right:

$$K_f\sqrt{\Delta S \Delta e E} = \sqrt{\Delta\sigma\Delta\varepsilon E}. \tag{1.28}$$

In case the nominal strains are elastic, this shortens to

$$K_f \Delta S = \sqrt{\Delta\sigma\Delta\varepsilon E}. \tag{1.29}$$

The approach yielded good prediction of notched fatigue life based on smooth specimens using fatigue data on 2024 and 7075 aluminium notched plates with ρ=1.2 mm. They found the parameter c_P in Eq. 1.22 based on long-life data, assuming that the difference between K_f and K_t is due to a material size effect while Neuber's rule accounts for plasticity effects.

Crack growth in notches

There are several factors influencing the discrepancy between K_t, K_f and K_f'. In a smooth specimen, the initiation life can be over 90% of the total fatigue life, while for a notched specimen the initiation period may be altogether missing, especially for sharp notches. This can explain the observed variations in notch sensitivity for different geometries and load levels.

Different methods have been proposed for taking crack growth effects into account. An empirical description for smooth specimens was proposed by Manson [68], who noted that the fraction N_0/N_f closely followed the relationship

$$\frac{N_0}{N_f} = 1 - 2.5N_f^{(-1/3)} \tag{1.30}$$

for 410 stainless steel, 4130 steel and a 2024-T4 aluminium alloy. The number of cycles to initiation was determined by visual inspection and corresponded to a crack length of about 0.2 mm.

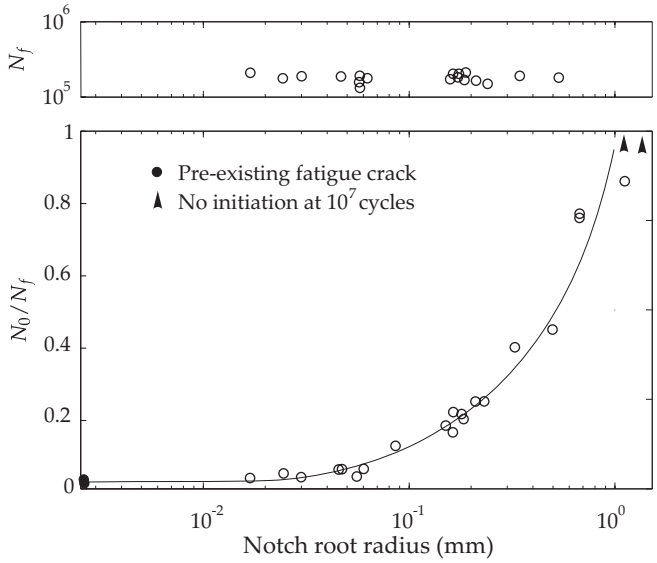

Figure 1.9: Influence of notch root radius on initiation/total life ratio [69]. The notch was 2 mm deep, and the same loading was applied in all tests, yielding similar total fatigue life N_f.

In the case of cracks growing from notches, Allery and Birkbeck [69] found that the N_0/N_f ratio varied with notch root radius ρ for a CMn steel alloy, as seen in Figure 1.9. Single edge-notch specimens, 6.3 mm wide, were stress relieved by annealing and subjected to the same reversed cyclic loading in three point bending. Initiation life was defined as the number of cycles to initiate a 0.1 mm long crack at the notch root. Using this definition, they found that an exponential equation such as Eq. 1.1 could describe the initiation life using Neuber's expression for K_f (Eq. 1.21). The time to total failure, defined at 5 mm crack length, was between 10^5 and 2×10^5 for all tests, with no correlation to notch root radius. The explanation given for this was that although the acute notches would have short initiation lives, the crack growth rate would decrease as the crack tip moved out of the notch stress field. For larger ρ, the long initiation life would be countered by shorter propagation life due to the larger notch stress field. This means that a K_f based on a S-N_f curve shows little or no dependence on nominal stress range, whereas a K_f based on S-N_0 will be highly dependent on stress range. This have been reported for aluminium alloys as well, as summarized by Leis and Topper [70].

1.2.6 Fracture mechanics

The term fracture mechanics was first used by Irwin [71] who introduced the stress intensity factor K as a measure of crack tip load:

$$K = \sigma\sqrt{\pi a}F, \tag{1.31}$$

where σ is the remotely applied stress, a is the crack length and F is a function of the geometry. For simple geometries, F can be determined analytically from linear elastic stress analysis, whereas for more complex geometries, the finite element method is used. In the special case of an infinite plate, containing a through-thickness crack $2a$ long and loaded perpendicularly to the crack plane, the geometry function takes the value of one.

The use of stress intensity factors was extended to fatigue problems by Paris et al. [72, 73], who related fatigue crack growth rate da/dN to the stress intensity factor range as

$$\frac{da}{dN} = C(\Delta K)^m, \tag{1.32}$$

where C and m are material parameters. The number of cycles to failure for a component with an initial crack or flaw of length a_0 is then found by integration:

$$N_\mathrm{f} = \int_{a_0}^{a_\mathrm{f}} \frac{da}{C(\Delta K)^m}, \tag{1.33}$$

where a_f is the critical crack length chosen to denote failure. This expression is integrated numerically, since the ΔK value will generally change as the crack grows.

An example of a fatigue crack growth curve is shown in Figure 1.10, where it can be seen that the crack growth rate deviates from the log-linear relation in Eq. 1.32 at high and low ΔK. This equation is therefore only used in Region II, also called the Paris regime. The growth rate in this region is influenced by the environment, with little effect of mean stress, microstructure and specimen thickness [34]. The unstable crack growth in Region III is controlled by the fracture toughness K_c, and is usually ignored in fatigue life prediction since the number of cycles spent there is insignificant compared to the total fatigue life. Region I is denoted the threshold fatigue or small crack region, which will be treated in more detail in Chapter 2.

The type of loading on a crack is distinguished by three different modes: Mode I is crack opening, Mode II is in-plane shearing and mode III is antiplane shear. Of these, the opening mode has received the greatest attention since this is the predominant mode of macroscopic fatigue crack growth [30].

Influence of load ratio

Rice [74] offered a mechanical model of the stress response ahead of a crack in an elastic- perfectly plastic material. The model allowed a calculation of the

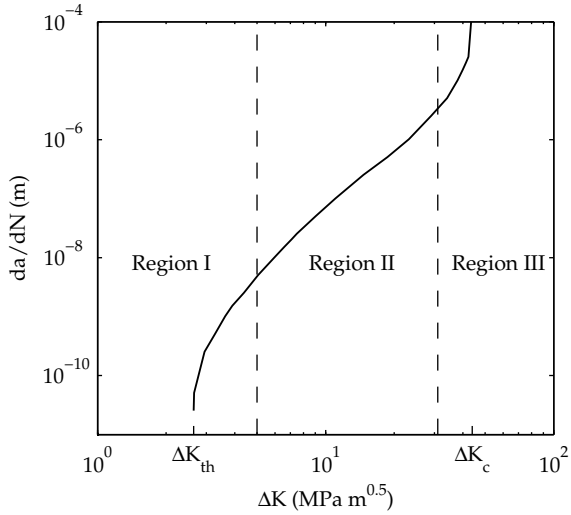

Figure 1.10: Different regions of crack growth rate, shown for an a 6061-T6 extruded material at R=0 [30].

reversed stress range at the crack tip caused by a given ΔK, as well as the size of the reversed plastic zone. This analysis assumes that the crack does not close, which intuitively seems wrong for the compressive part of the load cycle. From experiments on a 2024-T3 alloy, Elber [75] showed that cracks would close also for positive load ratios, as evidenced by a nonlinear response of load versus crack tip opening displacement. He suggested using an effective stress intensity factor range

$$\Delta K_{\text{eff}} = K_{\max} - K_{\text{op}}, \tag{1.34}$$

where K_{op} is the stress intensity calculated for the crack-opening load.

Several mechanisms have been proposed to explain this behavior, collectively referred to as *crack closure* corrections. The most important effects believed to influence crack closure are crack-tip plasticity, oxide formation on crack faces and contact due to crack face roughness [34]. There is considerable disagreement in the research community regarding the nature and even existence of crack closure under different load conditions [76–79], nevertheless, closure corrections have proved to describe crack growth rates for a variety of load cases and materials [14]. The effective stress intensity range can be found by considering several influences on crack closure, summarized by Sehitoglu [80] as

$$\Delta K_{\text{eff}} = f\left(\frac{S_{\max}}{\sigma_y}, R, \frac{H}{E}, \frac{\bar{\sigma}}{\sigma_H}, \text{Geometry}, \text{Microstructure}, a\right). \tag{1.35}$$

The effective stress intensity is here shown to depend on the hardening modulus H, the equivalent stress $\bar{\sigma}$, and the hydrostatic stress σ_H. These parameters

account for plastic zone size and variable amplitude loading ($S_{\max}/\sigma_0$, H/E), mean stress (R) and crack tip constraint ($\bar{\sigma}/\sigma_H$). With regard to the threshold regime, the effect of microstructural properties such as grain size and crystallographic orientations are particularly important, along with crack length and the size of geometric features such as notches.

Bergner et al. [81] suggested that different crack growth behavior observed in aluminium alloys can be described by different crack closure mechanisms. They showed that in the Paris regime, artificially age hardened alloys had similar crack growth rates at ΔK=10 MPa$\sqrt{\text{m}}$, although the slope m varied considerably. These were assigned to a group A, while a second group B of naturally aged alloys had lower crack growth rates than group A at ΔK=10 MPa$\sqrt{\text{m}}$. The difference in slope for group A was explained by different plasticity induced closure levels. The lower crack growth rate in group B was explained by a higher roughness level in the crack faces, leading to roughness induced closure.

When considering load ratio effects, Kujawski [82, 83] found that a modified stress concentration factor according to

$$\Delta K^* = (K_{\max})^p (\Delta K^+)^{1-p} \tag{1.36}$$

could be used without considering closure. ΔK^+ is the positive part of the applied ΔK, and the parameter p characterizes the material's sensitivity to $K_{\max}$, varying from 0 to 1 for very ductile and brittle materials respectively. With threshold values ΔK_{th} measured at R=0, the expected threshold at a given load ratio is:

$$\Delta K^*_{\text{th}} = \begin{cases} \Delta K_{\text{th}}(1-R)^p & :R > 0 \\ \Delta K_{\text{th}}(1-R) & :R \leq 0. \end{cases} \tag{1.37}$$

Walker proposed an empirical correction for the effective stress intensity factor [84]:

$$\Delta K^* = \Delta K (1-R)^{n-1}, \tag{1.38}$$

where n is a parameter with values from 0 to 1, and C and m have been determined at R=0.

1.2.7 Discussion

Fatigue properties are generally determined using standard specimens that do not resemble the actual components. Any differences between test specimens and components must therefore be accounted for, and usually involves empirical correction factors for the variables affecting fatigue life. The stress based approach has the advantage of being able to define SN curves for actual components, or component-like specimens, in which the influence of surface state from machining can be accounted for directly. The disadvantage is that these curves have very restricted validity, and relevant test data is often not available to the designer. Another disadvantage with the stress-life approach is that mean stress and sequence effects associated with plasticity in notches cannot accurately be

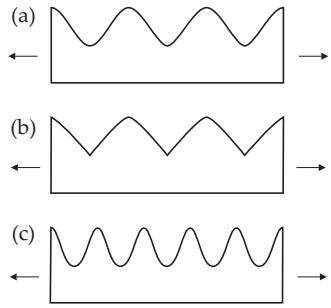

Figure 1.11: Three surfaces with different fatigue properties that cannot be distinguished by the commonly used surface parameters R_a, R_v, R_p and R_z.

described. The local strain approach is more rigorously based on the actual material behavior, and can account for plasticity in the notch root using the cyclic stress-strain response of the material.

The fatigue process has traditionally been divided into separate regimes, namely initiation and propagation. The surface state of the material affect the initiation period to a great extent, but the parameters that describe the surface state with regard to fatigue life are hard to define. Take for instance the geometric parameters given in Table 1.1. The problem with these parameters is that they cannot distinguish certain types of surface features known to affect fatigue life, the most significant being valley/peak spacing and valley tip radius. This is illustrated in Figure 1.11 by three different surface profiles that could have been produced by milling operations. The geometric parameters defined in Table 1.1 are the same for these profiles, although the geometries are clearly different; the surface in Figure 1.11(b) has smaller valley tip radii than the surfaces in (a) and (c), and the surface in (c) has more closely spaced valleys. The surface stresses and stress gradients will be different in these three cases, leading to differences in fatigue initiation life.

The effect of surface roughness is difficult to separate from the often more dominating effect of surface residual stresses. Steel alloys may be stress relieved by annealing after a machining procedure, but this will alter the mechanical properties of hardened aluminium alloys due to growth of precipitates and recrystallization of surface grains. It is therefore difficult to employ correction factors for a specific roughness, and when additional corrections for size, type of loading and environment are used, there is no guarantee that the combination of effects can be expressed by simply multiplying the separate reduction factors.

In notch fatigue life predictions, the theoretical stress concentration factor K_t is replaced by the fatigue concentration factor K_f. This is an empirical adjustment to account for the observation that K_f has less impact on strength reduction in fatigue than in monotonic loading. The difference between K_f and K_t is governed by the stress gradient, local plasticity, and the microstructure, leading to differences in early crack growth rates.

1.3 Objectives and scope

The objective of this study is to investigate new techniques for fatigue strength evaluation of components with a given surface roughness. The fundamental idea is that finite element analysis of the surface topography will provide better characterization of the surface than current empirical techniques. Tables or graphical aids, such as the one shown in Figure 1.5, are based on fatigue testing of the actual surface conditions and have little general applicability. This is especially true for aluminium alloys, which cannot readily be classified by tensile or ultimate strength.

Tensile and fatigue strength properties of aluminium alloys are related to the microstructure, although the influences of alloying elements and age-hardening on mechanical properties are not fully understood. In the current work, several variations of the material were available for testing purposes. Although this work is not so much concerned with the metallurgical aspects of fatigue, these test results are included for future reference. The testing was limited to constant amplitude, uniaxial loading in ambient air, thus load sequence, multiaxial loading and environmental effects have not been studied.

An isotropic, linear elastic material model will be used in the finite element analyses. The surface roughness is typically on the scale of microstructural features. Using a model based on bulk material properties cannot be relied upon to give accurate stress solutions ahead of small notches. The stress solutions near the surfaces are therefore not claimed to be representative for the material on the microscopic scale. The thesis set forth is that these stress fields will provide improved characterization of the fatigue initiation life, essentially describing the surface roughness in terms of linear elastic stress.

A notch fatigue analysis will be evaluated, using analytical Neuber type corrections for converting elastic to elastic-plastic stresses and strains. This is a generally accepted and widely used method for notch fatigue initiation problems. A more recent approach based on microstructural fracture mechanics will also be evaluated in terms of predicting the fatigue limit of rough surfaces. In order to understand these models, metallurgical aspects and mechanical models of fatigue will be discussed, with emphasis on cyclic material behavior and short crack growth. Although fatigue initiation has been recognized to consist of short crack growth, theories concerning the growth of such cracks has seen little use outside of academia. Virtual prototyping software already have implementations of strain life fatigue methods, thus it is of interest to evaluate these classical engineering approaches applied to surface roughness.

Chapter 2

Metal fatigue

Some commonly used models for fatigue life prediction were presented in Chapter 1. These models are highly empirical, which causes problems when applied to load cases, geometries, and surface finishes different from the ones tested. In order to evaluate the combined effects of these, a more fundamental understanding of the fatigue process is needed. Strengthening mechanisms, cyclic material models, and microstructural fatigue models will be discussed in this chapter, with emphasis on age hardened aluminium alloys.

2.1 Cyclic deformation

Since the work of Coffin and Manson, it has been well established that fatigue failure is caused by cyclic plastic straining. The bulk stress response of polycrystal materials are commonly studied under strain controlled cycling. When a constant strain amplitude is applied, the material shows a transient response of softening, hardening or a mixed behavior. Figure 2.1 illustrates a material that softens during the initial cycles, eventually reaching stable values of maximum and minimum stresses. Some of the microstructural aspects of this behavior will be studied next, along with mathematical models to describe cyclic plasticity.

2.1.1 Microstructural aspects

When a material is subjected to cyclic loading, changes can be observed in a microscope as numerous extrusions and intrusions on the surface of a polished specimen. These are associated with persistent slip bands forming in the surface grains. In the bulk material, dislocation density increases with the first few hundred cycles, after which a saturation level is reached [34]. The bulk dislocation density remains unchanged with further cycling, although the structure of the dislocations can change depending on temperature and load level. The dislocation structures that form are related to the cross-slip difficulty of the material, i.e., the tendency for dislocations to move from one slip system to another. Cross-slip

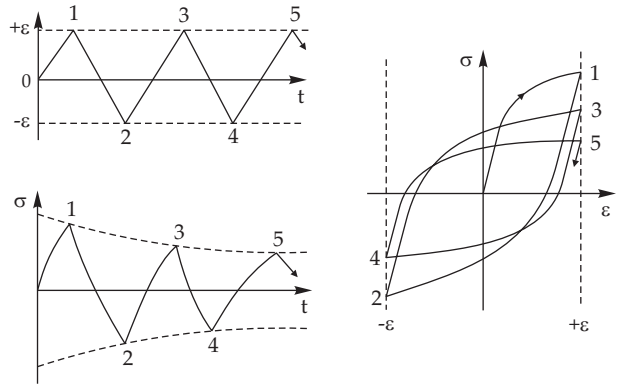

Figure 2.1: Cyclic softening for an alloy subjected to total strain cycling between the limits $+\varepsilon$ and $-\varepsilon$ [37].

difficulty is quantified quite well by the stacking fault energy. Aluminium has a relatively high stacking fault energy of $200\,\mathrm{mJ/m^2}$ [60], leading to easy cross slip. At high cyclic loads, or at N_f less than about 10^5, slip occurs on multiple slip systems, resulting in a space-cell dislocation structure. At lower load levels, dislocation loops form in distinct bands or linear arrays [34].

Hardenable aluminium alloys receive their strength from alloying phases that precipitate from solid solution during heat treatment. The precipitates act as obstacles to dislocation motion, with an additional effect of the strain field surrounding the precipitates. The strain field is largest when the precipitate lattice is coherent or semi-coherent with the matrix lattice, forming so-called Guinier-Preston (GP) zones. The most important parameter that influence the hardening effect of GP zones is the precipitate density. Dislocations will bypass precipitates if the inter-precipitate spacing is large enough, while for very high precipitate density, the GP zones will become less effective as their strain fields start to interact. The peak strength (T6 temper) is therefore attained when precipitates are within certain bounds of size and volume fraction, in which they contribute to strength most effectively if they are cut by the moving dislocations [60, 85, 86].

In the 6000 series of alloys, the strengthening is due to Mg-Si phases. To obtain peak strength, the material is quenched from 540°C and then age hardened at 190° [11]. During age hardening, a number of phases form as GP zones and smaller particles referred to as GP2 or β''. With further ageing, larger particles of a β' phase are formed until reaching an equilibrium phase of β Mg_2Si [87]. The pre-β particles have traditionally been assumed to consist of Mg_2Si as well, however, more recent investigations have identified the β'' phase as Mg_5Si_6 [88]. This has been identified as the main hardening phase, taking the form of semi-coherent, needle-shaped particles of approximately $4\times4\times50\,\mathrm{nm}^3$ in size [89]. The heavier alloying elements such as Cr and Zn form dispersoids that inhibit grain growth, while Fe and Mn are basically contaminants in this

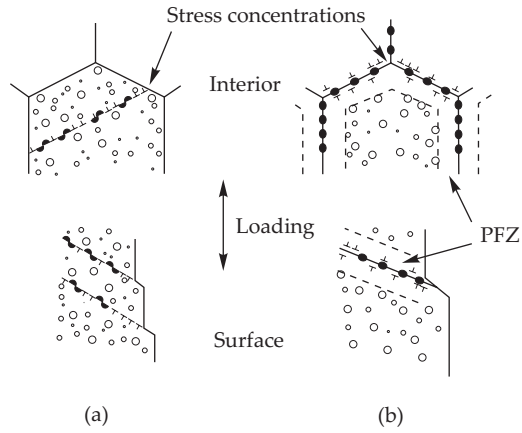

Figure 2.2: (a) Particle shearing and stress concentration from dislocation piling up at grain boundary. (b) Precipitate free zones (PFZ) at grain boundaries lead to stress concentration at triple points [90].

alloying system.

The particles are cut by by the dislocations, as illustrated in Figure 2.2(a). Dislocations piling up at grain boundaries cause microstructural stress concentrations in the interior, and steps are produced at the surface, introducing additional geometric stress concentrations. If the stress concentrations exceed the crack nucleation stress at grain boundaries, intergranular fracture starts. Stress concentrations also arise at grain boundary triple points near soft, precipitate free zones, shown in Figure 2.2(b). The precipitate free zones are found near grain boundaries, where the higher slip activity cause precipitates to be cut repeatedly until they reach a thermomechanical unstable state and revert to solid solution [34]. The mechanisms discussed here are important in smooth specimens, such as the ones commonly used in stress-life or strain-life testing. Persistent slip bands and triple points develop into microstructurally short cracks, which can either arrest or continue to propagate to failure. In most engineering components, the presence of surface roughness, manufacturing flaws and inclusions will promote immediate crack growth. This early stage is still often referred to as crack initiation due to the difficulty in observing such small cracks. These topics will be further discussed in Section 2.2.

2.1.2 Material models

Material models used in continuum mechanics ignore the microstructural features such as grains and particles. Material testing is done on specimens containing a representative volume, yielding bulk uniaxial or multiaxial material properties. A recorded hysteresis loop for the material used in this study is

shown in Figure 2.3, where the elastic $\Delta\varepsilon^{e}$ and plastic $\Delta\varepsilon^{p}$ strain ranges are defined. These quantities are related to the total strain range as:

$$\Delta\varepsilon = \Delta\varepsilon^{p} + \Delta\varepsilon^{e}. \tag{2.1}$$

The hysteresis loop is recorded from one cycle at $N_f/2$, and is denoted a stable hysteresis loop, even though this material softens throughout the fatigue life at this strain range. The use of cyclic material properties at $N_f/2$ is well established for intermediate to long fatigue lives, and only in very specific applications are the initial transient behavior accounted for. As will be shown in Chapter 3, the material softens in the first two to three cycles, after which moderate softening is displayed.

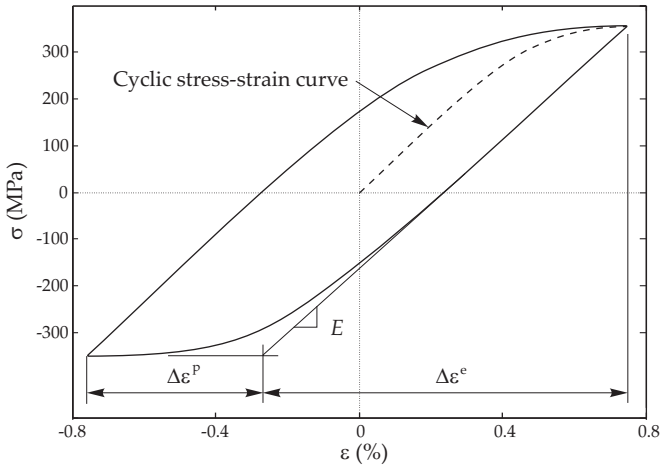

Figure 2.3: Hysteresis loop for the 6082-T6 alloy at $N_f/2$ and $\Delta\varepsilon$=1.5%. Recording the hysteresis loops at several fully reversed strain ranges yields the cyclic stress-strain curve.

The cyclic stress-strain curve

The cyclic stress-strain curve is found by recording the stress range of stabilized hysteresis loops for different strain ranges. As shown in Figure 2.3, the cyclic stress-strain curve describes the tip locations of hysteresis loops in fully reversed cycling. The stress ranges can be obtained from low cycle fatigue tests at constant total strain range $\Delta\varepsilon$ or constant plastic strain range $\Delta\varepsilon^{p}$, where the stress and strain response is recorded continuously throughout the duration of the test. The difference between curves obtained from constant $\Delta\varepsilon$ and constant $\Delta\varepsilon^{p}$ cycling is usually small for materials that stabilize quickly [91]. As a convention, the stress amplitude at $N = N_f/2$ for a given strain amplitude then correspond to one data point in the cyclic stress-strain curve [92]. The Ramberg-Osgood [93]

equation, which was originally developed for monotonic loading, is often used to model the cyclic stress-strain curve:

$$\frac{\Delta\varepsilon}{2} = \frac{\Delta\sigma}{2E} + \left(\frac{\Delta\sigma}{2K}\right)^{1/n}. \tag{2.2}$$

The plastic strain amplitude is assumed to follow a power-law relation with stress range:

$$\frac{\Delta\sigma}{2} = K\left(\frac{\Delta\varepsilon^{\mathrm{p}}}{2}\right)^{n}. \tag{2.3}$$

The above test method is referred to as companion specimen testing. An alternative is incremental-step testing, developed by Landgraf et al. [94], where a series of linearly increasing and decreasing total strain ranges are applied until the maxima and minima show no further change with continued loading. The stress and strain ranges in the last strain block are then used to form the complete cyclic stress-strain curve using a single specimen.

A third approach is multiple-step testing, where a specimen is cycled in multiple blocks of constant strain ranges. The strain range is increased when the material has stabilized at a given strain range, thus being similar to the incremental step test in that a single specimen can be used to find the cyclic stress-strain curve. The multiple-step test is usually conducted under plastic strain control. As for the companion specimen test, the multiple step test can also be conducted under total strain control, with little difference for materials that saturate quickly [91].

Several researchers have investigated the material response of aluminium alloys by using the techniques described above [91, 95–98]. These reports have been concerned with aircraft alloys, i.e. the 2000 and 7000 series. With regard to the latter, it can be summarized that these alloys show some differences between incremental-step tests on one hand and companion-tests and multiple-step tests on the other. The differences have been explained by the formation of load dependent dislocation structures, resulting in discrepancies at intermediate strain ranges due to deformation history effects. In the case of variable amplitude loading, the incremental-step test is believed to yield a more representative cyclic stress-strain curve.

Masing material behavior

The shape of the stable hysteresis loops are commonly found by scaling the cyclic stress-strain curve by a factor two. This was proposed by Masing in 1923, who modeled plastic material behavior by a set of parallel, elastic-perfectly plastic elements with different yield stresses [99]. Using Eq 2.2, the hysteresis loops can thus be described by:

$$\Delta\varepsilon = \frac{\Delta\sigma}{E} + 2\left(\frac{\Delta\sigma}{2K}\right)^{1/n}, \tag{2.4}$$

where the stress and strain ranges are relative to the current maximum or minimum point in stress-strain space. This model can describe the Bauschinger effect, which is used to denote the observation that strain hardening materials exhibit reduced absolute yield stress in compression following plastic tensile loading. Materials that develop strain range dependent dislocation structures may not display Masing behavior during constant amplitude cycling. The implication of this is that incorrect stress and strain values are predicted at turning points during variable amplitude loading. It has been shown, however, that materials with non-Masing behavior in constant amplitude cycling generally show Masing behavior in variable amplitude loading, including incremental-step tests [97–99].

2.1.3 Energy based notch correction

Neuber's rule was presented in Section 1.2.5, in which the assumption was made that the product of true stresses and strains equals the product of theoretical elastic stresses and strain in the notch root. A more recent notch correction has been proposed by Glinka, who assumed that the strain energy density at the notch root is the same for elastic and elastic-plastic material description when the material surrounding the notch is elastic [100]. Using the same nomenclature as in Section 1.2.5, the nominal strain energy density assuming plane stress is given by:

$$W_{\text{nom}} = \int_0^e S de = \int_0^S \frac{S}{E} dS = \frac{S^2}{2E}. \tag{2.5}$$

The strain energy density at the notch root for a linear elastic material is then

$$W_{\text{e}} = \frac{(K_t S)^2}{2E}. \tag{2.6}$$

As for the Neuber correction, the Ramberg-Osgood equation can be used to describe the stress-strain relationship at the notch root. The elastic-plastic strain energy density is then

$$W_{\text{p}} = \int_0^e \sigma d\varepsilon = \frac{\sigma^2}{2E} + \frac{\sigma}{n+1}\left(\frac{\sigma}{K}\right)^{1/n}. \tag{2.7}$$

For $W_{\text{e}} = W_{\text{p}}$, the following relation is found:

$$\frac{\sigma^2}{E} + \frac{2\sigma}{n+1}\left(\frac{\sigma}{K}\right)^{1/n} = \frac{(K_t S)^2}{E}. \tag{2.8}$$

Written in terms of stress and strain ranges, Eq. 2.8 becomes

$$\frac{(\Delta\sigma)^2}{E} + \frac{4\Delta\sigma}{n+1}\left(\frac{\Delta\sigma}{2K}\right)^{1/n} = \frac{(K_{\text{t}}\Delta S)^2}{E}. \tag{2.9}$$

This expression can be compared to the result obtained using Neuber's rule by substituting the inelastic strains in Eq. 1.27 with the Ramberg-Osgood relation

in Eq. 2.2:

$$\frac{(\Delta\sigma)^2}{E} + 2\Delta\sigma\left(\frac{\Delta\sigma}{2K}\right)^{1/n} = \frac{(K_t\Delta S)^2}{E}. \tag{2.10}$$

It can be seen that the difference lies in the plastic component, where Eq. 2.9 has an additional factor $2/(n+1)$. Since $n < 1$, it can be seen that the Glinka approach predicts smaller notch root stresses than the Neuber approach.

2.1.4 Generalized notch corrections

The cyclic stress-strain curves are found from unnotched specimens subjected to uniaxial loading. In the Neuber correction according to Topper et al. (Eq. 1.29), uniaxial material behavior is assumed for the notch root, however, this is only the case for geometries with low constraint. One example would be a notched, thin plate, where the material in the notch root is free to contract. The constraint can be quantified by the strain ratio

$$\alpha = \frac{\varepsilon_2}{\varepsilon_1}, \tag{2.11}$$

where $\alpha = -\nu$ implies plane stress and $\alpha = 0$ implies plane strain [101]. A similar ratio for stresses can be defined as

$$\beta = \frac{\sigma_2}{\sigma_1}. \tag{2.12}$$

For an elastic and isotropic material, a relation between α and β can be found from Hooke's law:

$$\alpha = \frac{\varepsilon_2}{\varepsilon_1} = \frac{(\sigma_2 - \nu\sigma_1)/E}{(\sigma_1 - \nu\sigma_2)/E} = \frac{\beta - \nu}{1 - \beta\nu}. \tag{2.13}$$

In the case of a plane stress model, the stress state at the notch root will be uniaxial. In general, a notch will be somewhere in between plane stress and plane strain, and the stress state in the notch root will be biaxial. Take, for instance, the circumferentially notched shaft in Figure 1.6 on page 14; the stress ratio $\alpha = -0.12$, and the notch tip stress state is biaxial, even though the global loading is uniaxial.

Hoffmann-Seeger

Hoffmann and Seeger [102] extended the Neuber approach to multiaxial, proportional loading by using equivalent stresses and strains, $\bar{\sigma}$ and $\bar{\varepsilon}$. Neuber's rule can be expressed in terms of equivalent values as

$$\bar{\varepsilon}\bar{\sigma} = \bar{K}_t^2\frac{S^2}{E}, \tag{2.14}$$

where von Mises equivalent values of stress and strain are defined in terms of the deviatoric tensor components:

$$\bar{\sigma} = \sqrt{\frac{3}{2}\sigma'_{ij}\sigma'_{ij}} \quad \text{and} \quad \bar{\varepsilon} = \sqrt{\frac{2}{3}\varepsilon'_{ij}\varepsilon'_{ij}}. \tag{2.15}$$

The nominal stress S in Eq. 2.14 can be found from either the net section or the gross section. Using the Mises yield criterion, $\bar{K}_t$ can be written in terms of elastic stress ratios for the principal stresses:

$$\bar{K}_t = \frac{K_t}{\sqrt{2}}\sqrt{\left(1-\frac{\sigma_{e2}}{\sigma_{e1}}\right)^2 + \left(1-\frac{\sigma_{e3}}{\sigma_{e1}}\right)^2 + \left(\frac{\sigma_{e2}}{\sigma_{e1}}-\frac{\sigma_{e3}}{\sigma_{e1}}\right)^2}, \tag{2.16}$$

where

$$K_t = \frac{\sigma_{e1}}{S}. \quad \text{and} \quad \bar{K}_t = \frac{\bar{\sigma}_e}{S}. \tag{2.17}$$

The subscript e denotes theoretical (total) elastic values. Hoffmann and Seeger related equivalent notch stresses and strains to principal notch stresses and strains using Hencky's flow rule:

$$\varepsilon_i^p = \frac{3}{2}\frac{\bar{\varepsilon}^p}{\bar{\sigma}}\sigma'_i, \tag{2.18}$$

where superscript p denotes the plastic part of the total strain as before. Quantities without labels are defined as elastic-plastic values in the notch root. Eq. 2.18 is a total stress-strain form of the incremental Prandtl-Reuss law, where a constant relation between the deviatoric stress components is assumed, corresponding to a radial loading path [see e.g. 103]. Hoffmann and Seeger argued that this is a reasonable assumption for constrained notches. Including total strains in Eq. 2.18, they arrived at a generalized form of Hooke's law:

$$\varepsilon_1 = \frac{\bar{\varepsilon}}{\bar{\sigma}}(\sigma_1 - \nu'\sigma_1) \tag{2.19}$$

$$\varepsilon_2 = \frac{\bar{\varepsilon}}{\bar{\sigma}}(\sigma_1 - \nu'\sigma_1) \tag{2.20}$$

$$\varepsilon_3 = -\frac{\bar{\varepsilon}}{\bar{\sigma}}\nu'(\sigma_1 + \sigma_2), \tag{2.21}$$

where

$$\nu' = \frac{1}{2} - \frac{\bar{\sigma}}{E\bar{\varepsilon}}\left(\frac{1}{2} - \nu\right), \tag{2.22}$$

and the free surface condition $\sigma_3 = 0$ has been used. Two additional equations are needed to solve this system of five unknowns. One is found from the Mises yield criterion:

$$\bar{\sigma} = \frac{1}{\sqrt{2}}\sqrt{(\sigma_1-\sigma_2)^2 + \sigma_1^2 + \sigma_2^2}, \tag{2.23}$$

and the other is found by assuming that the strain ratios are the same for both elastic-plastic and theoretical elastic solution:

$$\alpha = \frac{\varepsilon_2}{\varepsilon_1} = \frac{\varepsilon_{e2}}{\varepsilon_{e1}}. \tag{2.24}$$

The solutions for the first principal stress and strain are:

$$\sigma_1 = \frac{1}{\sqrt{1 - a + a^2}}\bar{\sigma} \tag{2.25}$$

$$\varepsilon_1 = \frac{1 - \nu' a}{\sqrt{1 - a + a^2}}\bar{\varepsilon}, \tag{2.26}$$

where

$$a = \frac{\alpha + \nu'}{1 + \nu'\alpha}.$$

Hoffmann and Seeger compared this approximation to elastic-plastic finite element analysis of a round bar with a deep circumferential notch, where the results showed an improved estimate over the traditional Neuber approach.

Extensions and comparative studies

Elastic net section behavior has been assumed in the current section, although this is not a restriction imposed by the Neuber correction. Seeger and Heuler [104] used the Ramberg-Osgood equation to calculate the net section strains as well as for the notch strains in Eq. 1.28. This can also be applied to the Hoffmann-Seeger correction [102], and allows calculation of notch stresses and strains with elastic-plastic net section. Härkegård and Sørbø [105] used a similar multiaxial formulation in terms of normalized equivalent stresses and strains and extended Neuber's rule to net section yielding and creep conditions.

The Glinka correction described in Section 2.1.3 can be developed for plane strain, as detailed by Glinka [100]. He found good agreement when comparing this formulation to elastic-plastic FEA of a circumferentially notched bar. The plane stress formulation was compared to strain gage measurements of notched plates found in the literature, showing good correlation. The Neuber correction showed consistently larger strains than the energy based notch corrections.

Sharpe et al. [101] performed elastic-plastic FE analyses of notched geometries and compared notch root strains to strain gage measurements found in the literature. They also investigated alternative Glinka corrections, assuming either constant strain ratio α or constant stress ratio β. They concluded that the Neuber correction is slightly better in plane stress conditions, giving conservative strain estimates compared to the plane stress Glinka correction. In plane strain, they concluded that the Neuber correction is unsuitable, while the plain strain Glinka correction gives good results. This was also found for the Glinka formulations with constant α or constant β. Härkegård and Mann [106] found that the generalized formulation used by Härkegård and Sørbø gave good results for confined plasticity, both in plane strain and plane stress.

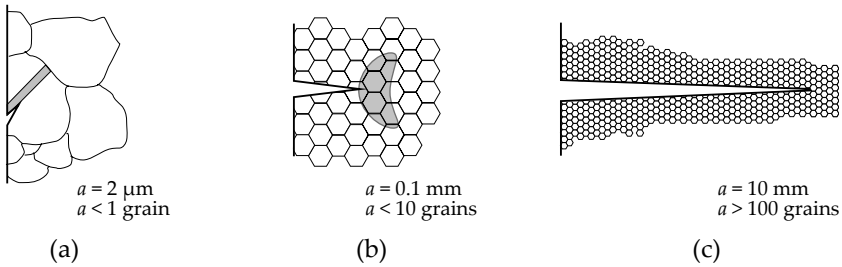

Figure 2.4: Classification of different crack growth regimes: (a) Microstructurally short crack, (b) physically short crack, and (c) long crack according to Miller [110].

Visvanatha et al. [107] compared the original Neuber formulation, the HS correction and the Glinka plain strain formulation to elastic-plastic FEA. They found that the HS correction closely matched the FEA strain solution, while the Neuber and Glinka estimates provided upper and lower bounds. This is consistent with other reports [108], although as noted by Visvanatha et al., the scatter in fatigue life tests, in their case a 7050-T7 alloy, may be larger than the differences in predicted fatigue lives from the different plasticity corrections. Tipton and Nelson [109] has summarized results and theories for non-proportional biaxial loading.

2.2 Fatigue crack growth

The term *fatigue initiation* was established at the time when the fracture mechanics concepts were introduced for crack propagation, and a distinction was needed to separate this new field from the already established stress-life methods and emerging strain-life methods. The separation of the fatigue process into initiation and propagation is still used in engineering practice due to the difficulties in testing and characterizing microscopic crack growth. Using a local stress or strain life method for the initiation life N_0 and a fracture mechanics method for crack propagation life N_p, the total fatigue life can be written

$$N_\mathrm{f} = N_0 + N_\mathrm{p}. \tag{2.27}$$

The initiation crack length is often somewhat arbitrarily defined. In strain controlled cycling, the initiation life can be defined at a certain drop in stress response or as a change in the measured tensile/compressive elastic modulus. Initiation life can also be determined from direct observation of the crack growth, defining propagation as the shortest crack where linear elastic fracture mechanics is valid. Depending on crack growth test conditions and the geometry of the components, this amounts to crack lengths on the order of 1 mm [30].

The classifications of cracks have been expanded as researchers have been striving to describe the growth of smaller cracks lengths. Figure 2.4 shows a

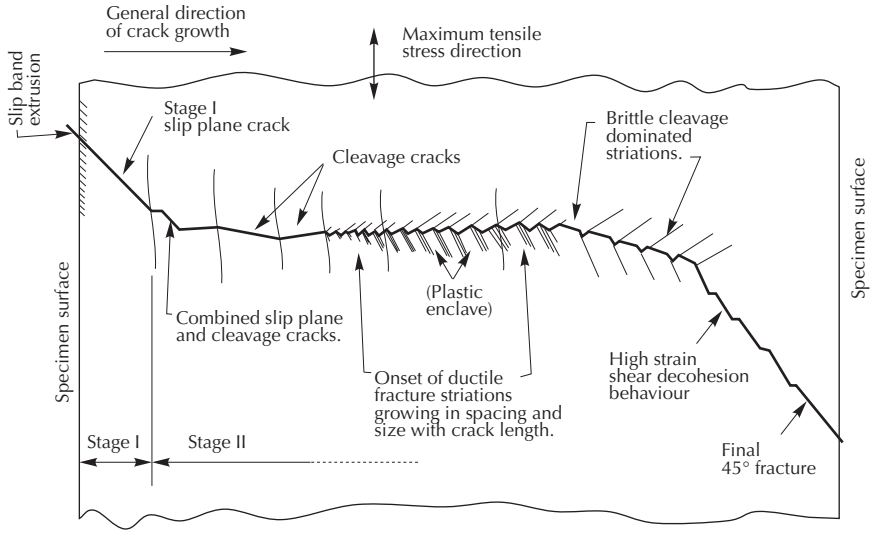

Figure 2.5: Illustration of the different fatigue fracture modes in an AlZnMg alloy according to Forsyth [112].

common way of classifying cracks, relating the crack length to grain size and the size of the plastic zone ahead of the crack [110]. Microstructurally short cracks, typically occurring within single grains, are heavily influenced by grain orientation and grain boundary properties. A physically short crack has a relatively large plastic zone ahead of the crack, invalidating the linear elastic fracture mechanics (LEFM) models described in Section 1.2.6. Long cracks have a small plastic zone compared to the crack length, thus LEFM models can adequately describe the crack tip loading conditions. In the following sections, the short crack growth regimes will be treated in further detail.

2.2.1 Crack growth stages

It was recognized from the early works of Gough in 1933, and later fortified by Forsyth and Wood among others [111], that fatigue failure starts as microscopic cracks formed at slip bands. Forsyth [112] noted that early crack growth occurs on planes inclined to the principal loading direction, corresponding to slip planes that experience the highest resolved shear stresses. Forsyth called this Stage I crack growth, illustrated schematically in Figure 2.5. After the first few grains have been passed by the growing crack, the crack tends to orient itself perpendicular to the loading direction, denoted by Stage II growth.

As mention in Section 2.1.1, the formation of microstructurally short cracks is preceded by a crack nucleation stage. Theories based on dislocation movement and their interaction with the microstructure have been proposed to model the mechanics of nucleation. It has been shown that nucleation by cyclic slip can

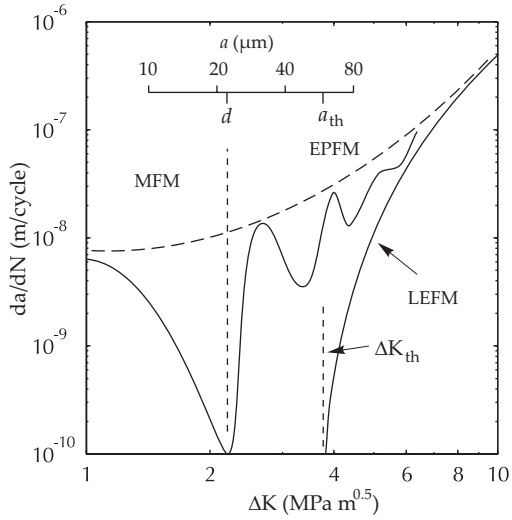

Figure 2.6: Short crack growth observed for AA7075-T6 by Lankford [117], where a is the estimated depth of a surface crack. Different mechanistic regimes for crack growth, and definitions of the two threshold d and a_{th} are according to Miller [110].

take up a considerable amount of time for single crystals [113], whereas for polycrystals this stage can be safely neglected [114, 115]. The reason is that polycrystals contain intrinsic stress concentration features in the form of grain boundaries, triple points and inclusions that can lead to crack initiation upon first loading. Furthermore, virtually all engineering structures feature extrinsic stress concentrations in the form of surface roughness and larger notches. The nucleation stage will therefore not be discussed further, turning the attention instead to microstructurally small cracks and the conditions for arrest and growth of these.

2.2.2 Short crack growth

Pearson [116] was the first to note that short cracks behaved differently from long cracks as predicted by linear elastic fracture mechanics (LEFM). He conducted experiments on an AlCuMg and an AlZnMg alloy using a traveling microscope to observe short crack growth, and found that the crack growth rates were much higher than would be expected from LEFM analysis.

The discrepancy between fatigue crack growth for short and long cracks is shown in Figure 2.6. Short cracks generally exhibit higher crack growth rates than longer cracks, although observations to the contrary have been reported. The crack growth rate vs. ΔK in the threshold region exhibit significant scatter compared to long crack growth data, and have shown to be bounded by the LEFM solution and an upper curve (dashed in Figure 2.6) that approaches the

LEFM solution as crack length increases. Another widely reported observation of short cracks is growth rate oscillations that decrease in magnitude as the crack grows [118]. These effects cannot be accounted for using classical continuum mechanics models, requiring microstructural fracture mechanics (MFM). Physically short cracks are associated with a plastic zone at the crack tip, which is large compared to the crack length. This invalidates the used of linear elastic stress intensity factors, requiring an elastic-plastic fracture mechanics (EPFM) approach.

The scales in Figure 2.6 are adopted from Lankford [117], who conducted experiments on a 7075-T6 aluminium sheet material. The crack length a was derived from observations of the surface crack length $2a$ of a penny-shaped crack with a known stress intensity factor solution. Cracks were found to initiate at inclusions, where the first values of ΔK-da/dN correspond to a cracked or de-bonded particle. Lankford found that short cracks decelerated at the first grain boundary and approached the LEFM solution as the cracks grew. This first deceleration has later been associated with a MFM threshold, denoted by the distance d in Figure 2.6. Based on fractographic studies, Lankford suggested that the actual crack growth rate for short cracks would follow an oscillating growth rate as indicated in Figure 2.6, although this was not observed directly.

Mechanical models

Hobson [119] proposed crack growth models for microstructurally short cracks and physically short cracks. The MFM crack growth equation was given as

$$\frac{da_s}{dN} = C'(d - a_s), \tag{2.28}$$

where a_s is the length of a surface crack. This equation correctly predicts crack arrest, temporary or permanent, for a surface crack length equal to the parameter d. This parameter was related to a microstructural threshold associated with the average depth of grain boundaries below the surface. Growth of physically short cracks was assumed to be independent of d, leading to the expression:

$$\frac{da_s}{dN} = Ga_s - D, \tag{2.29}$$

where G is a material function of the applied stress level and D represents a crack growth threshold. Hobson et al. [120] found good correlations with experimental data, expressing the parameters C' and G by the applied stress range.

A unified model for both microstructurally short and physically short cracks was proposed by Navarro and de los Rios [121] based on dislocation slip mechanisms:

$$\frac{da}{dN} = f\phi, \tag{2.30}$$

where f describes the degree of slip irreversibility for each stress cycle and ϕ is the crack tip displacement. Crack propagation could be described by successive

blocking of the crack tip plastic zone by the grain boundaries, and the subsequent initiation of slip in the next grain. This model can describe the oscillating crack growth rate commonly observed for short fatigue cracks, varying between an upper and lower limit as depicted in Figure 2.6.

2.3 Cracks in notches

It was mentioned in Section 1.2.5, that a threshold ΔK_{th} exists below which long fatigue cracks do not grow. Short cracks have a different threshold, and generally exhibit faster growth rates than long cracks. El Haddad et al. [122] proposed the following empirical expression for the threshold stress intensity factor of short cracks:

$$\Delta K_{\text{th}} = \Delta\sigma_{\text{th}}\sqrt{\pi(a + a_0)}, \tag{2.31}$$

where $\Delta\sigma$ is applied stress range and a_0 is a material parameter with unit of length. For very short cracks, the applied threshold stress becomes equal to the smooth specimen fatigue limit $\Delta\sigma_0$, thus Eq. 2.31 becomes:

$$\Delta K_{\text{th}} = \Delta\sigma_0\sqrt{\pi a_0}, \tag{2.32}$$

from which the material parameter a_0 can be derived:

$$a_0 = \frac{1}{\pi}\left(\frac{\Delta K_{\text{th}}}{\Delta\sigma_0}\right)^2. \tag{2.33}$$

El Haddad et al. [123] showed that Eq. 2.31 could describe the deviation from the long crack fatigue threshold observed for short cracks. Figure 2.7 shows the experimental and predicted values for fatigue threshold stresses for a steel alloy with different crack lengths. This type of plot is referred to as a Kitagawa-Takahashi [124] (KT) diagram, and is useful for illustrating the transition from short to long crack growth thresholds.

The a_0 parameter can be interpreted as a transition crack length between microstructurally dominated crack growth and long crack growth. Figure 2.8 shows a microstructural interpretation of a KT diagram according to Miller [110]. The conventional fatigue limit stress range is governed by a microstructural barrier at $a = d$, while the long crack threshold condition appears as a straight line for cracks longer than a_{th}. Physically small cracks, as defined in Figure 2.4(b), display a smooth transition between the microstructural threshold d and the long crack threshold a_{th}.

2.3.1 Fatigue limit of notched components

The expressions for K_{f} according to Neuber and Peterson, presented in Chapter 1.2.5, were based on an estimated notch stress field ahead of notches. Neuber derived his expression based on the average stress ahead of the notch, while

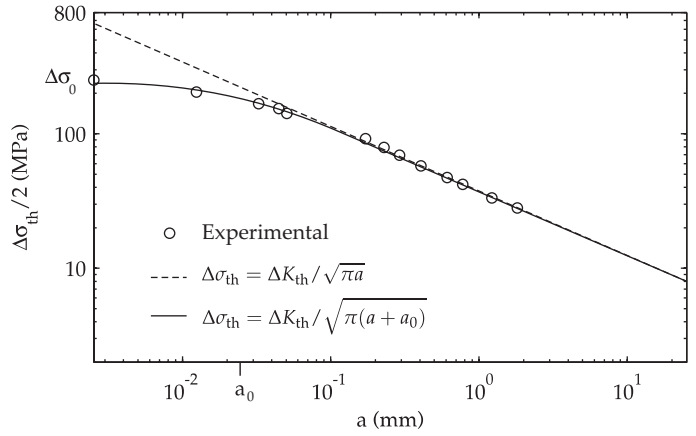

Figure 2.7: KT diagram illustrating the threshold growth condition for short cracks according to El Haddad et al. [123].

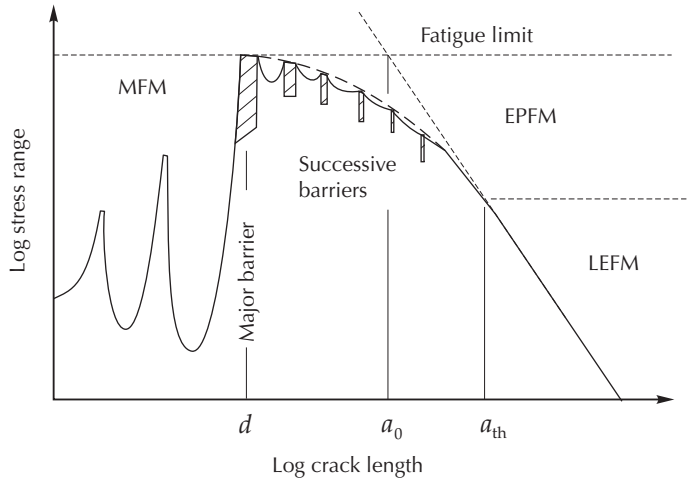

Figure 2.8: Schematic behavior of the condition da/dN=0 for short cracks [110].

Peterson used the stress estimated in a point some distance from the notch. This line of thought eventually found a more rigorous theoretical foundation in fracture mechanics theories. The commonly observed size effect observed in notch fatigue problems, or for any fatigue problem with stress gradients, can be conveniently explained by the threshold condition for propagation, since the parameter a_0 in Eq 2.33 has unit of length.

Frost and Dugdale [125] found that there exists a threshold length for small cracks in notches, below which they would cease to propagate at a given stress range. Smith and Miller [126, 127], later quantified these results in terms of

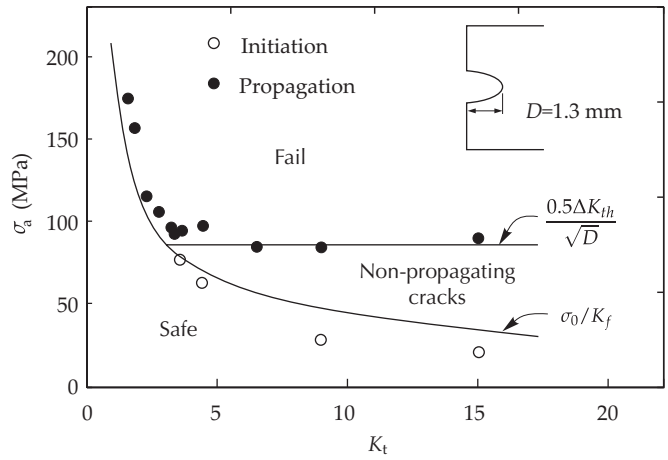

Figure 2.9: Fatigue regimes in notched components according to Smith and Miller [127]. The experimental data is for mild steel cylindrical specimens [128].

cracks in notch stress fields. The results of these analyses are shown in Figure 2.9, indicating that non-propagating cracks are expected in a certain region of stress range and notch geometry. This behavior can be explained by the extent of the notch stress field and the microstructural barriers of the material. A blunt notch will have a higher initiation stress than the threshold stress for propagation. An initiated crack in a blunt notch will therefore propagate to failure if the stress range exceeds the threshold stress range. In a sharp notch, the crack can arrest following initiation.

By using Newman's [129] stress intensity solutions for cracks emanating from elliptical notches, Smith and Miller [126] showed that similar crack growth rates could be expected in a smooth and a notched specimen if the notched specimen was treated as an equivalent crack in a smooth specimen. For cracks growing outside of the notch stress field, the equivalent crack length was simply stated as $a_n = D + a$, where D is the notch depth and a is the crack length. For cracks affected by the notch stress field, the equivalent crack length was approximated as:

$$a_n = a\left[1 + 7.69\sqrt{\frac{D}{\rho}}\right], \tag{2.34}$$

where $a < 0.13\sqrt{D\rho}$. This was equated to a fatigue notch factor:

$$K_f = \sqrt{1 + 7.69\sqrt{\frac{D}{\rho}}}, \tag{2.35}$$

which expresses the crack initiation condition shown in Figure 2.9. The crack threshold condition for sharp notches was derived from the assumption that

$a \ll D$ for a non-propagating crack, yielding [127]:

$$\Delta K_{\text{th}} = F\Delta\sigma_{\text{th}}\sqrt{\pi D}. \tag{2.36}$$

The geometry factor for an edge notch in an infinite plate ($F = 1.12$) was used to produce the approximate solution for the threshold stress:

$$\Delta\sigma_{\text{th}} = \frac{0.5\Delta K_{\text{th}}}{\sqrt{D}}, \tag{2.37}$$

which is independent of applied stress range, and appears as a straight line in Figure 2.9.

Klesnil and Lukas [34] derived a notched fatigue limit based on similar considerations of the threshold crack condition. They used the stress intensity factor according to Newman [129] for a crack in a notch characterized by the stress concentration factor K_{t} and the notch root radius ρ:

$$K_{\text{notch}} = F\frac{K_{\text{t}}\sigma\sqrt{\pi a}}{1 + 4.5(a/\rho)}, \tag{2.38}$$

where σ is the remotely applied stress. By combining Eq. 2.38 with the K solution for a smooth specimen:

$$K_{\text{smooth}} = F\sigma\sqrt{\pi a}, \tag{2.39}$$

they arrived at the following expression for the notched fatigue limit:

$$\sigma_{0\text{n}} = \frac{\sigma_0}{K_{\text{t}}}\sqrt{1 + 4.5(a_0/\rho)}, \tag{2.40}$$

where a_0 is the crack length at the fatigue limit. This can be restated to express K_{f} as:

$$K_{\text{f}} = \frac{K_{\text{t}}}{\sqrt{1 + 4.5a_0/\rho}}, \tag{2.41}$$

which is of the same form as Neuber's expression for K_{f} (Eq. 1.21 on page 15). The major difference is that while Neuber's approach is highly empirical, the value of a_0 in Eq. 2.41 is well defined according to Eq. 2.33.

Based on the ideas of El Haddad et al. [123] and Smith and Miller [127], a combination of a notch fatigue and linear elastic fracture mechanics concepts was developed by Taylor [130] and Lazzarin et al. [131]. Considering first the elastic solution according to Westergaard for a through-thickness crack in an infinite plate, with remotely applied stress $\Delta\sigma$ normal to the crack, the stress range at a distance r from the crack tip is:

$$\Delta\sigma(r) = \frac{\Delta\sigma}{\sqrt{1 - \left(\frac{a}{a+r}\right)^2}}. \tag{2.42}$$

For long cracks, where $r \ll a$, Eq. 2.42 can be written:

$$\Delta\sigma(r) = \Delta\sigma\sqrt{\frac{a}{2r}}. \tag{2.43}$$

Taylor used this result to derive the distance r where the stress normal to the crack equals the fatigue limit, i.e. $\Delta\sigma(r)$=$\Delta\sigma_0$. Assuming that the fatigue threshold condition can be described by Eq. 2.32, Eq. 2.43 gives

$$r = \frac{a_0}{2}. \tag{2.44}$$

The threshold condition for a long crack can thus be expressed by the stress in this point, fulfilling the condition

$$\Delta\sigma\left(\frac{a_0}{2}\right) = \Delta\sigma_0. \tag{2.45}$$

This is referred to as a *point method*. The average stress in a region ahead of the crack was used by Lazzarin et al. and Taylor to formulate an equivalent *line method*. Taylor used the average stress over a distance b ahead of the crack, given by

$$\overline{\Delta\sigma(r)}|_{r\in[0,b]} = \frac{1}{b}\int_0^b \Delta\sigma\sqrt{\frac{a}{2r}}dr, \tag{2.46}$$

where the threshold condition

$$\overline{\Delta\sigma(r)}|_{r\in[0,b]} = \Delta\sigma_0 \tag{2.47}$$

is obtained for b=$2a_0$. Lazzarin et al. [131] obtained the same result using a notch stress distribution according to Glinka and Newport [132]:

$$\Delta\sigma(r) = \frac{\Delta\sigma}{2\sqrt{2}}\left(\frac{r}{\rho}+\frac{1}{2}\right)^{-1/2}\left[1+\frac{1}{2}\left(\frac{r}{\rho}+\frac{1}{2}\right)^{-1}\right] \tag{2.48}$$

by investigating the threshold conditions for notch tip radii $\rho = 0$ and $\rho \to \infty$, corresponding to smooth and cracked specimens respectively. Taylor showed that the line and point methods could be used with notches by using Airy's stress solution for a hole in an infinite plate, and for small cracks using Eq. 2.42. Fatigue limit prediction using these methods have shown good results for a variety of notch geometries [133–135].

Discussion on critical distance methods

In the methods discussed above, linear elastic solutions have been used to quantify stresses in the fatigue process zone where plasticity is generally expected. Taylor [130] defended the use of elastic stresses as they are related to the traction energy in the process zone. A more rigorous claim was given by Cameron and

Smith [136], considering the point method. The condition for non-propagating cracks can be stated as:

$$\Delta\sigma(r) \leq \Delta\sigma_0, \tag{2.49}$$

at a distance r ahead of the notch. For steels, the fatigue limit is approximately equal to the cyclic yield strength σ_{cy}, while age-hardened aluminium alloys typically have $\sigma_0 < \sigma_{cy}$. The threshold condition can then be written:

$$\Delta\sigma(r) \leq \Delta\sigma_{cy}, \tag{2.50}$$

indicating that crack arrest can only occur in the elastic stress field.

El Haddad et al. and Taylor [137] assumed that the general geometric dependence in Eq. 2.31 could be discarded, since the material parameter a_0 is not a real crack length, rather an empirical correction factor for finding ΔK_{th}. Atzori et al. [138] showed that better results could be obtained for general notch geometries by including the geometry factor F, as suggested by Du Quesnay et al. [139]:

$$\Delta K_{th} = F\Delta\sigma_{th}\sqrt{\pi(a + a_0')}, \tag{2.51}$$

leading to a critical size parameter

$$a_0' = \frac{1}{\pi}\left(\frac{\Delta K_{th}}{F\Delta\sigma_0}\right)^2 = \frac{a_0}{F^2}. \tag{2.52}$$

El Haddad et al. [123] and others [128, 140] observed non-propagating cracks in notches, and found that the length of these cracks varied with applied stress level. Yates and Brown [141] provided a theoretical explanation for this. They expressed the KT diagram as a threshold stress intensity factor K_{th} and stated that cracks growing below the fatigue limit would arrest when $K = K_{th}$. Using Smith and Miller's equivalent crack length to compute K, the arrest length a_0 was found from:

$$F\Delta\sigma_0\sqrt{\pi a_0} = \Delta\sigma\sqrt{\pi(a_0 + D)}. \tag{2.53}$$

A more advanced model for the KT diagram was also used, with a smooth transition from $\Delta\sigma_0$ to the LEFM slope as seen in Figure 2.7. The model successfully described earlier published results of non-propagating crack lengths, and provided a lower and upper limit for such cracks.

2.3.2 Finite life calculations

When considering the finite life regime, notch fatigue life predictions become more complicated. As already mentioned, the fatigue process can be treated as separate initiation and propagation regimes according to Eq. 2.27 on page 34. The classical notch fatigue approach assumes that the number of cycles to initiate a crack of a given length equals the number of cycles to initiate a crack in a smooth specimen. The development of mechanistic models for the notch fatigue

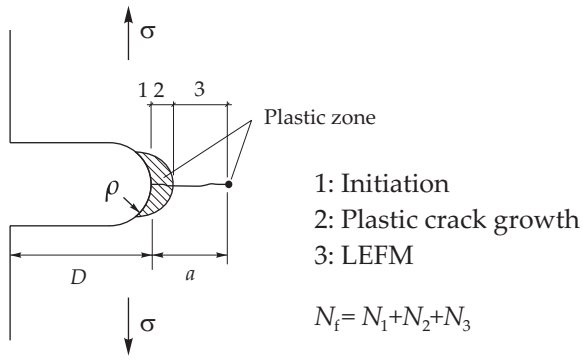

Figure 2.10: Different stages of crack growth in a notch stress field, according to Cameron and Smith [142]

problem, as opposed to the empirical methods described in Section 1.2.5, is complicated by the presence of a plastic zone and a stress gradient ahead of the notch, along with the size effect controlling the threshold condition.

Cameron and Smith [142] suggested dividing the crack propagation regime further into plastic and elastic crack growth regions, as illustrated in Figure 2.10. As before, the initiation condition was assumed to be described by strain controlled fatigue life data and a local notch analysis. For the demarcation of initiation, Cameron and Smith proposed using El Haddad's length parameter, retaining the geometry factor F according to Eq. 2.52. Crack growth in the plastic notch field, for $a > a_0$, was modeled using a strain intensity parameter:

$$\Delta K_\varepsilon = F K_\varepsilon(r) E \Delta\varepsilon_{\text{nom}} \sqrt{\pi r}, \tag{2.54}$$

where $K_\varepsilon(r)$ is the strain concentration factor a distance r ahead of an uncracked notch. Neuber's [56] solution for the elastic stress distribution ahead of a notch:

$$K(r) = K_t \sqrt{\frac{\rho}{\rho + 4r}} \tag{2.55}$$

was used to determine $K_\varepsilon(r)$ from Neuber's rule and the cyclic stress-strain response. The size of the plastic zone was estimated from Eq. 2.55, by finding the distance r_{cy} where $K^r \sigma_{\text{nom}}$ equals the cyclic yield strength σ_{cy}:

$$r_{\text{cy}} = \frac{\rho}{4} \left[\left(\frac{K_t \Delta\sigma_{\text{nom}}}{\Delta\sigma_{\text{cy}}} \right)^2 - 1 \right] \tag{2.56}$$

$$= \frac{\rho}{4} \left(\mu^2 - 1 \right). \tag{2.57}$$

Eq. 2.54 is thus valid in the region $a_0 < a < r_{\text{cy}}$. Cracks in the elastic region was calculated using LEFM.

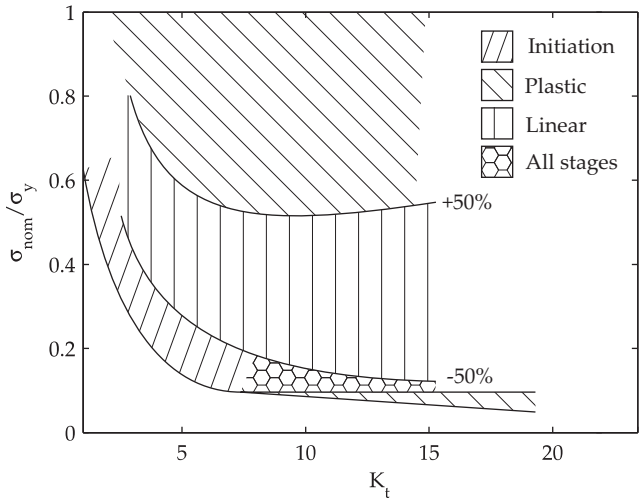

Figure 2.11: Dominating notch fatigue regimes according to Cameron and Smith [142]. The ±50% prediction interval is for a simple LEFM approach based on equivalent crack lengths in a notch.

Cameron and Smith verified these theories from tests of mild steel plates at R=0. Three different notches were tested, with K_t =3, K_t =6.5 and K_t =15. The approach gave good predictions, and it was found that in many cases the fatigue life could be described by a single model. Short crack growth rates were monitored, and were found to correlate well with Eq. 2.54. Crack growth lives in the notch plastic zone were found to dominate for the sharpest notch, and for all other notches at high stress levels. At intermediate load levels, the sharpest notch could be adequately described by LEFM alone. For the two blunter notches at low stress ranges, the initiation life was found to dominate over the lives calculated for the other stages.

The regions where different stages dominate are showed in Figure 2.11. The ±50% prediction interval for linear elastic analysis were found using the model of Smith and Miller [127], where the stress intensity factor for a crack according to Eq. 2.34 was used for $a < 0.13\sqrt{D\rho}$. For longer cracks, an equivalent crack length of $D + a$ was used. This shows that satisfactory prediction can be achieved following this approach for a range of notch geometries and load levels.

2.3.3 Application to surface roughness

Suhr [143] showed that the short crack threshold model by El Haddad et al. [123] could be used to predict the fatigue limit of a low alloy steel forging. Tensile and four-point bend specimens were machined from the forging, oriented in an axial and radial direction. Surface roughness was produced by grinding, followed by annealing to remove residual stresses. The fatigue limit was estimated from

Eq. 2.51, using F=1.12 for cracks at a free surface. Results are shown in Figure 2.12 for R=0.1 loading. Initiation occurred in grooves with depths ranging from 17 µm to 50 µm. This was determined from specimens with $N_f > 10^6$, failing at the same stress ranges as runouts ($N > 10^7$), since it was found that a stylus instrument could not accurately measure the valley depth. In the radial specimens, initiation occurred at inclusions of MnS, which were elongated in the axial direction and typically 40 µm deep. This value was added to the initiation groove depth in the radial specimens shown in Figure 2.12, improving the agreement with the theoretical model.

Taylor and Clancy [144] followed a similar approach as Suhr. A high strength steel was tested in three-point bending, where surface roughness had been introduced by milling and grinding. The specimens were annealed after machining to eliminate surface residual stresses, and the surface roughness was measured using a stylus instrument. The crack growth was monitored and load shedding was used to determine threshold crack lengths. The results could be presented in the form of a modified KT diagram, where the crack length was replaced by R_{max} as seen in Figure 2.13. Two different models were found to apply, depending on the character of the surface roughness. The short crack threshold of El Haddad (Eq. 2.33) can be seen to underpredict the threshold stress for the low-roughness surfaces. For the the rougher surfaces, there appears to be a notch type behavior, as the data follow Peterson's model.

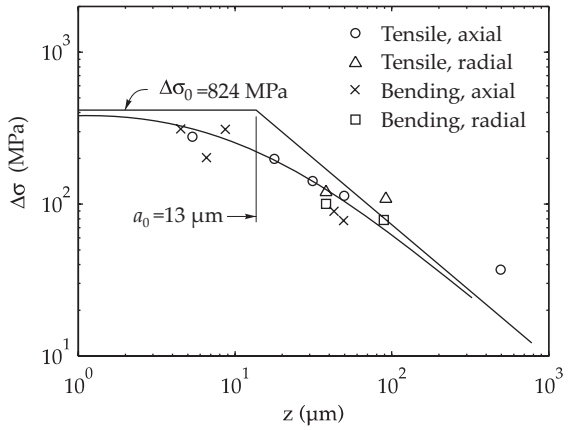

Figure 2.12: A short crack threshold model applied to surface roughness in a low alloys steel, tested in bending and axial loading at R=0.1 [143]. The depth z of grooves where initiation occurred is plotted against stress range according to Eq. 2.51 with $a = z$.

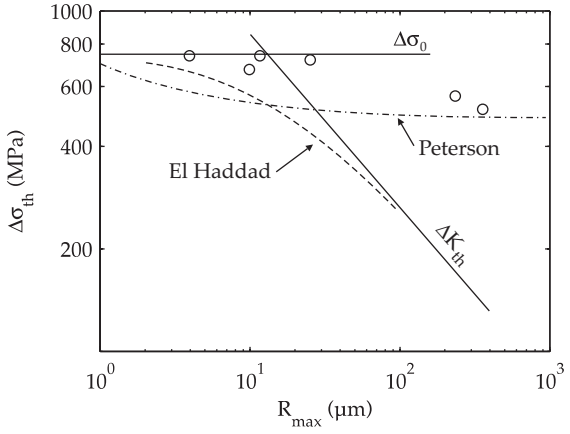

Figure 2.13: KT diagram of fatigue limits in specimens with surface roughness, where maximum valley depth $R_{\max}$ has replaced crack length [144].

Chapter 3

Experimental details

3.1 Test specimens

Test specimens were taken from different locations in the suspension arm, as shown in Figure 3.1. The test specimens have been named according to location and arm number, with designations <location><arm number>. For instance F21 and B21 are taken from locations F and B in suspension arm number 21. The majority of tests, however, were taken from the raw material for the forging process, available as extruded rods.

Figure 3.1: A suspension arm and locations of the different extraction locations.

Table 3.1: Chemical composition of the material (wt.%). AA denotes the Aluminium Association standard, and RA are the limits required by Raufoss Automotive.

Batch	Si	Fe	Cu	Mn	Mg	Cr	Zn	Ti	Other
I	1.23	0.30	0.067	0.53	0.81	0.14	0.084	0.020	0.07
II	1.16	0.29	0.091	0.53	0.81	0.14	0.069	0.028	0.10
III	1.14	0.27	0.062	0.49	0.79	0.15	0.051	0.036	0.09
AA6082	0.70-1.3	0.50	0.10	0.40-1.0	0.6-1.2	0.25	0.20	0.10	0.15
RA6082	0.80-1.2	0.30	0.10	0.40-0.70	0.70-1.10	0.20	0.10	0.05	0.15

Table 3.2: Tensile strength and proof stress for forged and extruded specimens (MPa). Standard deviation is given based on eight tests in each batch.

	Designation	$R_{p0.02}$	$R_{p0.2}$	R_m	E (GPa)
Forged, T5	F (I)	369±4	387±2	395±3	-
Forged, overaged (T7)	F_R(I)	265±4	286±4	315±4	-
Forged prototype, T6	F_P(I)	374±8	385±4	420±5	-
Extruded billet, T6	E (I)	382±7	408±2	424±2	72.5±0.1
Extruded billet, T6	E (II,III)	-	-	-	-

3.1.1 Material and designations

The raw material comes in the form of extruded billets with a diameter of 52 mm. Before forging, the billets are in an unspecified F temper. The billets were heat treated to T6 condition for this study, in order to evaluate the influence of microstructure of forged versus extruded material. From a product design standpoint, it is also of interest to be able to predict fatigue properties of future products based on raw material test data.

Three separate batches of material were received from the supplier over a two year period. The alloy is designated RA6082, and has tighter limits on the alloying elements than the Aluminium Association AA6082 standard[1], as seen from Table 3.1. Chemical compositions for the three different batches were determined by spark-source mass spectroscopy [145]. The chemical composition differs slightly between the batches, most notably for batch II that has more Cu and batch I that has more Si.

Table 3.2 shows yield strengths and ultimate tensile strengths for the specimens. All tensile tests were done on material from batch I. The elastic modulus was determined for the extruded material using two averaging extensometers mounted on opposite sides on the straight specimen gage section, according to the recommendations in ASTM E111. The roman numerals in parenthesis refer to material batch in Table 3.1.

[1]Other names used for this alloy are AlSi1MgMn (ISO 209-1) and AlMgSi1 (DIN 1712, 1725).

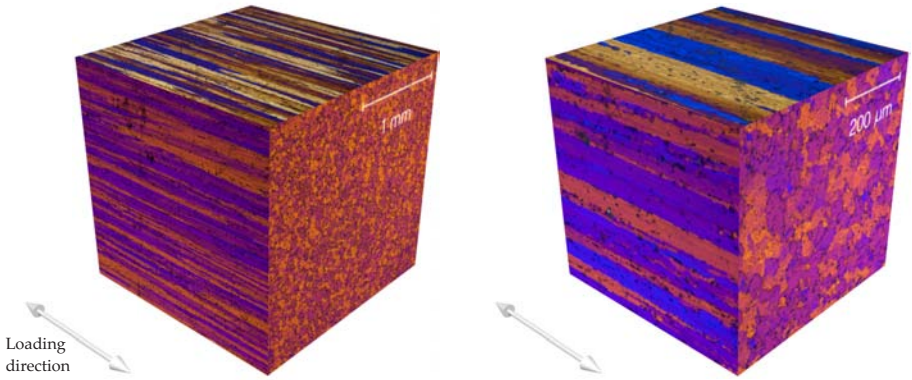

(a) Extruded material

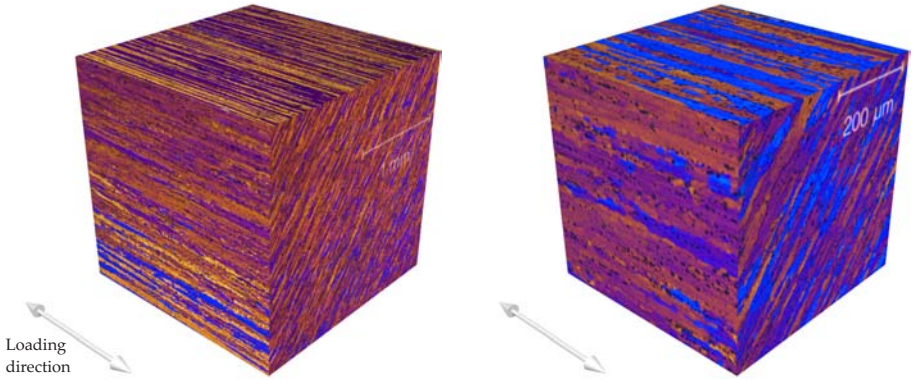

(b) Forged material

Figure 3.2: Grain structure visualized using crossed polarizers.

3.1.2 Microstructure

The microstructure for the forged and extruded material is shown in Figure 3.2. These images were captured using a light microscope with crossed polarizers after an anodization treatment [146]. By counting visible grain boundaries according to the lineal intercept method (ASTM E112), an estimate of the mean grain diameter was found for different directions. The extruded E(I) series specimen shown in Figure 3.2(a) has a mean grain diameter of 33 µm in the plane perpendicular to the loading axis. The grains are highly elongated in the loading direction, with lengths exceeding the 2.2 mm covered by the micrograph. The forged F(I) series specimen has a pancake type grain structure with mean grain

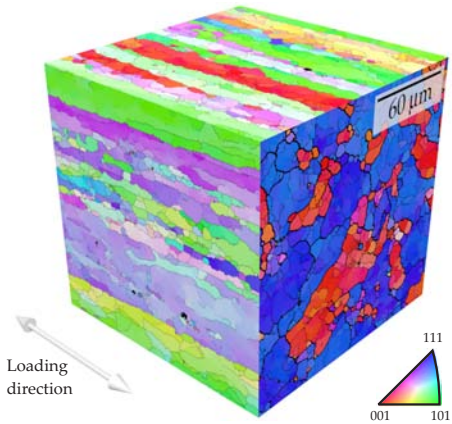

Figure 3.3: Inverse pole figure for the extruded E(III) material. The colors indicate crystallographic orientations with respect to the surface.

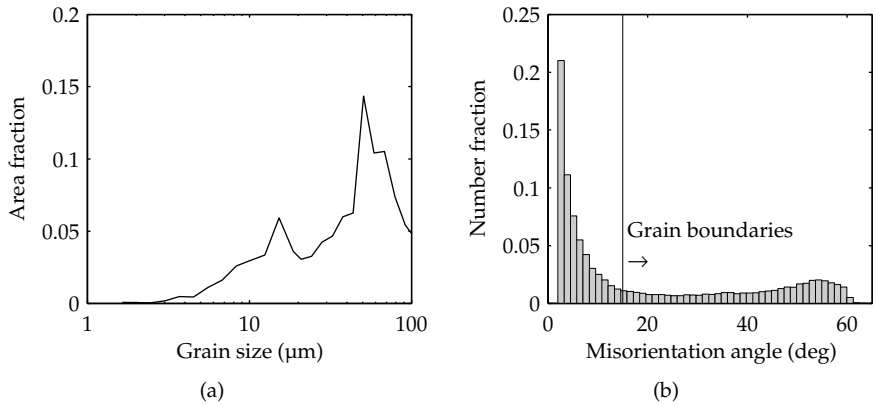

Figure 3.4: (a) Distribution of grain sizes and (b) crystallographic misorientation found from EBSD in the plane perpendicular to the loading direction. E(III) material.

diameters varying from 13 to 180 µm in the plane perpendicular to the loading direction.

The microstructure has also been studied using a field emission SEM in electron backscatter diffraction (EBSD) mode to achieve subgrain resolutions. This consists of automatically scanning the surface at an angle and recording the resulting backscatter diffraction for each scan point. A real-time computer analysis of the diffraction pattern then yields the crystallographic orientation for each point. A resolution of 1 µm was used in this case, and grain boundaries were identified by crystallographic misorientation angles exceeding 15°. Figure 3.3 shows three EBSD images for an extruded E(III) specimen, where

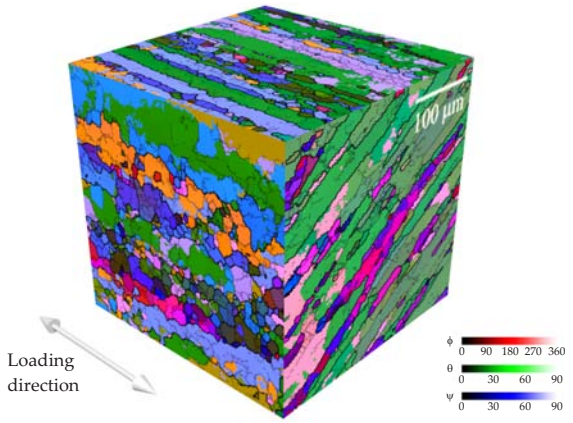

Figure 3.5: Crystallographic orientations in the forged material, illustrated by Euler angles.

grain boundaries are indicated by black lines. Low angle grain boundaries with misorientation in the range 2°-15° are marked by thinner lines. The colors correspond to crystallographic poles aligned with the surface normal; grains colored blue have (111) poles aligned with the surface normal while red grains are (100) oriented. The inverse pole plots reveal which slip systems are most likely to be activated during loading, while the misorientation angle is a measure of grain boundary energy.

Figure 3.4 shows the distribution of grain sizes in the E(III) material, where a grain boundary is defined as a >15° angle mismatch. The mean and median grain diameter is 29 and 19 µm respectively. Also shown is the distribution of angular misorientation at grain boundaries, where it can be seen that a large portion are low angle grain boundaries. Figure 3.5 shows the grain structure of a forged F(I) material with colors corresponding to crystallographic Euler angles [see e.g. 147].

3.1.3 Specimen geometry

Two specimen geometries, designated A and B, are used as shown in Figure 3.6. Geometry B has a 12 mm grip section diameter and is used for low cycle fatigue testing, since collet grip pressure is typically higher than for load controlled testing. Geometry A has a 10 mm grip section diameter and is used for the other series. Both geometries conform to ASTM E466 and E606 [148, 149]. The specimens were machined using initial cut depths of 1.25 mm on the radius, 0.3 $^{mm}/_{rev}$ feed rate and 2500 $^{rev}/_{min}$. The final cut depth was 0.1 mm with the same feed rate and speed. Due to problems with fretting fatigue in the grip section at long fatigue lives, the specimens were modified as shown later in Section 3.3.

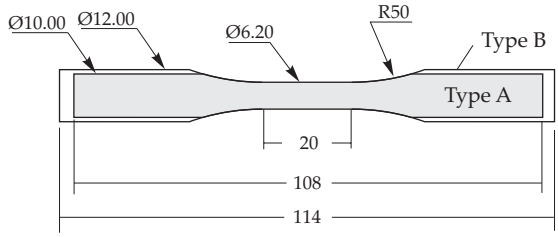

Figure 3.6: Geometry of the two test specimen used (mm).

3.1.4 Surface preparation

The polished specimens were prepared in multiple steps with emphasis on avoiding smearing of the surface layer. Wet grinding was done by rotating the specimens in a drilling machine, using 320 SiC grit paper for the first step and 2400 grit for the last. The final paper was also rubbed lengthwise on the specimen by hand to make sure the final scratches were parallel to the loading direction. Polishing was done in two steps, using 3 µm and 1 µm diamond cloths and an alcohol based lubricant. This was also done in the drilling machine with the final stage consisting of longitudinal polishing by hand. The complete polishing procedure resulted in a reduction of the gage area diameter of 15-30 µm.

The rough specimens were prepared with emery cloth belt of various grit. The aim was to create circumferential grooves where the surface profile could be used in axi-symmetric finite element models. To achieve this, a lever mechanism shown in Figure 3.7 was used. The weight at the end of the lever ensured that consistent pressure was applied, as the specimen turned in the lathe for 20 seconds with 45 $^{\text{rev}}/_{\text{min}}$. Three different surface types were created, designated M for medium, C for coarse and MC for medium-coarse. For the medium surface type, 120 grit was used, while 80 grit was used for the coarse type. The MC type was generated by first using 120 grit followed by 80 grit.

The width of the lever was 10 mm, and a strip of emery belt with the same width was attached underneath. A small adhesive cushion, about 1 mm thick, was placed between the emery belt and the lever to distribute the pressure and to keep the belt from sliding. In order to create a wider than 10 mm rough section, two runs in the lathe were done on some of the specimens, where the lever was shifted lengthwise to produce a rough section of approximately 15 mm. A fresh area of the emery belt was used for each run, so that the randomness of the surfaces would be better as well as to avoid material buildup. Synthetic fluid, diluted in water, was used for lubrication and cooling. The average roughness ranged from 2.2 µm to 11 µm and maximum valley depth ranged from 9.3 µm to 48 µm, determined from a length of 2 mm without filtering.

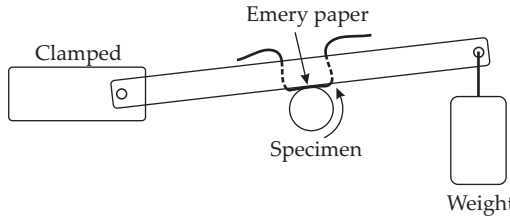

Figure 3.7: Device for making circumferential grooves, mounted in a lathe.

3.2 Fatigue testing

This section describes the layout and operation of the test equipment. Three different hydraulic test frames were used, and various modifications to these had to be made along the way.

3.2.1 Tensile load cycling

A Schenk 10 kN test frame with Instron 8800 control system and load cell was used for R=0.1 testing. A self aligning grip setup with ball joints was used as shown in Figure 3.8 on the following page. The test frame was originally equipped with hydraulic clamps that were aligned prior to installing the ball joint grips. The specimens were clamped as seen in Figure 3.8(b). The area in contact with the specimen was threaded to increase the local clamping pressure. Four screws were manually tightened using a torque wrench to ensure even and consistent clamping pressure. For alignment control, a type A aluminium specimen with four strain gages around the circumference was used, shown in Figure 3.8(c). With an applied tensile load of 4 kN, the maximum bending stress was less than 2% of the nominal axial stress.

3.2.2 Fully reversed load cycling

Strain controlled testing and load controlled testing with fully reversed cycles, were done in a 50 kN test frame with Instron actuator and Instron 8800 control system. The setup is shown in Figure 3.9. The specimens are fastened using Instron hydraulic grips with collet chucks. The hydraulic grips were aligned using a hardened steel specimen with a type B geometry (Figure 3.6). Eight strain gages were attached around the mid section, ie. four strain gages around the circumference at two longitudinal positions as shown in Figure 3.9. An Instron alignment kit was used for adjusting angular and lateral displacement of the lower grip fixture. The signals from the strain gages were processed and displayed as real time plots on a computer as bending and shear deformation separately for each of the two axes. Angular and transverse misalignment, as shown in Figure 3.10(a)-(b), can then quickly be corrected by turning the

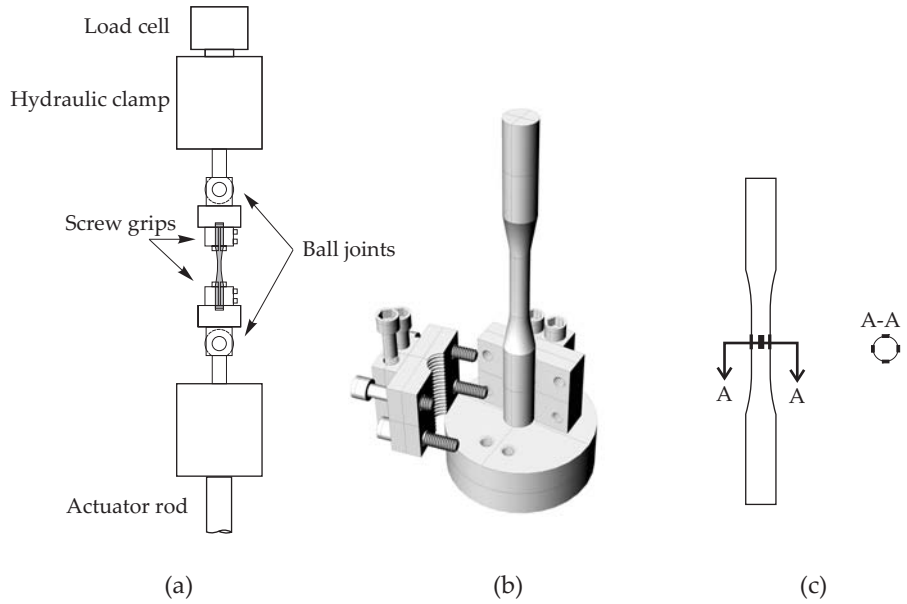

Figure 3.8: The 10 kN test frame: (a) frame layout, (b) a screw grip, (c) specimen with strain gages used for verifying alignment.

appropriate adjustment screws on the alignment kit. Misalignment can also arise if the the grip fixtures and the actuator rod are not coaxial, depicted in Figure 3.10(c). This type of misalignment can be revealed by observing the strain gage readings as the load is varied. If load dependent readings are observed, the upper grip needs to be unscrewed and refitted under tensile pre-loading. At axial loads of ± 6 kN the maximum difference between the lowest and highest strains was below 3% of the nominal axial strain.

Two standard milling machine collets, one with a 10–12 mm diametric clamping range and one with 8–10 mm range were purchased to cover a range of different specimen geometries. It turned out that the latter was not applicable in the Instron clamps, since the cone is reversed compared to standard milling machines. The 10-12 mm collet could be used for the type B geometry, but did not provide sufficient clamping pressure for the type A specimen geometry. Hardened steel bushings were therefore fitted to the specimen grip sections to give an effective outer diameter of 12 mm as shown in Figure 3.11. The bushings were manufactured with four slits on each end to accommodate deformation. Some variations on the bushings were made with regard to the inner surface finish. In addition to the as-machined surface finish, the inside of the bushings were sandblasted and threaded. The surface proved to have little influence on fretting fatigue compared to the effect of clamping pressure.

The problem with fretting fatigue appeared to stem from the way the specimens were polished; the specimens would get a smooth transition from the

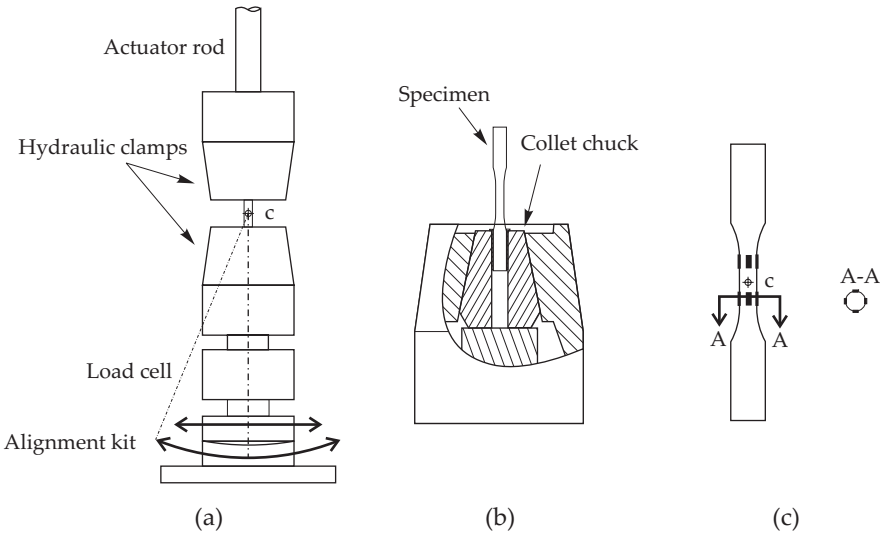

Figure 3.9: The 50 kN test frame: (a) frame layout, (b) cut-out view of a hydraulic clamp, (c) specimen with strain gages used for alignment adjustment.

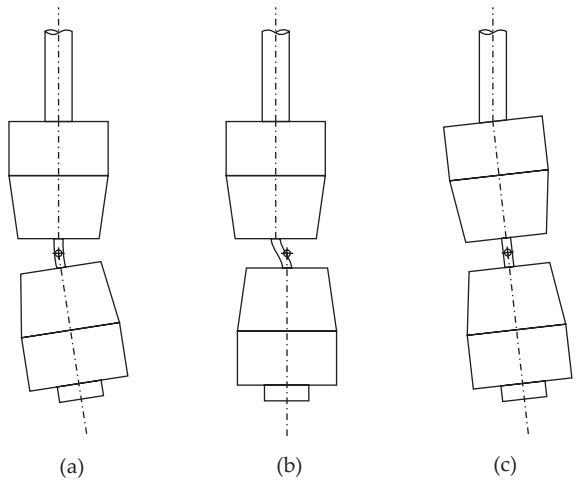

Figure 3.10: Different modes of misalignment;(a) angular misalignment, (b) transverse misalignment and (c) misalignment between the actuator rod and the upper hydraulic clamp.

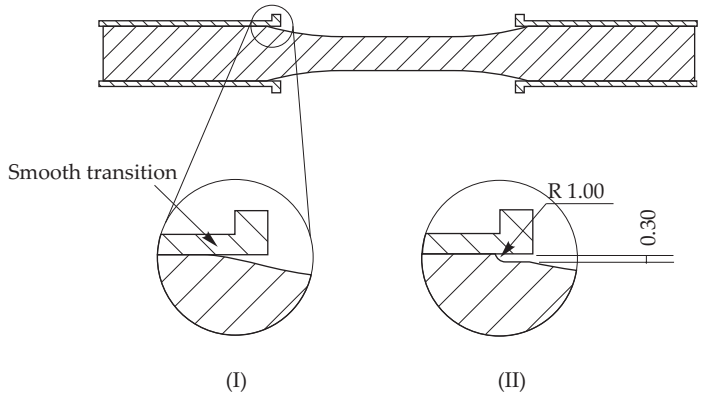

Figure 3.11: Specimen with steel bushings. (i) Area in which fretting fatigue occurred. (ii) Modified geometry to avid fretting.

notch area to the grip section, as depicted in Figure 3.11(i), thus leaving an area where the clamping pressure gradually decreases to zero. This may cause relative movement between the bushing surface and the specimen, and give rise to fretting fatigue at long fatigue lives. The specimens with expected fatigue lives of around one million cycles were therefore modified by machining a sharp notch (ii) in the grip section.

The cyclic stress-strain curve was obtained by incremental-step testing under total strain control. This was done in a 100 kN Instron test frame prior to the installation of the 50 kN test frame, and made use of Wood's-metal grips for proper alignment. The test specimens were of type B (Figure 3.6) with M12 threads in the grip area. The testing with this setup was abandoned for the low cycle fatigue testing due to problems with fatigue failure in the threaded grip section of the specimens.

3.2.3 Low cycle fatigue

Low cycle fatigue testing of the extruded material was done at total strain control with a nominal strain rate of 0.4 %/s and a strain ratio of R_ε=-1. The 50 kN test frame was used and an Instron extensometer with a 10 mm gauge length was used for measuring strain. Specimens from batch III with geometry B (Figure 3.6) were tested, in addition to three specimens from batch II (geometry A) for comparison. Steel bushings were not needed for the type B specimens, since sufficient clamping pressure could be obtained using the 10-12 mm collet, however, the required grip pressure resulted in plastic deformations in the grip section. This introduces uncertainties with regard to specimen alignment, although the plastic deformation appeared to be consistent around the circumference. Pictures of a the two types of specimens, along with the collet is shown in Appendix A

Low cycle fatigue testing of the forged F(I) material was conducted by West-

moreland Mechanical Testing and Research Ltd. The test specimens used were similar to geometry B, only with a 6.35 mm diameter gauge section. Testing was done at total strain control with a constant frequency of 0.5 Hz for all strain ranges. After 43,200 cycles, the tests were changed to constant amplitude loading with a frequency of 10 Hz.

3.3 Test results

Tests were terminated after reaching 2×10^6 cycles, however, some specimens failed due to fretting fatigue in the grip section at around 10^6 cycles. Test terminations (runouts) and failures outside the specimen gage area were statistically treated as right-censored observations according to the ASTM recommendations [149]. In this context, a right-censored observations means that there is no knowledge about the actual fatigue life of the specimen, only that the specimen survived for a given number of cycles. This information contribute to the regression of fitted parameters using maximum likelihood (ML) estimation as outlined in Section 1.2.3. The solution approach and interpretations of confidence levels are given in Appendix A3.

All failures are defined as full separation of the fracture surfaces. Some attempts were made at stopping the strain controlled cycling at a 5% load drop, at which the fatigue cracks were around 1 mm long. The remaining fatigue life at this point, however, was found to be insignificant compared to the total fatigue life.

3.3.1 High cycle fatigue

Figure 3.12 shows results from R=0.1 testing. The data has been fitted to Eq. 1.1 assuming constant standard deviation. The extruded material has better fatigue strength in the high cycle regime than the forged material. The amount of scatter in these tests initially raised questions about the accuracy of the test setup. Improvements were therefore made and the alignment was controlled and documented to minimize experimental errors. Data from the initial test setup was discarded, however, the scatter was still found to be high. The censored observations below 10^6 cycles are failures due to fretting in the the grip section.

Figure 3.13 on the next page shows results from load controlled R=0.1 tests. The forged F_R (I) series and the extruded E(II) series have been fitted to Eq. 1.1, using the maximum likelihood estimation described in Appendix A3 with variable standard deviation. These results show that the extruded material has better fatigue strength than the forged material. All results from the forged R=-1 tests are shown in Figure 3.14, fitted to Eq. 1.12 with variable standard deviation. It appears that all forged materials are similar with regard to fatigue strength in this test, although more tests are needed to confirm this. The over-aged material F_R may have lower fatigue strength at high loads, while the prototype process alloy F_P seems to have better high cycle fatigue strength. The fatigue limit as given

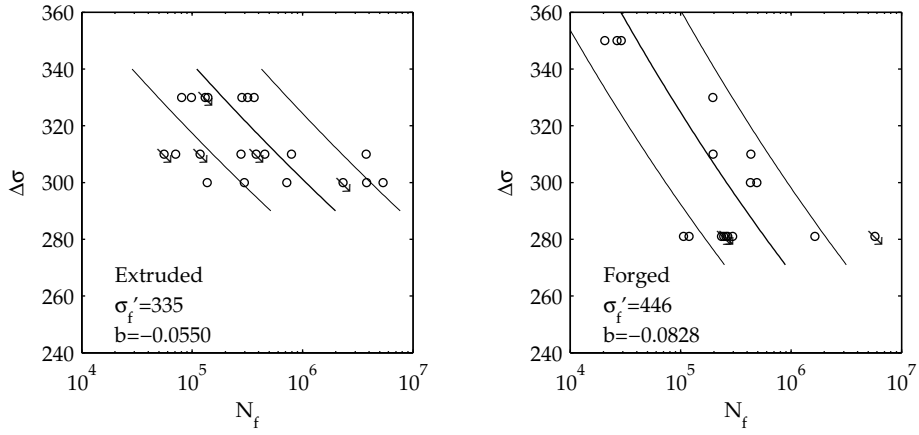

Figure 3.12: Tests of smooth specimens from forged and extruded material at R=0.1. Confidence of 5% and 95% are shown and arrows mark censored observations.

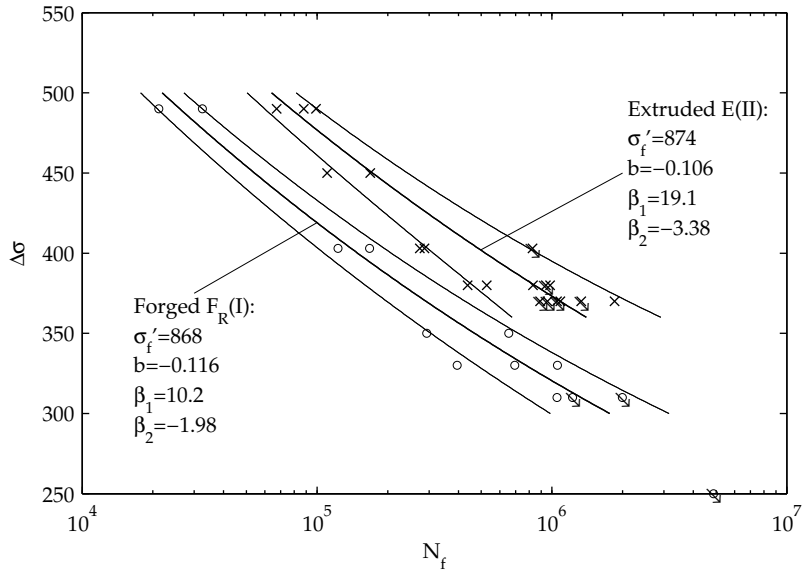

Figure 3.13: Test results for the extruded E(II) and forged F_R series at R=-1. Confidence lines at 5% and 95% and arrows mark censored observations. The β parameters are used to model spread according to Eq. 1.11.

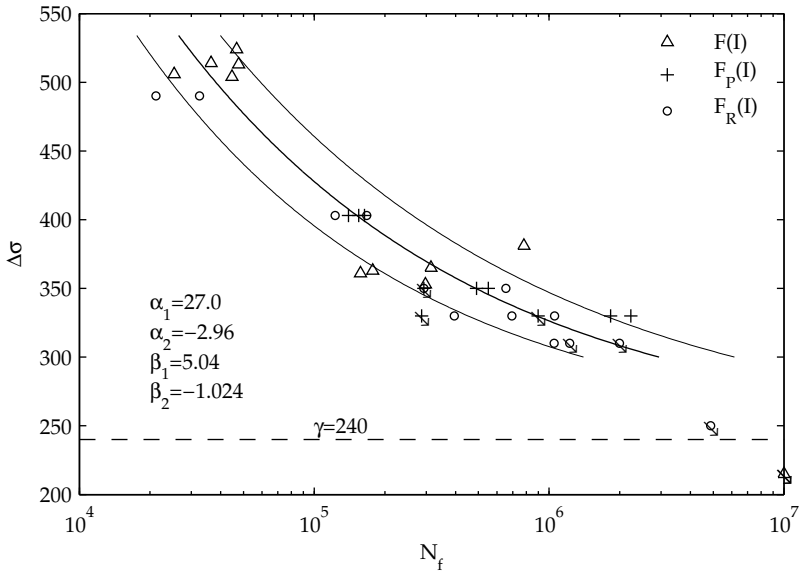

Figure 3.14: Test results for the forged series at *R*=-1, fitted to Eq. 1.12 and Eq. 1.11.

by Eq. 1.12 is $\gamma = \Delta\sigma = 236$ MPa, with 95% confidence intervals 234-245 MPa (see Appendix A3), however, this is more a feature of the mathematical model than an estimate of the true fatigue limit.

A maximum likelihood estimate of the five model parameters in Eq. 1.12 and Eq. 1.11 require a considerable number of observations to give numerical convergence. Good starting estimates of the parameters are typically required in ML estimation, and solution convergence can not generally be guaranteed. Test series other than the forged series had insufficient specimens for this five-parameter model.

Some mean stress corrections have been used on the *R*=-1 and *R*=0.1 data. The results are shown in Figure 3.15, where rhe correlation coefficient *r* (R-square) is given as a measure of goodness of fit. It can be seen that the SWT parameter (Eq. 1.8) is unable to describe the fatigue data using a common fit, while the Morrow mean stress correction (Eq. 1.6) gives better results. The Findley criterion (Eq. 1.9) shows a slightly improved prediction for the forged series, although the scatter is still quite high. The parameter *k* in Eq. 1.9 was found to be 0.22 for both forged and extruded material.

The results from all smooth specimens are shown in Figure 3.16 on page 63. It is clear that the extruded material has higher fatigue strength *R*=-1. This trend can be seen for *R*=0.1 as well, although the high degree of scatter produces wide prediction intervals for these tests.

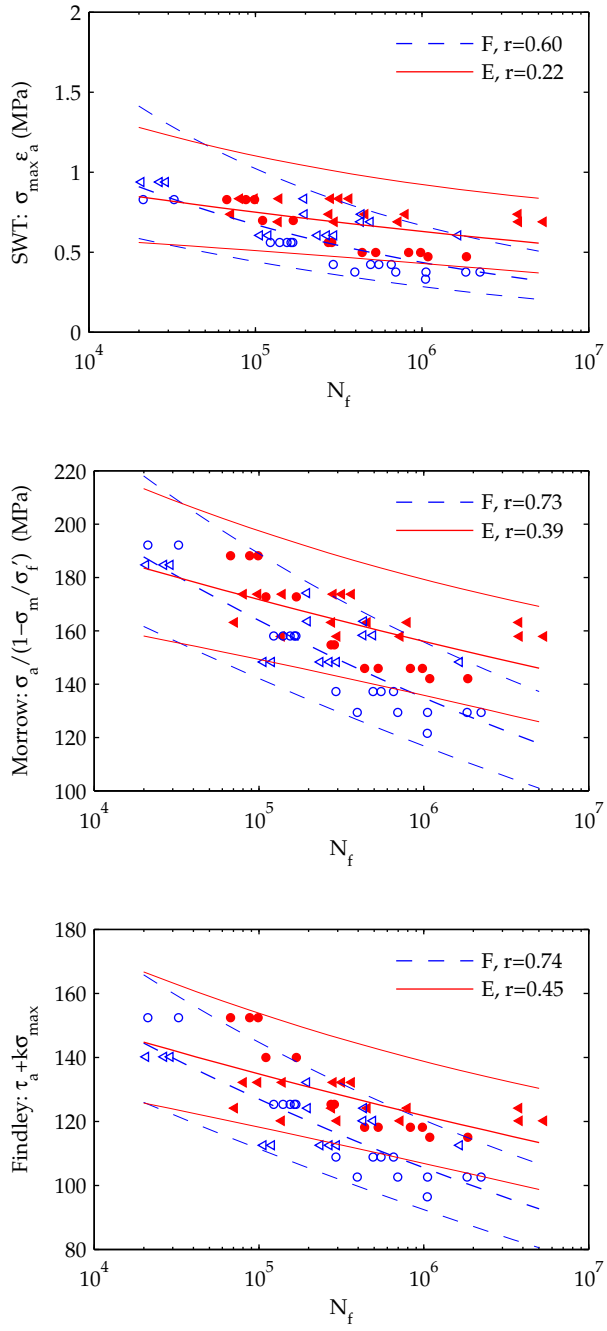

Figure 3.15: Mean stress corrections, following the models presented in Section 1.2.2. Forged (F) and extruded (E) have been fitted separately, shown with estimated 5% and 95% prediction intervals and correlation coefficient *r*. See Figure 3.16 for data legend.

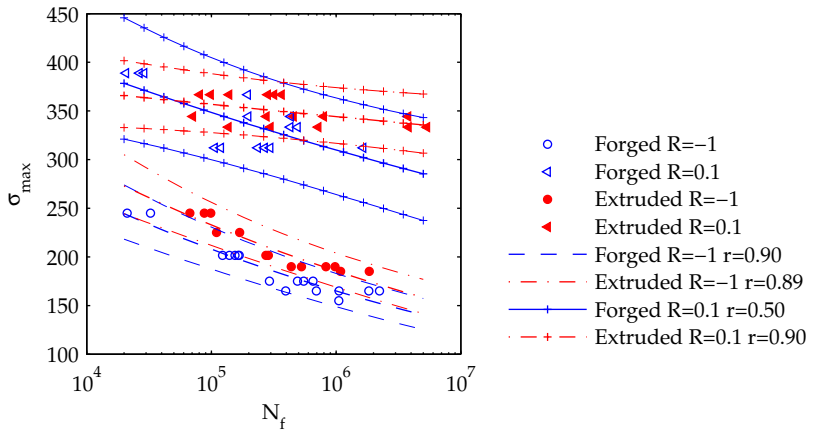

Figure 3.16: Comparison of all fatigue tests of smooth specimens. Prediction intervals of 5% and 95% are shown for each series.

3.3.2 Low cycle fatigue

The elastic and plastic strain amplitudes have been fitted to the total strain life equation by least squares regression. Figure 3.17(a) on the next page shows the individual fitting of the elastic and plastic terms of Eq. 1.3. The square symbols are results from the load controlled test, where the nominal stress have been scaled by the compliance. The transition life, i.e. the number of cycles where the elastic and plastic contributions are the same, can be seen to be quite low at N_t=68.

In Figure 3.17(b), the strain life relation for the forged F(I) material is shown, as obtained from Westmoreland Mechanical Testing. It can be seen that the forged material test exhibit more scatter than the extruded material test, both for load controlled and strain controlled cycling. It is unknown whether this is due to differences in testing procedures or due to more inherent variance in the forged material. The high cycle fatigue strength appears to be very similar for forged and extruded material in these plots. The forged material clearly has inferior strength in the low cycle regime, and an even lower transition life of N_t=22. It should be noted that the plastic strain amplitudes in the extruded tests were determined from hysteresis loop widths at σ=0, whereas in the forged tests, the plastic strain amplitude was determined as

$$\Delta\varepsilon^{\mathrm{p}} = \Delta\varepsilon - \Delta\varepsilon^{\mathrm{e}} = \Delta\varepsilon - \frac{\Delta\sigma}{\bar{E}}, \tag{3.1}$$

where $\bar{E}$ is the average of the observed tensile and compressive elastic moduli at half-life.

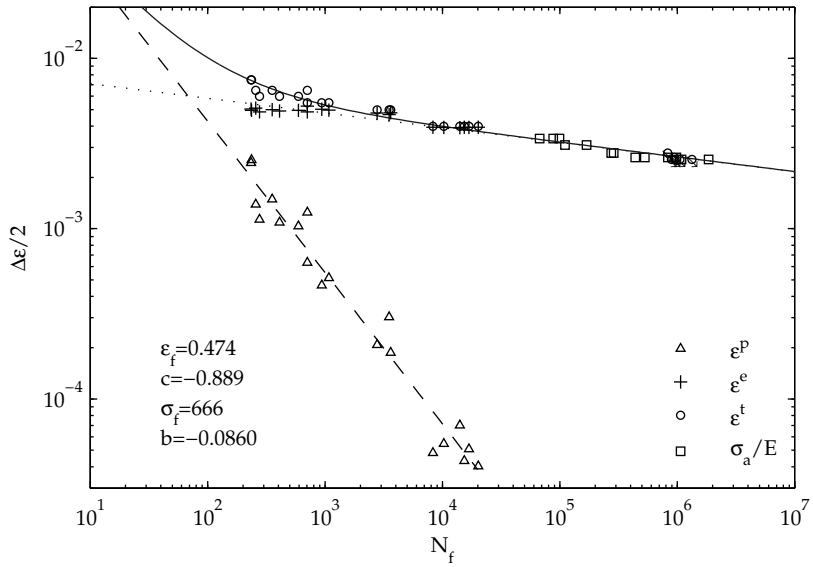

(a) Extruded material.

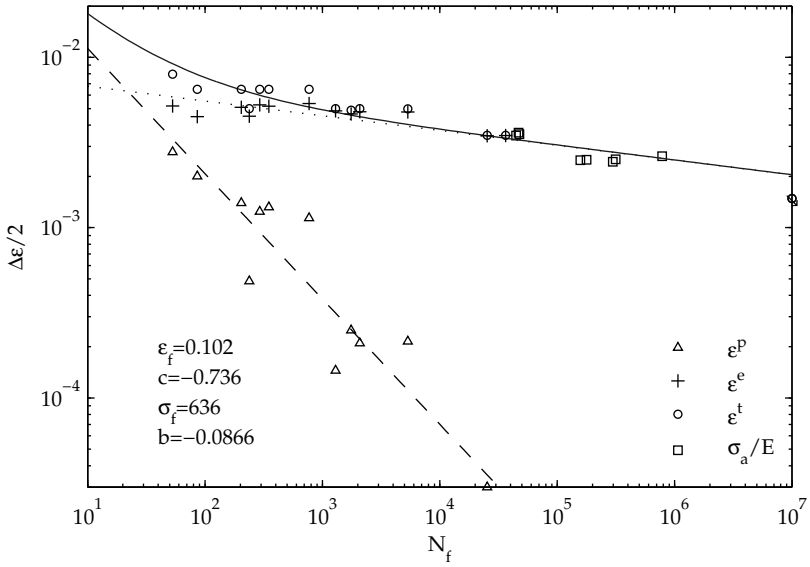

(b) Forged material.

Figure 3.17: Total strain life curves, with elastic and plastic fits shown.

Figure 3.18 shows the cyclic stress-strain curve with data points from an incremental step-test of the extruded E(I) material, where the parameters K and n have been estimated by least squares regression from the Ramberg-Osgood equation. Also shown is half-life values of stress vs. strain range, as measured during the LCF tests. It can be seen that the forged material has similar cyclic stress-strain behavior as the extruded material, even though the forged material has lower monotonic strength. The two extruded specimens tested at $\Delta\varepsilon$=1.5% show some deviations from the other tests. Although the alignment was confirmed to be very accurate, there were indications that the test frame had insufficient lateral stiffness at the highest loads. This could have introduced buckling in the specimens. One specimen tested at $\Delta\varepsilon$=1.6% buckled and was discarded. There were no visual sign of buckling in the two $\Delta\varepsilon$=1.5% tests, however, the stress-strain plot revealed a load drop in the first compressive half cycle, before the minimum strain value had been reached. This is shown for one specimen in Figure 3.22(a) on page 68, and is an indication of buckling in these tests.

Figure 3.19(a) on the next page shows the evolution of stress amplitude during the low cycle fatigue tests. The alloys exhibits softening throughout the fatigue life for strain ranges greater than 1%. For 0.8% strain range, the test specimens showed a mixed behavior of initial hardening followed by softening after about 10 cycles. The evolution of plastic strain range, as determined from hysteresis loop width, is shown in Figure 3.19(b). Plastic strain ranges increased with cycling for all strain ranges, except for $\Delta\varepsilon$=1.5%, which showed an initial

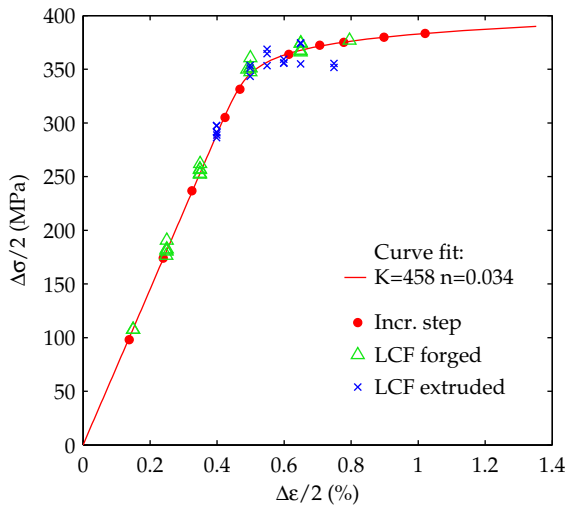

Figure 3.18: Cyclic stress-strain curve for the extruded material as found from incremental step testing and fitted to Eq. 2.2. Also shown are values at $N_f/2$ for LCF tests of forged and extruded material.

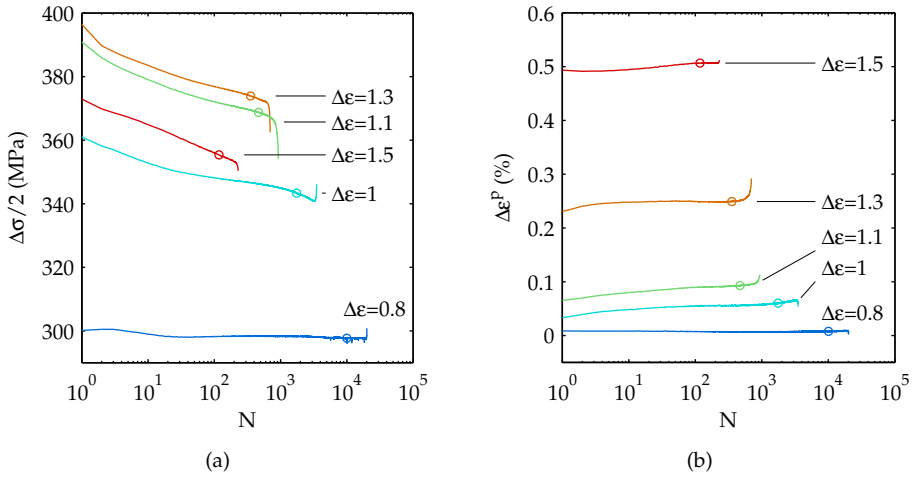

Figure 3.19: Evolution of stress amplitude (a) and plastic strain range (b) vs. number of cycles for various strain ranges. The circles mark the half life point.

decrease in $\Delta\varepsilon^{\mathrm{p}}$ for the first 10 cycles, followed by increasing values. Stress ranges and plastic strain ranges for the forged LCF test were recorded at the first and the mid-life cycle. The forged material generally showed less softening, as shown in Figure 3.20(a) for two specimens. The plastic strain ranges were, however, comparable to those observed for the extruded material, as seen in Figure 3.20(b).

The hysteresis loop energy, as found from

$$E_{\mathrm{p}} = \oint_{\mathrm{loop}} \sigma d\varepsilon, \tag{3.2}$$

was found to be near constant for the highest strain levels throughout the fatigue life. At lower strain levels, E_{p} increased steadily up to 30% at failure. The half-life values of $\log E_{\mathrm{p}}$ were found to form a linear relation with log life, as seen in Figure 3.21(a).

The hysteresis loop shape has been quantified by Abel [150] in terms of the parameter

$$\beta = \frac{\Delta\sigma\Delta\varepsilon^{\mathrm{p}} - \Delta E_{\mathrm{p}}}{\Delta E_{\mathrm{p}}}, \tag{3.3}$$

where $\Delta\sigma\Delta\varepsilon^{\mathrm{p}}$ represents the maximum possible hysteresis energy, corresponding to a parallelogram in $\varepsilon - \sigma$ space. Lower vales indicate that the dislocations experience a frictional resistance as they move through microstructural barriers. Larger values indicate that a larger portion of the energy required for dislocation-microstructure interaction is elastically recoverable [150, 151]. Half-life values of β are shown in Figure 3.21(b), indicating that there is a change in the hysteresis

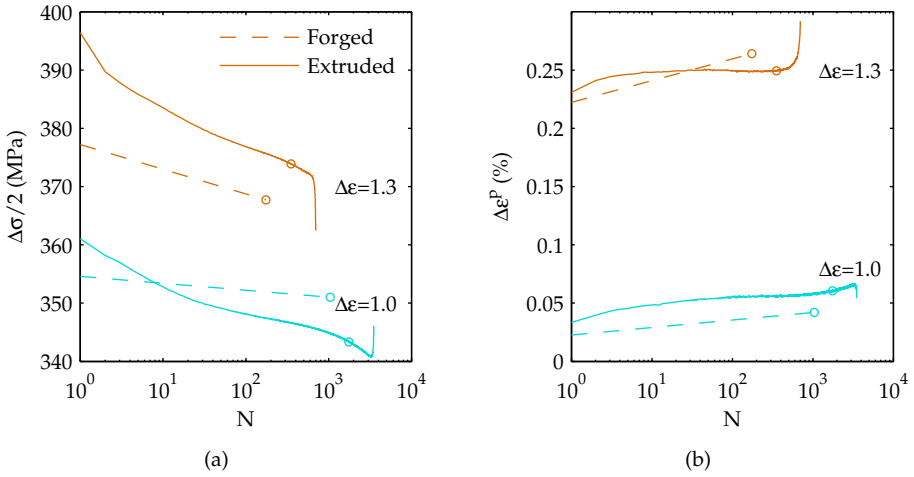

Figure 3.20: Stress range (a) and plastic strain range (b) for forged and extruded material at two strain ranges. The values for the forged alloy have only been recorded at the first cycle and the half-life cycle.

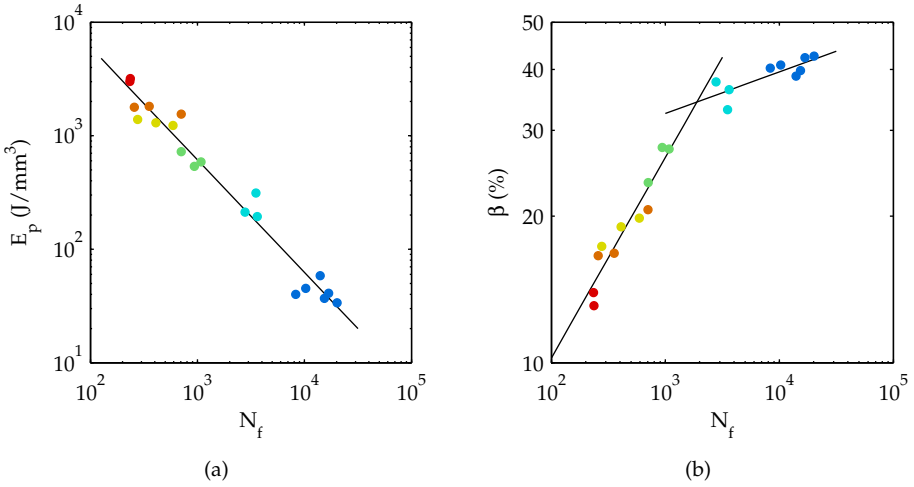

Figure 3.21: (a) Hysteresis loop energy at half life. (b) Hysteresis loop shape coefficients at half life.

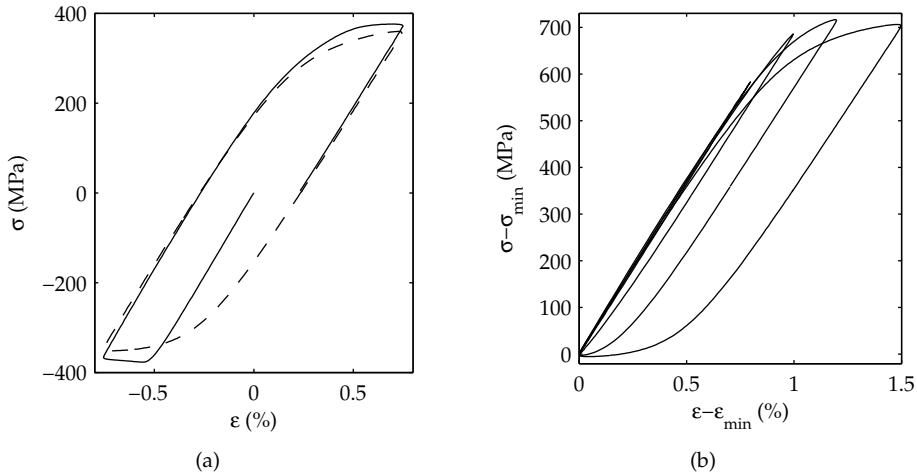

Figure 3.22: Hysteresis loops recorded during the LCF tests. (a) The first compressive half cycle indicates buckling. (b) Hysteresis loops at half-life for different specimens, showing that the material disobeys Masing material behavior.

loop shapes for specimens failing at around $N_f = 2000$. This indicates a change in the dislocation structures for higher strain levels, most likely a transition from dislocation bands to a dislocation cell structure, as noted in Section 2.1.1.

Comparison with literature data

The hysteresis loops at half-life in Figure 3.22(b) shows that this material does not conform to Masing material behavior. This has also been reported by Borrego et al. [152] for a 6082 alloy with similar composition.

A comparison of Borrego's strain life fatigue results with the material used here is shown in Figure 3.23. From these plots, it appears as if the fatigue strength is lower for the material used in this study. This is misleading, since the cyclic stress response of the current material is higher, as seen from Figure 3.24. Both monotonic and cyclic stress response is well above the figures reported in the literature of 6082-T6 [59, 153–156]; whereas $R_{p0.2}$ for the extruded E(I) material is 408 MPa, published results are in the range 245-310 MPa. The only comparable figures have been found in an article by the Leiber Group [157], where a $R_{p0.2}$ of 380 MPa is guaranteed for a wrought 6082-T6 alloy. In Figure 3.25, the total strain fatigue equations have been converted to stress range by using the cyclic stress-strain equation as defined by Eq 2.2. Stress range values at half-life for forged and extruded material are also shown. It can be seen that both the forged T5 and the extruded T6 material used in this study has better overall fatigue properties.

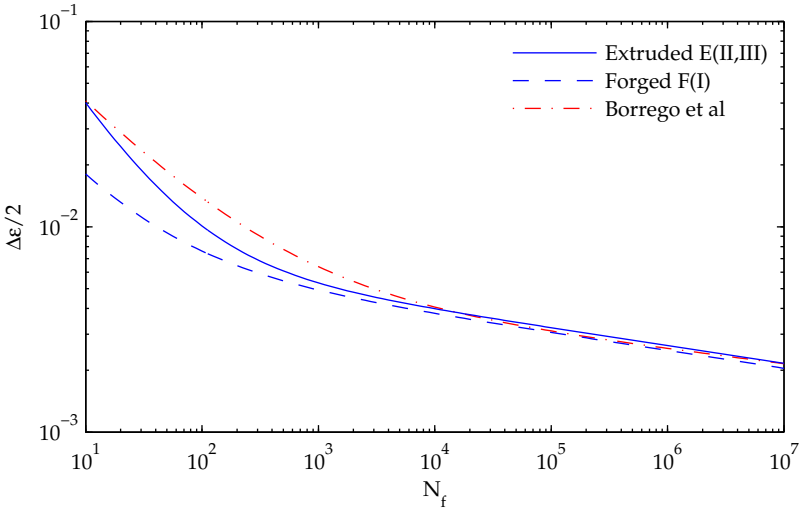

Figure 3.23: Total strain life for the forged and extruded material, compared to results by Borrego et al. [152].

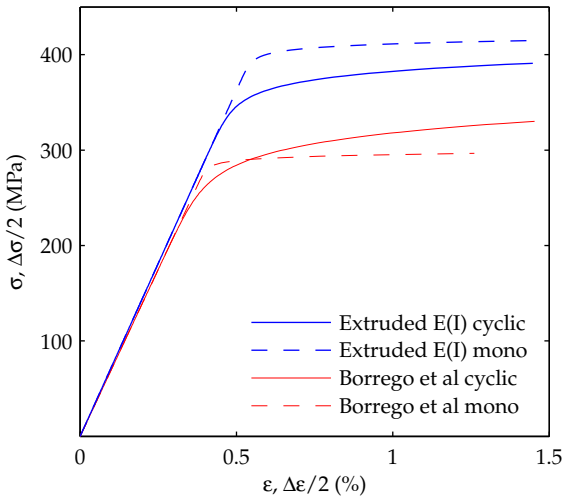

Figure 3.24: Cyclic (solid) and monotonic (dashed) stress-strain curves for the material used in this report, compared to published results of a nominally similar alloy (Borrego et al. [152]).

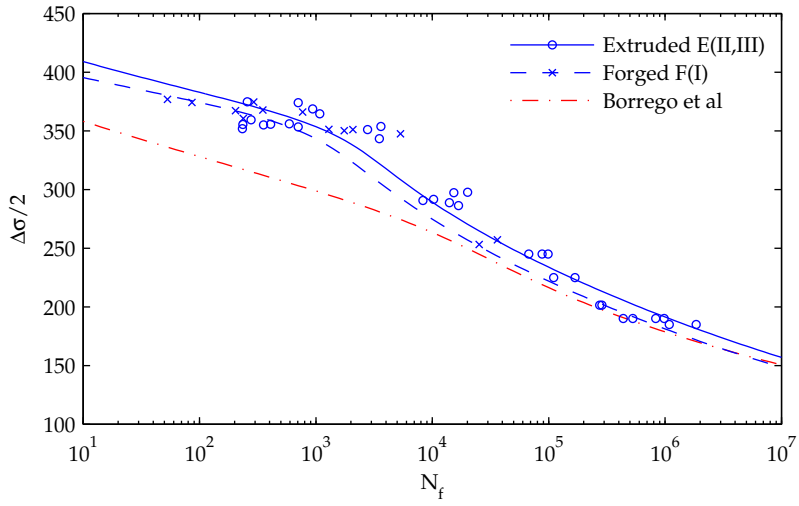

Figure 3.25: Total strain-life data converted to stress-life using the cyclic stress-strain curve. Results are compared to Borrego et al. [152].

3.4 Surface measurement

The rough specimens were measured using a Wyko NT2000 white light interference (WLI) profilometer. The profilometer consists of a Mirau-type interferometric microscope where the objective is moved by a piezoelectric transducer. A computer is used for controlling the objective and recording images from a CCD array. Measurements are made by moving the objective towards the surface and simultaneously recording the light intensity from each pixel in the array. The surface height at each pixel location is then determined from the objective position of maximum interference. Since white light has a short coherence length, the surface height can be measured with a high precision of 3 nm by using algorithms to demodulate the fringe data [28, 158]. The lateral resolution is limited by the optics, i.e. around 1 µm.

Topography measurements using WLI compares favorably to mechanical stylus instruments. Measurements are faster, and since it is a non-contact technique, errors associated with finite stylus tip radii and deformation in the measured surface are avoided. The latter is particularly important for soft materials such as aluminium alloys. Comparisons have been made by Ohlsson et al. [159] with an atomic force microscopy (AFM), which is considered the most accurate profilometer available. The WLI measurements showed good agreement with the AFM, but would produce some artifacts and exaggerate peaks compared to the AFM measurements. This may not be as relevant for the current study, where the peak-to-valley height is one order of magnitude larger.

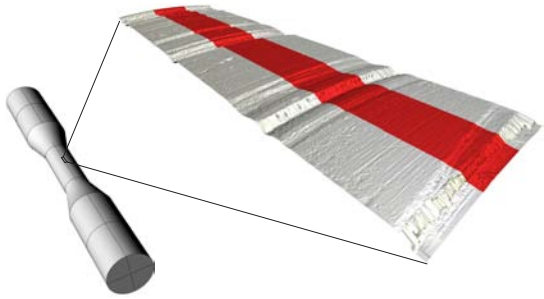

Figure 3.26: Three WLI scans taken from one specimen.

3.4.1 Measurement setup

A 10x (NA=1) objective with a secondary magnification of 0.52x was used, which gives a field of view of 744 by 1141 µm and a sampling interval of 3.1 µm. The mid-section of the specimens is 20 mm long, which means several images need to be captured to cover this length. This is done by using programmed stage movement in which images along the length of the specimen are captured, each of them overlapping by 139 µm.

The 3D measurements are used to construct 2D profiles, which are later used to generate axi-symmetric FE models. Each point in the 2D profile is found by averaging 80 samples in the circumferential direction, after the cylindrical curvature of the specimen have been subtracted from the 3D scans. In effect, the 2D profile is based on a 300 µm wide band along the center of the measurements as shown in Figure 3.26. This helps smoothing sampling errors or artifacts in the WLI measurements, and the final profile is then based on the samples with highest accuracy, since the intensity, and thereby accuracy, drops as the inclination of the surface increases towards the edges of the scans.

From the way the specimens were machined, it is not to be expected that the circumferential grooves are perfectly axi-symmetric. The specimens were therefore measured along four different angular positions designated 0, 3, 6 and 9, referring to clock values as perceived when looking down the centerline of the specimens. The complete 2D profile for one such angular position is assembled by stitching the separate scans into a continuous surface profile. It is not feasible to place the specimens on the microscope table so that the specimen axis is perfectly perpendicular to the microscope's optical axis. Each of the parts that constitute the full 2D profile must therefore be tilted and translated so that they form a continuous global profile.

Bottom radius estimates for the valleys were made using an algorithm which calculated the best fit of a parabola to the bottom points[2]. The parabola equation

[2]This algorithm, along with the 2D stitching algorithm was programmed by Børge Holme at SINTEF

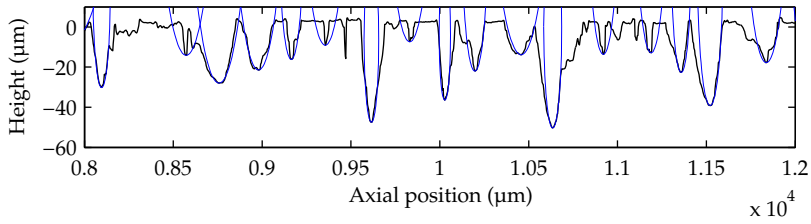

Figure 3.27: Estimates of valley-tip curvature for a specimen.

is

$$y = Az^2 + Bz + C, \tag{3.4}$$

where the curvature is found as $\rho=(2A)^{-1}$. Figure 3.27 shows fitted circles for a profile. It can be seen that the radius algorithm performs well in most cases, but irregularly shaped valleys are misinterpreted.

3.5 Residual stresses

X-ray diffraction strain measurements were used to estimate residual stresses in the specimen surfaces. V-filtered Cr Kα radiation was used with ψ angles from -60 to 60° in 15° increments, measuring the θ position of the Al 311 reflection. The beam width is 1 mm at zero tilt and 2 mm at $\pm 60°$, thus the measured strains are averages of peak and valley strains within this region. Further information on X-ray diffraction can be found in [160].

Table 3.3 shows the residual stress results obtained using an isotropic material model. Maximum principal stresses are given, where the angle between the σ_{11} direction and z is given by α. The shear stresses σ_{13} were insignificant and are therefore omitted. The repeated measurements in Table 3.3 were taken at different clock positions, indicating that the residual stresses are the same around the circumference. Specimen X17 clearly stands out, and an explanation for this will be given in Chapter 5. There is no significant change in residual stresses before and after cyclic loading in the rough section.

Attempts were also made to determine residual stresses for the whole surface profile using synchrotron radiation. X-ray radiation from a synchrotron source is more coherent and can attain a higher degree of collimation than the Cr radiation used in traditional goniometers. The measurements were made at HASYLAB at beamline G3, described in Ref. [161]. The experimental setup is shown in Figure 3.28. A surface resolution of 12 µm could be attained by using a micro-channel plate (MCP) consisting of hexagonal shaped channels with 12.5 µm between their centers. The thickness of the MCP was 4 mm, and the distance between the CCD and the MCP was 1 mm, resulting in an angular acceptance of 2.5 mrad. A Θ step size of 0.02° was used over 101 steps to determine the peak Θ location of the Al (400) reflection. In traditional diffraction experiments of

Table 3.3: Residual stresses (MPa) calculated from X-ray diffraction measurements. The two specimens marked with * were polished prior to roughening, thus the residual stresses are for a polished surface.

	Machined			Rough			
Specimen	σ_{11}	σ_{33}	α	σ_{11}	σ_{33}	α	Comment
E18*	-161±6	15±6	5°	-164±6	6±8	5°	
E18*	-120±6	7±4	1°	-154±10	6±8	5°	After failure
B23*	-118±12	4±7	2°	-156±5	7±6	3°	
X17	13±1	-3±4	10°	-173±7	0±4	0°	
X17	-4±8	3±4	8°				Repeated
X1	-148±6	4±1	2°	-117±14	1±6	0°	
X12	-165±6	2±6	1°	-158±8	2±3	1°	
X12				-165±3	2±1	1°	Repeated
X38				-164±11	6±7	2°	
X15				-167±4	5±1	2°	
B21				-135±11	4±1	2°	
B21				-135±9	3±5	1°	Repeated
B21				-151±13	3±8	1°	After failure
X19				-157±7	1±1	0°	
X19				-134±21	-3±8	1°	After failure
F19				-151±9	-1±4	0°	
A18				-173±7	-1±9	0°	
E22				-146±9	3±6	1°	
F21				-143±20	-1±4	0°	
X32				-138±7	1±2	0°	
X36				-141±3	4±4	2°	
X9				-139±5	-5±5	2°	
E19				-154±14	1±5	0°	

this type, the angle of incidence between the source radiation and the surface is varied by tilting either the beam or the sample. In this setup, the surface geometry itself provided an angular variation of ψ=0-90°. A problem with highly textured materials is that only a few grain will be oriented in such a way as to give lattice reflections for a given value of Θ and ψ. This was also found to be the case for these specimens, thus in order to obtain sufficient reflections for stress analysis, the specimen was continuously rotated during the scans. This was done under the assumption that residual stresses did not vary around the circumference, as indicated by the initial X-ray measurements at different clock positions. This appeared to be incorrect, thus quantitative stress results could not be obtained. Figure 3.29 shows a compacted form of the results. Peak locations in Θ have been assigned different shades of gray. The surface residual stresses along the surface does show some variation, as indicated by a shift in peak Θ positions for different ψ angles. Figure 3.30 shows that there is no clear fit for the d vs. $\sin^2 \psi$ values.

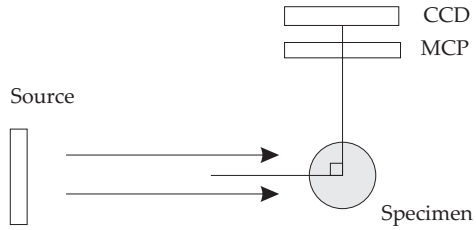

Figure 3.28: Schematic of the synchrotron measurement setup.

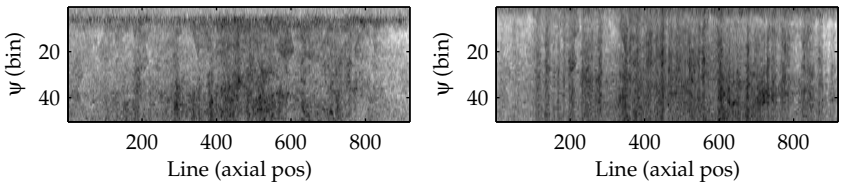

Figure 3.29: Peak locations of the Al400 reflection, shown as different shades of gray for two specimens. One line correspond to 12 µm, and one ψ bin correspond to 4°.

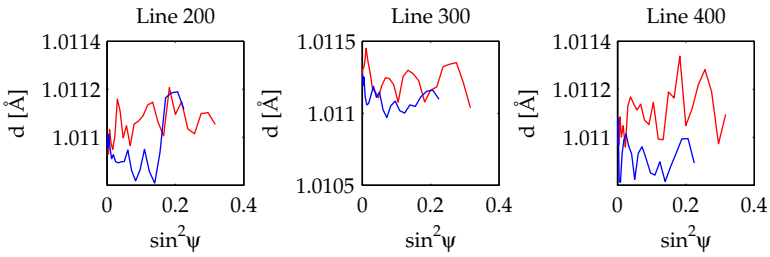

Figure 3.30: Lattice spacing parameter d for different surface–beam angles ψ.

3.6 Conclusions

Both the forged and the extruded material have a highly textured grain structure. The extruded material has long grains in the extrusion direction, and the forged material, which is manufactured from the extruded billets, has elongated, flattened grains. This presumably leads to anisotropic mechanical properties, although this has not been investigated in this work. Testing was done in the extrusion direction where the material most likely is strongest. For both the extruded and the forged material, larger grains are mainly (111) or (001) oriented, while smaller grains and sub-grains are oriented between (111) and (001).

High cycle fatigue tests at two different load ratios showed that the extruded material has better fatigue strength than the forged material. The SWT parameter was unable to describe mean stress effects, while the Morrow correction and the Findley criterion showed better predictions. The latter is a multiaxial parameter that may be applicable in multiaxial fatigue life predictions for this material.

The cyclic stress-strain curve was obtained for the extruded specimens using incremental step tests, and for the forged specimens using half-life values of stress and strain from the low cycle fatigue tests. The cyclic properties of the forged and the extruded material was similar in this case, although it should be noted that incremental step tests and half-life values are known to produce different results for certain materials.

The minor differences in chemical composition does not seem to have an effect on fatigue life. Fatigue testing at R=0.1 gave very high scatter in the observed stress vs. life, thus the associated fatigue strength coefficients should be used with caution. This could be due to variability in cyclic yield strength for the specimens, since peak stresses for lives around 10^6 cycles are very close to the cyclic yield stress. Variations, e.g in grain structure, could therefore lead to global yield at peak stresses in some specimens, which would significantly decrease the fatigue life. The R=-1 tests were mainly cycled in the elastic regime, where fatigue strength is determined by localized plasticity in weak regions in the material. Failure from this mechanism appears to be more predictable since the scatter at R=-1 testing is comparatively low.

The initial stress-strain response during the highest strain-range tests showed indications of buckling. It could be that the test frame has inadequate stiffness to perform this test. Another source of uncertainty with regard to alignment, is the observed plastic deformation in the specimen grip section for the type B geometry. The specimen used for alignment was made of high strength steel, and therefore cannot replicate this condition. The type A specimens with 10 mm grip section diameter and steel bushings turned out to be well suited for both HCF and LCF testing, but should be produced with a secondary notch as outlined to avoid fretting fatigue at high fatigue lives.

The material used in this study has higher cyclic and monotonic strength than similar 6082 alloys reported in the open literature. Some concern has been raised by one of the customers of the suspension arm, that the low cycle fatigue strength is lower than older suspension designs made of DC castings. The material data

for this comparison was not given, however, it has been shown that comparing low-cycle fatigue data based on strain may be misleading. A reformulation of strain range to stress range fatigue curves shows that the current material, both forged and extruded, has better fatigue properties than published results of 6082-T6, even though the strain-life curves are lower.

Chapter 4

Finite element modeling

FEMLAB[1] is used for finite element analysis (FEA) of the surface profiles. FEMLAB originated as a toolbox for MATLAB[2] for numerical solving of partial differential equations, with emphasis on interaction of physical phenomena such as heat transfer, fluid flow, electromagnetics and structural mechanics. The current version of the program (3.1) uses compiled C and Java code, and can be run as a stand-alone application. Integration with the MATLAB environment is still retained, which allows the extensive library of MATLAB algorithms to be used in modeling and post-processing of numerical simulations.

As described in Section 3.4, the white light interferometry (WLI) measurements yield 3D topographic data from which 2D profiles are derived. Due to the large number of geometries, all tasks from geometry creation to stress analysis is automated by MATLAB scripts. This chapter describes the routines used to generate FE geometries for these profiles along with details about the analysis. Theoretical background on the finite element method and associated algorithms can be found in standard textbooks, e.g. [162, 163].

The size of the surface features are on the same order as the grain size, however, for the reasons outlined in Section 1.3, the FE analysis is confined to isotropic and homogenous material models. All references to stresses and strains in this section are therefore purely theoretical, and are regarded as properties of the geometry.

4.1 Model description

Four axi-symmetric geometries are created for each specimen, that is, one for each of the four angular positions referred to as clock values 0, 3, 6 and 9, as described in Section 3.4. Referring to Figure 1.6 on page 14, the measured profile constitutes the outer surface boundary, running parallel with the z axis at a

[1] COMSOL AB. Starting from version 3.2, FEMLAB is now called Comsol Multiphysics.
[2] The MathWorks Inc.

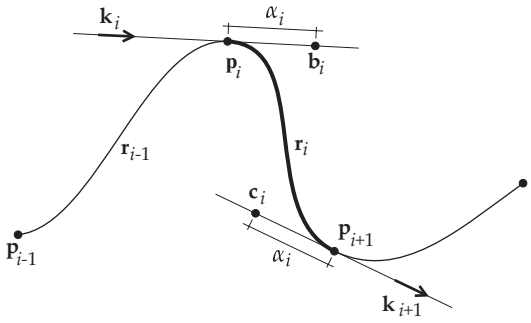

Figure 4.1: Bézier interpolation between sample points $\mathbf{p}_i$ and $\mathbf{p}_{i+1}$.

distance of 3.1 mm. An interpolation method must be used, since the profile consists of distinct samples, each spaced 3.13 µm apart in the horizontal direction. The simplest interpolation method would be a piecewise linear interpolation, however, this would introduce stress singularities in a continuum mechanics model. A higher order interpolation method should be used instead, where tangential continuity can be specified at the sample points. Cubic Bézier splines are used here, since FEMLAB has built-in support for this geometry type.

The surface profile is constructed by piecewise interpolation, where the geometry between sample points is represented by spline segments. A profile with $i = n$ sample points require $n - 1$ segments, each defined by the parametric equation [164]:

$$\mathbf{r}_i(t) = (1-t)^3\mathbf{p}_i + 3t(1-t)^2\mathbf{b}_i + 3t^2(1-t)\mathbf{c}_i + t^3\mathbf{p}_{i+1}, \tag{4.1}$$

where

$$t \in [0, 1].$$

Eq. 4.1 is a 2D vector function for the spline segment shown in Figure 4.1. The sample points from the WLI profile are denoted $\mathbf{p}$, and additional points used to control the spline shape are denoted $\mathbf{b}$ and $\mathbf{c}$. A total of four points are thus needed to define the spline interpolation between two sample points. The control points govern the tangent directions at the spline endpoints, which can be verified by taking the first order derivative of Eq. 4.1:

$$\dot{\mathbf{r}}_i(0) = 3(\mathbf{b}_i - \mathbf{p}_i) \tag{4.2a}$$

$$\dot{\mathbf{r}}_i(1) = 3(\mathbf{p}_{i+1} - \mathbf{c}_i). \tag{4.2b}$$

A smooth surface profile is obtained if these gradients are equal at adjoining endpoints, that is, $\dot{\mathbf{r}}_i(1) = \dot{\mathbf{r}}_{i+1}(0)$. However, this condition carries an unnecessary restriction, namely that the length of the tangent vector is continuous along the spline. Only the direction needs to be the same for geometric smoothness, which means that the normalized gradient should be equal in $\dot{\mathbf{r}}_i(1)$ and $\dot{\mathbf{r}}_{i+1}(0)$.

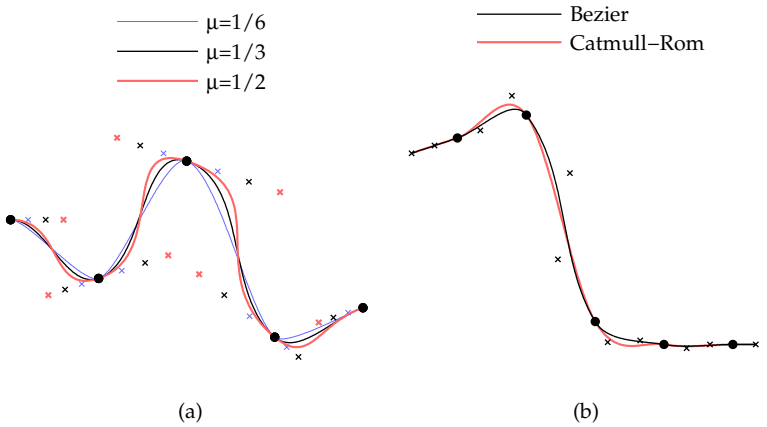

Figure 4.2: (a) Influence of the Bézier spline shape parameter μ in Eq. 4.6. (b) Comparison with Catmull-Rom interpolation and the Bézier interpolation used in the current work (μ=1/3).

Here, the tangent at $\dot{\mathbf{p}}_i$ is chosen so that it is parallel to the line going through the two neighboring points:

$$\mathbf{k}_i = \frac{\mathbf{p}_{i+1} - \mathbf{p}_{i-1}}{|\mathbf{p}_{i+1} - \mathbf{p}_{i-1}|}. \tag{4.3}$$

According to Eq. 4.2, the control points are located on the endpoint tangents, which can be generally expressed as

$$\mathbf{b}_i = \mathbf{p}_i + \alpha_i \mathbf{k}_i \tag{4.4}$$

$$\mathbf{c}_i = \mathbf{p}_{i+1} - \alpha_i \mathbf{k}_{i+1}, \tag{4.5}$$

where α_i is the distance from a control point to the corresponding sample point. The value of α_i for spline segment i is based on the distance between its endpoints:

$$\alpha_i = \mu |\mathbf{p}_{i+1} - \mathbf{p}_i|, \tag{4.6}$$

where μ is a scalar. The shape of the spline can now be adjusted by varying μ, while still adhering to the smoothness requirement.

In order to arrive at an appropriate value for μ, some properties of the spline formulation will be discussed next. The shape functions in Eq. 4.1 are third degree Bernstein polynomials [165], for which the sum $(1-t)^3 + 3t(1-t)^2 + 3t^2(1-t) + t^3 = 1$ for any t. Furthermore, the two weight functions for the internal control points can be seen to have their maximum values at t=1/3 and t=2/3, respectively. By placing the control points near these positions, the third degree polynomials yield a balanced interpolation between t=0 to t=1. With the

formulation used in Eq. 4.6, a value of

$$\mu = \frac{1}{3}$$

will give control points near the t=1/3 and t=2/3 locations on the spline segment. The influence of varying μ is seen in Figure 4.2(a). The spline for μ=1/3 appears intuitively better than the others, which either overshoot around bends for μ=1/2 or approach a sawtooth profile for μ=1/6.

The interpolation routine used here resembles the Catmull-Rom interpolation with a tension parameter [166]. The difference is that the length α_i is here set to be the same for spline segment i, whereas the Catmull-Rom formulation can be shown to use the same α_i for sample point i. This may cause the spline to overshoot at bends where two adjoining spline segments have very different lengths. Figure 4.2(b) shows a comparison between a Catmull-Rom interpolation and the current formulation. This is a realistic shape for surface roughness measurements, and uses equidistant spacing in the horizontal direction corresponding to the WLI sample interval. The Catmull-Rom gradient at point i is here

$$k_i = \frac{1}{2}\left(\mathbf{p}_{i+1} - \mathbf{p}_{i-1}\right). \tag{4.7}$$

The figure illustrates the problems of overshooting with this formulation.

4.1.1 Element mesh

A small section of an FE model is shown in Figure 4.3, where the Bézier interpolation between the WLI samples are shown as dots. As can be seen, the interpolation provides a curvature for the meshing routine to increase or decrease element sizes as necessary between sample points.

A Delaunay tessellation algorithm is used for creating triangular element meshes. This is generally regarded as the best way to generate high quality

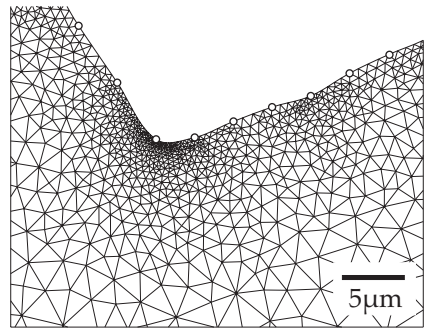

Figure 4.3: Finite element mesh showing geometry adaption to the interpolated profile, where the WLI sample points are shown as dots.

meshes without manual assistance [167]. Strains are related to the undeformed geometry, where assuming small strains, the axi-symmetric coordinate strains are:

$$\varepsilon_r = \frac{\partial u}{\partial r} \tag{4.8a}$$

$$\varepsilon_\phi = \frac{u}{r} \tag{4.8b}$$

$$\varepsilon_z = \frac{\partial w}{\partial z} \tag{4.8c}$$

$$\gamma_{rz} = \frac{\partial u}{\partial z} + \frac{\partial w}{\partial r}, \tag{4.8d}$$

where u and w are the radial and axial displacement respectively. The elements use quadratic shape functions for the displacement interpolation. A linear variation of strains across an element can therefore be described, since strains are first order derivatives of the deformation. The cubic shape functions are also used for the geometry of the element, allowing the element edges on the surface boundary to have curvature corresponding to the Bézier spline curvature at a given location.

Appropriate meshing parameters were found by studying solution convergence with increasing mesh density. A typical profile would yield between one million and three millions degrees of freedom (DOF), requiring computer hardware and solution schemes that can cope with such large systems. Details on this is given in Section 4.2.

Each profile is divided into smaller sections of about 3 mm length. The number of sections are determined from the length of the rough part of the specimen, which proved to be a good estimate for the number of DOF in the full mesh. Section end points are chosen so that they are outside valleys, overlapping adjoining sections by 860 to 1020 µm. The length of this overlap is sufficient to avoid dissimilar solutions in the middle of the overlapping regions, as shown in Figure 4.4 and Figure 4.5. Discrepancies larger than 2% were observed, however, this was in regions with low surface stress concentrations, and should have no influence on the notch root stresses.

The mesh density is controlled so that a good resolution around grooves is achieved. This is done by making the element size dependent on the surface curvature, however, a large part of the surface is typically not of interest, such as peaks and higher surface regions between grooves. Different mesh parameters are therefore applied, depending on the surface height, where 30% of the lowest surface segments are given very fine mesh parameters and coarser values are given to the highest 70% and 50% of the surface segments. In addition to the curvature based parameters, element growth rate factors and a global maximum element size is assigned. Figure 4.6(a) shows a specimen geometry divided into five parts. In Figure 4.6(b), one of the parts is shown, with magnified views in Figures (c) and (d), centered around the groove where fatigue initiation occurred.

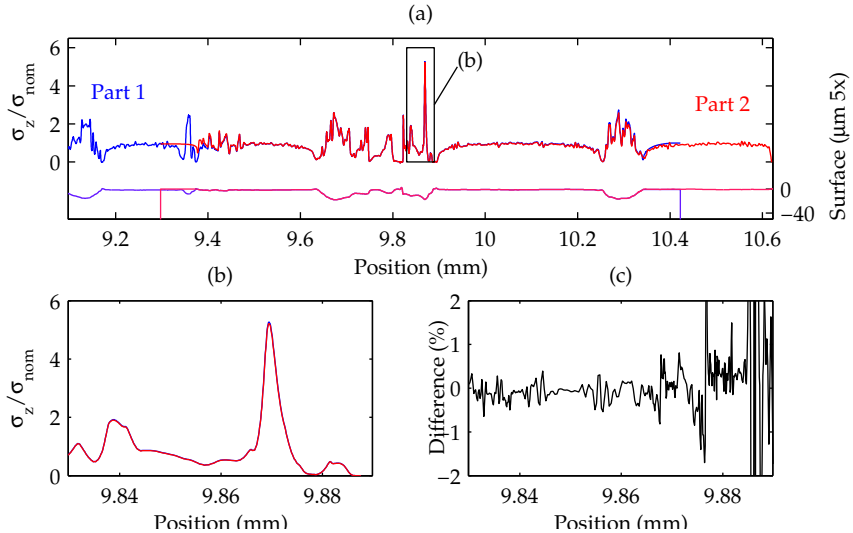

Figure 4.4: (a) Linear stress solution on the surface and geometry for two overlapping parts. The surface is scaled 5 times in the vertical direction. (b) Magnified view around the mid-point of the overlapping region, where the difference between σ_1 for Part 1 and 2 is shown in (c).

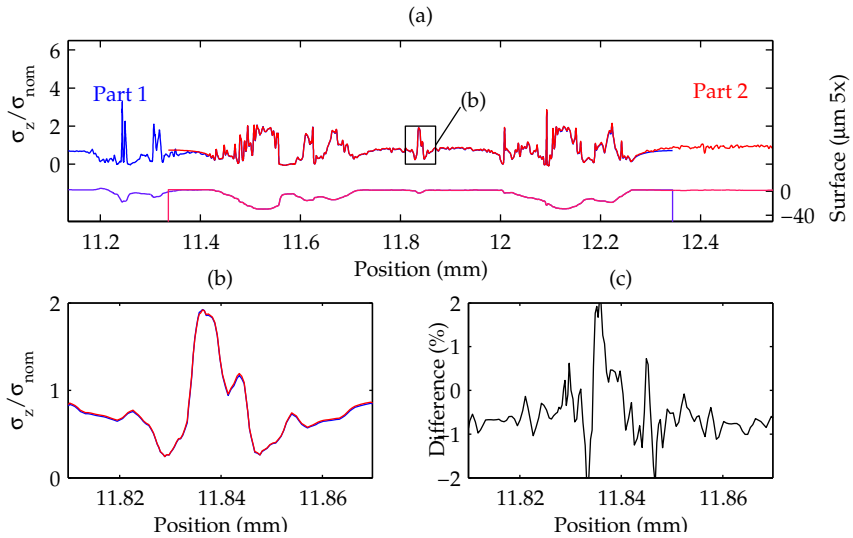

Figure 4.5: Similar plot as Figure 4.4 for an elastic-plastic material model.

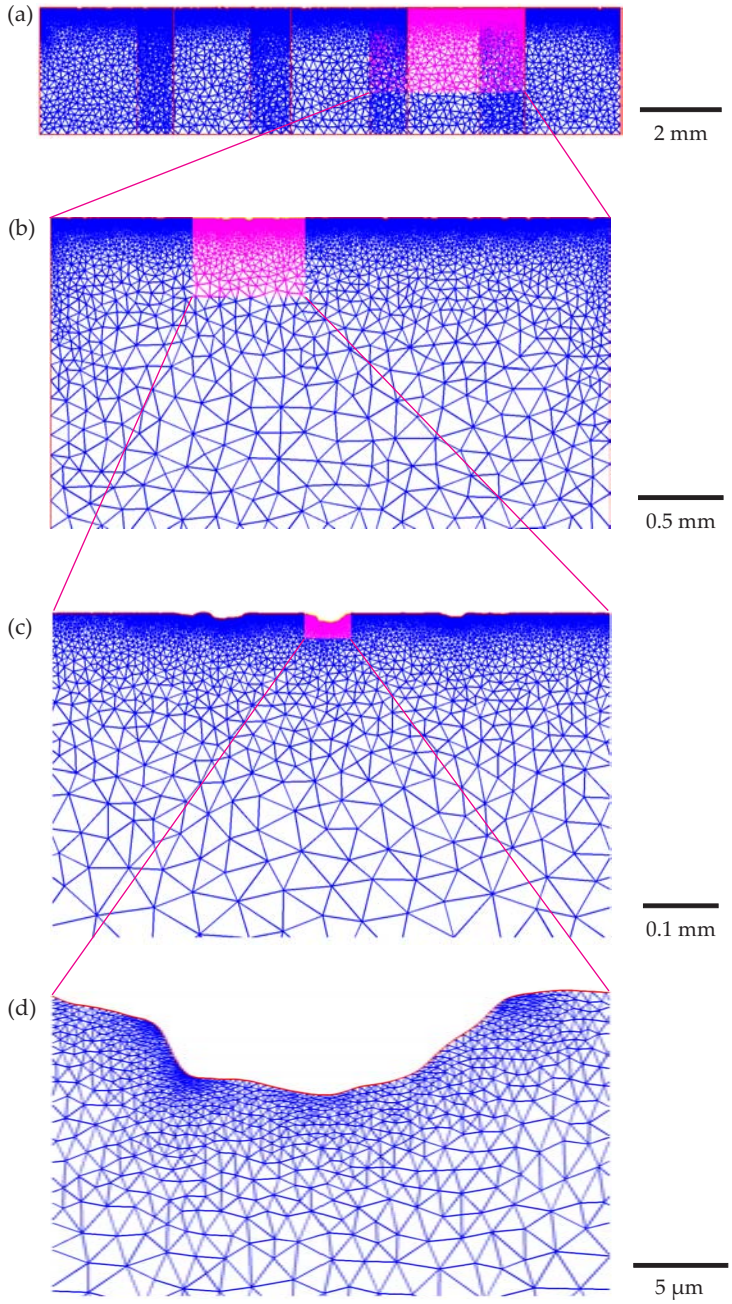

Figure 4.6: The rough section of this specimen is divided into five parts as shown in (a). Crack initiation occurred in part 4, shown in (b), with magnified views shown in (c) and (d). The total number of DOF in this model is 2.6×10^6.

4.1.2 Material models

The material is assumed to be isotropic and homogeneous. In general form, the linear elastic material model according to Hooke's law is

$$\sigma_{ij} = C_{ijkl}\varepsilon_{kl}, \tag{4.9}$$

where C_{ijkl} are elastic constants. In the case of isotropic material, $\boldsymbol{C}$ is reduced by symmetry considerations, and Eq. 4.9 can be expressed by the Lamé constants λ and μ

$$\sigma_{ij} = \lambda\delta_{ij}\varepsilon_{kk} + 2\mu\varepsilon_{ij}, \tag{4.10}$$

or using the more common uniaxial parameters E and Poisson's ratio ν:

$$\varepsilon_{ij} = \frac{1}{E}\left[(1+\nu)\sigma_{ij} - \nu\sigma_{kk}\delta_{ij}\right], \tag{4.11}$$

where δ_{ij} is the Kronecker delta.

A bilinear material model describing kinematic hardening has also been used. The stress-strain relation is

$$\sigma_{ij} = C_{ijkl}(\varepsilon_{kl} - \varepsilon^{\mathrm{p}}_{kl}), \tag{4.12}$$

where $\boldsymbol{\varepsilon}^{\mathrm{p}}$ is the plastic strain vector. The von Mises yield criterion is used, and associated plastic flow is assumed, where the plastic strain rate relate to the equivalent plastic strain rate as:

$$\dot{\boldsymbol{\varepsilon}}^{\mathrm{p}} = \frac{\partial f(\boldsymbol{\sigma} - \boldsymbol{\alpha})}{\partial \boldsymbol{\sigma}}\dot{\bar{\varepsilon}}^{\mathrm{p}}, \tag{4.13}$$

i.e. the direction of plastic flow is normal to the yield surface. $\boldsymbol{\alpha}$ is the backstress tensor, or the shift of the yield surface with plastic load increments. The size of the yield surface is constant, that is, the change in yield point during cycling is only due to the translation of the yield surface. The yield function is then given by

$$f = \phi(\boldsymbol{\sigma} - \boldsymbol{\alpha}) - \sigma_{\mathrm{ys}}. \tag{4.14}$$

The hardening is defined by the plastic tangent modulus, which, along with the yield stress, was fitted to the cyclic stress-strain curve.

4.2 Solution and analysis

FEMLAB includes several iterative algorithms to deal with larger systems. These were initially adopted for solving complete surface profiles, however, they were found to be rather unstable and very slow for the nonlinear analyses. As mentioned in Section 4.1.1, the geometry was therefore divided into smaller geometries that could be solved using a direct solver.

4.2.1 Program overview

Due to the large number of required geometries (58 specimens with four profiles each), scripting was relied upon to automate the FE analysis. Programs were developed in MATLAB, making use of both MathWorks toolboxes and FEMLAB programs. The main program is outlined in Algorithm 1.

```
1  Initialize using a MySQL database;
2  foreach specimen do
3      for clock ← 1 to 4 do
4          read profile from disc;
5          for part ← 1 to num_parts do
6              create_geom;
7              clear and defrag memory;
8              run_fea;
9              if Error or Warning then
10                 save restart information;
11                 go to next clock or specimen;
12             else
13                 postproc;
14                 save temporary solution to disc;
15             end
16         end
17         load all temporary solutions from disc;
18         assemble;
19         save full solution to disc;
20     end
21 end
```

Algorithm 1: `main`. Outline of program used to run FEA for all specimens.

The names of specimens and additional information such as load range and load ratio are collected from one or more specimens, using a MySQL call on Line 1. The length of the rough section for each profile is then used to estimate the number of parts required for the analysis to fit in memory. The finite element solver function `run_fea` is protected by a MATLAB `try/catch` block in order to avoid program termination and to detect warnings associated with convergence problems. If errors occur, the geometry and run-time variables are saved to disc (Line 10) so that this part can be reanalyzed later with manual tweaking of the iteration parameters. The function `create_geom` (6) creates a FEMLAB geometry based on Bézier interpolation as described in Section 4.1. The other functions, on Lines 8, 13 and 18, are described in Appendix B1.

4.2.2 Solution algorithms

Iterative algorithms are commonly used for factorization of large matrices, since memory allocation of the whole (or upper diagonal) matrix is not required. These solvers are less stable and also slower than direct solvers, however, iterative factorization may be the only choice for large FE problems, especially in 3D models that frequently have a large number of DOF and the system matrices are less sparse than in 2D. As mentioned in Section 4.1.1, the geometry used in this work was partitioned into smaller sections in order to be manageable by a direct solver.

A Cholesky factorization algorithm was used for both linear elastic and elastic-plastic analysis. Using this algorithm imposes some restrictions on the system stiffness matrix, namely that it is symmetric and positive definite. The FE formulation of structural mechanics problems are preferably developed to adhere to these conditions. It follows from energy considerations that the system stiffness matrix (Jacobian) is positive-definite, but the symmetry condition can be violated by constitutive relationships for the plastic strain. Moreover, when coupling different physical domains in the FE analysis, symmetry can no longer be guaranteed. FEMLAB, which is marketed as a multi-physics FE program, uses the general UMFPACK solver by default. An associative flow rule for the plastic strain increment is used in this work, effectively preserving symmetry in the system stiffness matrix.

Table 4.1 shows the solution times[3] using different solver algorithms for a small section of a profile, about 2 mm long. The mesh consists of 44,715 triangular elements with quadratic shape functions, yielding 183 kDOF (thousand degrees of freedom). In comparison, the sections used in the actual analyses had between 400 and 700 kDOF. The direct solvers, Cholesky and UMFPACK, are markedly faster than the iterative solvers. The UMFPACK solver uses a full LU factorization, limiting the size of the problem to about 350 kDOF on the hardware used. As seen from Table 4.1, the iterative solvers are much slower than the direct ones, partly due to the need for preconditioning of the matrix before the solver is called. An algorithm known as *geometric multigrid* was used as a preconditioner for the values given in 4.1, using UMFPACK for a set of two coarser mesh cases. See e.g. Ref. [168] for an overview on iterative factorization algorithms.

A pronounced increase in the solution times for the elastic plastic analyses was observed. The nonlinear solver in FEMLAB is based on a damped Newton method, where the current solution vector U_i is given by:

$$U_i = U_{i-1} + \lambda \delta U. \tag{4.15}$$

The damping factor λ scales the increment δU, where for λ=1, the classical Newton method is obtained. An initial value for λ as well as a minimum value and a growth factor can be given to allow the damping to throttle down if the relative error in the current iterative solution is larger than in the previous. A

[3]Windows XP laptop; 1.4 GHz Intel Pentium M 738 and 1.11 Gb RAM. Similar solution times were obtained on a stationary 2.8 GHz Intel Pentium 4 and 1 Gb RAM.

Table 4.1: Solution times for a small geometry section (183 kDOF) using linear and nonlinear solvers. Iterative solvers are marked with •. Fourth order Gauss interpolation was used for the linear analysis and second order was used for nonlinear analysis, except where stated otherwise.

Analysis	Factorization	Time (s)	$\bar{\sigma}$ (MPa)
Linear	Cholesky	14	957.6
	UMFPACK	18	957.6
	•GMRES	42	957.6
Nonlinear	Cholesky	191	427.6
	Cholesky, const. pred.	224	427.6
	UMFPACK	233	427.6
	Cholesky, 4th order Gauss	256	425.1
	•GMRES	348	427.6
	•Conjugate gradients	547	427.6

rather large amount of initial damping, on the order of 10^{-5}, was needed for the nonlinear analysis to converge.

In cases with highly nonlinear systems, or where load history effects are studied, it is necessary to apply the loads in increments as well. These increments are referred to as steps, and can be adjusted by the solution algorithm or explicitly specified by the user. The default behavior of the solver is to follow a tangential trajectory from the current control-state response. This approach proved to be unstable for some of the surface profile geometries. The predictor step would sometimes overshoot and be unable to iterate back to equilibrium response. A constant predictor step was found to be much more stable, although somewhat slower due to the increased number of steps required for convergence. The difference is seen in Table 4.1 for the nonlinear "Cholesky" and "Cholesky, const. pred" solvers. The linear tangent step update was generally used. For the geometries that did not converge, a constant step update was used instead, sometimes also with increased Newton damping and intermediate load steps.

In FEMLAB, the order of Gauss integration defaults to two times the order of the shape function, and in the elastic-plastic analyses, plastic strains are solved for in the Gauss points of the elements. Reducing the Gauss order from 4 to 2 in the case of a quadratic mesh, improved the solution performance as seen in Table 4.1. Solution time is reduced by 30% with little change in the stress solution. The reduction in Gauss order also reduces memory requirements, since the plastic strains are used in the equilibrium iterations.

4.2.3 Boundary solutions

The stress solutions on the surface boundaries are calculated using FEMLAB, where the gauss point solutions have been extrapolated to nodal points and made continuous by smoothing. The program outline for the MATLAB function

`postproc` is shown in Appendix B1. The equilibrium equations in z and r are [169]:

$$\frac{\partial \tau_{rz}}{\partial r} + \frac{\partial \sigma_z}{\partial z} + \frac{\partial \tau_{rz}}{\partial r} + F_z = 0 \tag{4.16}$$

$$\frac{\partial \sigma_r}{\partial r} + \frac{\partial \tau_{rz}}{\partial z} + \frac{\sigma_r - \sigma_\phi}{r} + F_r = 0 \tag{4.17}$$

To avoid division by zero, Equations 4.16 and 4.17 are multiplied by r and r^2 respectively. According to this, a transformed variable ξ is introduced:

$$\xi = \frac{u}{r} \tag{4.18}$$

that is solved for instead of u.

Generic expressions can be evaluated in FEMLAB, based on the governing variables and the partial derivatives of these. The stress gradient, as defined in Eq. 1.23, can be defined in terms strains using Hooke's law for a linear elastic and isotropic material:

$$\frac{\partial \sigma_z}{\partial r} = \frac{\partial}{\partial r}\left\{ \frac{E}{(1+\nu)(1-2\nu)} \left[(1-\nu)\varepsilon_z + \nu(\varepsilon_\phi + \varepsilon_r) \right] \right\}. \tag{4.19}$$

Inserting for the small strains in Eq. 4.8, and using the the chain rule for Eq. 4.8a:

$$\frac{\partial \varepsilon_r}{\partial r} = \frac{\partial^2 \xi}{\partial r^2} r + 2\frac{\partial \xi}{\partial r}, \tag{4.20}$$

the following expression for the stress gradient is found:

$$\frac{\partial \sigma_z}{\partial r} = \frac{E}{(1+\nu)(1-2\nu)} \left[(1-\nu)\frac{\partial^2 w}{\partial r \partial z} + \nu\left(\frac{\partial^2 \xi}{\partial r^2} r + 3\frac{\partial \xi}{\partial r} \right) \right]. \tag{4.21}$$

All partial derivatives on the right hand side of Eq. 4.21 are available in the FEMLAB post processing environment. The expression contains some terms with second derivatives of the displacements that will assume constant values when using quadratic shape functions. This may be a problem, since the solution of interest for $\frac{\partial \sigma_z}{\partial r}$ is at the surface boundary where steep stress gradients are expected for a linear elastic analysis. As noted earlier, the aim of the finite element solution procedure used here is to arrive at a mesh independent solution, although from a microstructural standpoint, the stress gradient may in fact be closer to constant within a grain. In order to resolve the (theoretical) geometric effect on stress gradient, higher order shape functions can be used, however, this comes with a high computational cost. Some tests for convergence were done by comparing second order and third order shape functions for a measured surface geometry. The third order element mesh showed convergence for a blunt and a sharp groove, while the second order elements showed mesh dependent variability even for very fine mesh. However, the quadratic solution approached the cubic one, showing better convergence when considering the total number of DOF for the model. Details can be found in Appendix C.

4.2.4 Solutions ahead of grooves

The solution ahead of grooves were also evaluated. Critical locations are presumed to be the deepest points within the grooves, but in order to limit the amount of postprocessing, a selection scheme based on rain-flow counting of the surface profile was used. Surface excursion smaller than 5 µm were discarded, effectively removing insignificant valleys as well as local perturbations within the larger grooves. A second criterion for finding critical locations was also used, where the maxima for axial stress at the surface was rain-flow filtered using a threshold of K_t =2. Figure 4.7 shows the selected points using the two algorithms, where V1 valleys are from the geometry based search algorithm and the V2 valleys were found from the stress solution. Stresses and strains up to a distance of 100 µm ahead of valley was evaluated at 60 logarithmically distributed points, indicated by vertical lines in Figure 4.7.

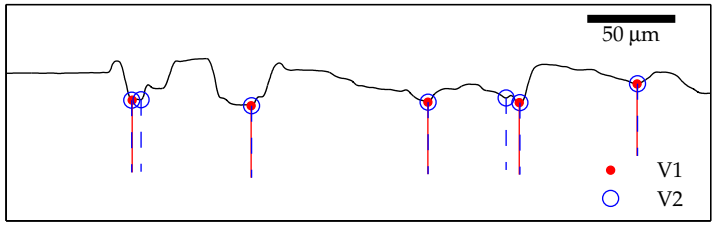

Figure 4.7: Critical locations as determined by two different algorithms.

4.2.5 Residual stress model

As shown in Section 3.5, compressive residual stresses were found in the surface of the specimens. A residual stress field has therefore been applied in the elastic-plastic analysis to study the influence on subsurface stress distributions in cyclic loading. The magnitude of the applied residual stresses at the surface corresponded to the measured values, while the subsurface distribution was assumed, based on studies by Jacobus et al. [170]. The depth and magnitude of the residual stress field was varied according to the surface profile. Trial and error led to a profile dependent stress field that would have acceptable values after the initial equilibrium iterations. In Figure 4.8, residual stress profiles before and after equilibrium iterations are shown. Figure 4.8(a) shows subsurface stresses in a flat surface region, and Figure 4.8(b) shows stresses ahead of a groove.

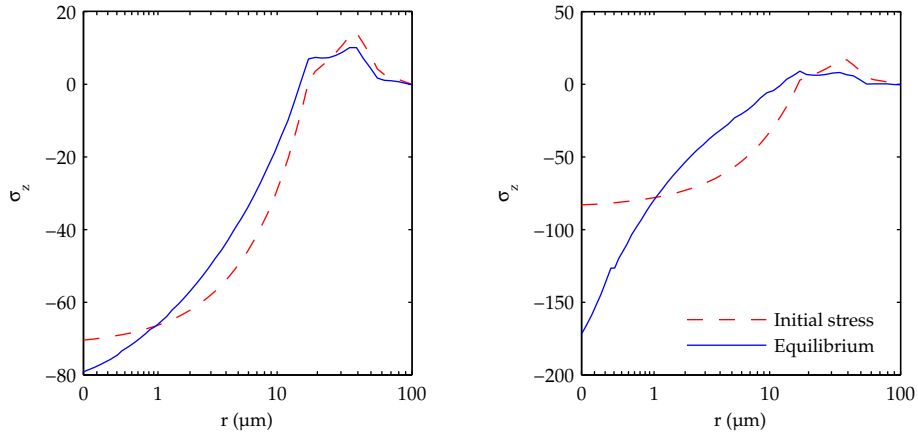

Figure 4.8: Initial stress distribution, and the resulting stress distribution after equilibrium iterations for (a) a flat surface region, and (b) ahead of a groove.

Chapter 5

Results

5.1 Surface measurements

When comparing the four surface profiles for a single specimen, some variations were typically observed. Figure 5.1, shows the profiles for one specimen given a type C (coarse) surface preparation. The deepest grooves vary in shape and depth, while a shallow groove in the 9 o'clock profile appear in an area where

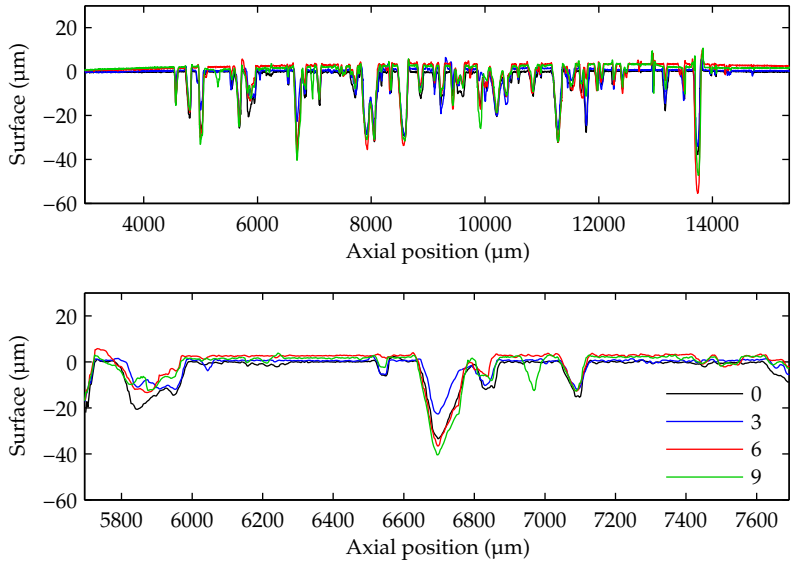

Figure 5.1: WLI measurements for all clock positions of a specimen. The top figure shows the full length of the profile, where the surface height has been scaled by 140. The bottom plot is centered around the initiation location, which occurred near the 6 o'clock profile. Height is scaled by 22.

the other profiles are flat. For this specimen, this was caused by initial lateral movement of the emery paper, as the lever was placed on the surface.

5.1.1 Measurement accuracy

The accuracy of the WLI measurements were checked using a scanning electron microscope (SEM). Although SEM offers a long depth of field, the images shown on the following pages are composites of several scans at different working distances. The measurements generally showed good accuracy, with some artifacts appearing at certain topographical features. Figure 5.2 and 5.3 show the WLI sample locations as dots, while the Bézier interpolation is drawn as a continuous line. The interpolation showed good agreement with the actual surface, as long as the WLI samples were accurate.

In some grooves with slanted side walls, the WLI measurement would fail to analyze the interference pattern from the surface. This is shown in Figure 5.4 and Figure 5.5. In Figure 5.4, there are two WLI samples that are incorrect, marked A and B. The straight slope to the left of B and one point halfway up to the right of A have been inserted by linear interpolation in the WLI post-processing software. The location of point B is 36 µm below the actual surface, and the width of the valley at the "true" point B location is 38 µm. The reason for the incorrect height measurement of B therefore seems to be caused by stray signals from the opposite side of the valley. This seems to be the case for point A too, as well as the two incorrect points in Figure 5.5. For a given groove, the errors would occur consistently around the circumference at the four clock positions, indicating that this behavior is indeed caused by the geometry and not just random measurement errors.

A MATLAB program was made for detecting and correcting the measurement errors. Given a point i with surface height $z(i)$, the height of the points $i-1$ and $i+1$ on either side were compared to $z(i)$. If the difference $z(i+1)-z(i)$ or $z(i-1)-z(i)$ was greater than 3 µm, the point i was marked as suspicious, since the WLI microscope has problems receiving any signal from such steep gradients. The points were checked manually before they were deleted. In most cases it was obvious that a given location was measured incorrectly, but in cases of doubt, SEM imaging was used to check the area. After the point, or points, were removed, the resulting gap in the profile was reconstructed by linear interpolation between the adjacent valid measurements. This is the same way as the WLI post-processor operates in cases where inadequate surface reflection gives no interference pattern. The only difference is that the WLI post-processor interpolates the 3D surface, while the error-checking algorithm works on the extracted 2D profile.

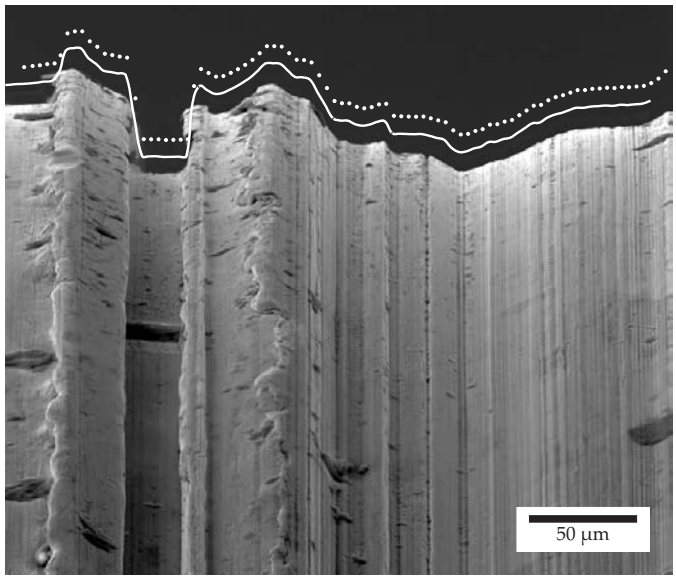

Figure 5.2: The profile obtained from WLI overlayed on an SEM image, showing good correlation. These side view images are composed of 4 to 6 scans, taken at different working distances to obtain a larger depth of field.

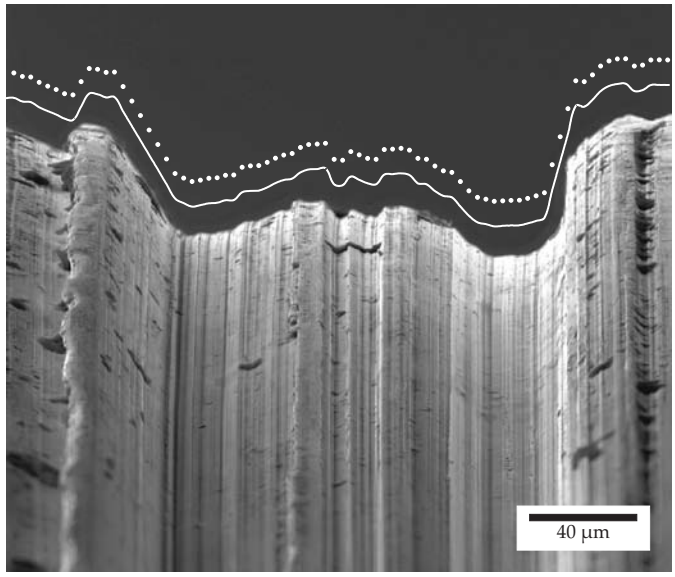

Figure 5.3: The profile obtained from WLI overlayed on an SEM image. The WLI microscope cannot measure very steep surfaces, such as the one to the right in this image.

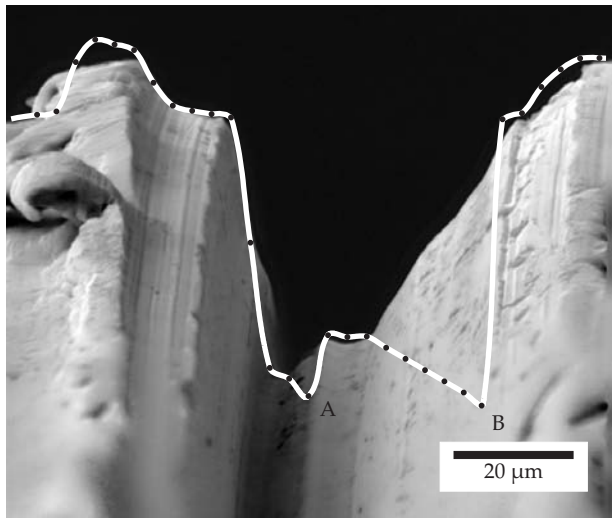

Figure 5.4: In this case, the WLI measurement is incorrect. It appears that the points A and B correspond to a double reflection from the opposite wall.

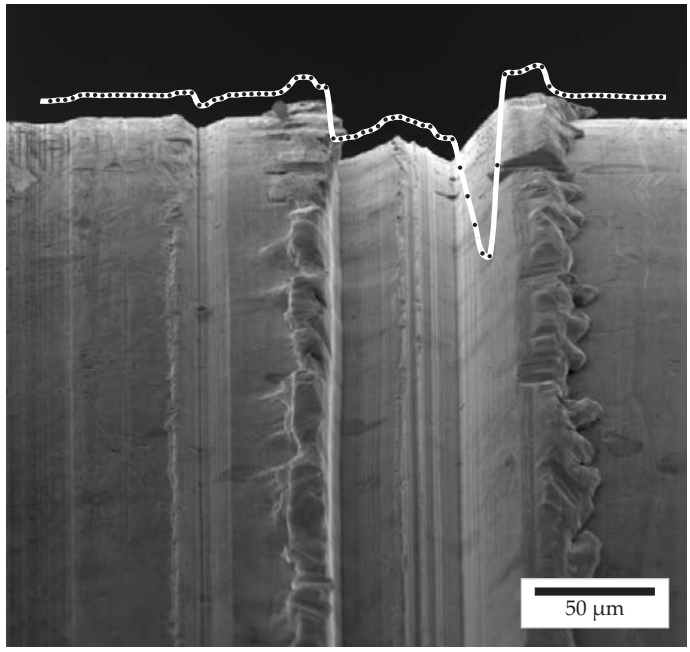

Figure 5.5: Another case of incorrect WLI measurement. The white line shows the Bézier interpolation.

5.2 Fractography

On a macroscopic scale, the crack growth appeared to be straight and perpendicular to the loading direction, as seen in Figure 5.6. This corresponds to Mode I loading in fracture mechanics, although a more irregular crack front is observed on a microscopic. Some specimens deviated from this, the most marked one seen in Figure 5.7. This is an indication of mixed Mode I – Mode II loading, although Mode I can be assumed to dominate also for this specimen.

The global fracture appearance was characterized based on the width of the

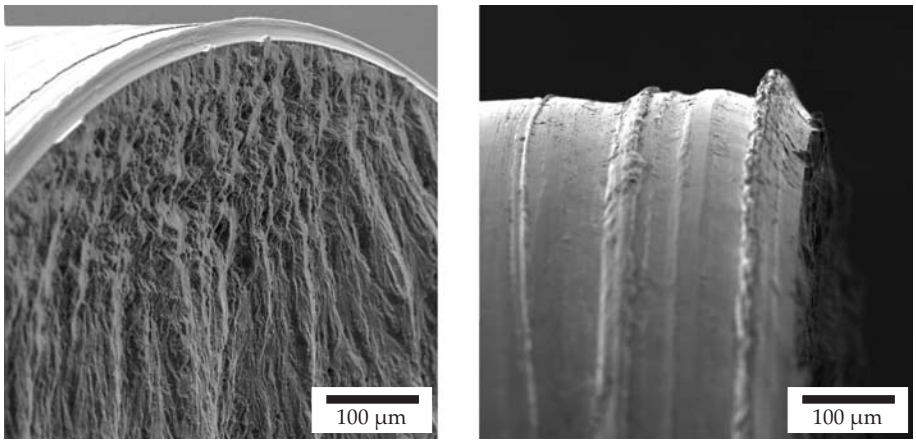

Figure 5.6: Specimen X23 showing macroscopic crack propagation perpendicular to the loading direction (R=-1 $\Delta\sigma$=290 N_f=831,492).

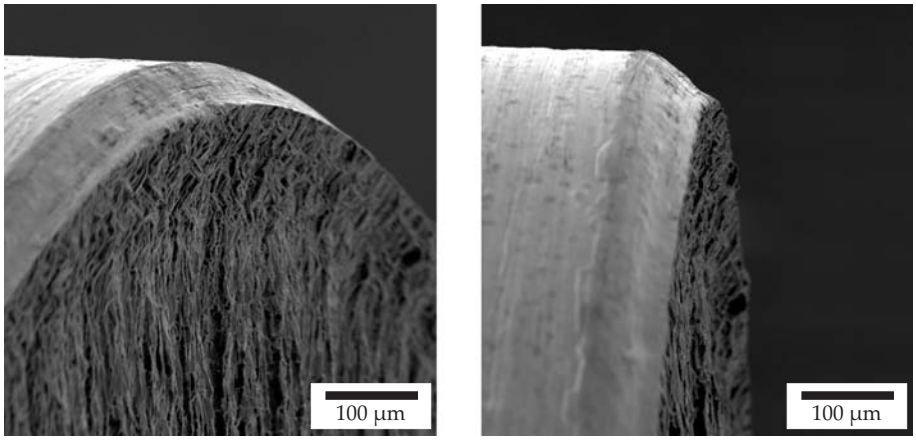

Figure 5.7: Specimen F45 with angled early crack propagation. (R=0.1 $\Delta\sigma$=300 N_f=18,679)

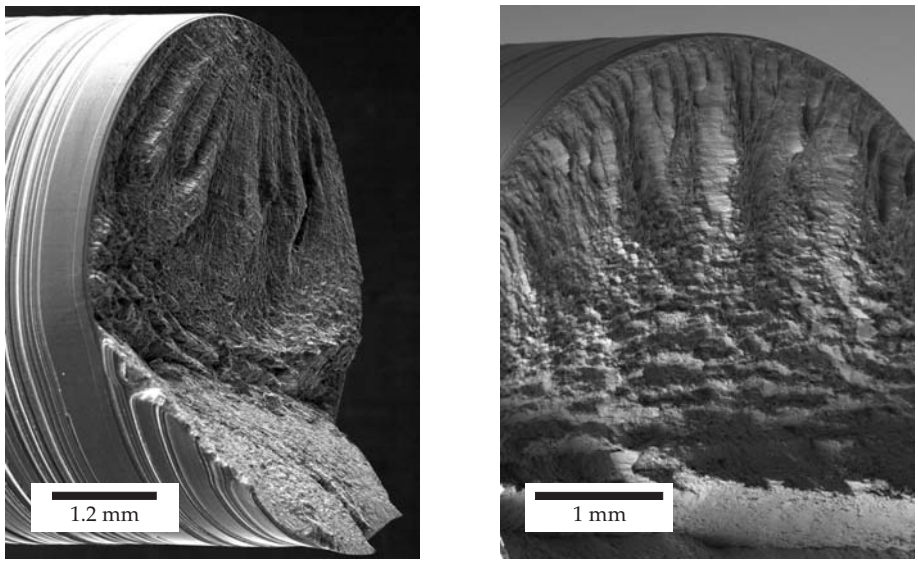

(a) (b)

Figure 5.8: Two types of distinct macroscopic fracture appearances: (a) local initiation in specimen E22, and (b) wide initiation in specimen X30.

initiation zone. Crack initiation over a wide portion of the circumference indicate that the notch at this location play a dominant role in the fatigue initiation process, whereas more local initiation indicates that a material weakness is present. Examples of pronounced local and wide initiation zones are shown in Figure 5.8. A third category was ascribed to fracture surfaces that had a somewhat local initiation zone, but not quite as marked as in Figure 5.8(a). The results for all rough specimens, excluding runouts, are shown in Figure 5.9, where the fracture appearance has been color coded. From these results it can be seen that the initiation characteristic changes around 10^5 cycles from a wide initiation zone to a local zone at higher fatigue lives. This indicates that a change in initiation behavior occurs. At high load levels, a shallow crack may be formed around the circumference during the first few load cycles. The propagation of this crack, going through the regimes of short crack growth, long crack growth and final fracture will govern the fatigue life of the specimen. On the other hand, the specimens cycled at moderate to low load levels show propagation from a local initiation zone. The initiation life in this case is believed to take up a larger part of the total life, controlled by the notch stress field and inherent material weaknesses.

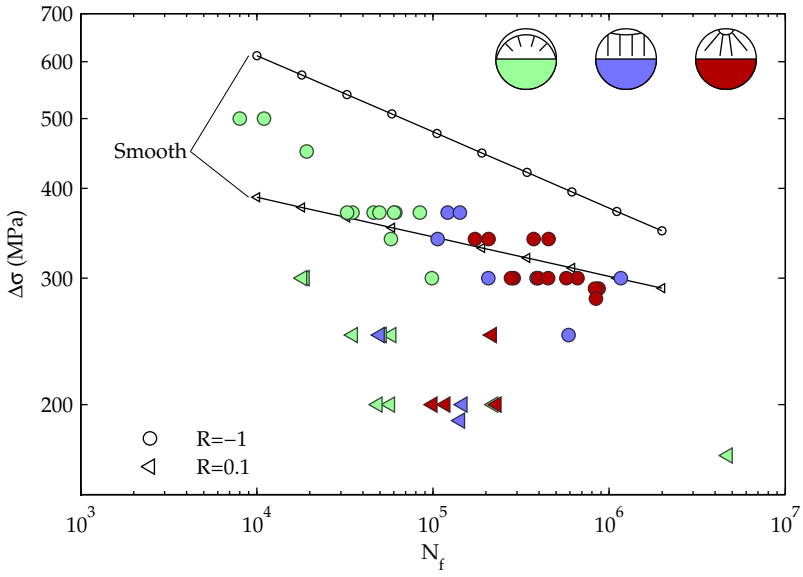

Figure 5.9: Fatigue life plot for the rough specimens, showing the macroscopic appearance of the fracture surface.

5.2.1 Crack initiation

Attempts were made to find incipient cracks during fatigue testing. Three specimens were stopped at several intervals and placed in a SEM. The FE results were useful in this context, to limit the regions to be investigated; as will be shown in Section 5.3, the possible initiation locations could be determined from the subsurface stress solutions. No surface cracks could be detected in these tests. After failure, two specimens showed secondary initiation zones close to the notch where failure occurred. In these cases, the incipient cracks were opened up due to the proximity of the ductile fracture region. One such specimen is shown in Figure 5.10, where the secondary initiation zone is marked by B. Striations were found 1.3 mm below the surface where the crack propagated to failure. This area is indicated in region A in Figure 5.10, and shown in detail in Figure 5.11(a). The striation spacing was found to be 0.5 µm, taken as an average for several distinct grains in this region.

A closeup of the secondary initiation zone is seen in Figure 5.11(b). This is the top-left area of Figure 5.10. The incipient crack was studied along the notch root, where it was found that the crack showed perturbations according to the characteristic grain diameter. Second phase particles in the surface were found to affect the crack path, as seen in Figure 5.11(c) and 5.11(d). In Figure 5.11(c), it can be observed that a particle has been dislodged, leaving a cavity in the crack path. A slight extrusion of material can be seen to the right, which may

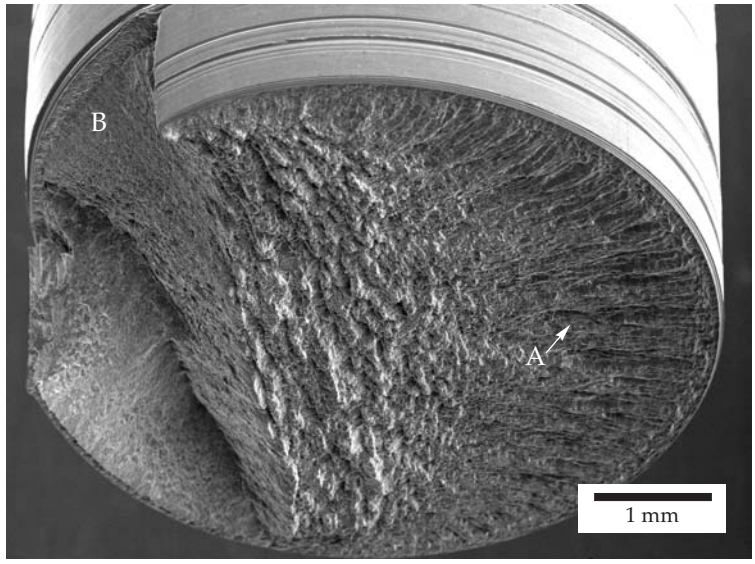

Figure 5.10: Specimen X32, showing a secondary initiation region (B).

be a particle that is partly dislodged. Figure 5.11(d) shows another partly dislodged particle which apparently is harder than the surrounding material. It cannot be ascertained from this that second phase particles has an impact on the fatigue initiation process in small notches, although it seems plausible that larger particles, or a cluster of such particles, can contribute locally to the notch stress concentration.

Figure 5.12 on page 100 shows light microscope images of a sectioned runout specimen. Failure occurred due to fretting in the grip section at N=853'000. Cracks could be found ahead of several notches, varying in length from about 5 µm to 8 µm. This specimen was examined in SEM at N=450'000, N=550'000 and N=700'000, with no detectable incipient cracks at the surface. This is most likely due to the constraint of the surrounding material, which effectively closes the cracks and make them difficult to observe at the surface. Second phase particles can be observed Figure 5.12, where the dark blue particles are believed to be Mg_2Si and the light blue particles in Figure 5.12(c) are composed of AlFeSi or AlSiFeMn [87, 146].

The cracks were found to be slightly angled with the loading direction, with some exceptions as shown in Figure 5.12(b). The crack emanates from a second phase particle, which may have caused early cracking and immediate Stage-II type growth. Figure 5.12(c) and (d) have been taken from the same groove at the 0 and 6 o'clock positions respectively, where the incipient crack can be found in both locations and can be assumed to exist around the circumference. A second phase particle can be seen at the surface in (c), with 2 µm long secondary

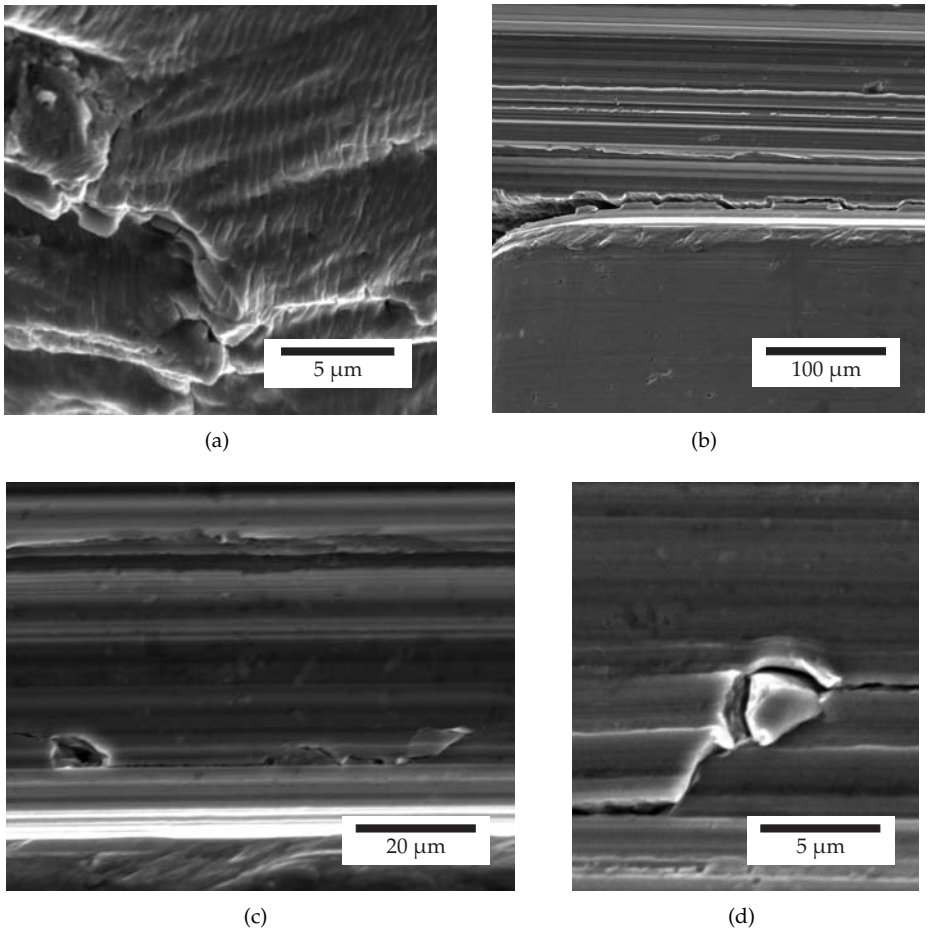

Figure 5.11: Specimen X32, showing (a) striations 0.5 μm apart at a crack length of 1.3 mm, (b) secondary initiation site, (c) a void and an extrusion caused by second phase particles, and (d) a second phase particle at the secondary initiation site.

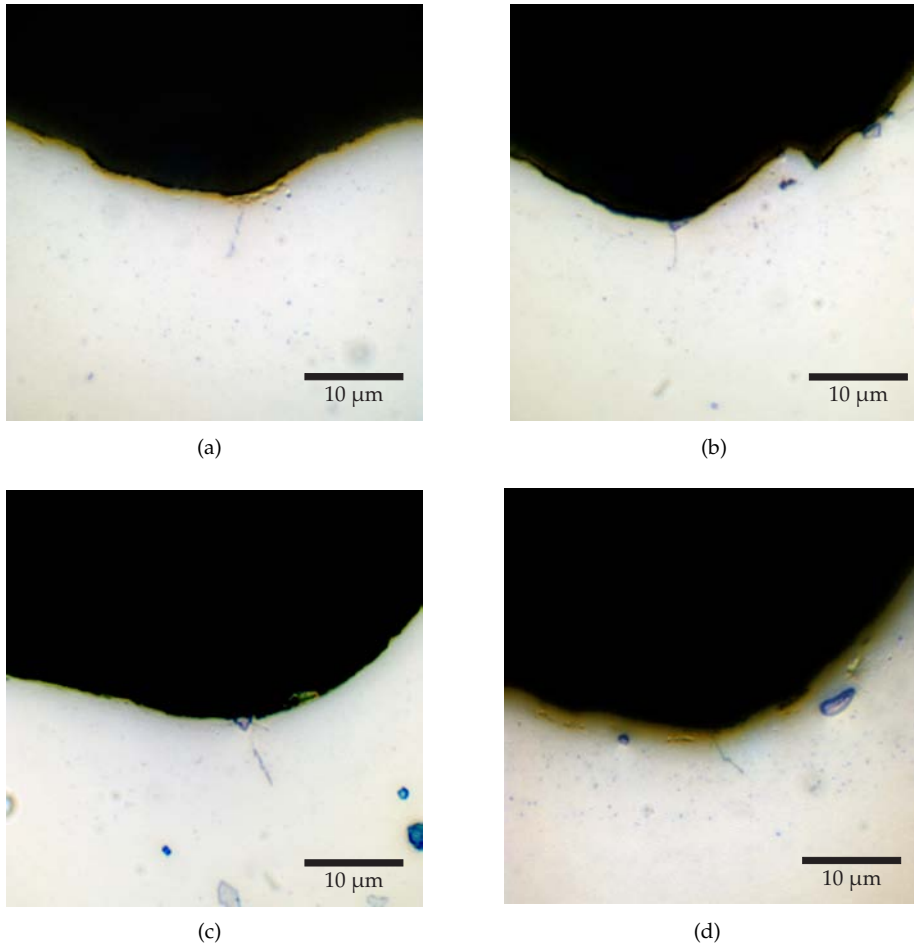

Figure 5.12: Micrographs from bright field microscopy of a forged F(I), runout specimen (R=0.1 $\Delta\sigma$=281 N=1.6 $\times$ 10^6). Incipient cracks can be observed in the grooves. Images (c) and (d) have been taken at opposite sides of the same groove, ie. at the 0 and 6 o'clock positions.

cracks emanating from both sides. The crack seen in (d) has a distinct change in orientation below the surface due to a grain boundary. The surface particle in (c) may have caused initial rapid growth, indicated by a longer crack compared to the one in (d), however, this may also have been caused by crack growth retardation at the shallow grain boundary in (d). Furthermore, given the 3D nature of the cracks, it is hard to infer from these observation whether the second phase particles influence early crack growth, since neighboring grains and particles are not revealed from such cross-section images.

5.3 Finite element results

Recall from Section 4.2.4 that subsurface stress solutions were calculated ahead of critical notches. Two criteria were used to detect the critical locations for post-processing: V1 valleys were based on the surface geometry, and V2 valleys were based on the calculated axial surface stress, σ_z. Figure 5.13 on the next page shows the result for the V1 type valleys for all clock positions in specimen A18. The axial stress has been scaled by the nominal stress, thus at r=0, the value correspond to K_t. The curves for which the highest ten values of K_t were found have been numbered, and their location on the surface are shown in the 10 plots to the right of each graph. The white lines in the center of these geometric plots indicate the positions from which the subsurface stress solutions have been calculated. The surface stress (σ_z) distributions in the area around the valley are shown as well, and have been scaled independently for each location to fit within the plot boxes.

For this specimen, the initiation started at 5 o'clock, thus the 6 o'clock position is the closest measured profile, and has been identified by an inset figure of the schematic appearance of the fracture area. The stress solution for the location where fatigue initiation occurred is drawn with a wider line, and the corresponding surface location (8) is highlighted. The K_t at this groove where initiation occurred therefore has the 8th highest K_t of all the surface grooves. The initiation-groove has been identified in the other clock positions as well, both in the subsurface stress-plots and in the geometry plots. It can be seen that the initiation-groove has a K_t of about 6 for all clock positions, with the exception of the 0 o'clock position, where the K_t value is closer to 5.

Figure 5.14 shows the corresponding plots for V2 valleys, i.e. critical valleys as determined by the highest K_t values. As a result of the threshold for rainflow filtering at K_t =2, no stress solutions are calculated for grooves with K_t <2. More grooves are identified as critical when using this selection algorithm; for this specimen, 150 grooves were identified, compared to 65 with the V1 algorithm. A notable difference between the V1 and V2 solution is that the latter tends to find stress solutions that have subsurface local maxima. This is due to the variation of the surface stresses within the grooves; as seen in the geometry plots, the axial surface stresses are typically highest on either side of the valley floor. Another consequence of this is that more than one V2 solution is found in the groove where initiation occurred. The bold black lines shown in Figure 5.14 are also found at the initiation location, but their K_t is smaller than the colored (blue) solution.

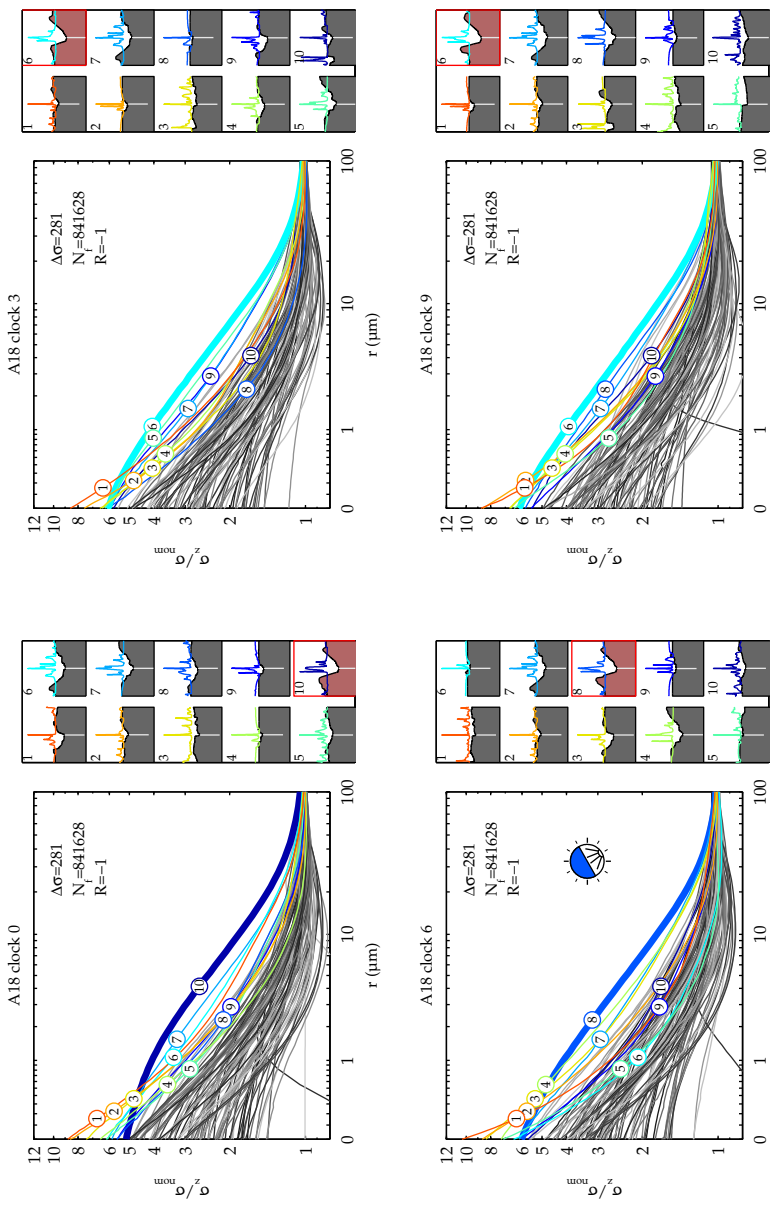

Figure 5.13: Linear FE solution ahead of V1 grooves. The locations with the ten highest K_t are shown to the right of each clock position.

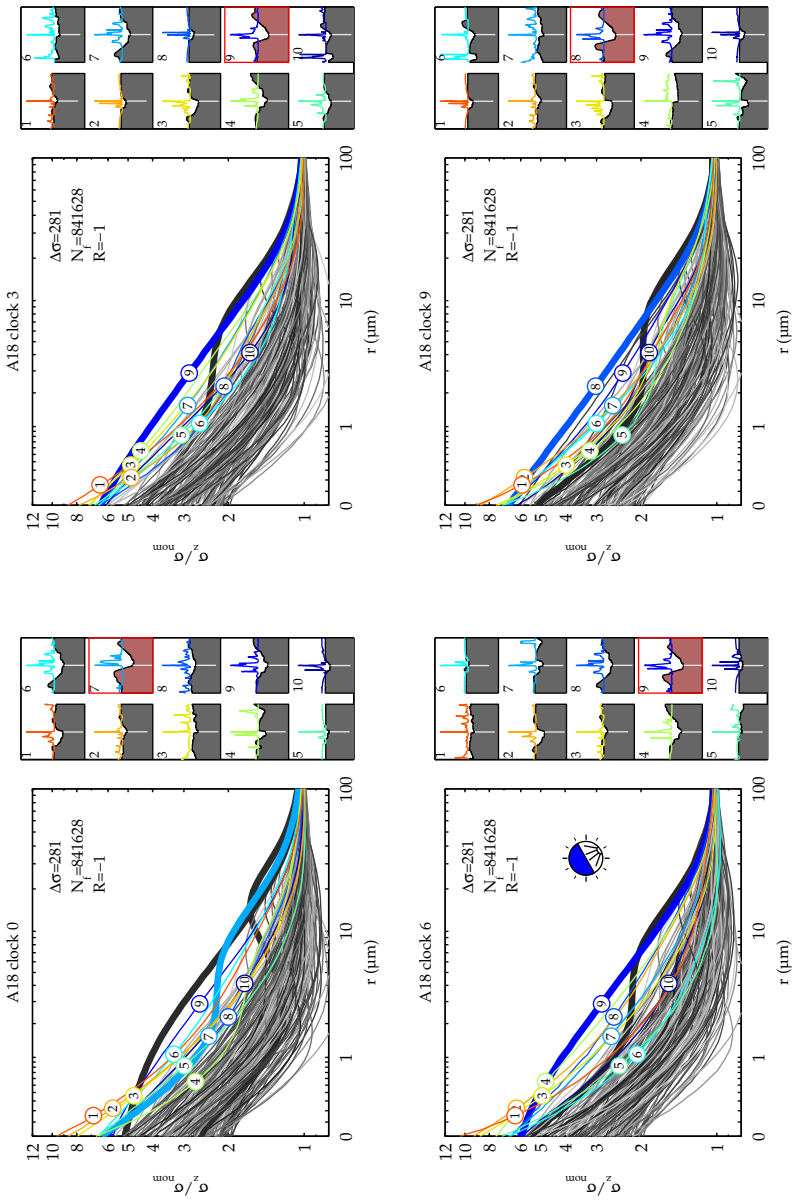

Figure 5.14: Linear FE solution ahead of V2 grooves.

While there are grooves with higher K_t than the initiation-groove, it can be seen from both Figure 5.13 and 5.14 that the subsurface stress solution for the initiation-groove dominates over the others for all clock positions. Since the V1 algorithm was found to be consistent with finding the highest subsurface stresses, the remaining figures are based on these stress solutions. Furthermore, to conserve space only the solutions for the clock position closest to the initiation site will be shown. In a few specimens, the different clock positions showed quite different solutions, which becomes problematic when the initiation location was right in-between two clocks. These results will be commented on later.

5.3.1 Linear elastic material

The plots on the following pages show linear elastic solutions for the clock profiles closest to the initiation locations. The plots are sorted first by ascending stress range, then increasing fatigue life. Results from R=-1 loading are shown on page 104 to 107 and results from R=0.1 loading are shown from page 107 to 108. The labels for the abscissa and ordinate have been omitted to conserve space, but are the same as in Figure 5.13, i.e. axial stress normalized by the nominal stress on the vertical axis and distance in µm ahead of the valley on the horizontal axis.

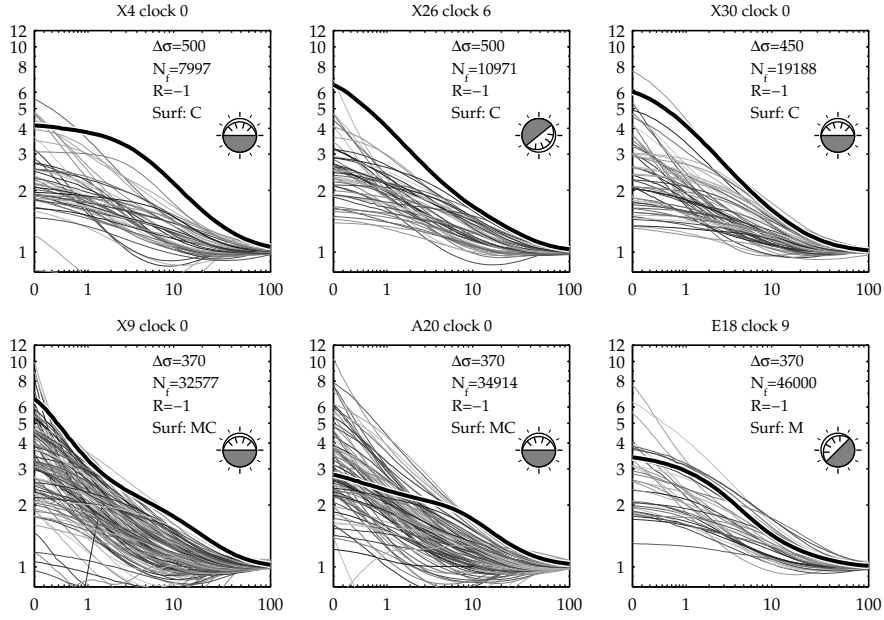

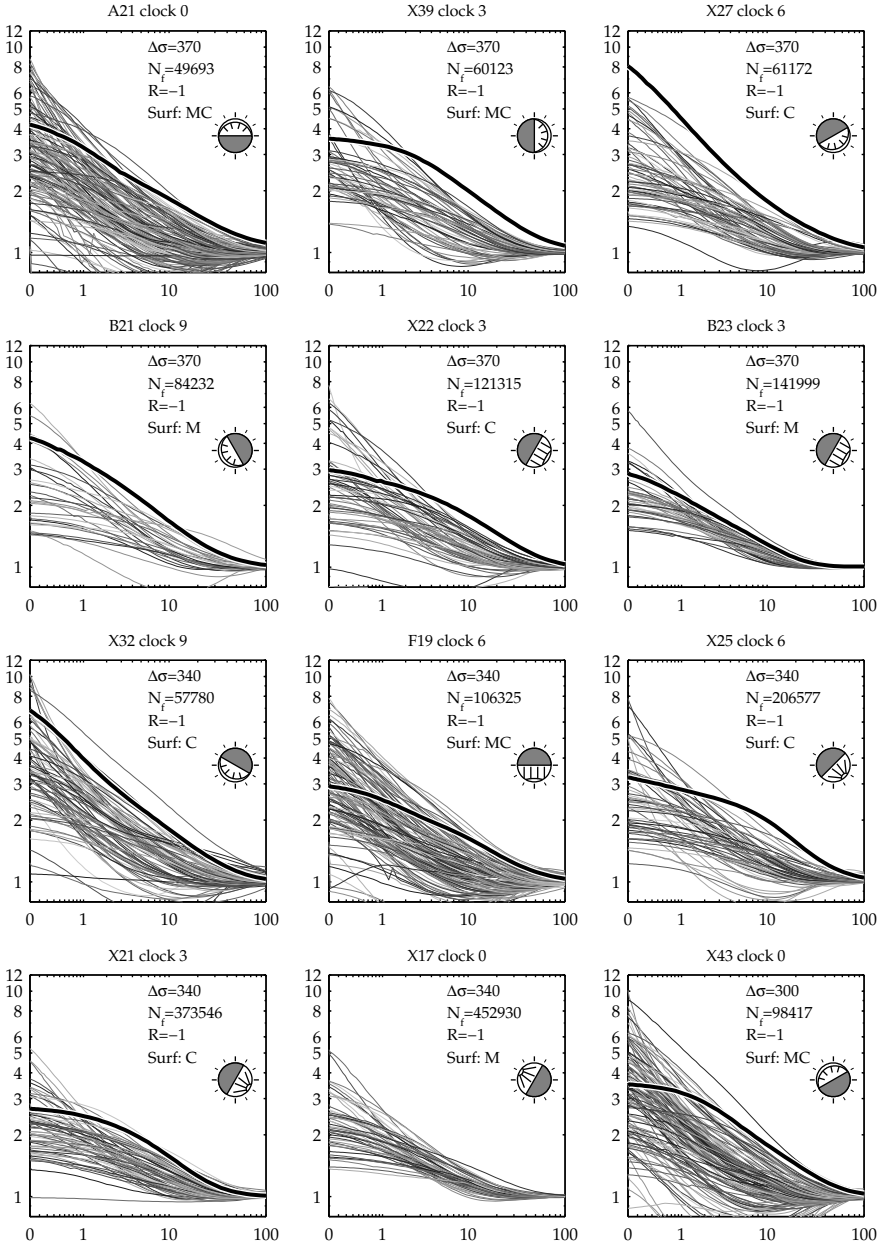
A21 clock 0
Δσ=370
N_f=49693
R=−1
Surf: MC
X39 clock 3
Δσ=370
N_f=60123
R=−1
Surf: MC
X27 clock 6
Δσ=370
N_f=61172
R=−1
Surf: C
B21 clock 9
Δσ=370
N_f=84232
R=−1
Surf: M
X22 clock 3
Δσ=370
N_f=121315
R=−1
Surf: C
B23 clock 3
Δσ=370
N_f=141999
R=−1
Surf: M
X32 clock 9
Δσ=340
N_f=57780
R=−1
Surf: C
F19 clock 6
Δσ=340
N_f=106325
R=−1
Surf: MC
X25 clock 6
Δσ=340
N_f=206577
R=−1
Surf: C
X21 clock 3
Δσ=340
N_f=373546
R=−1
Surf: C
X17 clock 0
Δσ=340
N_f=452930
R=−1
Surf: M
X43 clock 0
Δσ=300
N_f=98417
R=−1
Surf: MC
0 1 10 100
1 2 3 4 5 6 8 10 12

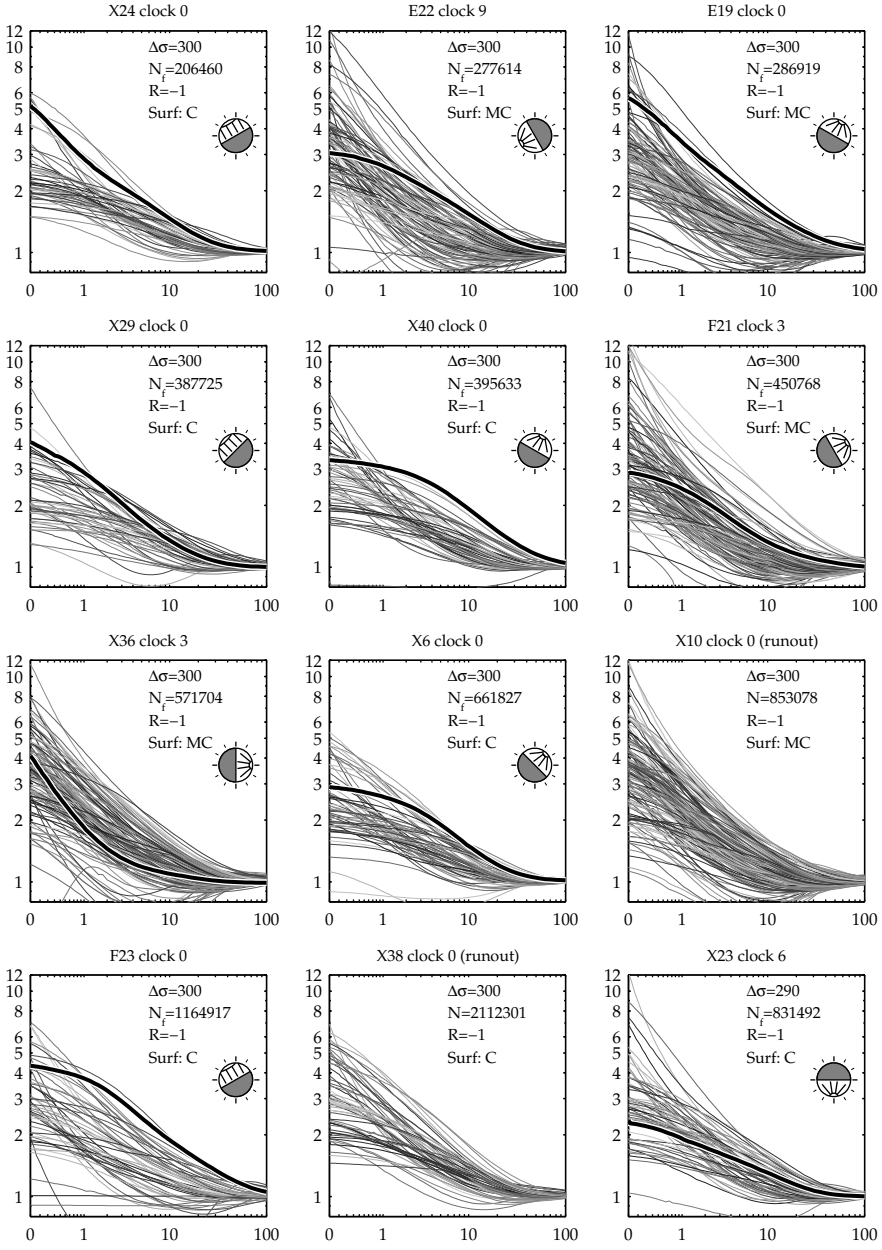
X24 clock 0
Δσ=300
N_f=206460
R=−1
Surf: C
E22 clock 9
Δσ=300
N_f=277614
R=−1
Surf: MC
E19 clock 0
Δσ=300
N_f=286919
R=−1
Surf: MC
X29 clock 0
Δσ=300
N_f=387725
R=−1
Surf: C
X40 clock 0
Δσ=300
N_f=395633
R=−1
Surf: C
F21 clock 3
Δσ=300
N_f=450768
R=−1
Surf: MC
X36 clock 3
Δσ=300
N_f=571704
R=−1
Surf: MC
X6 clock 0
Δσ=300
N_f=661827
R=−1
Surf: C
X10 clock 0 (runout)
Δσ=300
N=853078
R=−1
Surf: MC
F23 clock 0
Δσ=300
N_f=1164917
R=−1
Surf: C
X38 clock 0 (runout)
Δσ=300
N=2112301
R=−1
Surf: C
X23 clock 6
Δσ=290
N_f=831492
R=−1
Surf: C

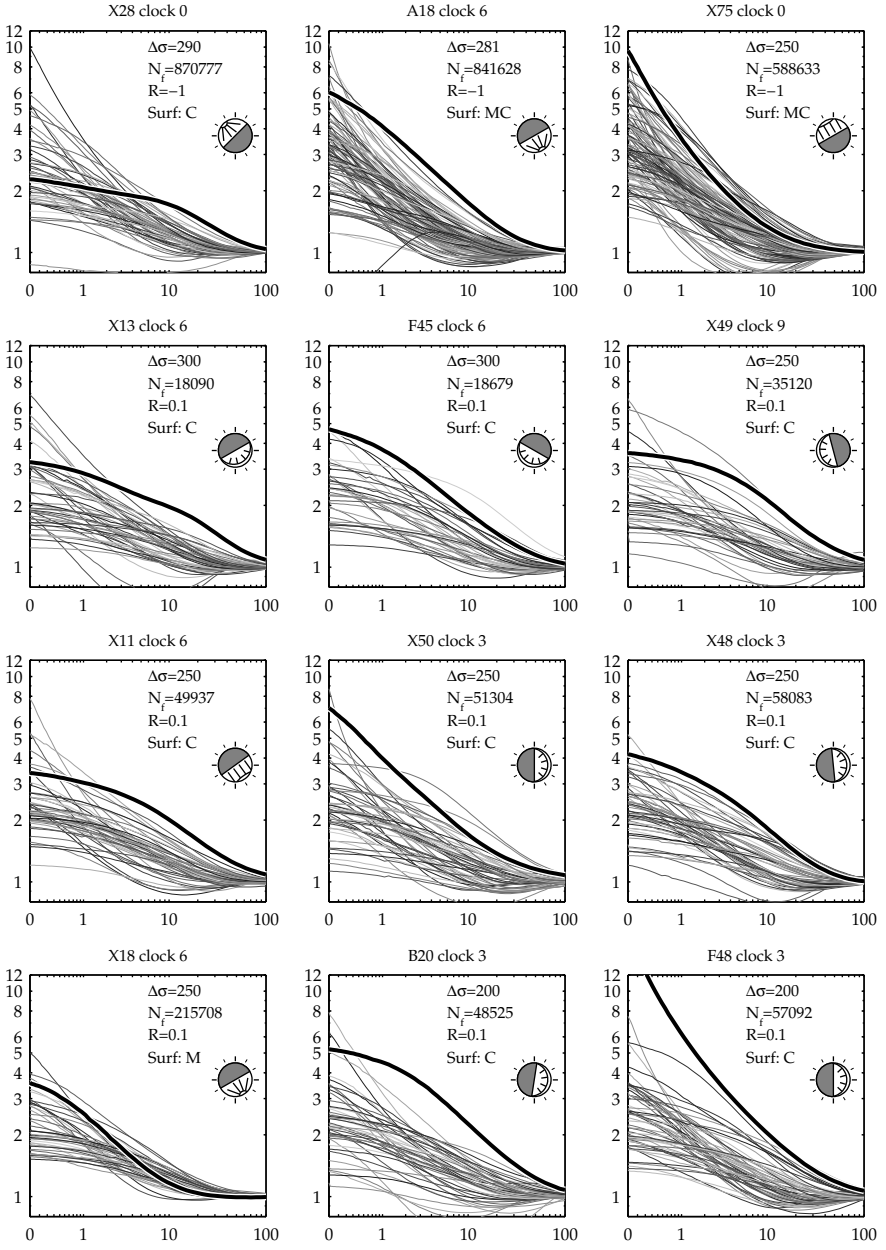
X28 clock 0
Δσ=290
N_f=870777
R=−1
Surf: C
A18 clock 6
Δσ=281
N_f=841628
R=−1
Surf: MC
X75 clock 0
Δσ=250
N_f=588633
R=−1
Surf: MC
X13 clock 6
Δσ=300
N_f=18090
R=0.1
Surf: C
F45 clock 6
Δσ=300
N_f=18679
R=0.1
Surf: C
X49 clock 9
Δσ=250
N_f=35120
R=0.1
Surf: C
X11 clock 6
Δσ=250
N_f=49937
R=0.1
Surf: C
X50 clock 3
Δσ=250
N_f=51304
R=0.1
Surf: C
X48 clock 3
Δσ=250
N_f=58083
R=0.1
Surf: C
X18 clock 6
Δσ=250
N_f=215708
R=0.1
Surf: M
B20 clock 3
Δσ=200
N_f=48525
R=0.1
Surf: C
F48 clock 3
Δσ=200
N_f=57092
R=0.1
Surf: C

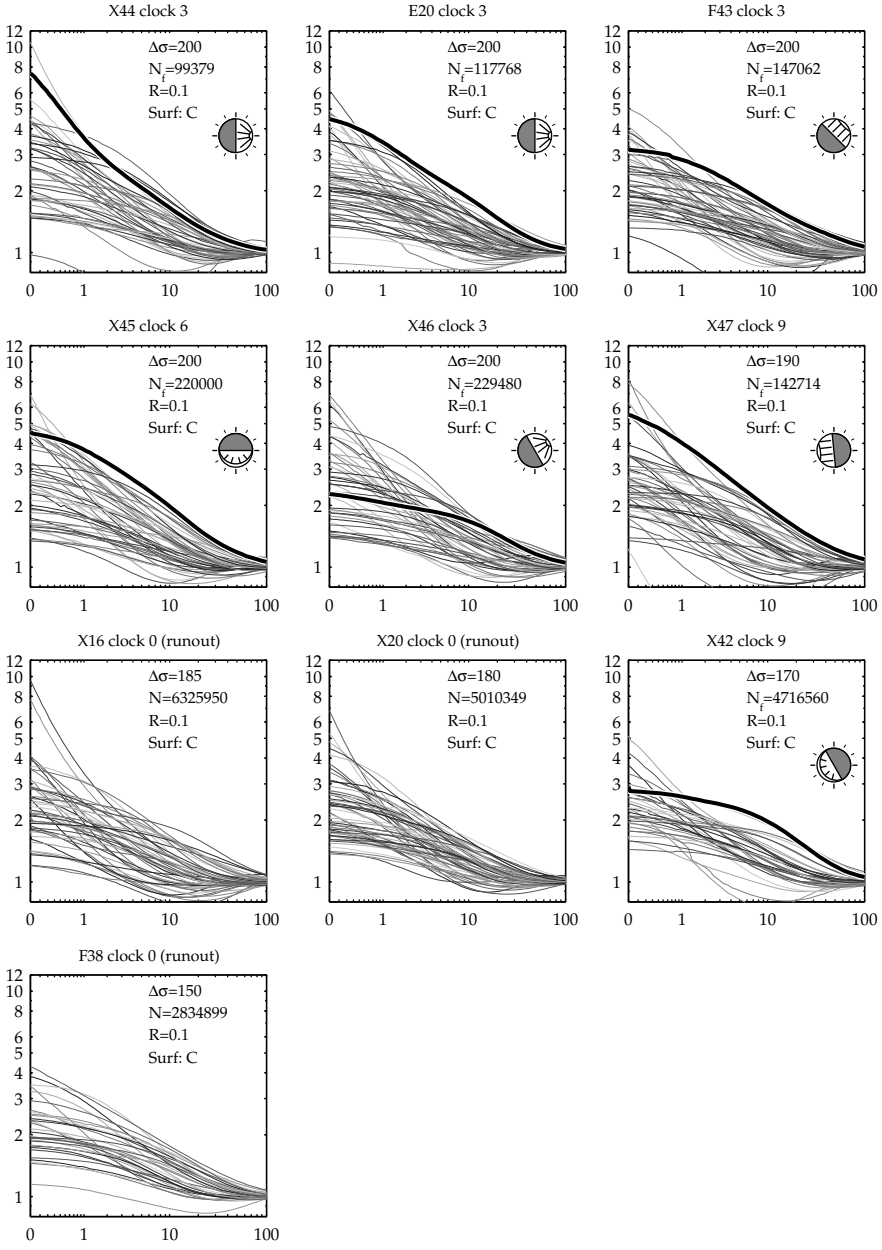
X44 clock 3
Δσ=200
N_f=99379
R=0.1
Surf: C
E20 clock 3
Δσ=200
N_f=117768
R=0.1
Surf: C
F43 clock 3
Δσ=200
N_f=147062
R=0.1
Surf: C
X45 clock 6
Δσ=200
N_f=220000
R=0.1
Surf: C
X46 clock 3
Δσ=200
N_f=229480
R=0.1
Surf: C
X47 clock 9
Δσ=190
N_f=142714
R=0.1
Surf: C
X16 clock 0 (runout)
Δσ=185
N=6325950
R=0.1
Surf: C
X20 clock 0 (runout)
Δσ=180
N=5010349
R=0.1
Surf: C
X42 clock 9
Δσ=170
N_f=4716560
R=0.1
Surf: C
F38 clock 0 (runout)
Δσ=150
N=2834899
R=0.1
Surf: C

Comments on linear elastic results

From the plots on pages 104 to 108, it can be seen that there is a distinct trend of dominating subsurface stresses for the initiation-groove. The runout specimens naturally has no indication of an initiation location, however, specimen X17 on page 105 failed, but still shows no bold line indicating the initiation location. This is because the V1 algorithm did not identify the failure notch, and therefore produced no stress solution ahead of the notch. The notch where initiation occurred was very shallow, and not very well characterized by the WLI measurement. Two SEM images are shown in Figure 5.15, revealing a number of corrosion-like defects in the grooves, as well as on the as-machined surface, which the WLI could not discern. It is not known why this specimen displayed such features.

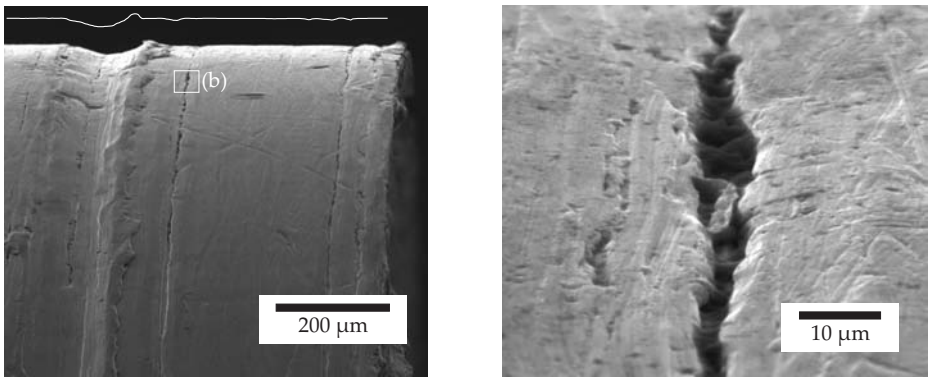

Figure 5.15: Specimen X17: The fracture location is shown in (a), along with the WLI measured profile. Initiation started in one of numerous defects as the one shown in (b), and these could not be well characterized by the WLI measurement.

Stress solutions for specimen F21, shown on page 106, had relatively low subsurface stresses at the initiation location. Studies in the SEM showed a strongly localized crack initiation, and also some variations in the groove shape around the circumference. As seen from the stress-solution plot, the exact initiation location was at 2 o'clock, thus the solutions used for 3 o'clock may not be representative of the actual initiation location.

Specimen X36, with solutions shown on page 106, also showed a very local initiation from a shallow groove. In this case, the initiation occurred at 3 o'clock, where the surface profile was measured. Figure 5.16(a) shows the macroscopic fracture appearance, and a secondary initiation site is revealed in the neighbor groove. Figure 5.16(b) shows a close-up, where the neighboring groove can be seen to be much deeper than the groove where initiation occurred. Early crack growth followed inclined planes, about about 40° with the loading direction. No

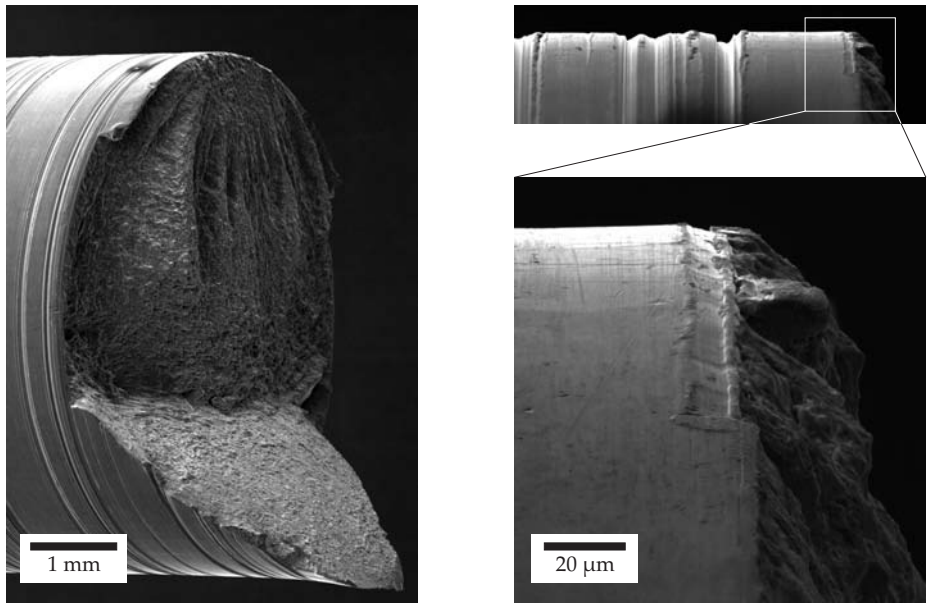

(a) (b)

Figure 5.16: Specimen X36, which failed in a relatively shallow groove, showed a very localized initiation zone in a shallow groove.

material defects or other clear reasons as to why the initiation started here were apparent for this specimen.

Another specimen that had quite low subsurface stresses was X23, as shown on page 106. SEM images of the initiation location are shown in Figure 5.17, where a material weakness seems to have caused crack initiation. It is likely that this material weakness was a de-bonded grain, since there is a protrusion on one side and an intrusion on the other with sizes corresponding to the grain diameter for this material. Initiation started within the root of a shallow notch, while subsequent crack propagation outside of the intrusion temporarily left the notch and followed the ridge. The image to the right reveals very large vertical striations, which may indicate that rapid crack propagation took place after the grain de-bonded.

5.3.2 Elastic-plastic material

The elastic-plastic material model was calibrated from the cyclic stress-strain curve (Figure 3.18). A plastic tangent modulus of E'=4.24 $\times$ 19^3 MPa with a yield stress of 350 MPa was found to describe the strain range of interest best. Figure 5.18 shows two simulated load cycles of a straight, axi-symmetric specimen compared to the half-life hysteresis loops at the same strain ranges. The

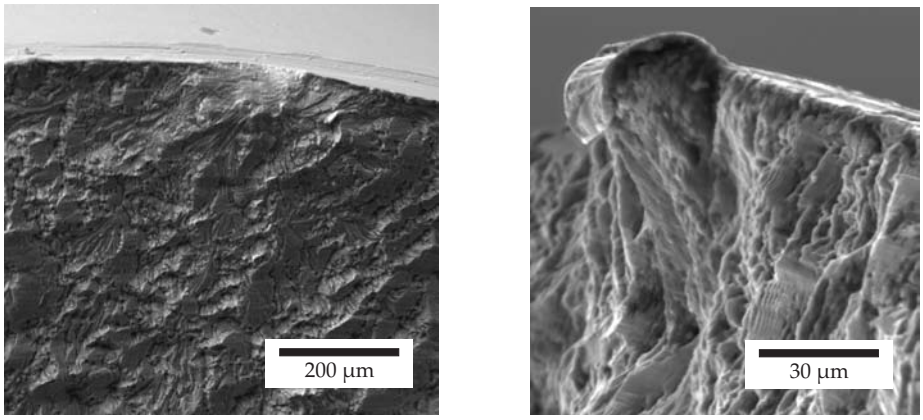

Figure 5.17: Specimen X23, which appeared to fail from a local material defect. The two images are taken of opposing crack faces.

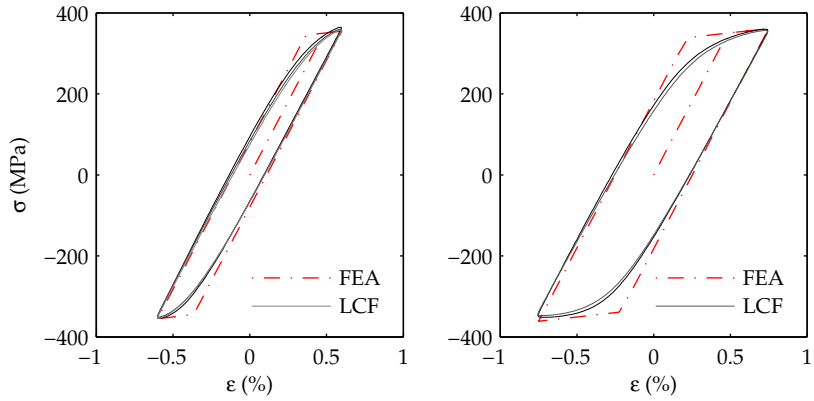

Figure 5.18: Comparison of FEA and hysteresis loops from LCF. Half-life hysteresis loops for three specimens cycled at $\Delta\varepsilon$=1.3% are shown to the left, and two specimens cycled at $\Delta\varepsilon$=1.5% are shown to the right.

simulations were very accurate with regard to maximum and minimum stress, but for variable amplitude loading the model should be used with caution since the shape of the hysteresis loop is poorly defined.

Solutions for the elastic-plastic material model and R=-1 are shown on the following pages, up until page 114. As before, the abscissa is $\sigma_z/\sigma_{\text{nom}}$ and the ordinate is distance in µm ahead of the notches.

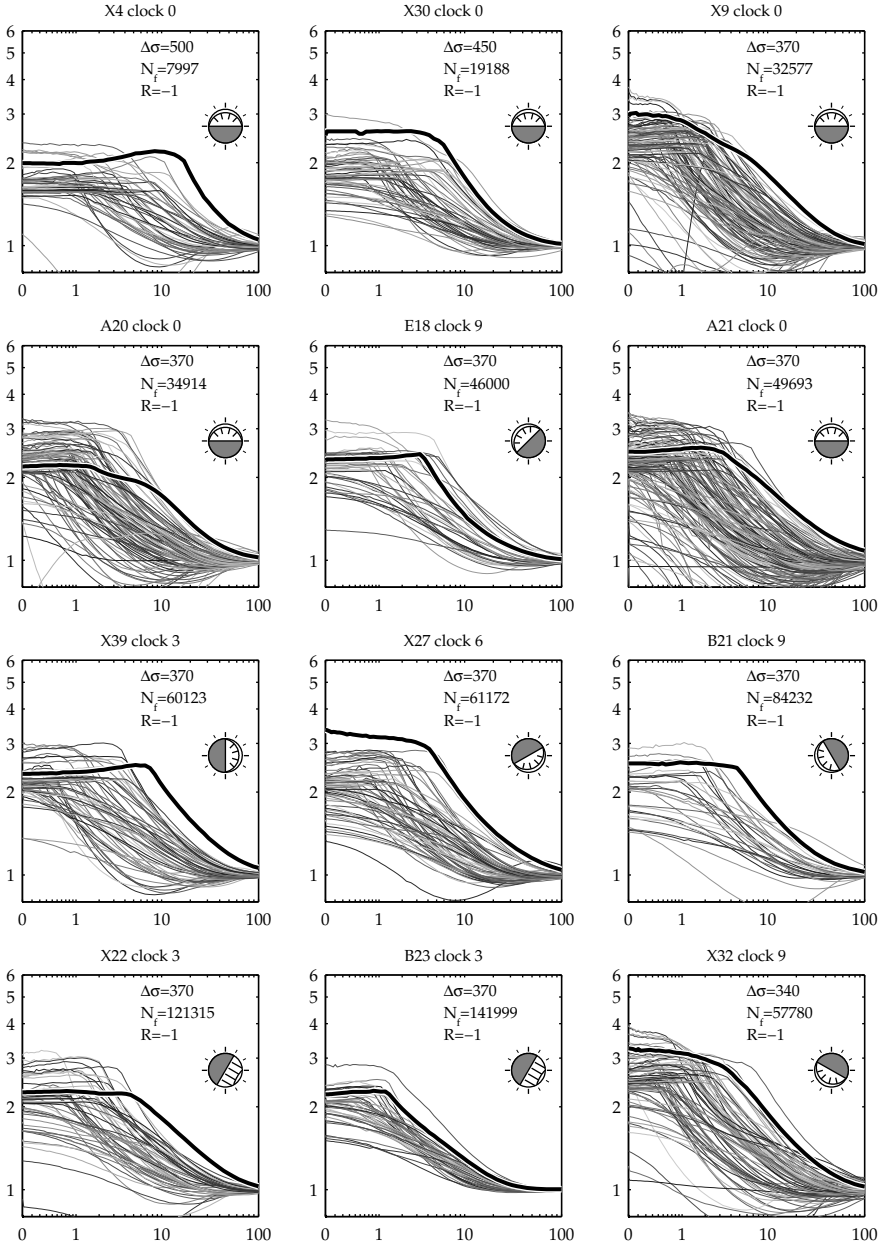
X4 clock 0
Δσ=500
N_f=7997
R=−1
X30 clock 0
Δσ=450
N_f=19188
R=−1
X9 clock 0
Δσ=370
N_f=32577
R=−1
A20 clock 0
Δσ=370
N_f=34914
R=−1
E18 clock 9
Δσ=370
N_f=46000
R=−1
A21 clock 0
Δσ=370
N_f=49693
R=−1
X39 clock 3
Δσ=370
N_f=60123
R=−1
X27 clock 6
Δσ=370
N_f=61172
R=−1
B21 clock 9
Δσ=370
N_f=84232
R=−1
X22 clock 3
Δσ=370
N_f=121315
R=−1
B23 clock 3
Δσ=370
N_f=141999
R=−1
X32 clock 9
Δσ=340
N_f=57780
R=−1

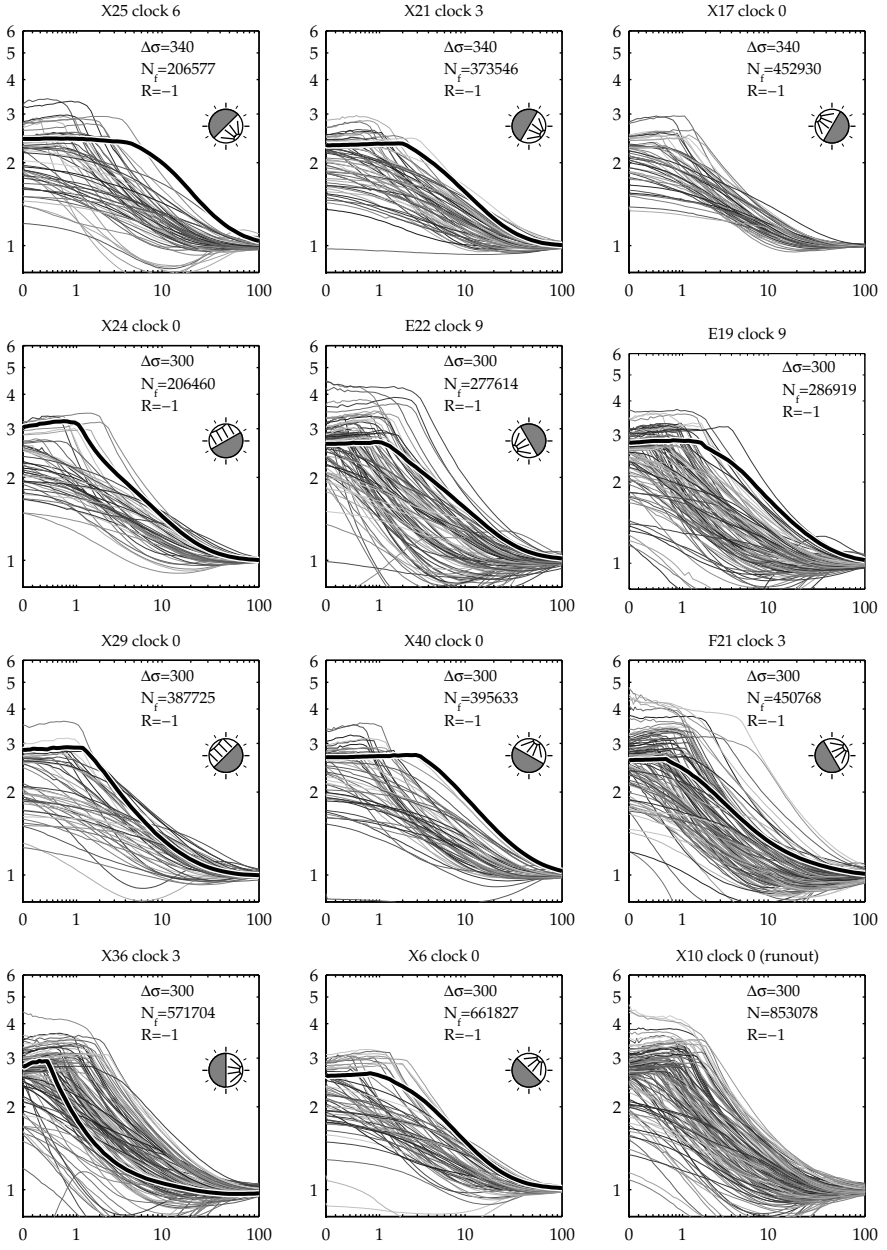
X25 clock 6
Δσ=340
N_f=206577
R=−1
X21 clock 3
Δσ=340
N_f=373546
R=−1
X17 clock 0
Δσ=340
N_f=452930
R=−1
X24 clock 0
Δσ=300
N_f=206460
R=−1
E22 clock 9
Δσ=300
N_f=277614
R=−1
E19 clock 9
Δσ=300
N_f=286919
R=−1
X29 clock 0
Δσ=300
N_f=387725
R=−1
X40 clock 0
Δσ=300
N_f=395633
R=−1
F21 clock 3
Δσ=300
N_f=450768
R=−1
X36 clock 3
Δσ=300
N_f=571704
R=−1
X6 clock 0
Δσ=300
N_f=661827
R=−1
X10 clock 0 (runout)
Δσ=300
N=853078
R=−1

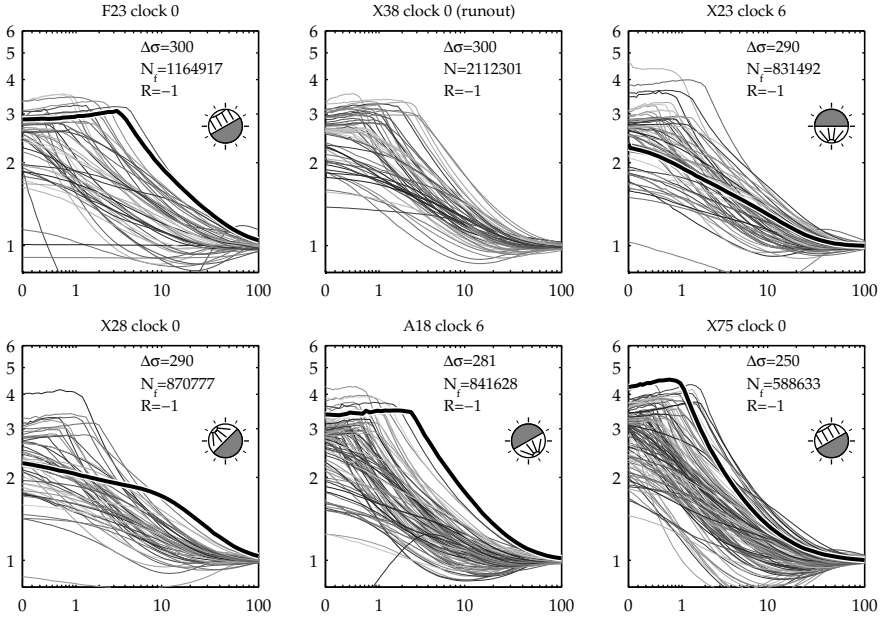

In the case of R=-1 loading, the absolute compressive stress solutions will be the same as the tensile solutions. For R=0.1 loading, this is not the case, and in the following plots, a plastic load ratio R_p has been introduced, which relate the minimum stress to the maximum stress in the valley root.

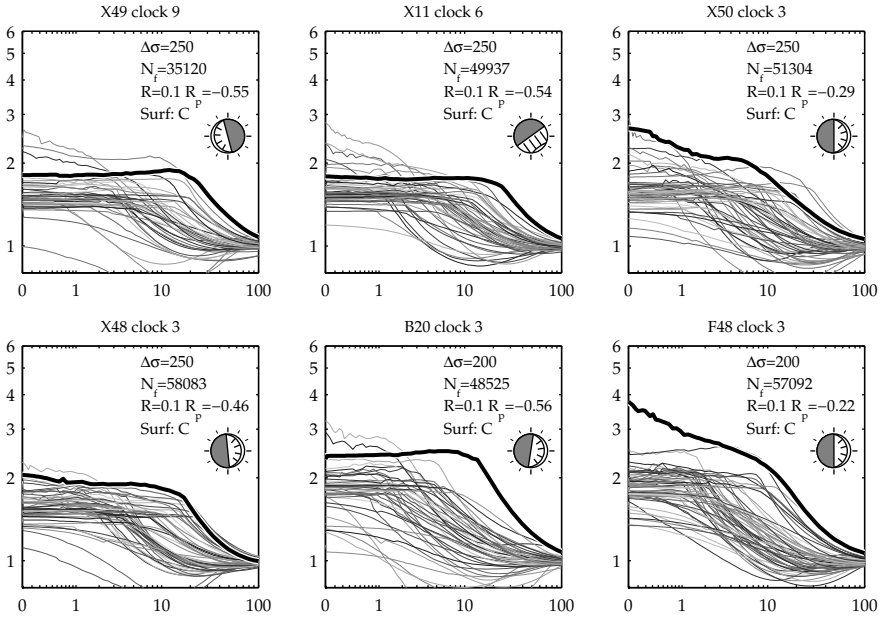

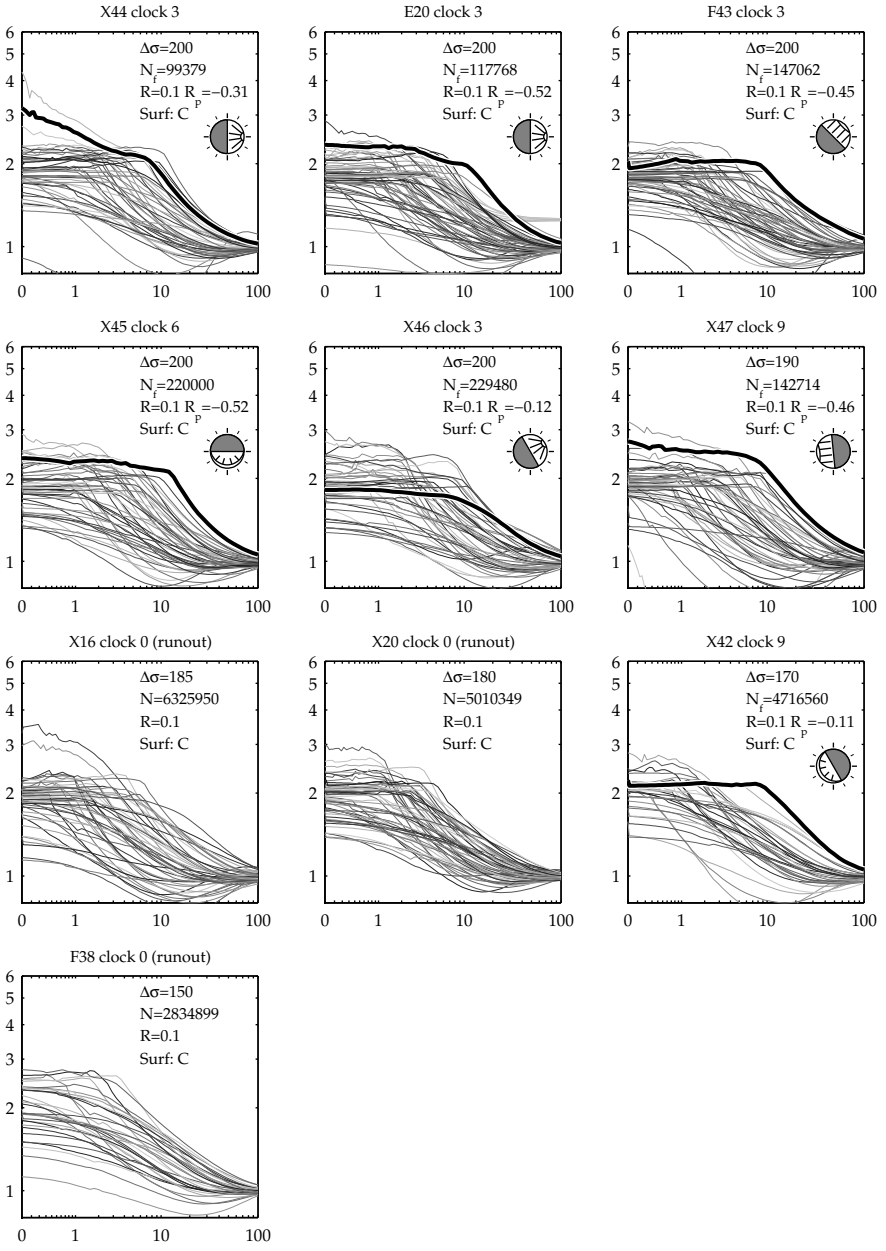

Residual stress results from nonlinear analysis

Some analyses of the influence from the assumed residual stress distribution are shown on the next page. The compressive load cycle in *R*=-1 loading was not

generally solved for, since FEMLAB's parametric solver would not converge or crash. This occurred after the maximum parameter value had been reached, at around zero global load. This could be due to parameter scaling, where the solver would run into problems for zero plastic strains, and could possibly have been overcome using manual scaling. Due to the relatively high uncertainty associated with these analyses, however, further attempts at obtaining converging results were not made.

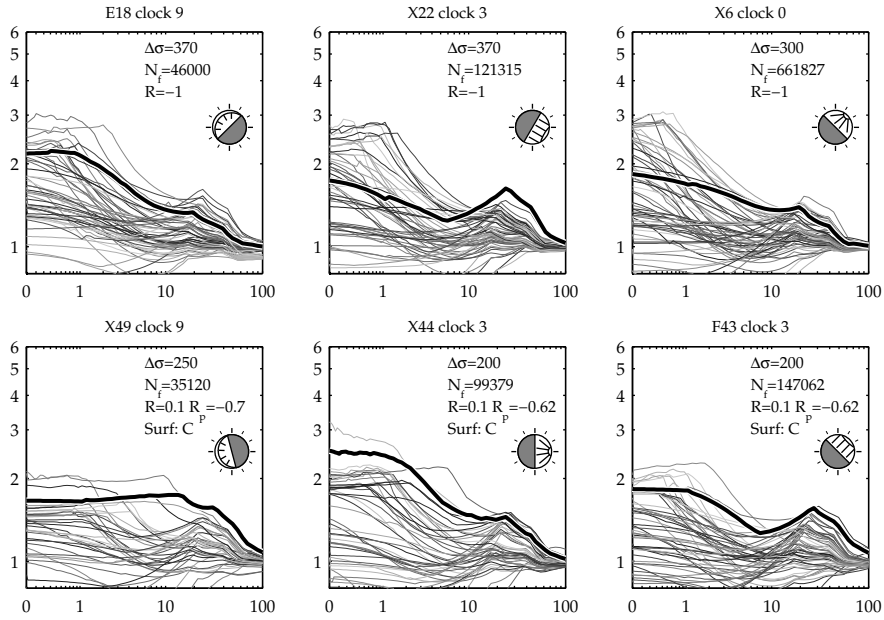

Comments on nonlinear results

The nonlinear solutions show, as expected, lower K_t values for the notches and also less difference between the highest and lowest K_t. This may partly explain why the very high values of K_t observed in the linear elastic analysis appear to be less significant in cyclic loading. The general trend observed for the linear elastic solutions is also found in the nonlinear solutions, where stresses about 10 µm ahead of the notch where initiation occurred are dominating over the other stress solutions.

5.3.3 Elastic-plastic notch correction

Figure 5.19 shows the results from the classic Neuber correction and the generalized Hoffmann-Seeger (HS) correction, compared to elastic-plastic FEA. Stress ranges have been calculated in the notches where fatigue crack initiation was observed. For R=-1 loading, it can be seen that the Neuber correction produces non-conservative results, with calculated stress ranges around 8% lower than

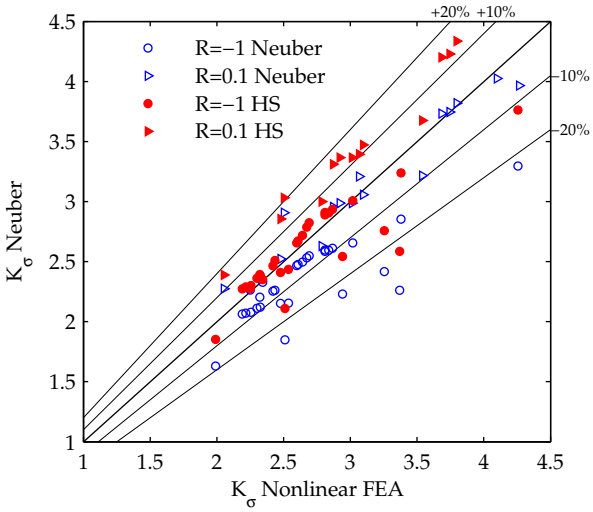

Figure 5.19: Comparison of Neuber corrected linear solutions and nonlinear FEA results.

the nonlinear FEA. A group of ten results are in the range 10% to 30% lower than the nonlinear FEA. In the case of R=0.1 loading, the Neuber prediction is more accurate, although it should be emphasized that the stress concentration is based on stress range without regard of mean stress. The Neuber correction actually predicts higher mean and maximum stress than HS. A comparison based on the Smith-Watson-Topper parameter is shown in Figure 5.20, where it is seen that the HS correction matches the nonlinear FEA results more closely than the Neuber correction. Both solutions, however, shows considerable conservatism, especially for the lowest stress ranges.

In Figure 5.21, the Neuber and HS corrections are compared based on strain range results. The differences between the two are larger, with the Neuber results consistently about 30% higher than the nonlinear FEA results. The HS correction on the other hand, exceeds the FEA results by maximum 22%, with the majority of results in the range 0% to 12% higher.

In conclusion, the HS correction provides a more accurate estimate of the elastic-plastic stresses and strains in the notch root. Some of the differences observed can be explained by the quite different models of the cyclic stress-strain response used; while the analytical corrections use the Ramberg-Osgood curve, the elastic-plastic FEA uses a bilinear curve that differ in yield point and hardening. This simplified material response may in fact be associated with inaccurate results in itself, especially for strain amplitudes around 0.5%, where the Ramberg-Osgood relation describes a lower stress amplitude than the bilinear model. Considering the scatter in cyclic stress-strain data, however, the difference between the two models is less critical (see Figure 3.18 on page 65).

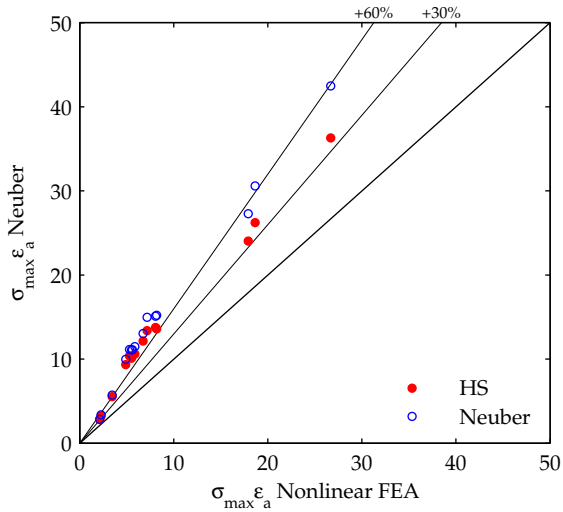

Figure 5.20: Comparison of R=0.1 results where the effects of mean stresses are assessed using the Smith-Watson-Topper parameter.

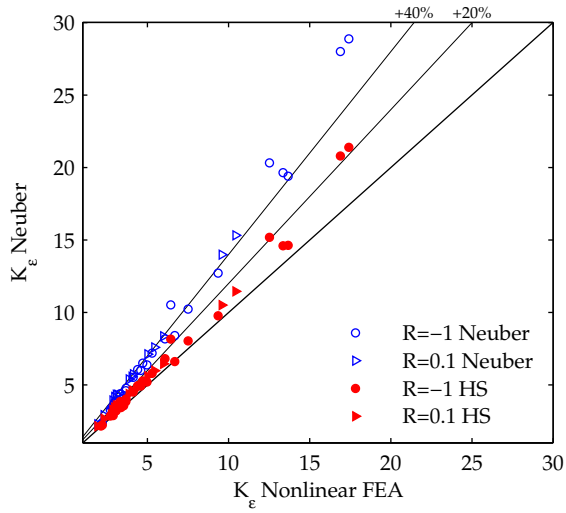

Figure 5.21: Comparison of Neuber corrected linear solutions and nonlinear FEA results.

5.4 Fatigue life prediction

It is of interest to see if established engineering methods can be used to determine the influence of surface roughness. Empirical models for notch sensitivity, found in Section 1.2.5, have been evaluated using stress and strain values calculated in the groove where initiation occurred.

Runout specimens are shown in Table 5.1. Two tests were terminated after 2×10^6 cycles, and two others were terminated after 5×10^6 cycles. Specimen X10 failed due to fretting in the grip section.

Notch sensitivity was calculated for the rough specimens that failed, using the geometry and linear FEA results of the notch root. Figure 5.22 shows notch sensitivities as found from Eq. 1.19. The fatigue notch factor K_f was found by comparing the stress life curves corresponding to the given load ratio and material. The stress life curve given in Figure 3.14 on page 61 was used for the forged R=-1 test series. The notch sensitivity shows considerable variations, and a generally increasing trend for increasing fatigue lives. Table 5.2 on the following page summarizes fatigue life data for R=-1 loading, along with surface roughness parameters and FEA results. Table 5.3 shows the same data for R=0.1 loading.

Table 5.1: Terminated tests of rough specimens (Runout=1), and a specimen that failed in the grip section (Runout=2).

Specimen	Type	Runout	R	$\Delta\sigma$	N	R_a	R_v	K_{AR}	R_{10}
F38	E(I)	1	0.1	150	2834899	8.62	-34.7	1.78	9.62
X20	E(II)	1	0.1	180	5010349	5.2	-18	1.25	9.22
X16	E(II)	1	0.1	185	6325950	7.07	-28.2	1.97	9.51
X38	E(II)	1	-1	300	2112301	4.96	-29.5	3.03	13.1
X10	E(II)	2	-1	300	853078	7.41	-29.9	2.55	26.7

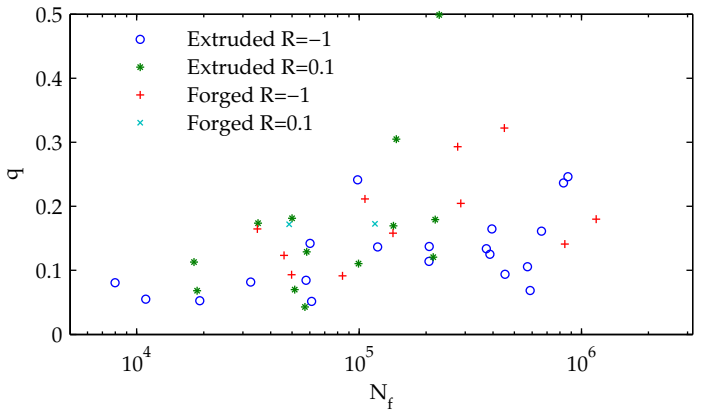

Figure 5.22: Notch sensitivity versus fatigue life.

Table 5.2: Fatigue data for rough specimens, fully reversed loading.

								Initiation location							
Specimen	Type	$\Delta\sigma$	N	R_a	R_v	K_{AR}	R_{10}	Clock	Height	K_t	$\sigma_z\|_1$	$\sigma_z\|_{10}$	χ	ρ	K_f	q
X4	E(II)	500	7997	5.18	-28.4	1.5	13.5	0	50.7	4.1	3.8	2.2	1311	11	1.3	0.081
X26	E(II)	500	10971	6.16	-26.9	1.79	7.73	6	33.4	4.8	3.8	1.7			1.2	0.055
X30	E(II)	450	19188	4.24	-26.1	1.64	10.3	0	26.6	6.1	4.1	1.6			1.3	0.052
X9	E(II)	370	32577	5.48	-26.7	2.19	22	0	33.9	6.6	3.3	1.8	1978	47	1.5	0.082
A20	F(I)	370	34914	6.17	-26.9	4.02	20.5	0	24.1	2.8	2.4	1.7	1217	58	1.4	0.21
E18	F(I)	370	46000	4.35	-28.1	1.95	22.1	9	17.9	3.4	2.9	1.4	702	5.3	1.3	0.13
A21	F(I)	370	49693	10.2	-29.8	2.35	25.5	0	58.2	4.2	3.2	1.8	5437	12	1.3	0.091
X39	E(II)	370	60123	4.91	-21.8	2.87	13.2	3	47.8	3.6	3.3	2	243	19	1.4	0.14
X27	E(II)	370	61172	4.94	-19.4	1.87	8.22	6	41	8.1	4.5	1.8	1135	15	1.4	0.052
B21	F(I)	370	84232	4.38	-19.5	2.22	5.61	9	28.2	4.3	3.3	1.7	358	14	1.2	0.057
X22	E(II)	370	121315	3.74	-13.4	1.56	8.06	3	35.7	3	2.6	1.8	172	44	1.3	0.14
B23	F(I)	370	141999	2.28	-9.38	1.51	4.1	3	11.7	2.9	2.2	1.3	404	27	1.1	0.052
X32	E(II)	340	57780	5.89	-20.4	5.29	14.4	9	36.3	6.8	4	1.8	1178	5.5	1.5	0.085
F19	F(I)	340	106325	8.44	-43.2	4.66	34.1	6	25.8	2.9	2.5	1.6	269	81	1.2	0.13
X25	E(II)	340	206577	4.6	-16.5	1.93	5.52	6	37.4	3.2	2.8	2	2216	20	1.3	0.14
X21	E(II)	340	373546	5.38	-22.7	2.19	7.91	3	20.6	2.7	2.5	1.6	594	23	1.2	0.13
X17	E(II)	340	452930	2.5	-11.6	1.89	4.59	0	4.65	3.1	1.6	0.99	1182		1.2	0.094
X43	E(II)	300	98417	5.03	-21.9	2.66	16.6	0	42.2	3.5	3.2	1.8	235	13	1.6	0.24
X24	E(II)	300	206460	2.25	-15.2	1.68	3.72	0	18.2	5.2	2.9	1.5	1180	15	1.5	0.11
E22	F(I)	300	277614	5.64	-34.7	3.79	18.6	9	22.3	3	2.6	1.5	13139	5.1	1.2	0.12
E19	F(I)	300	286919	6.23	-30.6	4.97	24.8	0	32.7	3.9	3.1	1.7	1387	17	1.2	0.081
X29	E(II)	300	387725	5.57	-16.2	2.91	4.94	0	13.2	4.1	2.9	1.4	542	22	1.4	0.13
X40	E(II)	300	395633	4.43	-26.2	1.99	10.4	0	35.4	3.3	3.1	1.9	642	38	1.4	0.16
F21	F(I)	300	450768	6.34	-27.4	3.87	16	3	16.8	2.9	2.4	1.3	383	7.3	1.2	0.094
X36	E(II)	300	571704	6.39	-24.8	2.64	19.3	3	4.84	4.1	1.8	1.1	1650	5	1.3	0.11
X6	E(II)	300	661827	4.82	-21.8	2.34	7.09	0	17.7	2.9	2.6	1.5	490	18	1.3	0.16
F23	F(I)	300	1164917	8.37	-29.9	2.35	18.9	0	42	4.3	3.8	1.9	1258	15	1.1	0.022
X23	E(II)	290	831492	4.35	-19.1	1.57	12.4	6	10.5	2.4	1.9	1.3	272	54	1.3	0.24
X28	E(II)	290	870777	5.39	-28.5	2.28	8.75	0	30.3	2.3	2.1	1.7	5437	74	1.3	0.25
A18	F(I)	281	841628	4.67	-22.8	11.3	8.91	6	29.7	6	4.1	1.8	547	5.9	1.2	0.036
X75	E(II)	250	588633	5.69	-23.5	5.95	15.4	0	16.8	9.6	3.6	1.3	2435	2	1.6	0.068

Table 5.3: Fatigue data for rough specimens with a load ratio of R=0.1.

								Initiation location								
Specimen	Type	$\Delta\sigma$	N	R_a	R_v	K_{AR}	R_{10}	Clock	Height	K_t	$\sigma_z\|_1$	$\sigma_z\|_{10}$	χ	ρ	K_f	q
X13	E(II)	300	18090	4.56	-15.5	1.51	3.51	6	46.8	3.2	2.9	2	1562	30	1.3	0.11
F45	E(I)	300	18679	6.14	-31.2	1.51	10.1	6	11.9	4.7	3.7	1.8	356	49	1.3	0.068
X49	E(II)	250	35120	8.43	-44.3	2.2	8.65	9	15.9	3.6	3.3	2.1	696	45	1.5	0.17
X11	E(II)	250	49937	6.46	-17.9	1.55	5.61	6	46.3	3.4	3	2	1548	50	1.4	0.18
X50	E(II)	250	51304	11.3	-42.4	1.93	19.6	3	38.3	7	4	1.7	1268	52	1.4	0.07
X48	E(II)	250	58083	7.24	-32.6	2.48	5.95	3	23.3	4.2	3.4	1.8	458	34	1.4	0.13
X18	E(II)	250	215708	3.37	-13.7	1.41	2.55	6	0.587	3.6	2.5	1.2	444	210	1.3	0.12
B20	F(I)	200	48525	6.67	-21.1	2.06	7.05	3	-1.51	5.2	4.5	2.3	2969	16	1.7	0.17
F48	E(I)	200	57092	6.97	-30.7	1.72	9.76	3	-0.734	19	6.2	2	2799	25	1.8	0.043
X44	E(II)	200	99379	7.56	-35.5	1.77	12.1	3	38.4	7.4	3.6	1.7	1986	74	1.7	0.11
E20	F(I)	200	117768	7.54	-20	1.64	10.5	3	7.07	4.5	3.4	1.8	923	42	1.6	0.17
F43	E(I)	200	147062	6.91	-24.3	2.7	3.08	3	3.89	3.2	2.8	1.7	287	74	1.7	0.3
X45	E(II)	200	220000	10	-29.9	1.91	18.2	6	44.9	4.6	3.7	2	275	36	1.6	0.18
X46	E(II)	200	229480	8.47	-41.1	1.81	3.69	3	-1.76	2.3	2.1	1.7	1960	43	1.6	0.5
X47	E(II)	190	142714	9.76	-37.2	2.63	7.84	9	26	5.5	4	2	569	32	1.8	0.17
X42	E(II)	170	4716560	8.03	-33.4	1.55	10.2	9	-2.12	2.9	2.6	2	672	46	1.6	0.33

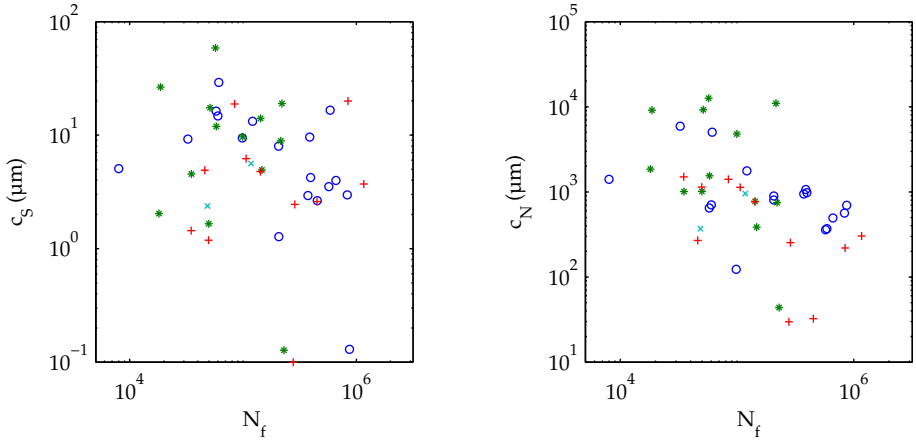

(a) Siebel and Stieler (b) Neuber

Figure 5.23: The parameters from Eq. 1.21 and Eq. 1.23 versus fatigue life.

From the discussion in Section 1.2.5, it is natural to assume that the variation in notch sensitivity may be explained by the stress gradient at the notch. The various expressions for K_f were checked by solving for the material parameters using the known K_f for the failed specimens. The material parameters from Eq. 1.23 and Eq. 1.21 on page 15 are plotted against fatigue failure life in Figure 5.23. The curvature ρ required in the Neuber expression was found by fitting parabolas to the lowest points in the notches, as described in Section 3.4.1. The parameters shows a variation of three orders of magnitude, and there seems to be no clear dependence on fatigue life.

5.4.1 Accounting for crack propagation

Following the traditional notch fatigue approach, only the initiation life can be predicted. When the crack grows out of the notch stress field, stress or strain ranges based on K_f are no longer valid. This is problematic in this context since the notches are very small and would require a nonlinear fracture mechanics approach or a closure corrected stress intensity factor. For the reasons stated in Section 1.3, this has not been undertaken in this work.

Crack growth data have been obtained from Leinum et al. [171], who conducted crack growth measurements on CT specimens (W=25 mm, B=5 mm) on an extruded 6082-T6 material with crack growth in the transverse-long and long-transverse direction. Testing was done at load control with R=0.5. In this study, load ratios of R=-1 and R=0.1 are used, thus a correction was made using a modification to Eq. 1.38. The modification consists of replacing ΔK with K_{max} for

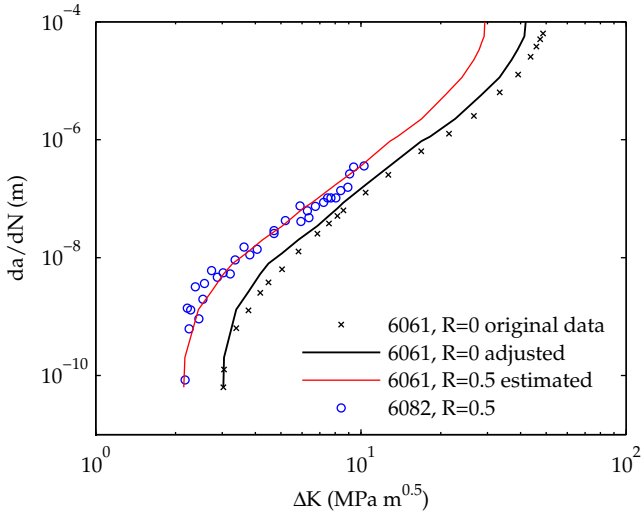

Figure 5.24: The original R=0 crack growth data for a 6061 material was adjusted so that the curve would coincide with 6082 R=0.5 data when the Walker mean stress correction was used.

negative load ratios, and also changing the sign of the exponent $(m-1)$ [172]:

$$\frac{da}{dN} = \begin{cases} C\left[\Delta K(1-R)^{m-1}\right]^n, & R \geqslant 0 \\ C\left[K_{\max}(1-R)^{1-m}\right]^n, & R < 0. \end{cases} \tag{5.1}$$

AFGROW [173], available from the US Air Force Research Laboratory, was used for fracture mechanics calculations, where Eq. 5.1 is applied on a point-by-point basis, requiring a value of m for each value of da/dN-ΔK. This data is available for extruded 6061-T6 in the AFGROW material database, and was slightly adjusted so that the crack growth rate curve would coincide with the 6082 data when the Walker mean stress correction was used. This is shown in Figure 5.24. In effect, the 6061 data was used with a slight correction to comply with the R=0.5 data. The estimated R=0.1 data fits well with observations made by Bergner et al. [81], who found that T6 aluminium alloys tend to have similar crack growth rates of 10^{-7} to 2×10^{-7} m/cycle at ΔK=10 MPa$\sqrt{\text{m}}$.

Several stress intensity factor solutions for standard specimens are included in AFGROW. A solution for a semi-circular crack in a cylindrical rod was used in this case, developed by Forman and Shivakumar [174]. An initial crack depth of 0.8 mm was used and the iterations were stopped when the remaining cross section failed by yielding. The initial crack depth was chosen as the minimum value that would give yield adequate crack propagation at the lowest load levels used in the experiments. For R=-1 loading, an effective load ratio of R=-0.3 was used due to the assumed crack face contact.

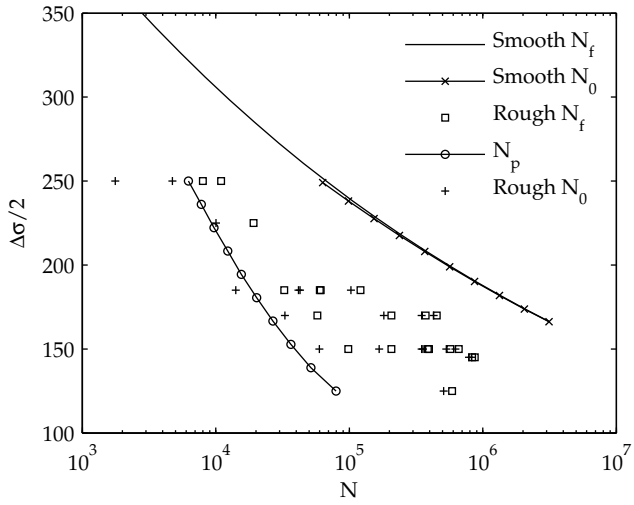

Figure 5.25: Propagation and initiation life curves in relation to smooth and rough fatigue lives.

Using this crack growth model, the da/dN value computed for specimen X32 was compared to the observed striation spacing, shown in Figure 5.11(a). At a crack length of 1.32 mm, the solution for ΔK was 8.95 MPa$\sqrt{\text{m}}$, giving a crack growth rate of 0.14 µm/cycle. Assuming that each striation corresponds to one cycle, the crack growth rate was 0.52 µm/cycle at this location. The fracture mechanics analysis assumes that the crack front is semi-circular, emanating from a single point and with an increasing crack front length. The crack front of specimen X32, however, was crescent shaped, with a decreasing crack front length with increasing crack depth. This gives a higher ΔK for the same crack length [174], and may explain the higher observed crack growth rate.

As mentioned in Section 2.2, the fatigue life can be thought to consist of initiation and propagation life according to Eq. 2.27. In this case, initiation life is assumed to end when the crack is 0.8 mm deep. By calculating the fatigue propagation life N_p for all stress levels used, the initiation life can be determined using N_f from the SN curves. A plot for R=-1 loading is shown in Figure 5.25. The propagation life can be seen to have little influence on smooth specimens and rough specimens with lives above 10^5 cycles. Rough specimens with shorter lives have crack propagation lives on the same order of initiation lives, with three specimens having shorter initiation lives than propagation lives.

It was mentioned in Section 3.4.1 that the curvature estimation algorithm would sometimes yield incorrect values for notch tip radii. Some of the scatter in Figure 5.23(b) can be attributed to these errors in radius estimates, thus in the

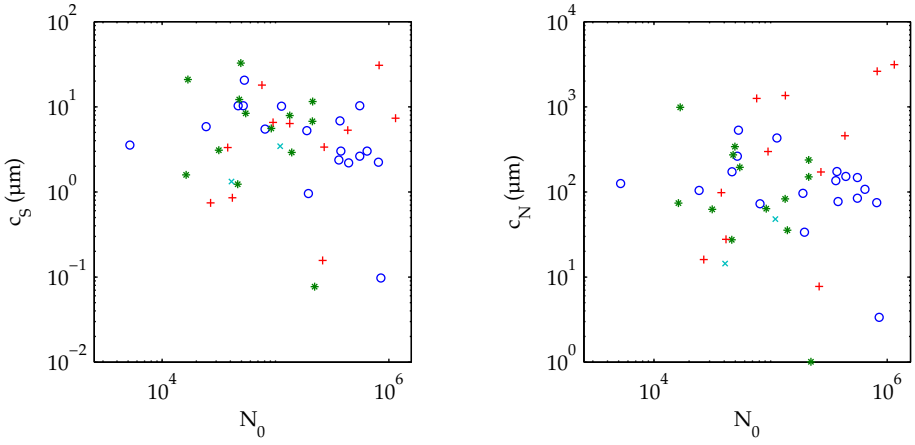

(a) Siebel and Stieler (b) Neuber

Figure 5.26: Same plot as Figure 5.23, where initiation life has been used instead of N_f.

following an approximation of the radius is used [34]:

$$\rho = \frac{2}{\chi}. \tag{5.2}$$

Figure 5.26 shows the calculated c_S and c_N when using initiation life and Eq. 5.2 for ρ in Eq. 1.21. It can be seen that the scatter is reduced, however, a variation by a factor of ten is still observed, disregarding the three outliers. From these results it can be concluded that a Neuber type approach cannot readily be applied to these types of notches. Figure 5.27 shows predictions of initiation life using Siebel and Stieler's expression for K_f for the extruded material. The median of the observed c_S was used in this case, which clearly cannot be used in fatigue life prediction for the finite life regime.

There is some uncertainty with regard to the crack growth rate curve used in the estimates of N_0. No crack growth data was available for the two load ratios used here, and closure measurements have not been made. A semi-elliptic, sigmoidal crack growth was assumed in the K estimates, which from Figure 5.9 can be seen to be the case only for fatigue lives below 10^5. This will not have much influence on the calculation of N_0, however, since for higher fatigue lives, the initiation life dominates over propagation life.

5.4.2 Critical distance approach

The empirical K_f expressions reviewed in the preceding section are sensitive to variations in the values of ρ and χ. These values in themselves are highly

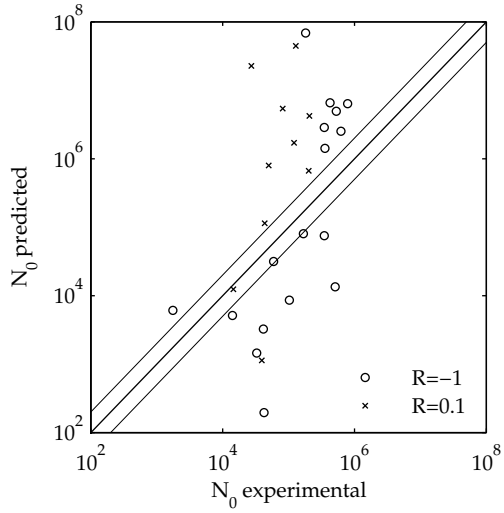

Figure 5.27: Fatigue initiation life prediction for the extruded material, using the median of the observed c_N parameter for calculation of K_f.

Table 5.4: Calculation of critical distances.

Test series	$\Delta\sigma_0$ (MPa)	ΔK_{th} (MPa$\sqrt{m}$)	a_0 (µm)
E R=-1	375	2.7	16
E R=0.1	302	2.9	29
F R=-1	326	2.7	21
F R=0.1	268	2.9	37

sensitive with regard to measurement errors and numerical algorithms. Instead of assuming a sub-surface distribution based on surface gradients, a better approach would be to use these results directly from FEA. Furthermore, predictions are made for the fatigue limit, in this case defined as N_f =10^6.

The fatigue thresholds have been estimated from the crack growth data given in Figure 5.24. The fatigue limit stress ranges were calculated from the 50% fit lines at N=10^6 for each test series. The El Haddad parameter was then found using Eq. 2.33 as shown in Table 5.4. Results from the point method approach are shown in Figure 5.28, where the critical stress range has been evaluated in a point located $r = a_0/2$ ahead of the notch root from the elastic FEA. The stress ranges below the smooth specimen fatigue limits have been highlighted in green, indicating that this is a "safe" region where cracks will not propagate to failure. It can be seen that this holds for most specimens, with the exception of two extruded and two forged specimens in R=-1 loading.

A second method used in the critical distance concept is to average the stress ranges ahead of the notches over a distance corresponding to $2a_0$. It is seen

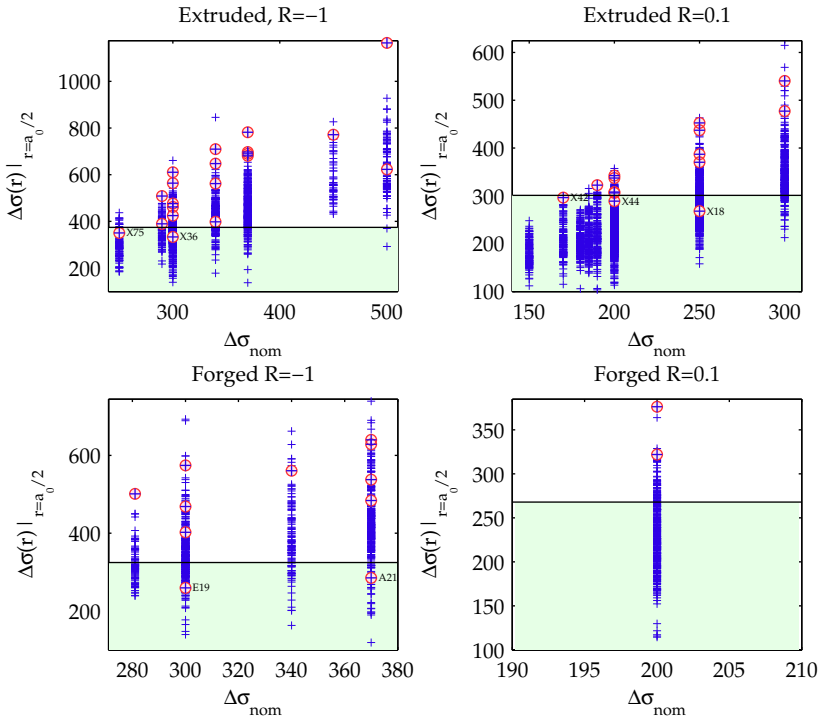

Figure 5.28: Stress ranges in the critical points ahead of all notches. Notches where fatigue cracks originated are marked by red circles.

from Figure 5.29 on the next page that the results are very similar to the point evaluation method. Apart from some small variations in the extruded results, a trend was observed that the line method was less consistent in identifying the notch where failure occurred. This is best observed for forged, R=-1 loading in Figure 5.29.

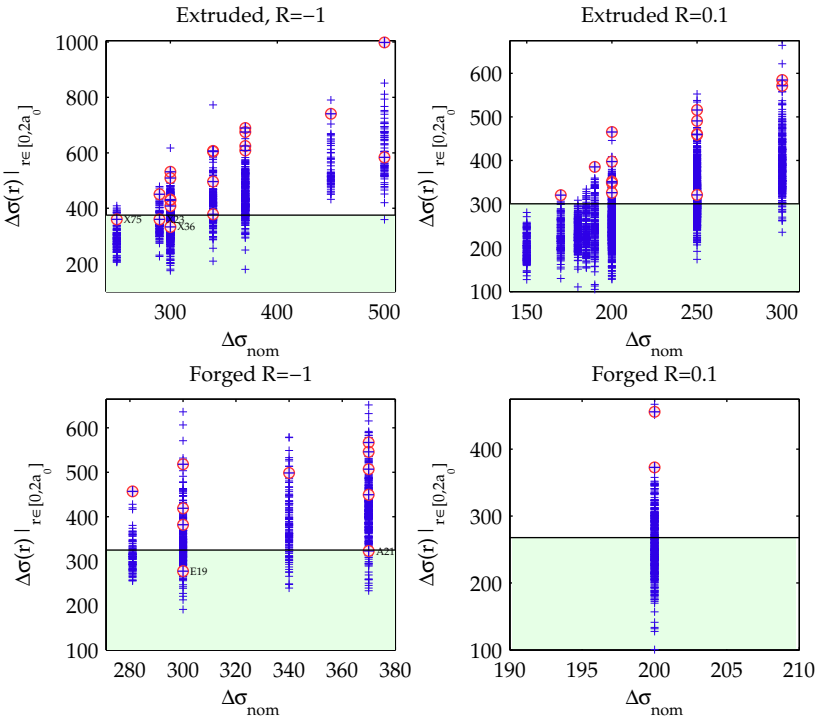

Figure 5.29: Average stress ranges ahead of all notches. Notches where fatigue cracks originated are marked by red circles.

Chapter 6

Summary

Engineering design is today heavily based on numerical simulations. This is especially true in the automotive industry, where development time is crucial for competitiveness. Software suites are today available that model all aspects of vehicle simulation, and play a crucial role in reducing the time and money spent in design iterations. Fatigue life prediction is often the most critical step in such analyses, owing to the fact that little information is usually available to the designer about the fatigue performance of surface finishes stemming from the various machining processes.

A series of tests on smooth and rough cylindrical specimens have been done. The material is a 6082 aluminium alloy used in a forged car suspension arm. Test specimens were machined from cut-outs of the suspension arms, as well as from the extruded billets used as raw material for the forging. The suspension arm components are quenched from the elevated temperature forging operations and then age-hardened to produce a T5 temper, while the extruded billets were given a T6 heat treatment for the purpose of comparing the influence of the forging process on material strength. The T6 condition represents the optimum strength for this material, thus providing a benchmark for optimizing manufacturing processes.

The forged material was separated in three batches: standard, prototype and over-aged standard batch. The prototype batch was manufactured manually and given a T6 heat treatment. No significant difference was found between the three batches for R=-1 fatigue loading, while the extruded billet material showed slightly better fatigue properties. The cyclic stress-strain response was found to be the same for both the forged and extruded material, even though the monotonic response was quite different, with the extruded material showing higher strength.

Surface roughness was created using emery papers of various coarseness. The specimens were rotated while a stationary arm was pressed against the surface, creating a series of circumferential grooves. Topography measurements were made using a white light interferometry (WLI) microscope along the length

of the specimens at four different angular positions. The axial symmetry of the surface roughness was found to be good when comparing these for each specimen. The WLI measurements showed some misreadings and artifacts around certain geometrical features as verified by scanning electron microscope (SEM). The artifacts were easy to identify in most cases, and were removed manually by linearly interpolating between the nearest correct measurements.

Residual stresses were measured using X-rays for the machined, polished and roughened surfaces. Compressive residual stresses of around 150 MPa were found in all cases, except from one specimen that showed anomalous surface grooves resembling a corrosion attack. No significant change in residual stresses could be observed after cyclic loading. The residual stresses were average values over 1 mm in the axial direction, and it is likely that the stresses vary within this region depending on the topography. Attempts were made to measure residual stresses in further detail using synchrotron X-rays and a beam/detector setup capable of 12.5 µm spatial resolution. Stress variations on this scale could be identified, but the magnitude of stresses could not be determined due to the apparently failed assumption that stresses did not vary considerably around the circumference.

The measurements from WLI were converted to 2D profiles and used in axi-symmetric models of the specimens. A cubic interpolation was used for the FE model in order to avoid stress singularities. Linear elastic and nonlinear, elastic-plastic material models were used. A bilinear, kinematic hardening model was used to approximate the cyclic stress-strain response of material. A nonlinear analysis with an assumed residual stress distribution was also done. In all analyses, a clear trend was observed: At a certain distance from the notch root, the notches in which fatigue failure initiated had a higher local stress field than other notches. Some exceptions were observed where the subsurface stress solution for the initiation notch was not among the highest. These specimens showed a very localized initiation zone, indicating that the notch played a lesser role in the initiation process. In one case, the failure appeared to stem from the de-bonding of a large grain, while in other cases, evidence was found that large particles had been present in the initiation zone. On a few specimens, non-propagating cracks could be observed with SEM. The images showed that hard particles in the notch root would de-bond and interact with the initiation crack path. It is likely that when larger clusters of such particles appear in a notch root, initiation will be accelerated beyond what would be predicted by the notch geometry alone.

Attempts were made at fatigue life prediction following a traditional notch approach commonly used in larger geometries. The classical Neuber correction for notch plasticity was used, along with a generalized Neuber approach, according to Hoffmann and Seeger, accounting for notch constraint. The generalized method showed improved stress and strain estimates over the classical method when comparing the solutions to elastic-plastic FEA. For fatigue loading with mean stress, the classical Neuber approach appeared to be more accurate with regard to stress solution, however, the maximum and minimum stresses as well

as the strain range were less accurate. The generalized method was more accurate when comparing these results based on the Smith-Watson-Topper damage parameter.

Classical formulations for the notch influence (q and K_f) were evaluated, however these were found to be unsuitable. These methods are strictly only valid for initiation problems, where analytically derived stress and strain conditions in the fatigue initiation zone can be used in conjunction with empirical formulations for the notch sensitivity and the stress field. Adding to this, the gradient stress solution and estimates of notch root radii were found to be quite unstable, depending on mesh and numerical algorithms respectively. The initiation life was not observed directly, but estimated based on a long crack growth rate relation for the given material. The minimum initial crack length that could be used with this approach was 0.8 mm, which means that the crack is well beyond the notch stress field. The initiation life predictions are based on the assumption that incipient cracks grow within the notch stress field, which in this case is on the order of 10 µm. Growth rates of such small cracks have not been assessed in this work, thus there is a 10 µm-0.8 mm region ahead of the notch where little is known about the actual crack growth rate. To improve initiation life prediction using a notch approach, it is suggested that small crack growth is investigated to improve the crack growth life predictions. The size of the notch stress fields are on the same order of magnitude as the grain structure, thus microstructural fracture mechanics must be considered.

The finite element analysis used to determine notch influence was based on linear elastic, isotropic material behavior. This is clearly not the case at the scale of the microscopic notches encountered, thus a considerable uncertainty exists with regard to the validity of stress solutions. Evaluation of stress gradients at the surface were found to be mesh dependent unless a very fine element mesh was used. The gradient solution, along with estimated curvatures in the notch roots, are used for notch sensitivity calculations, however, the accuracy required from the surface measurements seems to be inadequate in defining these parameters in a stable manner. This may have contributed to the very large scatter observed for geometry-based notch sensitivity parameters. The observed notch sensitivity from experiments (q) shows less scatter, and an increasing trend with increasing fatigue lives. This suggests that a fatigue notch factor derived directly from $q(N_f)$ may improve predictions. This will, however, limit the applicability of the approach to surface profiles similar to the ones tested, without being able to determine geometric influences. The previously mentioned problem with regard to initiation life and short crack growth will not be resolved, resulting in a q that depends on specimen geometry.

Two critical distance concepts were applied, assuming the fatigue limit to be 10^6. Using an estimate of the long crack fatigue threshold, the condition for failure below $N = 10^6$ could be evaluated for all notches. Critical stress ranges in all failed notches were, with few exceptions, found to be above the plain specimen fatigue limit. Run-out specimens were correctly predicted, with all notch stresses below this limit. The method appears to be very robust,

considering that the long crack fatigue threshold was not directly measured, but estimated based on 6061 and 6082 crack growth data for other load ratios.

Main findings

- Extruded 6082-T6 material has better fatigue properties than an equivalent forged 6082-T5 material.
- The temper of the forged material (T5, T6, T7) does not influence high cycle fatigue life at R=-1.
- All of the mean stress corrections investigated in this work showed quite high scatter when applied to the R=-1 and R=0.1 results for forged and extruded material separately. The Morrow mean stress correction and the Findley multiaxial damage criterion showed the least scatter.
- A white light interferometry microscope provides fast and accurate measurements of the surface topography, although some artifacts were found for certain surface geometries. These must be removed in an automated fashion, either by using a search algorithm or by signal processing.
- Finite element analysis (FEA) of the rough surfaces showed a clear trend, that initiation would occur in grooves where stresses 10 µm below the surface were higher than for other grooves. A few deviations from this was observed, and these were ascribed to inherent material weaknesses located in shallow grooves.
- Elastic-plastic FEA was compared to the classical Neuber rule, as well as a generalized formulation according to Hoffmann and Seeger (HS). Neuber's rule was found to give non-conservative stress results compared to FEA, while HS showed improved results on the conservative side. In terms of strain, Neuber is very conservative, while HS gives similar results as the FEA.
- The Neuber approaches failed to predict initiation life. The initiation life was defined as $N_0 = N_f - N_p$, where N_p is the estimated propagation life for a 0.8 mm deep, semi-circular crack.
- The surface grooves or notches were around 40 µm deep, which is on the same scale as the microstructure. Initiation life prediction based on notch stress fields is problematic in this regard, due to the breakdown of continuum mechanics analyses and also the difficulty in monitoring initiation life experimentally.
- Some specimens were investigated in SEM at different intervals during testing, however, no incipient cracks could be found at critical locations. Sectioning of a runout specimen after testing revealed 5 µm-8 µm long incipient cracks under a light microscope.
- Different initiation behavior was observed for specimens with fatigue lives above and below 10^5 cycles. A wide, circumferential initiation zone was found in specimens with $N_f \lesssim 10^5$, and was attributed to short initiation life. Local initiation zones were found at longer lives, which may have

been caused by local notch severities or inherent material weaknesses in notch stress fields.

- The short crack parameter a_0 according to El Haddad et al. [123] was found to be in the range 19 µm-37 µm. This can be considered an estimate of when linear elastic fracture mechanics is valid for a growing crack.
- The fatigue limit, defined at 10^6 cycles, could be predicted for the rough surfaces using a critical distance approach based on a_0.

Chapter 7

Further work

The emphasis in this work has been to establish new measurement and testing procedures for numerical simulation of surface roughness. Some classical and more recent methods were used for fatigue life assessment based on linear elastic analysis. A theory based on non-propagating cracks was found to give adequate predictions of the fatigue limit of the rough surfaces. The concept could be integrated with current software for virtual prototyping, or written as a standalone post-processor to component level FE simulations. Processing times are short due to the foundation on linear elastic analyses, thus making the approach suitable for in-line manufacturing inspection.

A natural extension of this work would be to model the microstructure numerically. The orientation of grains can either be determined or estimated in order to study the grain orientation influence. Three dimensional analysis is required to model the constraint and the anisotropic response of single grains. This would require smaller test specimens than used here, and would pose some challenges with regard to specimen manufacturing and testing.

Some of the rough specimens failed from inherent material defects, in areas with relatively shallow notches. In order to predict these failures, a statistical description of material defects is needed. The surface roughness may also be described with regard to critical distance stresses according to a Weibull or Gumbel type distribution, in order to predict the occurrence of more detrimental grooves outside of the confined area of measurement. Paired with a distribution of inherent defects, a lower fatigue limit for a given surface can be found by defining a desired probability of failure.

Fatigue testing has not been done on the forged component surface. The actual forged surface has three distinct surface types: one stemming from the forging tools, one from a cutting/deburring process and one from milling. The critical surface with regard to fatigue has been recognized as the deburred area, running around the midst of the component. While the artificially created surface roughness studied in this work resembles the deburred surface roughness, residual stresses and near-surface microstructure are most likely very different. These

characteristics must be studied with regard to initiation life, and will require specific fatigue tests on the actual component surface to verify mathematical models.

Appendices

A Fatigue testing

A1 Specimens

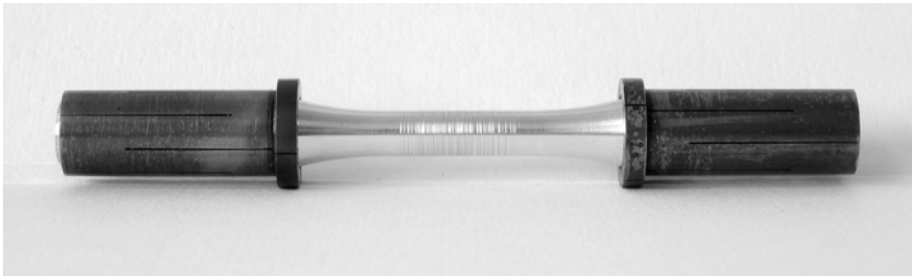

(a) Specimen with steel bushings.

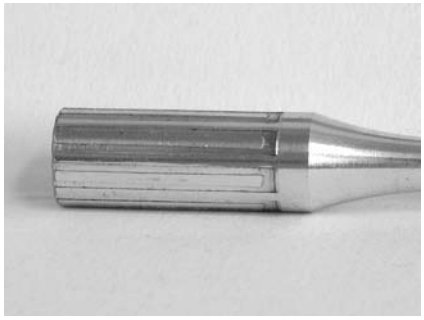

(b) Deformed grip section.

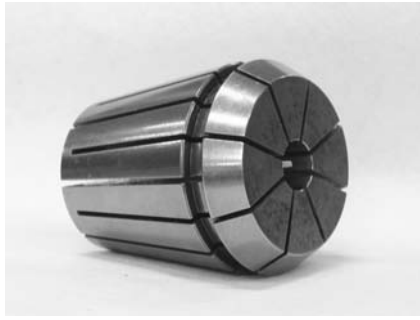

(c) Collet chuck.

Figure A-1: Type A specimen geometry (a) and deformed grip section in a type B specimen geometry (b). The markings stem from the collet (c) used for clamping in the reversed fatigue tests.

A2 Fatigue data

Fatigue data in tabular form is included in this section. Details on the different material designations are given in Section 3.1.1. The codes used to describe the validity of tests are as follows:

0: Valid test

1: Test terminated, no failure

2: Specimen failed in the grip section

3: Specimen failed in the notch fillet

Table A-1: Fatigue data for forged material: R=0.1 load control.

Specimen	Type	$\Delta\sigma$	N	Runout
E21	F(I)	350	20599	0
B18	F(I)	350	26493	0
F20	F(I)	350	28930	0
B24	F(I)	330	195340	0
F15	F(I)	310	196930	0
B17	F(I)	310	431976	0
B16	F(I)	300	428045	0
E16	F(I)	300	490242	0
E6	F_R(I)	281	105984	0
E14	F(I)	281	119292	0
E23	F(I)	281	234979	0
B22	F(I)	281	245968	0
A19	F(I)	281	256972	0
E17	F(I)	281	267268	0
E25	F(I)	281	296206	0
B25	F(I)	281	1645858	0
E15	F(I)	281	5734391	1

Table A-2: Fatigue data for extruded material: R=0.1 load control.

Specimen	Type	$\Delta\sigma$	N	Runout
X74	E(II)	330	80531	0
X2	E(II)	330	98581	0
F41	E(I)	330	131100	3
F44	E(I)	330	138738	0
F37	E(I)	330	282545	0
F28	E(I)	330	318089	0
F25	E(I)	330	364521	0
F27	E(I)	310	55761	3
Y101	E(III)	310	71046	0
X34	E(II)	310	118056	2
F39	E(I)	310	276562	0
X35	E(II)	310	379136	2
Y102	E(III)	310	454803	0
F47	E(I)	310	794739	0
F40	E(I)	310	3777090	0
X5	E(II)	300	137092	0
X31	E(II)	300	297663	0
F22s	E(I)	300	718942	0
F29	E(I)	300	2322558	2
F24	E(I)	300	3804782	0
F30	E(I)	300	5355467	0

Table A-3: Fatigue data for extruded material: R=-1 load control.

Specimen	Type	$\Delta\sigma$	N	Runout
X59	E(II)	490	67326	0
X62	E(II)	490	87760	0
X57	E(II)	490	98912	0
X61	E(II)	450	110290	0
X66	E(II)	450	168461	0
X64	E(II)	403	274043	0
X67	E(II)	403	286741	0
X51	E(II)	403	826800	2
X70	E(II)	380	437307	0
X65	E(II)	380	528105	0
X53	E(II)	380	830209	0
X63	E(II)	380	943131	2
X58	E(II)	380	981632	0
X52	E(II)	370	889868	2
X56	E(II)	370	957410	2
X68	E(II)	370	1051192	2
X54	E(II)	370	1085644	0
X60	E(II)	370	1333733	2
X55	E(II)	370	1850365	0

Table A-4: Fatigue data for forged material: R=-1 load control.

Specimen	Type	$\Delta\sigma$	N	Runout
F9	F_R(I)	490	21167	0
E8	F_R(I)	490	32518	0
B9	F_R(I)	403	122904	0
E104	F_P(I)	403	139840	0
A104	F_P(I)	403	154566	0
A101	F_P(I)	403	163764	0
F8	F_R(I)	403	167471	0
B6	F_R(I)	350	292891	0
B104	F_P(I)	350	292906	2
B101	F_P(I)	350	491536	0
B103	F_P(I)	350	550795	0
E7	F_R(I)	350	654335	0
F103	F_P(I)	330	286854	2
B7	F_R(I)	330	394602	0
A7	F_R(I)	330	694689	0
B102	F_P(I)	330	898132	2
F7	F_R(I)	330	1054973	0
F102	F_P(I)	330	1828781	0
F104	F_P(I)	330	2229147	0
A8	F_R(I)	310	1051023	0
E9	F_R(I)	310	1223051	2
A6	F_R(I)	310	1997123	2
F6	F_R(I)	250	4880775	2

Table A-5: Fatigue data for extruded material: strain control.

					Half-life		
Name	Batch	$\Delta\varepsilon$	N_f	f (Hz)	$\Delta\sigma$ (MPa)	E (GPa)	$\Delta\varepsilon^P$
Y25	III	1.50	234	0.13	696	69.2	0.4876
Y24	III	1.50	236	0.13	702	71.5	0.5067
Y22	III	1.30	257	0.15	743	73.1	0.2776
Y15	III	1.20	277	0.17	715	74.1	0.2260
Y17	III	1.30	355	0.15	704	70.7	0.2980
Y20	III	1.20	409	0.17	707	72.4	0.2177
Y23	III	1.20	592	0.17	708	71.6	0.2069
YX33	II	1.30	705	0.15	744	70.9	0.2496
Y19	III	1.10	706	0.18	704	72.8	0.1267
Y21	III	1.10	937	0.18	736	73.4	0.0932
Y18	III	1.10	1078	0.18	728	73.6	0.1028
Y10	III	1.00	2781	0.25	702	73.8	0.0411
Y11	III	1.00	3515	0.20	686	73.5	0.0607
Y9	III	1.00	3620	0.20	707	73.8	0.0379
Y16	III	0.80	8307	0.25	581	73.8	0.0096
Y12	III	0.80	10269	0.20	583	74.1	0.0112
Y14	III	0.80	14023	0.25	578	73.8	0.0138
YX8	II	0.80	15332	0.25	594	74.5	0.0087
Y13	III	0.80	16806	0.20	572	72.9	0.0100
X71	II	0.80	20149	0.25	595	75.4	0.0080

Table A-6: Fatigue data for the forged F(I) material. Strain controlled cycling was used for $N < 43200$. For longer lives, testing was switched to load control with a frequency of 10 Hz. Testing was done by Westmoreland Mechanical Testing and Research Ltd.

				Half-life		
Name	$\Delta\varepsilon$	N_f	f (Hz)	$\Delta\sigma$ (MPa)	E (GPa)	$\Delta\varepsilon^P$
A34	1.60	53	0.50	754	70.2	0.5560
E67	1.30	86	0.50	748	75.2	0.4010
A41	1.30	204	0.50	734	70.6	0.2800
A65	1.30	293	0.50	749	70.0	0.2490
E58	1.30	350	0.50	735	69.4	0.2640
A39	1.30	769	0.50	732	67.9	0.2280
E36	1.00	238	0.50	721	76.6	0.0970
A61	1.00	1294	0.50	703	71.9	0.0290
E50	1.00	1755	0.50	700	72.5	0.0500
A53	1.00	2084	0.50	702	72.2	0.0420
E48	1.00	5335	0.50	695	71.1	0.0430
A56	0.70	25328	0.50	506	72.8	0.0060
E34	0.70	36356	0.50	514	73.8	0.0040
E62	0.70	44702	0.50 - 10	504	73.6	0.0000
A68	0.70	46716	0.50 - 10	524	74.8	0.0010
A63	0.70	47714	0.50 - 10	513	73.3	0.0010
E60	0.50	157413	0.50 - 10	361	72.6	0.0000
A37	0.50	177445	0.50 - 10	363	73.5	0.0030
A58	0.50	297713	0.50 - 10	353	74.3	0.0000
A44	0.50	314268	0.50 - 10	365	74.1	0.0000
E65	0.50	781393	0.50 - 10	381	76.8	0.0010
E43	0.30	10000000	0.50 - 10	215	71.9	0.0100
A51	0.30	10000000	0.50 - 10	215	73.7	0.0000

A3 Regression analysis

Fatigue life is usually assumed to follow a log-normal distribution. The cumulative distribution function (CDF) and probability density function (PDF) can then be used to establish the likelihood function of the two different observations; failed and not failed:

$$L = \prod_{i=1}^{n} \left[\frac{\phi(z_i)}{s(\Delta\sigma_i)N_i} \right]^{\delta_i} [1 - \Phi(z_i)]^{1-\delta_i}, \tag{A-1}$$

where i is specimen number, Φ and ϕ are the CDF and PDF respectively, and δ_i equals 1 if specimen i failed, and 0 if it survived. The distribution functions are:

$$\Phi = \frac{1}{2}\text{erf}^{-1}\left(\frac{-z_i}{\sqrt{2}}\right) \tag{A-2}$$

$$\phi = \exp\left(\frac{-z_i^2}{2\sqrt{2\pi}s(\Delta\sigma_i)}\right), \tag{A-3}$$

where the standard normal variable is given by:

$$z_i = \frac{\ln(N_i) - \mu(\Delta\sigma_i)}{s(\Delta\sigma_i)}, \tag{A-4}$$

and erf^{-1} is the complimentary error function:

$$\text{erf}^{-1}(x) = \frac{2}{\sqrt{2\pi}} \int_x^\infty e^{-t^2} dt. \tag{A-5}$$

Considering here a stress based life analysis, the fatigue life N is modeled as a random variable with mean μ as a function of stress range $\Delta\sigma$. The analysis for strain life fatigue is more complicated, as it involves joint effects of scatter in material stress-strain relations and fatigue parameters Zhao [175], Kandarpa et al. [176], Williams et al. [177, see e.g.]. Taking the logarithm of Eq. 1.1 and rearranging, leads to:

$$\mu(\Delta\sigma_i) = \text{E}[\ln(N_i)] = \ln\left[\frac{1}{2}\exp\left\{\ln\left(\frac{\Delta\sigma_i}{2\sigma_\text{f}'}\right)/b\right\}\right] \tag{A-6}$$

The standard deviation s for $\ln(N_i)$ is modeled as a function of stress level as:

$$s(\Delta\sigma_i) = \sqrt{\text{Var}(\ln(N_i))} = \exp\left(\beta_1 + \beta_2 \ln(\Delta\sigma_i)\right), \tag{A-7}$$

where $\beta_2 = 0$ results in a constant standard deviation. Pascual and Meeker's [48] fatigue life equation (Eq. 1.12 on page 10) can be restated with the nomenclature used here:

$$\mu(\Delta\sigma_i) = \alpha_1 + \alpha_2 \ln(\Delta\sigma_i - \gamma). \tag{A-8}$$

Numerical solution

The parameters are found by maximizing the likelihood function numerically. This can prove to be very difficult unless very good starting values for the iteration are given. A least squares regression of the "failed" observations can be used to find the starting values. To improve convergence, a reparametrization of z is used:

$$z_i = \begin{cases} k_1 + \dfrac{z_i - k_1}{1 + (z_i - k_1)/k_{1m}} & \text{for } z_i > k_1 \\ -k_2 - \dfrac{z_i + k_2}{-1 + (z_i + k_2)/k_{2m}} & \text{for } z_i < -k_2, \end{cases} \tag{A-9}$$

where the k parameters are adjusted to avoid infinite values of L and divide by zero problems. Details can be found in Ref. [178, p. 394]. The maximum likelihood estimators are found by maximizing $\ln(L)$, which is easier to manipulate mathematically than L.

Confidence levels for a given model parameter β_0 are found by evaluating the profile likelihood:

$$R(\beta_0) = \frac{L(\bar{\boldsymbol{\beta}}, \beta_0)}{L(\hat{\boldsymbol{\beta}})}, \tag{A-10}$$

where $\hat{\boldsymbol{\beta}}$ is a vector containing the ML estimates and $\bar{\boldsymbol{\beta}}$ are the ML estimates with β_0 removed. The profile likelihood will take values from 0 to 1 indicating the likelihood of the given parameter value β_0. A confidence interval $(1 - \alpha)$ for β_0 can be found using the chi-squared distribution with one degree of freedom:

$$R(\beta_0) \geq \exp\left[-\frac{\chi^2_{(1;1-\alpha)}}{2} \right]. \tag{A-11}$$

In fitting the various models to data, plots of the residuals and probability plots for the residuals are necessary in order to assess the goodness of fit. The residuals are given by

$$\epsilon_i = \ln(N_i) - \mu(\hat{\boldsymbol{\beta}}, \Delta\sigma_i). \tag{A-12}$$

Standardized residuals should be used, since the standard deviation can vary for different stress levels:

$$\bar{\epsilon}_i = \frac{\epsilon_i}{s(\hat{\boldsymbol{\beta}}, \Delta\sigma_i)} \tag{A-13}$$

Figure A-2 shows Eq. A-11 evaluated for β_1 and γ in the forged SN data. The indicated values are the lower β_0 values satisfying Eq. A-11 using $\alpha = 0.05$, i.e. a 95% confidence interval.

If a lognormal distribution is assumed, the residuals should form a straight line in a normal probability plot, and plots of residuals versus observed stress and mean estimate should appear patternless. In Figure A-3, residuals for the model in Figure 3.14 indicate that the model assumptions are reasonable, although the runout at $N = 10^7$ clearly stands out as it is far from the mean estimate μ.

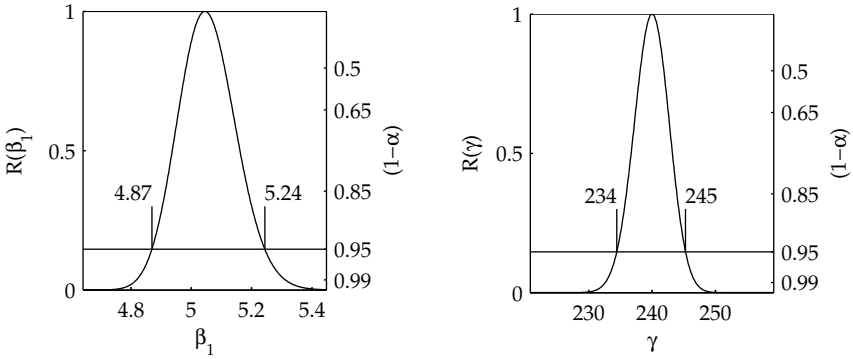

Figure A-2: 95% confidence interval for two of the parameters in Figure 3.14.

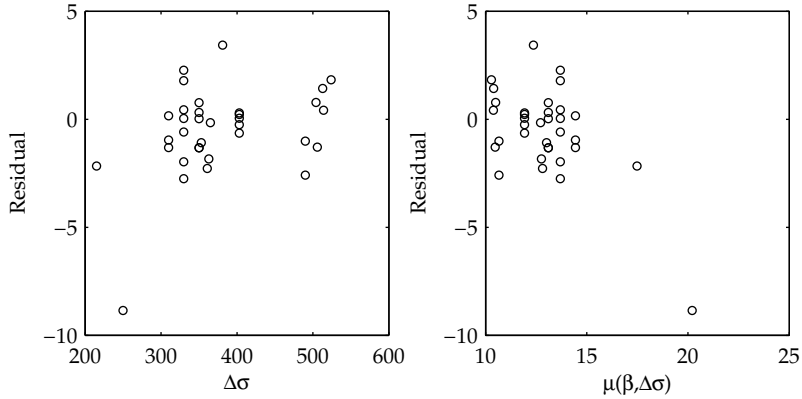

(a) Standardized residuals for stress range and fatigue life, ln(N).

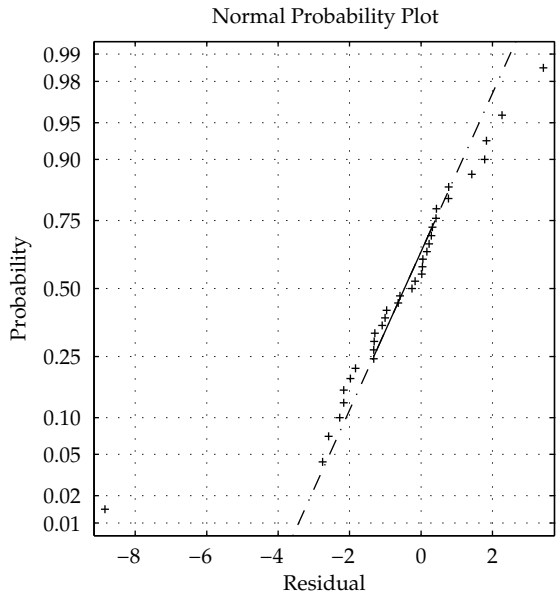

(b) Normal probability plot of standardized residuals.

Figure A-3: Plots of residuals for the fatigue limit model.

B Matlab code

General information and FEA results for each specimen are stored in a MATLAB structure array and stored as a binary file. This section provides an overview of algorithms for FEA, leaving out the ones pertaining to WLI data processing. The structure is arranged as follows:

specimen (struct)
- ⊢ initiation location (array)
- ⊢ SN data (array)
- ⊢ clock{i} (cell) where $i = 1, 2, 3, 4$
  - ⊢ WLI profile (array)
  - ⊢ radius data (array)
  - ⊢ surface parameters (array)
  - ⊢ dominant valleys (array)
  - ⊢ stress/strain solutions ahead of valleys (struct)
    - ⊢ σ_z (array)
    - ⊢ ε_z (array)
    - ⋮
    - $\sigma_r, \sigma_\phi, \tau_{rz}, \varepsilon_r, \varepsilon_\phi, \gamma_{rz}$ (arrays)
  - ⊢ surface σ_z (array)
  - ⊢ surface σ_1 (array)
  - ⊢ surface χ (array)

The initiation location array contains the angular and axial position of where the crack initiated, and the SN data contains the stress range and number of cycles to failure for the test. For each clock value, a cell array holds the measured WLI profile and additional information such as the notch root radius of dominant valleys, the position of these valleys and geometric surface parameters such as R_a and R_z. All smaller arrays, i.e. all information except profile and FE solutions, are also stored in a MYSQL database for fast retrieval.

B1 Analysis programs

This section gives an outline of the functions called by the main program, Algorithm 1 on page 85. The FEMLAB solver is called within the function `run_fea` once the geometry has been created. This program is outlined in Algorithm 2. The mesh iteration on Line 2-5 ensures that the number of DOF are kept below a certain level: By adjusting the element growth rate for the whole model, the total number of DOF is reduced without affecting the resolution of the surface boundary. A mesh optimizer `meshoptim` is used at the end of the iteration, since FEMLAB by default produces low quality triangles. The nonlinear solution for R=-1 loading and applied residual stress would not generally converge, so the solution at Line 22 was only obtained for R=0.1 loading.

Input: geometry, load range and solver parameters
Output: FE displacement solution contained in a structure array

```
1  make initial mesh with default parameters;
2  while number of vertices > threshold do
3  |  increase element growth rate;
4  |  make mesh;
5  end
6  optimize mesh using FEMLAB's meshoptim;
7  if residual stress analysis then
8  |  apply residual stress as a function of the geometry;
9  |  set as initial value for subsequent analyses;
10 end
11 if linear elastic then
12 |  define linear material model;
13 |  apply unit load to upper boundary;
14 |  call linear FEMLAB solver;
15 else
16 |  define elastic-plastic material model;
17 |  apply displacement to boundary corresponding to max load;
18 |  call parametric FEMLAB solver;
19 |  if R=0.1 or residual stress analysis then
20 |  |  use the solution from Line 18 as initial solution;
21 |  |  prescribe unloading to R$\sigma_{max}$;
22 |  |  call parametric FEMLAB solver;
23 |  end
24 end
```

Algorithm 2: `run_fea`. This function sets up the boundary conditions and solution parameters used by the FEMLAB functions `femlin` and `femnlin`.

Algorithm 3 lists the post-processing program, invoked from Algorithm 1. The rain-flow analysis used by `postproc` is based on the `dat2tp` function from the WAFO toolbox [179]. The function `postinterp` calculates stress and strain values for arbitrary points by interpolation from gauss point solutions, while `posteval` uses an extrapolation from gauss points to find nodal solutions.

Algorithm 4 describes the function that assembles the solutions for all parts into a complete solution structure for a given surface profile. The parts overlap by a certain amount to avoid end-constraint effects, so the solution for each part is retrieved from half of the overlapped region as indicated on Line 7.

Input: Structure array with displacements for one part
Output: Solutions of stress and strain at the surface boundary and ahead of notches

```
find location of critical valleys (V1) by rain-flow analysis of the profile;
V1z ← log-distribution of points ahead of V1;
forall V1z do
    call FEMLAB's postinterp to calculate stress and strain
end
call FEMLAB's posteval to calculate stress and strain at surface nodes;
find critical valleys (V2) by rain-flow analysis of the surface stress solution;
V2z ← log-distribution of points ahead of V2;
forall V2z do
    call FEMLAB's postinterp to calculate stress and strain
end
```

Algorithm 3: `postproc`. Function for calculating stresses and strains from a FE displacement solution.

Input: Stress and strain solutions for all parts
Output: Stress and strain solutions for a complete profile

```
solution ← [];
forall parts do
    partsol ← solution data for this part;
    startpos(i) ← start position of this part;
    endpos(i) ← end position of this part;
    startpos(i + 1) ← start position of next part;
    split_location(i) ← [endpos(i)+startpos(i + 1)]/2;
    adjust split_location to avoid valleys and peaks;
    solution ←(append) partsol ∈ split_location[i, i + 1];
end
```

Algorithm 4: `assemble`. This function assembles stress and strain solutions from single parts.

C FEA results

C1 Mesh variations

Mesh density was adjusted using a curvature factor that controlled the mesh density at the surface boundary. The mesh size is determined by multiplying the curvature factor with the local radius of curvature. Figure A-4 shows linear elastic solutions for Mises equivalent stress (σ^e) and stress gradient (χ Eq. 4.21) at a sharp and a blunt notch in a 3 mm long subsection of a specimen geometry. The left column shows the influence of the curvature factor, and the right column shows the same data plotted against degrees of freedom for the whole mesh. Quadratic and a cubic lagrange shape functions were used for each mesh case, shown as full and dashed lines respectively. All values are normalized with respect to the cubic mesh solution, having 460 kDOF (thousand DOF).

Quadratic lagrange functions and a curvature factor of 0.12 was used for the linear analyses in order to resolve the stress gradient. An element growth factor of 1.2 was used in the majority of cases, though it would be incrementally adjusted upwards to 1.3 if the number of mesh vertices exceeded 85,000. This would correspond to about 700 kDOF, which was the limit for what could be solved without resorting to slow disk cache. It can be seen from Figure A-4 that the solutions for Mises stress stabilizes for both the short and blunt notch at a curvature factor of 0.3. The stress gradient solutions still show some mesh dependent variations for the quadratic mesh, while the cubic solutions appear to converge. (See Section 4.2.3 for an explanation). The quadratic solution is more effective than the cubic solution when comparing the two based on DOF. The solution times for these analyses ranged from 9 to 50 s for this geometry section, which may not sound as much, but it adds up when considering this is one out of four profile sections, and there are four such profiles for each specimen. Post-processing typically takes the same amount of time as solving, thus the corresponding total solution times for the range of curvature factors used here would be about 5 and 30 min.

C2 Analysis using ABAQUS

ABAQUS was initially intended for finite element analysis, since it was available on an SGI Origin supercomputer, and also due to its more robust non-linear solver. FEMLAB was used to generate ABAQUS input-files for full profile geometries with meshes. A non-linear hardening model was used according to Lemaitre and Chaboche, where the Mises yield surface is described as:

$$f(\boldsymbol{\sigma} - \boldsymbol{\alpha}) = \sqrt{\frac{3}{2}(\boldsymbol{S} - \boldsymbol{\alpha}') : (\boldsymbol{S} - \boldsymbol{\alpha}')}. \tag{A-14}$$

$f(\boldsymbol{\sigma} - \boldsymbol{\alpha}) = \sigma_0$ is the size of the yield surface, $\boldsymbol{\alpha}$ is the backstress tensor and $\boldsymbol{S}$ and $\boldsymbol{\alpha}'$ are the deviator stress and deviator backstress tensors respectively. In

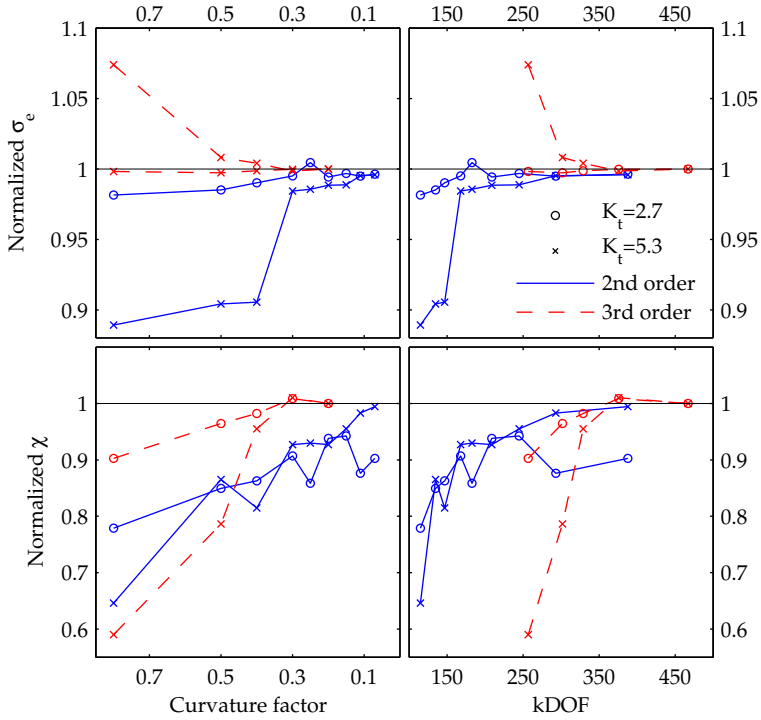

Figure A-4: Solution convergence test using von Mises stress and stress gradient, normalized with respect to the largest element mesh solution. Full lines are solutions from quadratic shape functions and dashed lines are from cubic shape functions, using the same element vertices for a given curvature factor.

this analysis, the size of the yield surface is constant, whereby Eq. A-14 only depends on the kinematic hardening component:

$$\dot{\boldsymbol{\alpha}} = \frac{C}{\sigma_0}(\boldsymbol{\sigma} - \boldsymbol{\alpha})\,\dot{\bar{\varepsilon}}^p - \gamma\boldsymbol{\alpha}\dot{\bar{\varepsilon}}^p, \tag{A-15}$$

where C is the initial kinematic hardening modulus and γ controls the rate at which the kinematic hardening modulus decreases with increased plastic strain. This model approximate the measured cyclic stress-strain curve better than the bilinear hardening model available in FEMLAB. Post-processing was done in Python, which is the ABAQUS native post-processing language.

The problem with this approach appeared to be insufficient precision in the native Python library. When solutions were requested for elements below a certain size, the returned solution would be incorrect. A Python program, similar to the one outlined in Algorithm 3 on page 151, was written to extract

solutions ahead of notches from the ABAQUS result files. Solutions for a notch[1] is shown in Figure A-5, where an elastic-plastic and a linear elastic analysis from ABAQUS have been compared to FEMLAB.

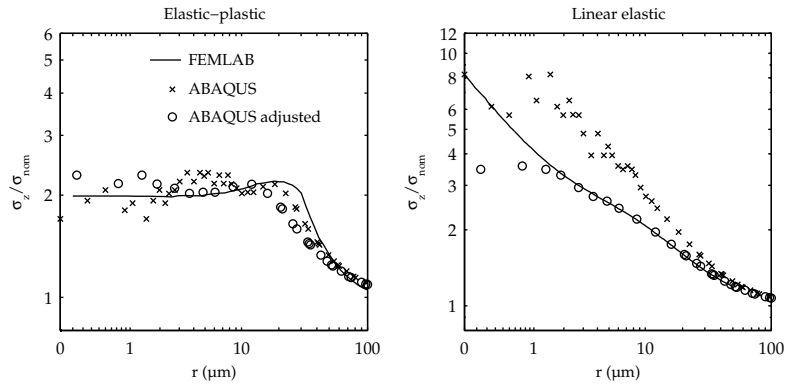

Figure A-5: Solutions returned from ABAQUS post-processing (red circles) compared to the FEMLAB solution. The blue circles correspond to an adjustment of the ABAQUS solution, so that it coincides with the larger element edges. (σ_{nom}=250 MPa).

When calculating a solution along a line, the ABAQUS post-processing routine returns solutions where this line intersects element edges. The positions of the calculated intersections were found to be in disagreement with the element mesh. By adding a certain length to these positions, they were found to coincide with larger element edges further away from the surface, but the positions for smaller element edges would then be prescribed outside of the model, as seen in FigureA-6. The solution with this adjustment is seen in Figure A-5, where 6.4 µm have been subtracted for all r values. It can be seen that the adjusted solution approaches the linear elastic FEMLAB solution for larger elements, while the "small element" solution is still wrong. For the elastic-plastic solution, the FEMLAB and MATLAB solution differ for larger elements as well due to the different hardening models used. Assuming that the ABAQUS solution is correct for r>10 µm, it can be stated that the non-linear hardening model predicts a smaller plastic zone than the bilinear model for this load level, while the magnitude of σ_z is about the same.

The ABAQUS results were the same, whether the post-processing was done on the 64 bit Origin computer or a 32 bit Windows computer. The FEMLAB results were obtained using double precision, so it could be that the problem stems from the ABAQUS Python libraries using 32 bit single precision, in disregard of the computer platform. A MATLAB post-processing program could have been made to do the interpolation from an ABAQUS result file, however, this was not undertaken since the ABAQUS support team indicated that they would look into it. As of yet, they have not provided a solution.

[1]Specimen X4, where initiation occurred

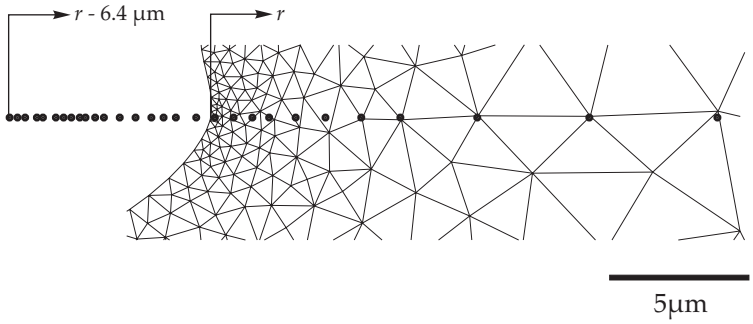

Figure A-6: Positions returned from ABAQUS post-processing, moved 6.42 μm to the left so that they coincide with the larger element edges.

Bibliography

[1] L. F. Coffin. Fatigue in machines and structures – power generation. In M. Meshii, editor, *Fatigue and Microstructure*, pages 1–27. ASM, 1979. (pp 2)

[2] F. Clymer. *Henry's wonderful Model T 1908-1927*. Bonanza Books, New York, 1955. (pp 2)

[3] N. L. Homeister. Vehicle emission standards around the globe. 2001 Ford Motor Company. `http://www.worldenergy.org/wec-geis/global/downloads/NZConf/03.pdf`. Online: www.worldenergy.com. (pp 3)

[4] J. D. Johnson. *Driving America*. AEI Press, 1997. (pp 3)

[5] W. S. Miller, L. Zhuang, J. Bottema, A. J. Wittebrood, P. De Smet, A. Haszler, and A. Vieregge. Recent development in aluminium alloys for the automotive industry. *Materials Science and Engineering A*, 2000 280(1):37–49. `http://dx.doi.org/10.1016/S0921-5093(99)00653-X`. (pp 3, 5)

[6] J. Dwigth. *Aluminium design and construction*. Routledge, 1999. Online edition (ebrary). (pp 3, 4)

[7] *Light-Duty Automotive Technology and Fuel Economy Trends: 1975 through 2006*. Number EPA420-S-06-003. United States Environmental Protection Agency, executive summary edition, 2006. (pp 4)

[8] S. C. Davis and S. W. Diegel. *Transportation energy data book*. Oak Ridge National Laboratories, 25 edition, 2006. `http://cta.ornl.gov/data/download25.shtml`. (pp 4)

[9] J. T. Staley and D. J. Lege. Advances in aluminum-alloy products for structural applications in transportation. *J. De Physique Iv*, 3:179–190, 1993. (pp 4)

[10] D. Carle and G. Blount. The suitability of aluminium as an alternative material for car bodies. *Materials & Design*, 1999 20(5):267–272. `http://dx.doi.org/10.1016/S0261-3069(99)00003-5`. (pp 4)

[11] O. Jensrud, R. Østhus, and H. Solerød. New improved forging technology and high volume serial production of aluminium wheel suspension arms. *Steel Grips*, 2006. To be published. (pp 4, 26)

[12] E. A. Starke, Jr. and J. T. Staley. Application of modern aluminum alloys to aircraft. *Progress in Aerospace Sciences*, 32(2-3):131–172, 1996. http://dx.doi.org/10.1016/0376-0421(95)00004-6. (pp 4)

[13] B. Cotterell. The past, present, and future of fracture mechanics. *Engineering Fracture Mechanics*, 2002 69(5):533–553. http://dx.doi.org/10.1016/S0013-7944(01)00101-1. (pp 4)

[14] J. C. Newman. The emerging of fatigue and fracture mechanics concepts: a historical perspective. *Progress in Aerospace Sciences*, 34:347–390, 1998. (pp 4, 20)

[15] D. Broek. Concepts of fracture control and damage tolerance analysis. In *Fatigue and fracture*, volume 19 of *ASM Handbook*. ASM, 1996. (pp 4)

[16] M. L. Sharp, G. E. Nordmark, and C. C. Menzemer. *Fatigue design of aluminum components and structures*. McGraw Hill, 1996. (pp 4)

[17] K. Spencer, S. F. Corbin, and D. J. Lloyd. Notch fracture behaviour of 5754 automotive aluminium alloys. *Materials Science and Engineering A*, 2002 332(1-2):81–90. http://dx.doi.org/10.1016/S0921-5093(01)01708-7. (pp 5)

[18] P. Heuler and O. Birk. Durability assessment of automotive aluminium parts. *Fatigue & Fracture of Engineering Materials and Structures*, 25(12):1135–1148, 2002. http://dx.doi.org/10.1046/j.1460-2695.2002.00590.x. (pp 5)

[19] V. V. Grubisic and G. Fischer. Methodology for effective design evaluation and durability approval of car suspension components. Technical Paper Series 970094, SAE, 1997. (pp 5)

[20] A. May and C. Carter. A case study of virtual team working in the European automotive industry. *International Journal of Industrial Ergonomics*, 2001 27(3):171–186. http://dx.doi.org/10.1016/S0169-8141(00)00048-2. (pp 5)

[21] A. Gomes de Sa and G. Zachmann. Virtual reality as a tool for verification of assembly and maintenance processes. *Computers & Graphics*, 1999 23(3): 389–403. http://dx.doi.org/10.1016/S0097-8493(99)00047-3. (pp 5)

[22] W. B. Ferry, P. R. Frise, G. T. Andrews, and M. A. Malik. Combining virtual simulation and physical vehicle test data to optimize durability testing. *Fatigue & Fracture Engineering Materials & Structures*, 25:1127–1134, 2002. http://dx.doi.org/10.1046/j.1460-2695.2002.00605.x. (pp 5)

[23] S. K. Ås. Fatigue life assessment of aluminium automotive structures. Master's thesis, Norwegian University of Science and Technology, 2002. http://folk.ntnu.no/as/Aas_thesis.pdf. (pp 5, 6)

[24] S. K. Ås and B. Skallerud. On virtual fatigue testing of aluminium automotive structures. In B. Skallerud and H.I. Andersson, editors, *Proc. Mekit'03 Second National Conference on Computational Mechanics*. Tapir Academic Press, 2003. http://folk.ntnu.no/as/mekit03_Aas_Skallerud.pdf. (pp 5, 6)

[25] U. Kocabicak and M. Firat. A simple approach for multiaxial fatigue damage prediction based on FEM post-processing. *Materials & Design*, 2004 25 (1):73–82. http://dx.doi.org/10.1016/S0261-3069(03)00157-2. (pp 6)

[26] J. J. Thomas, T.M.L. Nguyen-Tajan, and P. Burry. Structural durability in automotive design. *Materialwissenschaft und Werkstofftechnik*, 36(11): 650–658, 2005. http://dx.doi.org/10.1002/mawe.200500934. (pp 6)

[27] F. Couweleers, Ø. Skotheim, and B. W. Tveiten. Optical measurement of welded toe geometry with structured light. 2004 In *Proc. 8th International Symposium on Measurement and Quality Control in Production*. (pp 6)

[28] P. J. Caber. Interferometric profiler for rough surfaces. *Applied Optics*, 19: 3438–3441, 1993. http://www.opticsinfobase.org/abstract.cfm?URI=ao-32-19-3438. (pp 6, 70)

[29] W. Schutz. A history of fatigue. *Engineering Fracture Mechanics*, 1996 54(2): 263–300. http://dx.doi.org/10.1016/0013-7944(95)00178-6. (pp 7, 14)

[30] R. I. Stephens, A. Fatemi, R. R. Stephens, and H. O. Fuchs. *Metal fatigue in engineering*. Wiley, 2nd edition, 2001. (pp 7, 8, 19, 20, 34)

[31] H. Mughrabi. On 'multi-stage' fatigue life diagrams and the relevant life-controlling mechanisms in ultrahigh-cycle fatigue. *Fatigue & Fracture of Engineering Materials and Structures*, 25(8-9):755–764, 2002. http://dx.doi.org/10.1046/j.1460-2695.2002.00550.x. (pp 7)

[32] K. J. Miller and W. J. O'Donnell. The fatigue limit and its elimination. *Fatigue & Fracture of Engineering Materials and Structures*, 22(7):545–557, 1999. http://dx.doi.org/10.1046/j.1460-2695.1999.00204.x. (pp 7)

[33] S. E. Stanzl-Tschegg and H. Mayer. Fatigue and fatigue crack growth of aluminium alloys at very high numbers of cycles. *International Journal of Fatigue*, 23(Supplement 1):231–237, 2001. http://dx.doi.org/10.1016/S0142-1123(01)00167-0. (pp 7)

[34] M. Klesnil and P. Lukáš. *Fatigue of metallic materials*. Elsevier, 2nd edition, 1992. (pp 8, 19, 20, 25, 26, 27, 41, 125)

[35] J.F. Tavernelli and L.F. Coffin, Jr. Experimental support for generalized equation predicting low cycle fatigue. *Trans. ASME, Journal of Basic Engineering*, 84(4):533–537, 1962. Discussion by Manson, S. S., p437. (pp 7)

[36] M. A. Meggiolaro and J. T. P. Castro. Statistical evaluation of strain-life fatigue crack initiation predictions. *International Journal of Fatigue*, 2004 26(5):463–476. http://dx.doi.org/10.1016/j.ijfatigue.2003.10.003. (pp 8)

[37] M. R. Mitchell. Fundamentals of modern fatigue analysis for design. In *Fatigue and fracture*, volume 19 of *ASM Handbook*. ASM International, 2002. (pp 9, 11, 26)

[38] J. Morrow. Fatigue properties of metals. In J. A. Graham, editor, *Fatigue design handbook*. SAE, 1968. (pp 9)

[39] K.N. Smith, P. Watson, and T.H. Topper. A stress-strain function for the fatigue of metals. *ASTM Journal of Materials*, 5:767–778, 1970. (pp 9)

[40] D. F. Socie and G. B. Marquis. *Multiaxial fatigue*. SAE, 1999. (pp 9)

[41] W. N. Findley. A theory for the effect of mean stress on fatigue of metals under combined torsion and axial load or bending. *ournal of Engineering for Industry - Trans. ASME*, 81:301–306, 1959. (pp 9)

[42] M. W. Brown and K. J Miller. A theory for fatigue failure under mulitaxial stress-strain conditions. *Proceedings of the Institution of Mechanical Engineers*, 187:745–755, 1973. (pp 10)

[43] F. A. Kandil, M. W. Brown, and K. J. Miller. Biaxial low cycle fatigue of 316 stainless steel at elevated temperature. *Metals Society, London*, 280:203–210, 1982. (pp 10)

[44] Ying-Yu Wang and Wei-Xing Yao. Evaluation and comparison of several multiaxial fatigue criteria. *International Journal of Fatigue*, 2004 26(1):17–25. http://dx.doi.org/10.1016/S0142-1123(03)00110-5. (pp 10)

[45] J. Schijve. Fatigue predictions and scatter. *Fatigue & Fracture of Engineering Materials and Structures*, 17(4):381–396, 1994. (pp 10)

[46] Prakash Chandra Gope. Determination of minimum number of specimens in S-N testing. *Journal of Engineering Materials and Technology*, 124(4):421–427, 2002. http://link.aip.org/link/?JYT/124/421/1. (pp 10)

[47] R. C. Rice. Statistical aspects of design. In *Materials selection and design*, volume 20 of *ASM Handbook*. ASM, 1997. (pp 10)

[48] F. G. Pascual and W. Q. Meeker. Estimating fatigue curves with the random fatigue-limit model. *Technometrics*, 1999 41(4):277–290. (pp 10, 145)

[49] G. Minak. Comparison of different methods for fatigue limit evaluation by means of the Monte Carlo method. *Journal of Testing and Evaluation*, 32: 8, 2006. (pp 11)

[50] F. G. Pascual. Theory for optimal test plans for the random fatigue-limit model. *Technometrics*, 45(2):130 – 141, 2003. ISSN 0040-1706. http://dx.doi.org/10.1198/004017003188618760. (pp 11)

[51] B. Leis. Effect of surface conditions and processing on fatigue performance. In *Fatigue and fracture*, volume 19 of *ASM Handbook*. ASM International, 1996. (pp 11)

[52] G. R. Leverant, B. S. Langer, A. Yuen, and S. W. Hopkins. Surface residual-stresses, surface-topography and the fatigue behavior of Ti-6Al-4v. *Metallurgical Transactions A-Physical Metallurgy and Materials Science*, 10(2): 251–257, 1979. (pp 11)

[53] L. Wagner. Mechanical surface treatments on titanium, aluminum and magnesium alloys. *Materials Science and Engineering A*, 1999 263(2):210–216. http://dx.doi.org/10.1016/S0921-5093(98)01168-X. (pp 11)

[54] R. C. Juvinall. *Engineering Considerations of Stress, Strain, and Strength*. McGraw Hill, 1967. (pp 12, 16)

[55] D. Novovic, R. C. Dewes, D. K. Aspinwall, W. Voice, and P. Bowen. The effect of machined topography and integrity on fatigue life. *Machine Tools and Manufacture*, 44:125–134, 2004. http://dx.doi.org/10.1016/j.ijmachtools.2003.10.018. (pp 12)

[56] H. Neuber. *Theory of notch stresses: principles for exact stress calculation.* J. W. Edwards, 1946. Translation of *Kerbspannungslehre*, 1937. (pp 12, 15, 44)

[57] D. Arola and C.L. Williams. Estimating the fatigue stress concentration factor of machined surfaces. *International Journal of Fatigue*, 24:923–930, 2002. http://dx.doi.org/10.1016/S0142-1123(02)00012-9. (pp 13)

[58] C. Q. Bowles. Fracture and structure. In *Fatigue and fracture*, volume 19 of *ASM Handbook*. ASM, 1996. (pp 13)

[59] S. Güngör and L. Edwards. Effect of surface texture on the initiation and propagation of small fatigue cracks in a forged 6082 aluminium alloy. *Materials Science and Engineering A*, 1993 160(1):17–24. http://dx.doi.org/10.1016/0921-5093(93)90493-X. (pp 13, 68)

[60] G. E. Dieter. *Mechanical metallurgy*. McGraw-Hill, 3rd edition, 1986. (pp 13, 26)

[61] R. E. Peterson. Notch sensitivity. In G. Sines and J. L. Waisman, editors, *Metal Fatigue*. McGraw Hill, 1959. (pp 15)

[62] E. Siebel and M. Stieler. Ungleichförmige Spannungsverteilung bei schwingender Beanspruchung. *Z Ver Deutsch Ing*, 97:121–126, 1955. (pp 15)

[63] R. C. Juvinall and K.M. Marshek. *Fundamentals of Machine Component Design*. John Wiley & Sons, 1991. (pp 15)

[64] J. E. Shigley and C. R. Mischke. *Mechanical engineering design*. McGraw Hill, 6th edition, 2001. (pp 15)

[65] E. Dowling. Estimating fatigue life. In *Fatigue and fracture*, volume 19 of *ASM Handbook*. ASM, 1996. (pp 16)

[66] H. Neuber. Theory of stress concentration for shear-strained prismatic bodies with arbitrary nonlinear stress-strain law. *Journal of Applied Mechanics – Trans. ASME*, 28:544–550, 1961. (pp 17)

[67] T. H. Topper, R. M. Wetzel, and J. Morrow. Neuber's rule applied to fatigue of notched specimens. *Journal of Materials*, 4(1):200 – 209, 1969. (pp 17)

[68] S. S. Manson. Fatigue – A complex subject – Some simple approximations. *Experimental Mechanics*, 5(7):193 – 226, 1965. (pp 17)

[69] M. B. P. Allery and G. Birkbeck. Effect of notch root radius on the initiation and propagation of fatigue cracks. *Engineering Fracture Mechanics*, 1972 4(2): 325–331. `http://dx.doi.org/10.1016/0013-7944(72)90047-1`. (pp 18)

[70] B. N. Leis and T. H. Topper. Cyclic deformation and fatigue analysis for notched components. *Nuclear Engineering and Design*, 29(3):370–383, 1974. `http://dx.doi.org/10.1016/0029-5493(75)90047-3`. (pp 18)

[71] G.R. Irwin. Analysis of stresses and strains near end of crack traversing plate. *American Society of Mechanical Engineers – Transactions – Journal of Applied Mechanics*, 24(3):361 – 364, 1957. (pp 19)

[72] P. C. Paris, M. P. Gomez, and W. E. Anderson. A rational analytical theory of fatigue. *The Trend in Engineering*, 13:9–14, 1961. (pp 19)

[73] P. Paris and F. Erdogan. Critical analysis of crack propagation laws. *American Society of Mechanical Engineers – Papers*, 85:8 –, 1962. (pp 19)

[74] J. R. Rice. Mechanics of crack tip deformation and extension by fatigue. *Fatigue Crack Propagation, ASTM STP*, 415:247–309, 1967. (pp 19)

[75] W. Elber. The significance of fatigue crack closure. *Damage Tolerance in Aircraft Structures, ASTM STP*, 486:230 – 42, 1971. (pp 20)

[76] R. W. Hertzberg, C. H. Newton, and R. Jaccard. Crack closure: correlation and confusion. *Mechanics of Fatigue Crack Closure, ASTM STP*, 982:139–148, 1988. (pp 20)

[77] N. Louat, K. Sadananda, M. Duesbery, and A.K. Vasudevan. A theoretical evaluation of crack closure. *Metallurgical Transactions A (Physical Metallurgy and Materials Science)*, 24A(10):2225–2232, 1993. (pp 20)

[78] A. K. Vasudevan, K. Sadananda, and N. Louat. A review of crack closure, fatigue crack threshold and related phenomena. *Material Science and Engineering*, A188:1–22, 1994. (pp 20)

[79] D. Kujawski. On assumptions associated with ΔK_{eff} and their implications on FCG predictions. *International Journal of Fatigue*, 27(10-12):1267–1276, 2005. http://dx.doi.org/10.1016/j.ijfatigue.2005.07.020. (pp 20)

[80] H. Sehitoglu, K. Gall, and A. M. Garcia. Recent advances in fatigue crack growth modeling. *International Journal of Fracture*, 80(2-3):165–192, 1996. (pp 20)

[81] F. Bergner, G. Zouhar, and G. Tempus. The material-dependent variability of fatigue crack growth rates of aluminium alloys in the Paris regime. *International Journal of Fatigue*, 2001 23(5):383–394. http://dx.doi.org/10.1016/S0142-1123(01)00006-8. (pp 21, 123)

[82] D Kujawski. A new $(\Delta K^{+}\Delta K_{\text{max}})^{0.5}$ driving force parameter for crack growth in aluminium alloys. *International Journal of Fatigue*, 23:733–740, 2001. (pp 21)

[83] D. Kujawski. ΔK_{eff} parameter under re-examination. *International Journal of Fatigue*, 25:793–800, 2003. (pp 21)

[84] E. K. Walker. The effect of stress ratio during crack propagation and fatigue for 2024-T3 and 7075-T6 aluminum. *Effects of Environment and Complex Load History on Fatigue Life, ASTM STP*, 462:1–14, 1970. (pp 21)

[85] I. J. Polmear. *Light alloys: metallurgy of the light metals*. Edward Arnold, 2nd edition, 1989. (pp 26)

[86] H. J. Christ. Cyclic stress-strain response and microstructure. In *Fatigue and fracture*, volume 19 of *ASM Handbook*. ASM, 1996. (pp 26)

[87] C. D. Marioara, S. J. Andersen, J. Jansen, and H. W. Zandbergen. The influence of temperature and storage time at RT on nucleation of the [beta]″ phase in a 6082 Al–Mg–Si alloy. *Acta Materialia*, 2003 51(3): 789–796. http://dx.doi.org/10.1016/S1359-6454(02)00470-6. (pp 26, 98)

[88] H. W. Zandbergen, S. J. Andersen, and J. Jansen. Structure determination of Mg5Si6 particles in Al by dynamic electron diffraction studies. *Science*, 277: 1221–1225, 1997. http://dx.doi.org/10.1126/science.277.5330.1221. (pp 26)

[89] S. J. Andersen, H. W. Zandbergen, J. Jansen, C. Træholt, U. Tundal, and O. Reiso. The crystal structure of the beta' phase in Al-Mg-Si alloys. *Acta Materialia*, 1998 46(9):3283–3298. http://dx.doi.org/10.1016/S1359-6454(97)00493-X. (pp 26)

[90] R. J. Bucci, G. Nordmark, and E. A. Starke Jr. Selecting aluminum alloys to resist failure by fracture mechanisms. In *Fatigue and fracture*, volume 19 of *ASM Handbook*. ASM, 1996. (pp 27)

[91] A. C. Pickard and J. F. Knott. Effects of testing method on cyclic hardening behavior in face-centered-cubic alloys. Technical Report cyclic stress-strain, ASTM STP, Bolton Landing, NY, USA, 1987. (pp 28, 29)

[92] J. A. Bannantine, J. J. Comer, and J. L. Handrock. *Fundamentals of metal fatigue analysis*. Prentice Hall, Englewood Cliffs, N.J., 1990. (pp 28)

[93] W. Ramberg and W. R. Osgood. Description of stress-strain curves by three parameters. Technical Report 902, NACA, 1948. `http://hdl.handle.net/2060/19930081614`. (pp 28)

[94] R. W. Landgraf, J. Morrow, and T. Endo. Determination of cyclic stress-strain curve. *Journal of Materials*, 4(1):176–, 1969. (pp 29)

[95] J. Polak, M. Klesnil, and P. Lukas. On the cyclic stress-strain curve evaluation in low cycle fatigue. *Materials Science and Engineering*, 1977 28(1): 109–117. `http://dx.doi.org/10.1016/0025-5416(77)90094-5`. (pp 29)

[96] B. Skallerud and A. F. Blom. Application of a transient cyclic plasticity model for determination of the incremental step test material curve. In *The third international conference on low cycle fatigue and elasto-plastic behaviour of materials*, Berlin, 1992. (pp 29)

[97] S. Raman and K. A. Padmanabhan. Determination of the room-temperature cyclic stress–strain curve of AISI 304LN austenitic stainless steel by two different methods. *International Journal of Fatigue*, 1992 14(5): 295–304. `http://dx.doi.org/10.1016/0142-1123(92)90480-Z`. (pp 29, 30)

[98] H.-J. Christ and H. Mughrabi. Cyclic stress-strain response and microstructure under variable amplitude loading. *Fatigue and Fracture of Engineering Materials and Structures*, 19(2-3):335 – 348, 1996. ISSN 8756-758X. (pp 29, 30)

[99] R. P. Skelton, H. J. Maier, and H. J. Christ. The Bauschinger effect, Masing model and the Ramberg-Osgood relation for cyclic deformation in metals. *Materials Science and Engineering A*, 1997 238(2):377–390. `http://dx.doi.org/10.1016/S0921-5093(97)00465-6`. (pp 29, 30)

[100] G. Glinka. Energy density approach to calculation of inelastic strain-stress near notches and cracks. *Engineering Fracture Mechanics*, 22(3):485–508, 1985. `http://dx.doi.org/10.1016/0013-7944(85)90148-1`. (pp 30, 33)

[101] W. N. Sharpe, C. H. Yang, and R. L. Tregoning. An evaluation of the Neuber and Glinka relations for monotonic loading. *Journal Of Applied Mechanics – Trans. ASME*, 1992 59(2):S50–S56. (pp 31, 33)

[102] M. Hoffmann and T. A. Seeger. A generalized method for estimating multiaxial elastic-plastic notch stresses and strains. *Journal of Engineering Materials and Techonolgy*, 107:250–254, 1985. (pp 31, 33)

[103] J. Lubliner. *Plasticity theory*. MacMillan Publishing Company, 1990. (pp 32)

[104] T. Seeger and P. Heuler. Generalized application of neuber's rule. *Journal of Eesting & Evaluation*, 8(4):199 – 204, 1980. ISSN 0090-3973. (pp 33)

[105] G. Harkegard and S. Sorbo. Applicability of Neuber's rule to the analysis of stress and strain concentration under creep conditions. *Journal of Engineering Materials and Technology, Transactions of the ASME*, 120(3):224 – 229, 1998. ISSN 0094-4289. Neuber's rule;Viscoplastic notch problems;. (pp 33)

[106] G. Harkegard and T. Mann. Neuber prediction of elastic-plastic strain concentration in notched tensile specimens under large-scale yielding. *Journal of Strain Analysis for Engineering Design*, 38(1):79 – 94, 2003. ISSN 0309-3247. http://dx.doi.org/10.1243/030932403762671917. Neuber prediction;Large scale yielding;Notch stress;Strain energy density;. (pp 33)

[107] S. K. Visvanatha, P. V. Straznicky, and R. L. Hewitt. Influence of strain estimation methods on life predictions using the local strain approach. *International Journal of Fatigue*, 2000 22(8):675–681. http://dx.doi.org/10.1016/S0142-1123(00)00042-6. (pp 34)

[108] Jae-Yong Lim, Seong-Gu Hong, and Soon-Bok Lee. Application of local stress-strain approaches in the prediction of fatigue crack initiation life for cyclically non-stabilized and non-Masing steel. *International Journal of Fatigue*, 27(10-12):1653–1660, 2005. http://dx.doi.org/10.1016/j.ijfatigue.2005.07.014. (pp 34)

[109] S. M. Tipton and D. V. Nelson. Advances in multiaxial fatigue life prediction for components with stress concentrations. *International Journal of Fatigue*, 1997 19(6):503–515. http://dx.doi.org/10.1016/S0142-1123(96)00070-9. (pp 34)

[110] K. J. Miller. The two thresholds of fatigue behavior. *Fatigue and fracture of engineering materials and structures*, 1993 16(9):931–939. (pp 34, 35, 36, 38, 39)

[111] W. A. Wood. Formation of fatigue cracks. *Philosophical Magazine*, 3(31): 692–, 1958. (pp 35)

[112] P. J. E. Forsyth. Fatigue damage and crack growth in aluminium alloys. *Acta Metallurgica*, 1963 11(7):703–715. http://dx.doi.org/10.1016/0001-6160(63)90008-7. (pp 35)

[113] L. M. Brown and S. L. Ogin. Role of internal stresses in the nucleation of fatigue cracks. In Bilby, Miller, and Willis, editors, *Fundamentals of deforamtion and fracture*, pages 501–528. Eshelby Memorial Symposium, 1984. (pp 36)

[114] D. L. McDowell. Basic issues in the mechanics of high cycle metal fatigue. *International Journal of Fracture*, 80(2-3):103–145, 1996. (pp 36)

[115] K. J. Miller. Materials science perspective of metal fatigue resistance. *Materials science and technology*, 9:453–462, 1993. (pp 36)

[116] S. Pearson. Initiation of fatigue cracks in commerical aluminium alloys and the subsequent propagation of very short cracks. *Engineering Fracture Mechanics*, 1975 7(2):235–247. http://dx.doi.org/10.1016/0013-7944(75)90004-1. (pp 36)

[117] J. Lankford. The growth of small fatigue cracks in 7075-T6 aluminum. *Fatigue of Engineering Materials and Structures*, 5(3):233–248, 1982. (pp 36, 37)

[118] K. J. Miller. The short crack problem. *Fatigue of engineering materials and structures*, 5(3):223 – 232, 1982. ISSN 0160-4112. (pp 37)

[119] P. D. Hobson. The formulation of a crack growth equation for short cracks. *Fatigue of Engineering Materials and Structures*, 5:323–327, 1982. (pp 37)

[120] P. D. Hobson, M. W. Brown, and E. R. de los Rios. Two phases of short crack growth in a medium carbon steel. In K. J. Miller and E. R. de los Rios, editors, *The Behaviour of Short Fatigue Cracks*, pages 479–490. Mechanical Engineering Publications, 1986. (pp 37)

[121] A. Navarro and E. R. de los Rios. Short and long fatigue crack-growtha unified model. *Philosophical Magazine A-Physics of Condensed Matter Structure Defects And Mechanical Properties*, 1988 57(1):15–36. (pp 37)

[122] M. H. El Haddad, K. N. Smith, and T. H. Topper. Fatigue crack propagation of short cracks. In *ASME/CSME Joint Conference on Pressure Vessets and Piping Nuclear Energy and Materials*, 1978. (pp 38)

[123] M. H. ElHaddad, T. H. Topper, and K. N. Smith. Prediction of non propagating cracks. *Engineering Fracture Mechanics*, 11(3):573–584, 1979. http://dx.doi.org/10.1016/0013-7944(79)90081-X. (pp 38, 39, 41, 43, 45, 133)

[124] H. Kitagawa and S. Takahashi. Applicability of fracture mechanics to very small cracks or the cracks in the early stage. In *Proceedings of the Second International Conference on Mechanical Behavior of Materials*, pages 627–31, 1976. (pp 38)

[125] N. E. Frost and D. S. Dugdale. Fatigue tests on notched mild steel plates with measurements of fatigue cracks. *Journal of the Mechanics and Physics of Solids*, 5(3):182–188, 1957. http://dx.doi.org/10.1016/0022-5096(57)90004-2. (pp 39)

[126] R. A. Smith and K. J. Miller. Fatigue cracks at notches. *International Journal of Mechanical Sciences*, 1977 19(1):11–22. http://dx.doi.org/10.1016/0020-7403(77)90011-X. (pp 39, 40)

[127] R. A. Smith and K. J. Miller. Prediction of fatigue regimes in notched components. *International Journal of Mechanical Sciences*, 20(4):201–206, 1978. http://dx.doi.org/10.1016/0020-7403(78)90082-6. (pp 39, 40, 41, 45)

[128] N. E. Frost. A relation between the critical alternating propagation stress and crack length for mild steel. *Proceedings of the Institution of Mechanical Engineers*, 173:811–827, 1959. (pp 40, 43)

[129] J. C. Newman. An improved method of collocation for the stress analysis of cracked plates with various shaped boundaries. Technical report, NASA Technical Note D-6376, 1971. (pp 40, 41)

[130] D. Taylor. Geometrical effects in fatigue: a unifying theoretical model. *International Journal of Fatigue*, 1999 21(5):413–420. http://dx.doi.org/10.1016/S0142-1123(99)00007-9. (pp 41, 42)

[131] P. Lazzarin, R. Tovo, and G. Meneghetti. Fatigue crack initiation and propagation phases near notches in metals with low notch sensitivity. *International Journal of Fatigue*, 19(8-9):647–657, 1997. http://dx.doi.org/10.1016/S0142-1123(97)00091-1. (pp 41, 42)

[132] G. Glinka and A. Newport. Universal features of elastic notch-tip stress-fields. *International Journal of Fatigue*, 9:143–150, 1987. http://dx.doi.org/10.1016/0142-1123(87)90069-7. (pp 42)

[133] D. Taylor and G. Wang. The validation of some methods of notch fatigue analysis. *Fatigue & Fracture of Engineering Materials and Structures*, 23(5):387–394, 2000. http://dx.doi.org/10.1046/j.1460-2695.2000.00302.x. (pp 42)

[134] D. Taylor, P. Bologna, and K. Bel Knani. Prediction of fatigue failure location on a component using a critical distance method. *International Journal of Fatigue*, 2000 22(9):735–742. http://dx.doi.org/10.1016/S0142-1123(00)00062-1. (pp 42)

[135] D. B. Lanning, T. Nicholas, and A. Palazotto. The effect of notch geometry on critical distance high cycle fatigue predictions. *International Journal of Fatigue*, 27(10-12):1623–1627, 2005. http://dx.doi.org/10.1016/j.ijfatigue.2005.06.017. (pp 42)

[136] A. D. Cameron and R. A. Smith. Upper and lower bounds for the lengths of non-propagating cracks. *International Journal of Fatigue*, 1981 3(1):9–15. http://dx.doi.org/10.1016/0142-1123(81)90043-8. (pp 43)

[137] D. Taylor. A mechanistic approach to critical-distance methods in notch fatigue. *Fatigue & Fracture of Engineering Materials and Structures*, 24(4): 215–224, 2001. http://dx.doi.org/10.1046/j.1460-2695.2001.00401.x. (pp 43)

[138] B. Atzori, P. Lazzarin, and G. Meneghetti. Fracture mechanics and notch sensitivity. *Fatigue & Fracture of Engineering Materials and Structures*, 26(3): 257–267, 2003. http://dx.doi.org/10.1046/j.1460-2695.2003.00633.x. (pp 43)

[139] D. L. Du Quesnay, M. T. Yu, and T. H. Topper. An analysis of notch size effect on the fatigue limit. *Journal of Testing and Evaluation*, 4:375–385, 1998. (pp 43)

[140] K. Tanaka and Y. Nakai. Propagation and non-propagation of short fatigue cracks at a sharp notch. *Fatigue of Engineering Materials and Structures*, 6(4): 315–327, 1983. (pp 43)

[141] J. R. Yates and M. W. Brown. Prediction of the length of non-propagating fatigue cracks. *Fatigue & Fracture of Engineering Materials and Structures*, 10: 187–201, 1987. (pp 43)

[142] A. D. Cameron and R. A. Smith. Fatigue life prediction for notched members. *International Journal of Pressure Vessels and Piping*, 1982 10(3): 205–217. http://dx.doi.org/10.1016/0308-0161(82)90033-3. (pp 44, 45)

[143] R. W. Suhr. The effect of surface finish on high cycle fatigue of a low alloy steel. In K. J. Miller and E. R. de los Rios, editors, *The Behaviour of Short Fatigue Cracks*, pages 479–490. Mechanical Engineering Publications, 1986. (pp 45, 47)

[144] D. Taylor and O. M. Clancy. The fatigue performance of machined surfaces. *Fatigue & Fracture of Engineering Materials and Structures*, 14(2-3):329–336, 1991. (pp 46, 47)

[145] D. L. Donohue and J. A. Carter. Spark source mass spectrometry. In *Materials characterization*, volume 10 of *ASM Handbook*. ASM, 1986. (pp 50)

[146] G. F. Vander Voort. Color metallography. In *Metallography and Microstructures*, volume 9 of *ASM Handbook*. ASM, 2004. (pp 51, 98)

[147] D. P. Field. Textured structures. In *Metallography and Microstructures*, volume 9 of *ASM Handbook*. ASM, 2004. (pp 53)

[148] American Society for Testing and Materials. Standard recommended practice for constant amplitude axial fatigue tests of metallic materials - ASTM E466-96. In *Annual book of ASTM standards*, volume 03.01. ASTM, 2004. (pp 53)

[149] American Society for Testing and Materials. Standard practice for strain-controlled fatigue testing - ASTM E606-92. In *Annual book of ASTM standards*, volume 03.01. ASTM, 2004. (pp 53, 59)

[150] A. Abel. Dislocation-associated elastic energy storage in mechanical deformations. *Materials Science & Engineering A*, 164(1-2):220 – 225, 1993. ISSN 0921-5093. http://dx.doi.org/10.1016/0921-5093(93)90666-3. (pp 66)

[151] Y. S. Chung and A. Abel. Low cycle fatigue of some aluminum alloys. *ASTM STP*, 942:94 – 106, 1988. (pp 66)

[152] L. P. Borrego, L. M. Abreu, J. M. Costa, and J. M. Ferreira. Analysis of low cycle fatigue in AlMgSi aluminium alloys. *Engineering Failure Analysis*, 2004 11(5):715–725. http://dx.doi.org/10.1016/j.engfailanal.2003.09.003. (pp 68, 69, 70)

[153] F. V. Antunes, l. F. P. Borrego, j. D. Costa, and J. M. Ferreira. A numerical study of fatigue crack closure induced by plasticity. *Fatigue and fracture of engineering materials and structures*, 27(9):825–835, 2004. http://www.blackwell-synergy.com/doi/abs/doi4.00738.x. (pp 68)

[154] L. P. Borrego, J. M. Ferreira, and J. M. Costa. Fatigue crack growth and crack closure in an AlMgSi alloy. *Fatigue & Fracture of Engineering Materials and Structures*, 24(4):255–265, 2001. http://dx.doi.org/10.1046/j.1460-2695.2001.00383.x. (pp 68)

[155] M. Benedetti, T. Bortolamedi, V. Fontanari, and F. Frendo. Bending fatigue behaviour of differently shot peened Al 6082 T5 alloy. *International Journal of Fatigue*, 2004 26(8):889–897. http://dx.doi.org/10.1016/j.ijfatigue.2003.12.003. (pp 68)

[156] D. Jiang and C. Wang. Influence of microstructure on deformation behavior and fracture mode of Al–Mg–Si alloys. *Materials Science and Engineering A*, 2003 352(1-2):29–33. http://dx.doi.org/10.1016/S0921-5093(02)00456-2. (pp 68)

[157] R. Valentijn. Hoogbelaste stalen onderdelen nu ook uit aluminium maakbaar? *Aluminium*, 2005 5. (pp 68)

[158] B. Bowe and V. Toal. White light interferometric surface profiler. *Optical Engineering*, 37(6):1796–1799, 1998. (pp 70)

[159] R. Ohlsson, A. Wihlborg, and H. Westberg. The accuracy of fast 3D topography measurements. *Machine Tools and Manufacture*, 41:1899–1907, 2001. http://dx.doi.org/10.1016/S0890-6955(01)00054-2. (pp 70)

[160] B. D. Cullity and S. Stock. *Elements of X-ray diffraction*. Addison-Wesley, 2001. (pp 72)

[161] T. Wroblewski, O. Clauss, H. A. Crostack, A. Ertel, F. Fandrich, Ch. Genzel, K. Hradil, W. Ternes, and E. Woldt. A new diffractometer for materials science and imaging at HASYLAB beamline G3. *Nuclear instruments and methods in physics research*, 428:570–582, 1999. (pp 72)

[162] N. Ottosen and H. Petersson. *Introduction to the finite element method*. Prentice Hall, 1992. (pp 77)

[163] T. Belytschko, W. K. Liu, and B. Moran. *Nonlinear finite elements for continua and structures*. Wiley, 2000. (pp 77)

[164] E. W. Weisstein. Bézier curve. From MathWorld–A Wolfram Web Resource, . http://mathworld.wolfram.com/BezierCurve.html. online. (pp 78)

[165] E. W. Weisstein. Bernstein polynomial. From MathWorld–A Wolfram Web Resource, . http://mathworld.wolfram.com/BernsteinPolynomial.html. online. (pp 79)

[166] D. Hearn and M. P. Baker. *Computer graphics*. Prentice Hall, 1994. (pp 80)

[167] P. L. George. *Automatic mesh generation : application to finite element methods*. Wiley, 1991. (pp 81)

[168] Y. Saad and H. A. van der Vorst. Iterative solution of linear systems in the 20th century. *Journal of Computational and Applied Mathematics*, 2000 123(1-2):1–33. http://dx.doi.org/10.1016/S0377-0427(00)00412-X. (pp 86)

[169] *FEMLAB documentation*. Version 3.1. (pp 88)

[170] K. Jacobus, R. E. DeVor, S. G. Kapoor, and R. A. Peascoe. Predictive model for the full biaxial surface and subsurface residual stress profiles from turning. *Journal of Manufacturing Science and Engineering*, 123(4):537–546, 2001. http://dx.doi.org/10.1115/1.1372197. (pp 89)

[171] J. R. Leinum, K. Pedersen, and H. J. Roven. Effects of crack direction on fatigue crack propagation mechanisms in an unrecrystallized AlMgSi alloy. In *The 3rd international conference on aluminium alloys*, pages 521–525, 1992. (pp 122)

[172] Harter J. A. *AFGROW: users guide and technical manual*. Air Vehicles Directorate, Air Force Research Laboratory OH, 2004. http://afgrow.wpafb.af.mil/downloads/afgrow/techman.zip. (pp 123)

[173] J. A. Harter. Comparison of contemporary FCG life prediction tools. *International Journal of Fatigue*, 1999 21(Supplement 1):181–185. http://dx.doi.org/10.1016/S0142-1123(99)00070-5. (pp 123)

[174] R. G. Forman and V. Shivakumar. Growth behavior of surface cracks in the circumferential plane of solid and hollow cylinders. *ASTM STP 905*, 17:59 – 74, 1986. (pp 123, 124)

[175] Y. X. Zhao. A methodology for strain-based fatigue reliability analysis. *Reliability Engineering & System Safety*, 2000 70(2):205–213. http://dx.doi.org/10.1016/S0951-8320(00)00062-4. (pp 145)

[176] S. Kandarpa, B. F. Spencer, Jr, and D. J. Kirkner. Reliability analysis of structural components utilizing the strain-life method. *Engineering Fracture Mechanics*, 1996 53(5):761–774. http://dx.doi.org/10.1016/0013-7944(95)00135-2. (pp 145)

[177] C. R. Williams, Y. L. Lee, and J. T. Rilly. A practical method for statistical analysis of strain-life fatigue data. *International Journal of Fatigue*, 2003 25(5):427–436. http://dx.doi.org/10.1016/S0142-1123(02)00119-6. (pp 145)

[178] W. Nelson. *Applied life data analysis*. Wiley, 1982. (pp 146)

[179] WAFO: Wave analysis for fatigue and oceanography. http://www.maths.lth.se/matstat/wafo/. (pp 150)

Thank you for waiting, Sarahbelle!

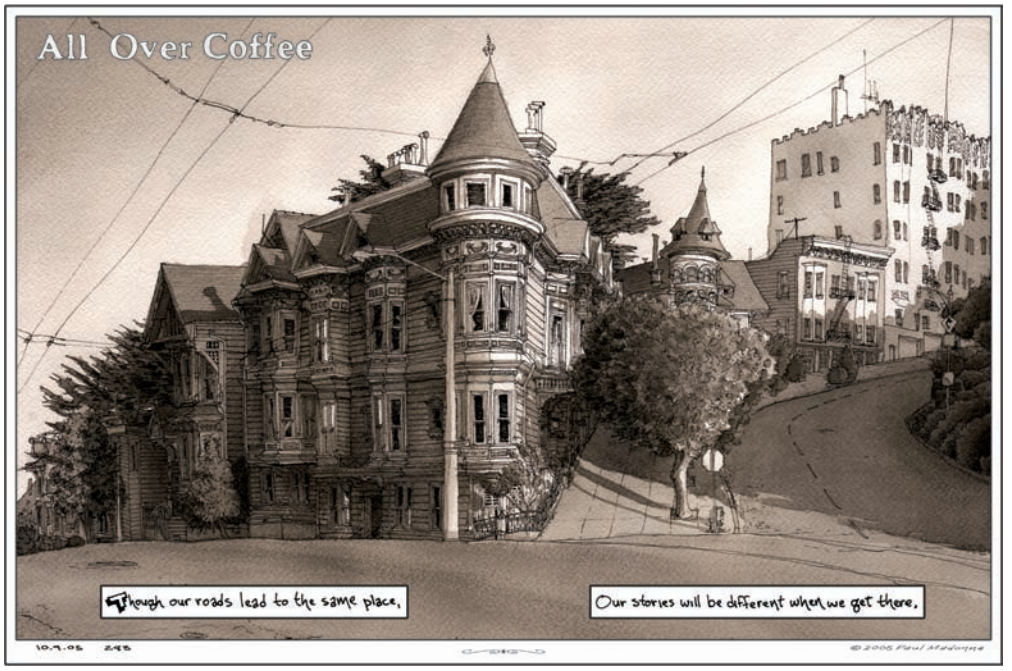
All Over Coffee
Though our roads lead to the same place,
Our stories will be different when we get there.
10.7.05 245
©2005 Paul Maddigan

DEPARTMENT OF STRUCTURAL ENGINEERING
NORWEGIAN UNIVERSITY OF SCIENCE AND TECHNOLOGY

N-7491 TRONDHEIM, NORWAY
Telephone: +47 73 59 47 00 Telefax: +47 73 59 47 01

"Reliability Analysis of Structural Systems using Nonlinear Finite Element Methods", C. A. Holm, 1990:23, ISBN 82-7119-178-0.

"Uniform Stratified Flow Interaction with a Submerged Horizontal Cylinder", Ø. Arntsen, 1990:32, ISBN 82-7119-188-8.

"Large Displacement Analysis of Flexible and Rigid Systems Considering Displacement-Dependent Loads and Nonlinear Constraints", K. M. Mathisen, 1990:33, ISBN 82-7119-189-6.

"Solid Mechanics and Material Models including Large Deformations", E. Levold, 1990:56, ISBN 82-7119-214-0, ISSN 0802-3271.

"Inelastic Deformation Capacity of Flexurally-Loaded Aluminium Alloy Structures", T. Welo, 1990:62, ISBN 82-7119-220-5, ISSN 0802-3271.

"Visualization of Results from Mechanical Engineering Analysis", K. Aamnes, 1990:63, ISBN 82-7119-221-3, ISSN 0802-3271.

"Object-Oriented Product Modeling for Structural Design", S. I. Dale, 1991:6, ISBN 82-7119-258-2, ISSN 0802-3271.

"Parallel Techniques for Solving Finite Element Problems on Transputer Networks", T. H. Hansen, 1991:19, ISBN 82-7119-273-6, ISSN 0802-3271.

"Statistical Description and Estimation of Ocean Drift Ice Environments", R. Korsnes, 1991:24, ISBN 82-7119-278-7, ISSN 0802-3271.

"Properties of concrete related to fatigue damage: with emphasis on high strength concrete", G. Petkovic, 1991:35, ISBN 82-7119-290-6, ISSN 0802-3271.

"Turbidity Current Modelling", B. Brørs, 1991:38, ISBN 82-7119-293-0, ISSN 0802-3271.

"Zero-Slump Concrete: Rheology, Degree of Compaction and Strength. Effects of Fillers as Part Cement-Replacement", C. Sørensen, 1992:8, ISBN 82-7119-357-0, ISSN 0802-3271.

"Nonlinear Analysis of Reinforced Concrete Structures Exposed to Transient Loading", K. V. Høiseth, 1992:15, ISBN 82-7119-364-3, ISSN 0802-3271.

"Finite Element Formulations and Solution Algorithms for Buckling and Collapse Analysis of Thin Shells", R. O. Bjærum, 1992:30, ISBN 82-7119-380-5, ISSN 0802-3271.

"Response Statistics of Nonlinear Dynamic Systems", J. M. Johnsen, 1992:42, ISBN 82-7119-393-7, ISSN 0802-3271.

"Digital Models in Engineering. A Study on why and how engineers build and operate

digital models for decisison support", J. Høyte, 1992:75, ISBN 82-7119-429-1, ISSN 0802-3271.

"Sparse Solution of Finite Element Equations", A. C. Damhaug, 1992:76, ISBN 82-7119-430-5, ISSN 0802-3271.

"Some Aspects of Floating Ice Related to Sea Surface Operations in the Barents Sea", S. Løset, 1992:95, ISBN 82-7119-452-6, ISSN 0802-3271.

"Modelling of Cyclic Plasticity with Application to Steel and Aluminium Structures", O. S. Hopperstad, 1993:7, ISBN 82-7119-461-5, ISSN 0802-3271.

"The Free Formulation: Linear Theory and Extensions with Applications to Tetrahedral Elements with Rotational Freedoms", G. Skeie, 1993:17, ISBN 82-7119-472-0, ISSN 0802-3271.

"Høyfast betongs motstand mot piggdekkslitasje. Analyse av resultater fra prøving i Veisliter'n", T. Tveter, 1993:62, ISBN 82-7119-522-0, ISSN 0802-3271.

"A Nonlinear Finite Element Based on Free Formulation Theory for Analysis of Sandwich Structures", O. Aamlid, 1993:72, ISBN 82-7119-534-4, ISSN 0802-3271.

"The Effect of Curing Temperature and Silica Fume on Chloride Migration and Pore Structure of High Strength Concrete", C. J. Hauck, 1993:90, ISBN 82-7119-553-0, ISSN 0802-3271.

"Failure of Concrete under Compressive Strain Gradients", G. Markeset, 1993:110, ISBN 82-7119-575-1, ISSN 0802-3271.

"An experimental study of internal tidal amphidromes in Vestfjorden", J. H. Nilsen, 1994:39, ISBN 82-7119-640-5, ISSN 0802-3271.

"Structural analysis of oil wells with emphasis on conductor design", H. Larsen, 1994:46, ISBN 82-7119-648-0, ISSN 0802-3271.

"Adaptive methods for non-linear finite element analysis of shell structures", K. M. Okstad, 1994:66, ISBN 82-7119-670-7, ISSN 0802-3271.

"On constitutive modelling in nonlinear analysis of concrete structures", O. Fyrileiv, 1994:115, ISBN 82-7119-725-8, ISSN 0802-3271.

"Fluctuating wind load and response of a line-like engineering structure with emphasis on motion-induced wind forces", J. Bogunovic Jakobsen, 1995:62, ISBN 82-7119-809-2, ISSN 0802-3271.

"An experimental study of beam-columns subjected to combined torsion, bending and axial actions", A. Aalberg, 1995:66, ISBN 82-7119-813-0, ISSN 0802-3271.

"Scaling and cracking in unsealed freeze/thaw testing of Portland cement and silica fume concretes", S. Jacobsen, 1995:101, ISBN 82-7119-851-3, ISSN 0802-3271.

"Damping of water waves by submerged vegetation. A case study of laminaria

hyperborea", A. M. Dubi, 1995:108, ISBN 82-7119-859-9, ISSN 0802-3271.

"The dynamics of a slope current in the Barents Sea", Sheng Li, 1995:109, ISBN 82-7119-860-2, ISSN 0802-3271.

"Modellering av delmaterialenes betydning for betongens konsistens", Ernst Mørtsell, 1996:12, ISBN 82-7119-894-7, ISSN 0802-3271.

"Bending of thin-walled aluminium extrusions", Birgit Søvik Opheim, 1996:60, ISBN 82-7119-947-1, ISSN 0802-3271.

"Material modelling of aluminium for crashworthiness analysis", Torodd Berstad, 1996:89, ISBN 82-7119-980-3, ISSN 0802-3271.

"Estimation of structural parameters from response measurements on submerged floating tunnels", Rolf Magne Larssen, 1996:119, ISBN 82-471-0014-2, ISSN 0802-3271.

"Numerical modelling of plain and reinforced concrete by damage mechanics", Mario A. Polanco-Loria, 1997:20, ISBN 82-471-0049-5, ISSN 0802-3271.

"Nonlinear random vibrations - numerical analysis by path integration methods", Vibeke Moe, 1997:26, ISBN 82-471-0056-8, ISSN 0802-3271.

"Numerical prediction of vortex-induced vibration by the finite element method", Joar Martin Dalheim, 1997:63, ISBN 82-471-0096-7, ISSN 0802-3271.

"Time domain calculations of buffeting response for wind sensitive structures", Ketil Aas-Jakobsen, 1997:148, ISBN 82-471-0189-0, ISSN 0802-3271.

"A numerical study of flow about fixed and flexibly mounted circular cylinders", Trond Stokka Meling, 1998:48, ISBN 82-471-0244-7, ISSN 0802-3271.

"Estimation of chloride penetration into concrete bridges in coastal areas", Per Egil Steen, 1998:89, ISBN 82-471-0290-0, ISSN 0802-3271.

"Stress-resultant material models for reinforced concrete plates and shells", Jan Arve Øverli, 1998:95, ISBN 82-471-0297-8, ISSN 0802-3271.

"Chloride binding in concrete. Effect of surrounding environment and concrete composition", Claus Kenneth Larsen, 1998:101, ISBN 82-471-0337-0, ISSN 0802-3271.

"Rotational capacity of aluminium alloy beams", Lars A. Moen, 1999:1, ISBN 82-471-0365-6, ISSN 0802-3271.

"Stretch Bending of Aluminium Extrusions", Arild H. Clausen, 1999:29, ISBN 82-471-0396-6, ISSN 0802-3271.

"Aluminium and Steel Beams under Concentrated Loading", Tore Tryland, 1999:30, ISBN 82-471-0397-4, ISSN 0802-3271.

"Engineering Models of Elastoplasticity and Fracture for Aluminium Alloys", Odd-Geir Lademo, 1999:39, ISBN 82-471-0406-7, ISSN 0802-3271.

"Kapasitet og duktilitet av dybelforbindelser i trekonstruksjoner", Jan Siem, 1999:46, ISBN 82-471-0414-8, ISSN 0802-3271.

"Etablering av distribuert ingeniørarbeid; Teknologiske og organisatoriske erfaringer fra en norsk ingeniørbedrift", Lars Line, 1999:52, ISBN 82-471-0420-2, ISSN 0802-3271.

"Estimation of Earthquake-Induced Response", Símon Ólafsson, 1999:73, ISBN 82-471-0443-1, ISSN 0802-3271.

"Coastal Concrete Bridges: Moisture State, Chloride Permeability and Aging Effects", Ragnhild Holen Relling, 1999:74, ISBN 82-471-0445-8, ISSN 0802-3271.

"Capacity Assessment of Titanium Pipes Subjected to Bending and External Pressure", Arve Bjørset, 1999:100, ISBN 82-471-0473-3, ISSN 0802-3271.

"Validation of Numerical Collapse Behaviour of Thin-Walled Corrugated Panels", Håvar Ilstad, 1999:101, ISBN 82-471-0474-1, ISSN 0802-3271.

"Strength and Ductility of Welded Structures in Aluminium Alloys", Miroslaw Matusiak, 1999:113, ISBN 82-471-0487-3, ISSN 0802-3271.

"Thermal Dilation and Autogenous Deformation as Driving Forces to Self-Induced Stresses in High Performance Concrete", Øyvind Bjøntegaard, 1999:121, ISBN 82-7984-002-8, ISSN 0802-3271.

"Some Aspects of Ski Base Sliding Friction and Ski Base Structure", Dag Anders Moldestad, 1999:137, ISBN 82-7984-019-2, ISSN 0802-3271.

"Electrode reactions and corrosion resistance for steel in mortar and concrete", Roy Antonsen, 2000:10, ISBN 82-7984-030-3, ISSN 0802-3271.

"Hydro-Physical Conditions in Kelp Forests and the Effect on Wave Damping and Dune Erosion. A case study on Laminaria Hyperborea", Stig Magnar Løvås, 2000:28, ISBN 82-7984-050-8, ISSN 0802-3271.

"Random Vibration and the Path Integral Method", Christian Skaug, 2000:39, ISBN 82-7984-061-3, ISSN 0802-3271.

"Buckling and geometrical nonlinear beam-type analyses of timber structures", Trond Even Eggen, 2000:56, ISBN 82-7984-081-8, ISSN 0802-3271.

"Structural Crashworthiness of Aluminium Foam-Based Components", Arve Grønsund Hanssen, 2000:76, ISBN 82-7984-102-4, ISSN 0809-103X.

"Measurements and simulations of the consolidation in first-year sea ice ridges, and some aspects of mechanical behaviour", Knut V. Høyland, 2000:94, ISBN 82-7984-121-0, ISSN 0809-103X.

"Kinematics in Regular and Irregular Waves based on a Lagrangian Formulation", Svein Helge Gjøsund, 2000-86, ISBN 82-7984-112-1, ISSN 0809-103X.

"Self-Induced Cracking Problems in Hardening Concrete Structures", Daniela Bosnjak,

2000-121, ISBN 82-7984-151-2, ISSN 0809-103X.

“Ballistic Penetration and Perforation of Steel Plates”, Tore Børvik, 2000:124, ISBN 82-7984-154-7, ISSN 0809-103X.

“Freeze-Thaw resistance of Concrete. Effect of: Curing Conditions, Moisture Exchange and Materials”, Terje Finnerup Rønning, 2001:14, ISBN 82-7984-165-2, ISSN 0809-103X

Structural behaviour of post tensioned concrete structures. Flat slab. Slabs on ground”, Steinar Trygstad, 2001:52, ISBN 82-471-5314-9, ISSN 0809-103X.

“Slipforming of Vertical Concrete Structures. Friction between concrete and slipform panel”, Kjell Tore Fosså, 2001:61, ISBN 82-471-5325-4, ISSN 0809-103X.

“Some numerical methods for the simulation of laminar and turbulent incompressible flows”, Jens Holmen, 2002:6, ISBN 82-471-5396-3, ISSN 0809-103X.

“Improved Fatigue Performance of Threaded Drillstring Connections by Cold Rolling”, Steinar Kristoffersen, 2002:11, ISBN: 82-421-5402-1, ISSN 0809-103X.

“Deformations in Concrete Cantilever Bridges: Observations and Theoretical Modelling”, Peter F. Takâcs, 2002:23, ISBN 82-471-5415-3, ISSN 0809-103X.

“Stiffened aluminium plates subjected to impact loading”, Hilde Giæver Hildrum, 2002:69, ISBN 82-471-5467-6, ISSN 0809-103X.

“Full- and model scale study of wind effects on a medium-rise building in a built up area”, Jónas Thór Snæbjørnsson, 2002:95, ISBN82-471-5495-1, ISSN 0809-103X.

“Evaluation of Concepts for Loading of Hydrocarbons in Ice-infested water”, Arnor Jensen, 2002:114, ISBN 82-417-5506-0, ISSN 0809-103X.

“Numerical and Physical Modelling of Oil Spreading in Broken Ice”, Janne K. Økland Gjøsteen, 2002:130, ISBN 82-471-5523-0, ISSN 0809-103X.

“Diagnosis and protection of corroding steel in concrete”, Franz Pruckner, 20002:140, ISBN 82-471-5555-4, ISSN 0809-103X.

“Tensile and Compressive Creep of Young Concrete: Testing and Modelling”, Dawood Atrushi, 2003:17, ISBN 82-471-5565-6, ISSN 0809-103X.

“Rheology of Particle Suspensions. Fresh Concrete, Mortar and Cement Paste with Various Types of Lignosulfonates”, Jon Elvar Wallevik, 2003:18, ISBN 82-471-5566-4, ISSN 0809-103X.

“Oblique Loading of Aluminium Crash Components”, Aase Reyes, 2003:15, ISBN 82-471-5562-1, ISSN 0809-103X.

“Utilization of Ethiopian Natural Pozzolans”, Surafel Ketema Desta, 2003:26, ISSN 82-471-5574-5, ISSN:0809-103X.

“Behaviour and strength prediction of reinforced concrete structures with discontinuity

regions", Helge Brå, 2004:11, ISBN 82-471-6222-9, ISSN 1503-8181.

"High-strength steel plates subjected to projectile impact. An experimental and numerical study", Sumita Dey, 2004:38, ISBN 82-471-6281-4 (pdf), ISBN 82-471-6282-2 (printed), ISSN 1503-8181.

"Alkali-reactive and inert fillers in concrete. Rheology of fresh mixtures and expansive reactions", Bård M. Pedersen, 2004:92, ISBN 82-471-6401-9 (printed), ISBN 82-471-6400-0 (pdf), ISSN 1503-8181.

"On the Shear Capacity of Steel Girders with Large Web Openings". Nils Christian Hagen, 2005:9 ISBN 82-471-6878-2 (printed), ISBN 82-471-6877-4 (pdf), ISSN 1503-8181.

"Behaviour of aluminium extrusions subjected to axial loading". Østen Jensen, 2005:7, ISBN 82-471-6872-3 (pdf) , ISBN 82-471-6873-1 (printed), ISSN 1503-8181.

"Thermal Aspects of corrosion of Steel in Concrete". Jan-Magnus Østvik, 2005:5, ISBN 82-471-6869-3 (printed) ISBN 82-471-6868 (pdf), ISSN 1503-8181.

"Mechanical and adaptive behaviour of bone in relation to hip replacement", A study of bone remodelling and bone grafting. Sébastien Muller, 2005:34, ISBN 82-471-6933-9 (printed) ISBN 82-471-6932-0 (pdf), ISSN 1503-8181.

"Analysis of geometrical nonlinearities with applications to timber structures". Lars Wollebæk, 2005:74, ISBN 82-471-7050-5 (printed), ISBN 82-471-7019-1 (pdf), ISSN 1503-8181.

"Pedestrian induced lateral vibrations of slender footbridges", Anders Rönnquist, 2005:102, ISBN 82-471-7082-5 (printed), ISBN 82-471-7081-7 (pdf), ISSN 1503-8181.

"Initial Strength Development of Fly Ash and Limestone Blended Cements at Various Temperatures Predicted by Ultrasonic Pulse Velocity", Tom Ivar Fredvik, 2005:112, ISBN 82-471-7105-8 (printed), ISBN 82-471-7103-1 (pdf), ISSN 1503-8181.

"Behaviour and modelling of thin-walled cast components", Cato Dørum, 2005:128, ISBN 82-471-7140-6 (printed), ISBN 82-471-7139-2 (pdf), ISSN 1503-8181.

"Behaviour and modelling of selfpiercing riveted connections", Raffaele Porcaro, 2005:165, ISBN 82-471-7219-4 (printed), ISBN 82-471-7218-6 (pdf), ISSN 1503-8181.

"Behaviour and Modelling og Aluminium Plates subjected to Compressive Load", Lars Rønning, 2005:154, ISBN 82-471-7169-1 (printed), ISBN 82-471-7195-3 (pdf), ISSN 1503-8181

"Bumper beam-longitudinal system subjected to offset impact loading", Satyanarayana Kokkula, 2005:193, ISBN 82-471-7280-1 (printed), ISBN 82-471-7279-8 (pdf), ISSN 1503-8181.

"Control of Chloride Penetration into Concrete Structures at Early Age", Guofei Liu, 2006:46, ISBN 82-471-7838-9 (printed), ISBN 82-471-7837-0 (pdf), ISSN 1503-8181.

"Modelling of Welded Thin-Walled Aluminium Structures", Ting Wang, 2006:78, ISBN 82-471-7907-5 (printed), ISBN 82-471-7906-7 (pdf), ISSN 1503-8181.

"Time-variant reliability of dynamic systems by importance sampling and probabilistic analysis of ice loads", Anna Ivanova Olsen, 2006:139, ISBN 82-471-8041-3 (printed), ISBN 82-471-8040-5 (pdf), ISSN 1503-8181.